AFRL-RX-WP-TR-2008-4176

ACCELERATED METALS DEVELOPMENT BY COMPUTATION

Hamish L. Fraser, Michael J. Mills, Rudolph G. Buchheit, Yunzhi Wang, Somnath Ghosh, James C. Williams, Gerald S. Frankel, Anthony D. Rollett, and Alten F. Grandt

The Ohio State University

FEBRUARY 2008
Final Report

STINFO COPY

AIR FORCE RESEARCH LABORATORY
MATERIALS AND MANUFACTURING DIRECTORATE
WRIGHT-PATTERSON AIR FORCE BASE, OH 45433-7750
AIR FORCE MATERIEL COMMAND
UNITED STATES AIR FORCE

NOTICE AND SIGNATURE PAGE

Using Government drawings, specifications, or other data included in this document for any purpose other than Government procurement does not in any way obligate the U.S. Government. The fact that the Government formulated or supplied the drawings, specifications, or other data does not license the holder or any other person or corporation; or convey any rights or permission to manufacture, use, or sell any patented invention that may relate to them.

This report was cleared for public release by the Air Force Research Laboratory Wright-Patterson Air Force Base (AFRL/WPAFB) Public Affairs Office (PAO) and is available to the general public, including foreign nationals. Copies may be obtained from the Defense Technical Information Center (DTIC) (http://www.dtic.mil).

AFRL-RX-WP-TR-2008-4176 HAS BEEN REVIEWED AND IS APPROVED FOR PUBLICATION IN ACCORDANCE WITH ASSIGNED DISTRIBUTION STATEMENT.

This report is published in the interest of scientific and technical information exchange and its publication does not constitute the Government's approval or disapproval of its ideas or findings.

*Disseminated copies will show "//Signature//" stamped or typed above the signature blocks.

REPORT DOCUMENTATION PAGE

Form Approved
OMB No. 0704-0188

The public reporting burden for this collection of information is estimated to average 1 hour per response, including the time for reviewing instructions, searching existing data sources, searching existing data sources, gathering and maintaining the data needed, and completing and reviewing the collection of information. Send comments regarding this burden estimate or any other aspect of this collection of information, including suggestions for reducing this burden, to Department of Defense, Washington Headquarters Services, Directorate for Information Operations and Reports (0704-0188), 1215 Jefferson Davis Highway, Suite 1204, Arlington, VA 22202-4302. Respondents should be aware that notwithstanding any other provision of law, no person shall be subject to any penalty for failing to comply with a collection of information if it does not display a currently valid OMB control number. **PLEASE DO NOT RETURN YOUR FORM TO THE ABOVE ADDRESS.**

1. REPORT DATE *(DD-MM-YY)*	2. REPORT TYPE	3. DATES COVERED *(From - To)*
February 2008	Final	01 September 2001 – 30 December 2007

4. TITLE AND SUBTITLE
ACCELERATED METALS DEVELOPMENT BY COMPUTATION

5a. CONTRACT NUMBER
F33615-01-2-5225

5b. GRANT NUMBER

5c. PROGRAM ELEMENT NUMBER
62102F

6. AUTHOR(S)

Hamish L. Fraser, Michael J. Mills, Rudolph G. Buchheit, Yunzhi Wang, Somnath Ghosh, James C. Williams, and Gerald S. Frankel (The Ohio State University)
Anthony D. Rollett (Carnegie Mellon University)
Alten F. Grandt (Purdue University)

5d. PROJECT NUMBER
4347

5e. TASK NUMBER
21

5f. WORK UNIT NUMBER
43472104

7. PERFORMING ORGANIZATION NAME(S) AND ADDRESS(ES)

The Ohio State University
The Department Materials Science and Engineering
2041 College Road
Columbus, OH 43210

Carnegie Mellon University

Purdue University

8. PERFORMING ORGANIZATION REPORT NUMBER

9. SPONSORING/MONITORING AGENCY NAME(S) AND ADDRESS(ES)
Air Force Research Laboratory
Materials and Manufacturing Directorate
Wright-Patterson Air Force Base, OH 45433-7750
Air Force Materiel Command
United States Air Force

10. SPONSORING/MONITORING AGENCY ACRONYM(S)
AFRL/RXLM

11. SPONSORING/MONITORING AGENCY REPORT NUMBER(S)
AFRL-RX-WP-TR-2008-4176

12. DISTRIBUTION/AVAILABILITY STATEMENT
Approved for public release; distribution unlimited.

13. SUPPLEMENTARY NOTES
PAO Case Number: WPAFB 08-3115, 29 Apr 2008. Report contains color.

14. ABSTRACT
This program was centered upon the formation of the Collaborative Center for Materials Design (CCMD), an entity coupled with Ohio State University's (OSU) Center for the Accelerated Maturation of Materials (CAMM). There are two foci upon which CCMD, established by the Cooperative Agreement F33615-01-2-5225, is based, the first promoting and developing a strong interaction between scientists and technologists at AFRL and faculty, post-doctoral fellows and research students comprising the team centered at the OSU and the second involving research aimed at furthering the ability to accelerate the maturation and insertion of materials, specifically metals and alloys of interest to the Air Force. The overall technical theme, namely accelerated metals development, represents a problem of tremendous interest to the Air Force. The research areas studies were developed and evolved in three phases of effort. In phase 1, four sub-programs were initiated and these have evolved into five tasks, namely Tasks 1, 2, 3, 4 and 8. Phase two involved the initiation of three additional tasks which evolved into Tasks 5, 6, and 7. Phase 3 involved the initiation of the remaining Tasks 9, 10 and 11. All of these tasks make a contribution to the general theme of the accelerated maturation/insertion of materials.

15. SUBJECT TERMS

16. SECURITY CLASSIFICATION OF:			17. LIMITATION OF ABSTRACT:	18. NUMBER OF PAGES	19a. NAME OF RESPONSIBLE PERSON (Monitor)
a. REPORT Unclassified	**b. ABSTRACT** Unclassified	**c. THIS PAGE** Unclassified	SAR	216	Kenneth Davidson
					19b. TELEPHONE NUMBER *(Include Area Code)* N/A

Standard Form 298 (Rev. 8-98)
Prescribed by ANSI Std. Z39-18

TABLE OF CONTENTS

Each Task includes:

   I. RESULTS and DISCUSSION
     1. Introduction
     2. Methods, Assumptions, Procedures
     3. Results
     4. Discussion
     5. Conclusions
     6. Recommendations
     7. References
     8. Names of Personnel (PI (s), Students, Pos Docs, AFRL Mentors)

Collaborative Center for Materials Design

A Proposed Continuation to the Cooperative Agreement F33615-01-2-5225,
"Accelerated Metals Development by Computation"

The Cooperative Agreement, "Accelerated Metals Development by Computation," F33615-01-2-5225, was centered upon the formation of the Collaborative Center for Materials Design (CCMD), an entity coupled with Ohio State University's (OSU) Center for the Accelerated Maturation of Materials (CAMM). This agreement was started in response to an Air Force Research Laboratory (AFRL) "Science and Technology Workforce for the 21st Century (STW-21)" initiative to shape the AFRL science and engineer workforce by providing workforce agility and responsiveness to deal with dynamic technical and resource challenges. The goal was to provide the opportunity for increase collaboration with world-class technology leaders by promoting and developing a strong interaction between scientists and technologists at AFRL and the faculty, post-doctoral fellows and research students comprising the team centered at the OSU. The research was aimed at furthering the ability to accelerate the maturation and insertion of materials, specifically metals and alloys of interest to the Air Force. The effort was jointly sponsored by the Air Force Office of Scientific Research (AFOSR) and Materials and Manufacturing Directorate (AFRL/RX). These collaborations allowed AFRL/RX to augment its staff, facilities, and equipment by leveraging the resources of OSU. This program focused on accelerating materials development through improved modeling and simulation methods, and innovative experiments using advanced instrumentation. This partnership took advantage of OSU's international reputation in metallurgical materials and processes and its status as a corrosion center of excellence. The overall technical theme, namely accelerated metals development, represents a problem of tremendous interest to the Air Force. In the following, a summary of the efforts of the CCMD is presented.

The program of research that has been developed under this Cooperative Agreement has been extremely successful regarding meeting its objectives. Thus, not only has the interaction between personnel from both sides (i.e., academia and the Air Force) been established and promoted but also the technical effort has yielded several notable successes. These advances in science and technology are described in detail below. Key to the success of this program of research is access to state-of-the-art equipment. A major outcome of this program based on the STW-21 Initiative has been the acquisition of major equipment items, detailed below, purchased with Air Force and significant cost-sharing funds from OSU and the State of Ohio.

Regarding the research areas studies, detailed descriptions are given below. Here, the specific tasks are identified. These were developed and evolved in three phases of effort. In phase 1, four sub-programs were initiated and these have evolved into five tasks, namely Tasks 1, 2, 3, 4 and 8 (see list below). Phase two involved the initiation of three additional tasks which evolved into Tasks 5, 6, and 7. Phase 3 involved the initiation of the remaining Tasks 9, 10 and 11. All of these tasks make a contribution to the general theme of the accelerated maturation/insertion of materials. The sustaining tasks are as follows:

Tasks
Task 1. Microsample Mechanical Testing of a Single Crystal Nickel Based Superalloy
Task 2. Development of Constitutive Relations from Phase Field Modeling of Microstructural Evolution
Task 3. Modeling and Experiment for Accelerated Insertion of Corrosion Resistant Structural Components
Task 4. Development of Image- Based Crystal Plasticity Computational Models for Fatigue Analysis
Task 5. Accelerated Assessment and Representation of Materials Behavior via Integrated Electron-Optical, Focused Ion beam and MEMS-based Characterization Methods
Task 6. Physically-based Monte-Carlo Models of Grain Growth and Texture Evolution
Task 7. Development of Microstructurally-Based Models for the Prediction of the Fatigue Response in Ti Alloys
Task 8. Microstructural Representation for Development of Materials Prognosis Methodologies
Task 9. Quantification of High Cycle Fatigue Damage Mode Dependence on Microstructure
Task 10. Development and Characterization of high Temperature Titanium Alloys for High Mach Aerospace Structural Applications
Task 11. Development of a Methodology for Hydrogen Embrittlement Resistance

As noted above, a key goal of the CCMD was to promote interaction and collaboration between academics, including faculty, post-doctoral fellows and students and researchers from AFRL, the latter persons including scientists and technologists on UES on-site contracts. Of course, in some instances equipment necessary to perform the research would be found only at OSU which limited the amount of time a given student could spend at AFRL, but in the main the collaborative efforts were highly successful. This aspect of the program has been particularly successful. The collaborating members of CCMD are listed below.

Personnel

- *Faculty*
  Rudy Buchheit
  Gerald Frankel
  Hamish Fraser
  Somnath Ghosh
  Alten Grandt (Purdue)
  Michael Mills
  Anthony Rollett (CMU)
  Jim Williams
  Yunzhi Wang

- *AFRL (& UES) Mentors*
  Jeff Calcaterra
  Donna Ballard
  Dennis Dimiduk
  Daniel Evans
  Pat Golden
  Dallis Hardwick
  Kumar Jata
  James Larsen
  Patrick Martin
  Ryan Morrissey
  Andy Rosenberger
  Lee Semiatin
  Jeff Simmons
  Jay Tiley
  Michael Uchic
  Youhai Wen
  Robert Wheeler

- *Post-doctoral fellows*
  Rajarshi Banerjee
  Peter Collins
  Vladimir Levitt
  Babu Viswanathan

- *Students*
  Daniel Garcia (Purdue)
  N. Gingo
  Michael Groeber
  X. Liu
  David Norfleet
  Ben Peterson
  Alison Polasik
  Stephen Polasik
  Christopher Roberts (CMU)
  Paul Shade
  Billie Wang
  Robert Williams

An important aspect of the program has involved the acquisition of a significant number of highly sophisticated pieces of equipment. A comprehensive list of the equipment acquired is given below. Emphasis should be made regarding the quality of the instrumentation. Thus, based on these acquisitions, it is fair to say that the Materials Characterization Facility at AFRL has become without doubt the premier materials characterization facility in the Department of Defense, and CAMM's facilities at OSU are without question the leading such facility in any academic department, probably world-wide. Both of these facilities are now, as a result of this program, truly *world-class*. In many ways, collaboration has been the basis of choice of instruments to purchase. An example can be given regarding the acquisition of the two FEI Titan

80-300 (S)TEM instruments. Thus, the configuration of the instrument at AFRL, the image corrected instrument, is such as to maximize high resolution transmission electron microscopy while also providing Z-contrast and analytical electron microscopy capabilities. In contrast, the instrument at OSU, with the monochromator, probe corrector and ultra-high resolution GIF, optimizes performance for Z-contrast imaging in STEM and analytical electron microscopy (i.e., spectroscopy). It is
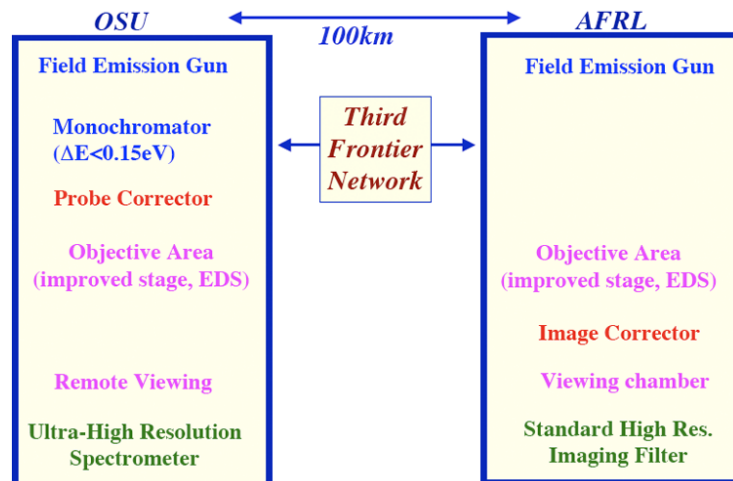
Figure 1. OSU/AFRL Microscope Concept

intended to make use of these two instruments remotely, as depicted in Fig. 1, once the problems regarding AFRL's firewall have been solved. The performance of the instrument currently being installed at AFRL was first assessed at OSU, see Fig. 2, and subsequently, the probe-corrected instrument has been installed at OSU, Fig.3. A list of the equipment acquired during this program follows.

Equipment
- OIM facilities on all dual-beams and three SEMs
- Energy Dispersive X-ray Spectrometers and Phase ID
- Automated Optical Metallography
- Two Nova Dual-Beam Focused Ion Beam instruments
- Helios Dual-Beam Focused Ion Beam instrument
- Electro-thermal mechanical test system
- FEI Titan 80-300 FEG (S)TEM, with a spherical aberration corrector for the probe, electron source monochromator, ultrahigh resolution GIF, and EDS
- FEI Titan 80-300 FEG (S)TEM, with a spherical aberration corrector for the image, GIF, and EDS
- Electron microprobe
- FEG Ultra-high resolution SEM
- Orientation Imaging Microscope
- Heat Treatment and Testing Facility
- Five 4PI systems

In the following sections of this report, a detailed assessment of progress made in each of the tasks is given.

4
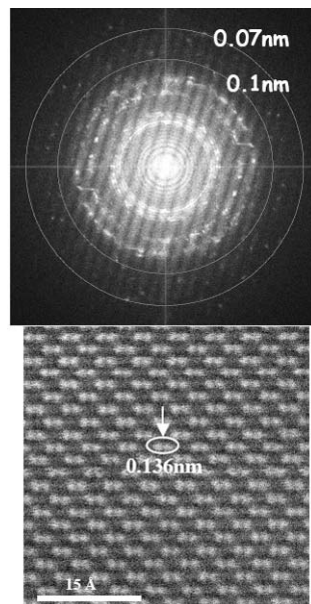
Figure 2. Installation and Performance of CCMD's Image-Corrected Titan

Figure 3. Installation of CCMD's Titan with probe-corrected and monochromator

Task 1
Microsample Mechanical Testing of a Single Crystal Nickel Based Superalloy
Hamish Fraser (OSU Faculty Member), Michael Uchic (AFRL/RX Mentor), Dennis Dimiduk
(AFRL/RX Mentor), Robert Wheeler (UES Mentor), Paul Shade (OSU Graduate Student)

I. RESULTS and DISCUSSION

1. Introduction

Recent technological developments, such as the widespread availability of focused ion beam (FIB) microscopes, have enabled specimen fabrication and testing at the micron scale. One example has been the development of a micro-compression test methodology which involves the machining of micron scale cylindrical specimens via the FIB and subsequently testing these in uniaxial compression in a nanoindenter equipped with a flat punch diamond tip [1,2]. Studies which have incorporated the micro-compression technique include those on single-crystal Au [3-5], Ni [6], Cu [7], LiF [8] and Mo alloy [9]. Advantages of testing at this scale include the ability to probe localized material properties (i.e. measure the 'single-crystal' response of individual grains in a polycrystalline material) and search for intrinsic size effects. Localized material properties may also be measured with other techniques such as indentation, however, the complicated stress and strain states combined with possible strain gradient effects [10] make interpretation difficult. The micro-compression test methodology provides a small scale property measurement technique which is applicable to practically any inorganic material and allows for the collection of conventional stress-strain flow curves in the absence of strain gradients [1]. Size effects, and the idea that smaller is stronger, has been a common theme of materials science, where classic strength / size scale relations include the strengthening of a metallic matrix by grain boundaries or particles [11]. However, traditional elasticity and plasticity theories have not incorporated a length scale and thus ignore size scale effects [12]. The development of micro-fabrication technologies, such as the fabrication of thin films or micro-machined components used in microelectronic and micromechanical applications has renewed interest in understanding behavior at small length scales [11,12].

The material chosen for this work is Rene N5, a second generation single-crystal nickel based superalloy commonly used in turbine blade applications [13]. The composition of Rene N5 is nominally Ni-8Co-7Cr-7Ta-6.2Al-5W-3Re-2Mo-0.2Hf [13]. Despite being a single-crystal engineering alloy, Rene N5 contains heterogeneities at multiple scales. Figure 1A is a low magnification backscatter electron image which shows a dendritic macro-structure as well as the presence of carbide particles and micro-porosity located between the dendrite arms. At a higher magnification, Figure 1B shows that Rene N5 consists of a Ni matrix (white) with a high volume fraction of cuboidal Ni_3Al precipitates (dark). The Ni matrix phase is called γ and has the FCC crystal structure while the Ni3Al precipitates are known as γ' and have the ordered $L1_2$ crystal structure. An a/2 <1 -1 0> {111} dislocation traveling in the γ phase will form an anti-phase boundary (APB) upon cutting a γ' particle and as such, these dislocations must travel through the structure in pairs [14]. Additionally, screw dislocations in the γ' phase may experience a cross-slip locking process, a topic of significant debate and interest [15-17]. These briefly mentioned factors may cause a significant deviation in behavior from the single crystal pure metal micro-compression studies reported in detail in the literature.
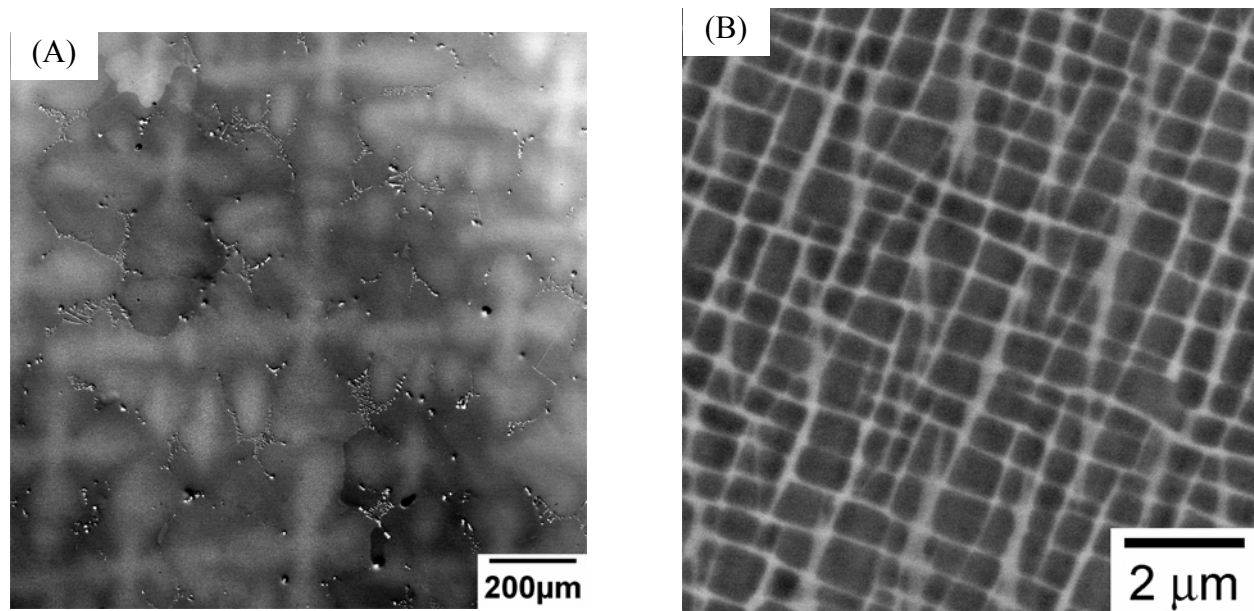
Figure 1. Electron backscatter images of Rene N5. (A) Low magnification, showing a dendritic macro-structure and the presence of carbides and micro-porosity. (B) High magnification, showing the g/g' microstructure.

The aim of this work is to continue the development of small scale mechanical testing techniques while applying them to the industrially relevant engineering alloy Rene N5. While preliminary micro-compression results have been reported for another nickel based superalloy [1,2], that study was based on an experimental alloy, included tests from a limited specimen size range and tested in a multiple slip orientation which may complicate interpretation. Further, that study ignored the location of samples relative to the underlying structure [1,2]. Desired outcomes include determining if Rene N5 experiences a size effect, if there is a transition size from bulk to size-affected behavior and understanding the underlying deformation mechanisms. The localized property measurements afforded by small scale testing will be exploited to assess the local mechanical properties in various regions of the dendritic macro-structure. Additionally, efforts will be undertaken to develop SEM based in-situ small scale mechanical testing techniques, with the intent of gaining insight into the spatial and temporal evolution of deformation structures [18]. The ability to manipulate and test inside the SEM makes more complex test setups, such as micro-tension, feasible.

2. Methods, Assumptions, Procedures

Micro-compression specimens have been fabricated using FEI dual beam FIB models DB235 and Nova. As part of this work, a microscope control script has been developed which fully automates the machining of multiple micro-compression samples. An example specimen is shown in Figure 2. Samples have been machined with an aspect ratio of 2.3:1 and a diameter range of 2.5-40 μm. The micro-compression specimens were tested at room temperature with a MTS Nano XP nanoindenter. The imposed strain rate for most of the testing was 10^{-4} s^{-1}, although the nanoindenter is inherently a load-controlled system and allows for the observation of rapid strain bursts. The data acquisition rate was 50 Hz. A detailed account of the micro-compression specimen fabrication and testing methodology can be found in [2,3,6].
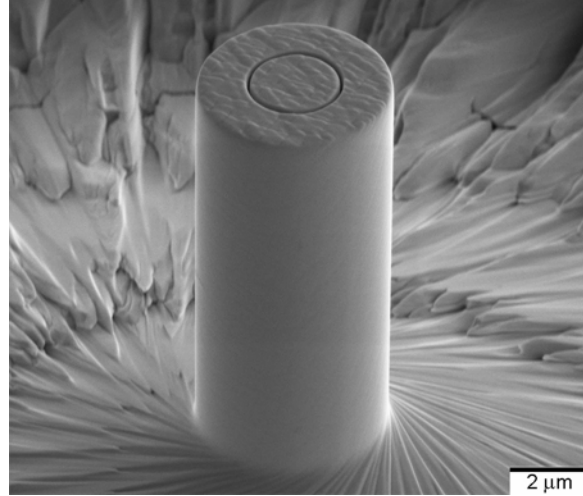
Figure 2. Typical micro-compression sample.

Electron probe micro analysis (EPMA) was conducted with a Cameca SX100 to analyze variations in chemical concentration. An example of how concentration varies across a dendrite is shown in Figure 3. Note that W and Re are enriched in the dendrite core while Al and Ta are depleted. Scanning electron microscopy (SEM) was conducted with FEI and Leica microscopes to assess variations in microstructure. One of the goals of this study has been to account for the chemical concentration (Figure 3) and structural (Figure 1A) variability. As such, initial specimens were machined at dendrite cores to keep chemical concentration nominally constant and avoid the presence of carbides and micro-porosity. In later experiments, samples were machined both inside and outside of dendrite arms and the composition of each specimen was measured using EPMA. Figure 4 is an image of several specimens machined both inside and outside of dendrite cores.
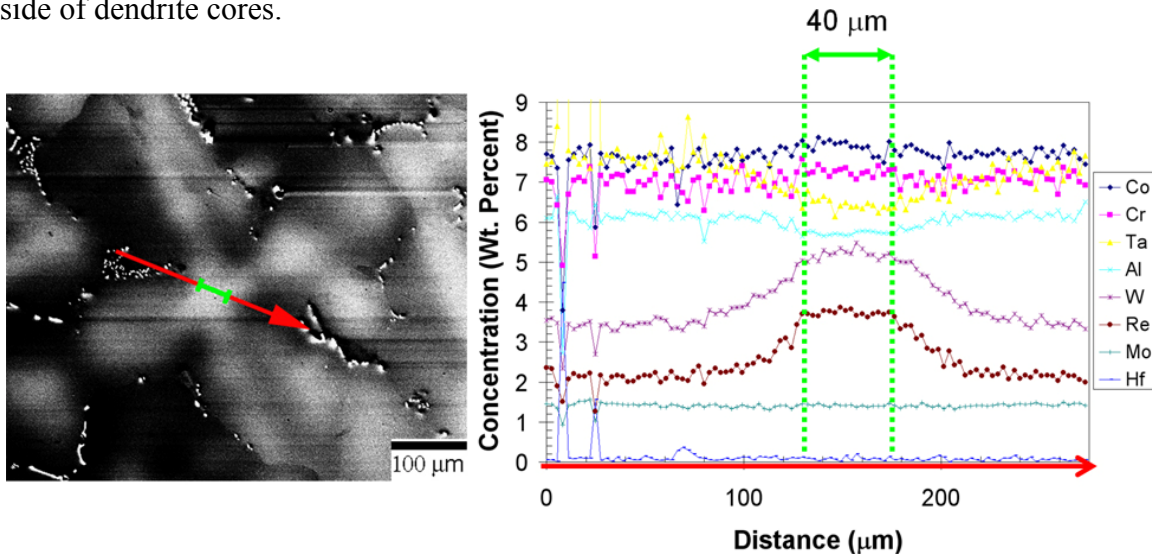
Figure 3. EPMA scan across a dendrite. Note that W and Re are enriched in the dendrite core while Al and Ta are depleted.
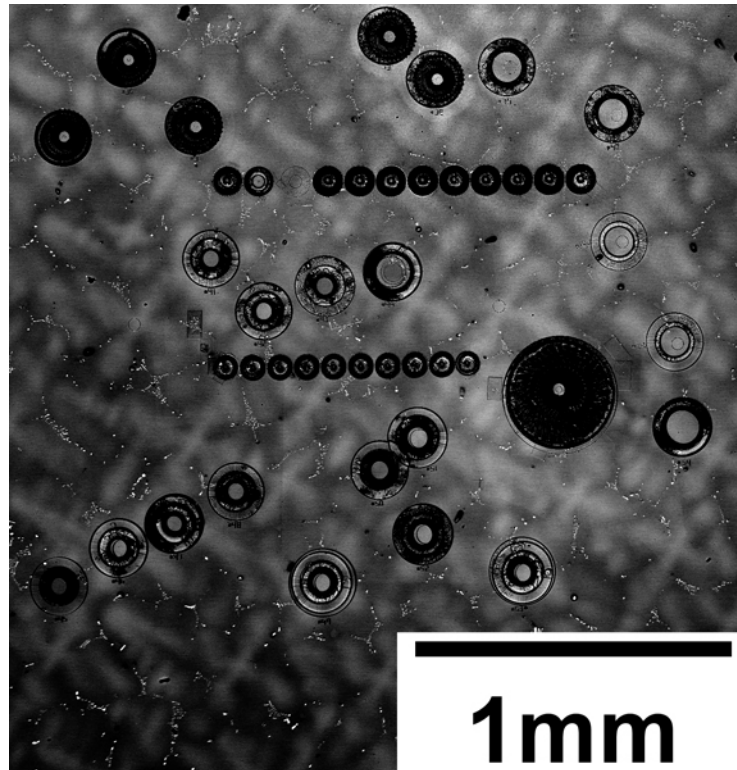
Figure 4. Example of micro-compression samples
machined both inside and outside of dendrite cores.

The Laue technique was used to crystallographically orient specimen compression axes. The majority of the testing was done with a <1 2 3> compression axis (single-slip orientation) although <1 1 1> (multiple-slip orientation) specimens have also been tested. Room temperature bulk compression tests on <1 2 3> oriented samples were conducted for comparison.

Extensive efforts have been undertaken to extend the micro-compression testing technique to the SEM. A piezoelectric positioning stage is used to align samples with a flat punch diamond tip. Loads are measured with a 100 g load cell and are applied with a piezoelectric linear actuator. Figure 5 shows the construction of the in-situ test rig. Labview based software has been developed which automates force actuation, data acquisition and control of the microscope. Another Labview based program has been developed to calculate strain by using image correlation to track displacements. The in-situ test rig can be modified by replacing the diamond compression platen with a SiC fiber in which a grip for tension samples has been machined. Figure 6 shows this modification. Additionally, compression testing with a SiC fiber, which minimizes lateral stiffness of the compression platen, has been explored. Micro-compression and micro-tension samples are machined with the FIB at the edge of a bulk sample. A large amount of material needs to be removed in order to provide a clear view of the samples during testing and so a Sarix micro-EDM is used to pre-machine the in-situ samples.
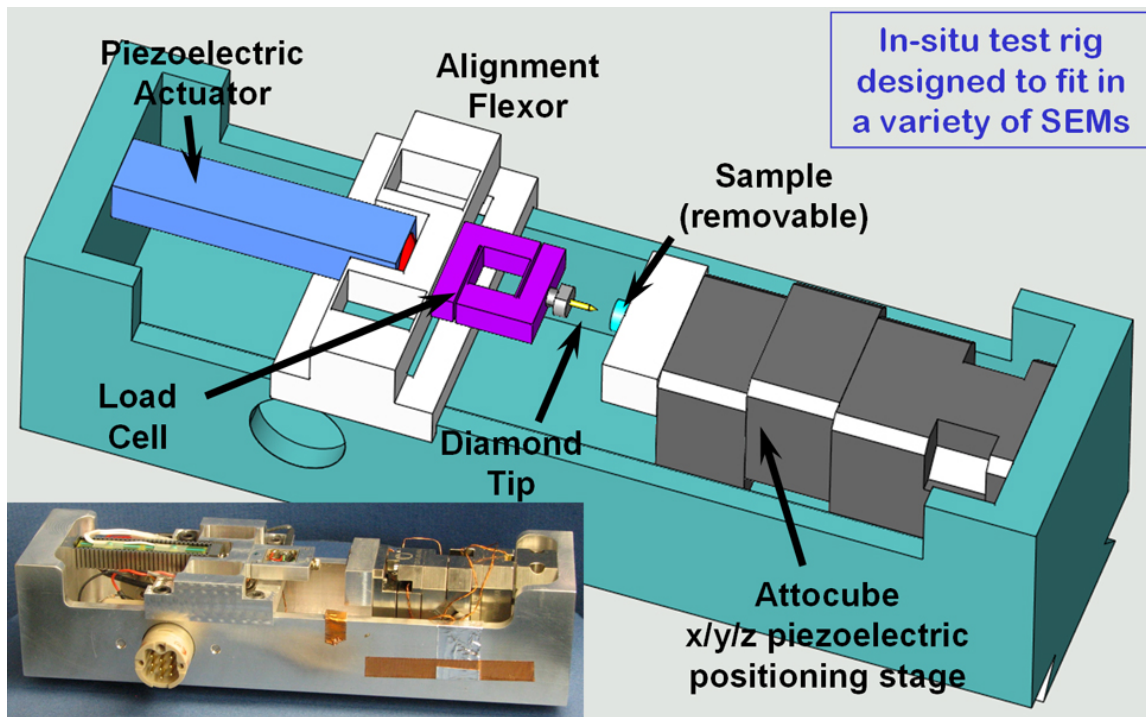
Figure 5. In-situ mechanical test rig.
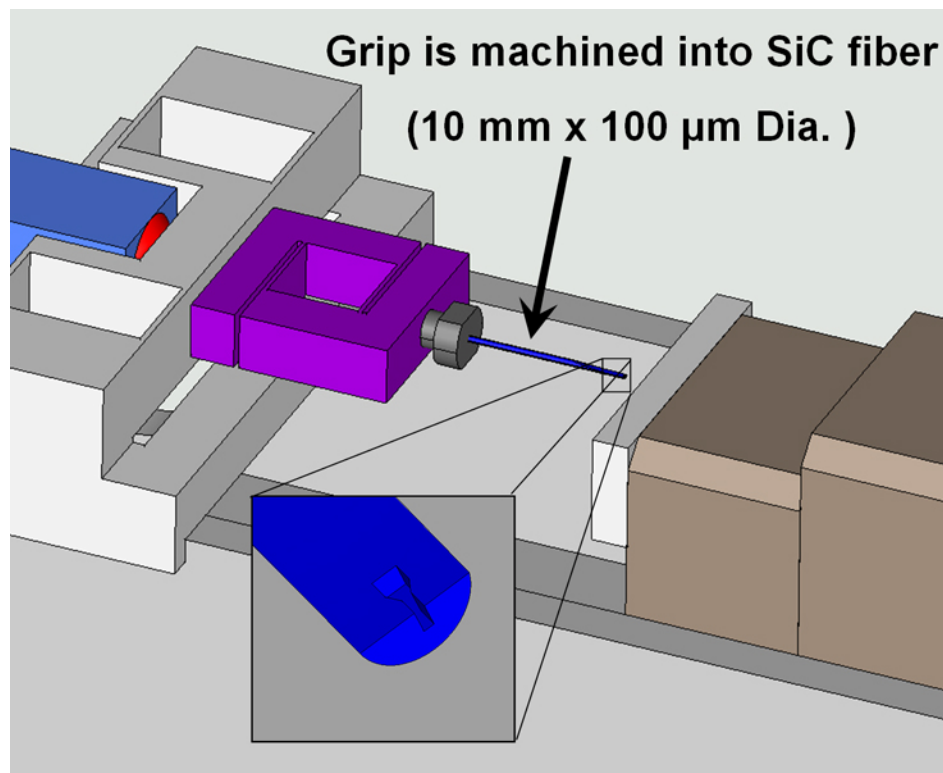
Figure 6. Modification of the in-situ test rig to conduct micro-tension experiments.

3. Results and Discussion

Engineering stress-strain curves for <1 2 3> oriented dendrite core samples with a diameter of 20 μm are shown in Figure 7A. In the figure, a bulk compression test with the same orientation is shown in blue for comparison. The bulk test yields at an engineering stress of ~930 MPa, initially work hardens at a rate of 1200 MPa and changes to a work hardening rate of 3500 MPa around 4 % strain. The micro-sample curves are noticeably different than the bulk tests. The yield stress is stochastic but always elevated above that of bulk. Following yield, the micro-samples experience a period of almost no work hardening. At about 8 % engineering strain, the micro-samples begin work hardening at an average rate of 1200 MPa. Notice, however, that the micro-sample work hardening is actually composed of strain bursts with no work hardening followed by periods of very rapid hardening ('stair-step' shape). Figure 7B is post-test image of a typical 20 μm diameter sample. First, note that deformation is confined to the gage section (center of crystal, not contacting the diamond platen or sample base). Second, note that the slip bands are finely distributed (no single dominant slip band which produces much of the deformation). The stochastic flow stress, strain bursts and 'stair-step' hardening have been observed in prior micro-compression testing [1-6,8]. Clearly, size effects are being observed even for 20 μm diameter samples. This is somewhat surprising in that these samples have in excess of 40 γ' precipitates spanning their width. 10 μm diameter specimens have shown a similar response, although with a flow stress elevated above that of the 20 μm samples.

(A)
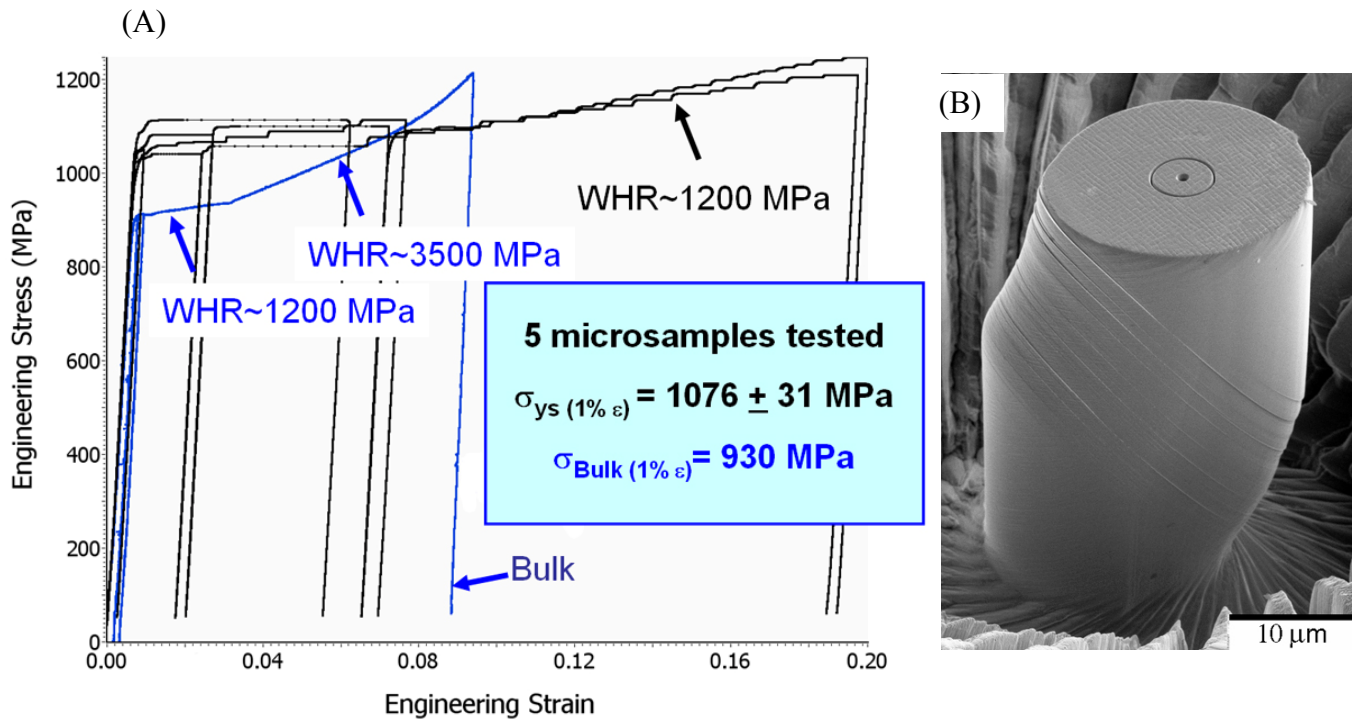
Figure 7. (A) Engineering stress-strain curves from nanoindenter testing of <1 2 3> oriented dendrite core samples with a diameter of 20 mm. (B) Typical 20 mm diameter sample following testing.

Figure 8A shows a series of engineering stress-strain curves for 5 μm diameter specimens with a <1 2 3> compression axis and located at dendrite cores. A bulk test is again included for reference. Note that a stochastic flow stress, strain bursts and 'stair-step' hardening are again observed in the micro-samples. The 5 μm diameter samples have a flow stress elevated above both the bulk and 20 μm diameter tests. The 5 μm diameter tests do not, however, show the initial low work hardening period at low strains as in the 20 μm samples. Rather, they experience very rapid hardening at small strains followed by a stable work hardening rate of on average 1500 MPa. When a flow stress of 1400 MPa is reached, the samples deform rapidly and uncontrollably. Figure 8B is a post-test image of a typical 5 μm diameter sample. Note that again the deformation is confined to the sample gage section. In this case, however, the deformation is limited to a few dominant slip bands. In fact, in many of the tests a correlation can be found between the number of dominant slip bands and the number of large strain bursts observed. 2.5 μm diameter samples behaved similarly but with a higher small-strain hardening rate, further elevated flow stress and even more localized slip bands.
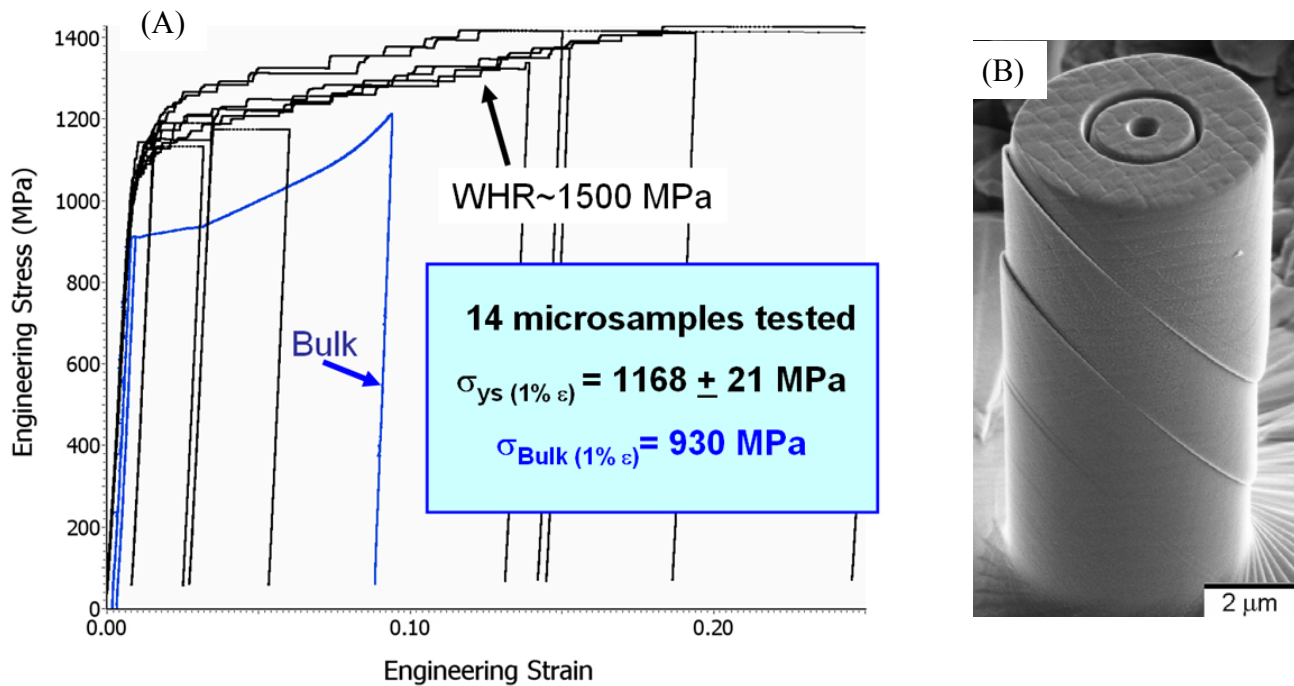
Figure 8. (A) Engineering stress-strain curves from nanoindenter testing of <1 2 3> oriented dendrite core samples with a diameter of 5 μm. (B) Typical 5 μm diameter sample following testing.

Figure 9 is a plot with representative engineering stress-strain curves from a range of sample sizes in <1 2 3> oriented compression tests from dendrite cores. There are several interesting details to note from the plot. First, that the behavior of Rene N5 can clearly be affected by sample size. Next, note that the work hardening rate at low strains is strongly affected by sample size, with smaller samples hardening more rapidly. The elastic limit for the different tests does not vary much, particularly for 2.5-20 μm diameter samples. However, a comparison of flow stresses at 1% strain shows a size effect and a comparison at 5% strain shows an even stronger size effect. Additionally, the intermittency of deformation (stair-step nature of curves) becomes

12

more apparent for smaller samples. The 40 μm diameter samples also behave differently than bulk, which is perhaps surprising in that more than 80 γ' particles span the width of the crystal. It should be noted, however, that the difference in behavior between bulk tests and the 40 μm diameter samples is likely not entirely attributable to size effects.   The micro-samples were machined at dendrite cores to keep chemical concentration and structure a constant which means the micro-sample tests were conducted on effectively a different material than the bulk tests.
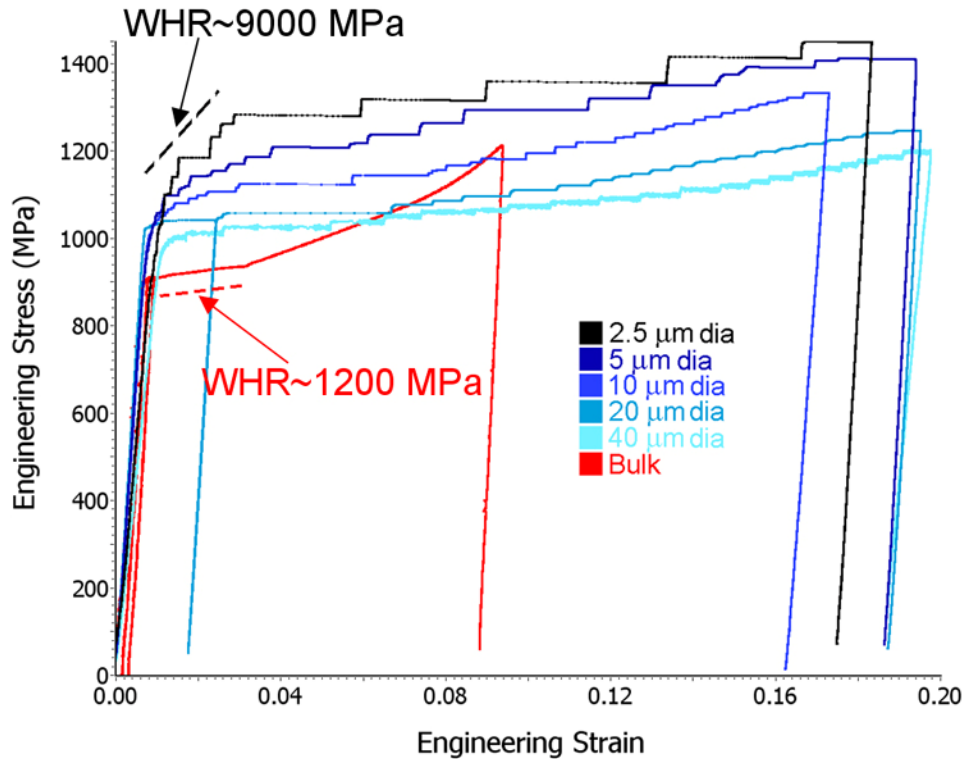
Figure 9. Representative engineering stress-strain curves from a range of sample sizes in <1 2 3> oriented dendrite core compression tests.

<1 2 3> oriented micro-compression tests were also conducted outside of the dendrite cores. Figure 10 is a plot of 1% engineering flow stress versus Re concentration for 5 and 10 μm diameter samples. The use of Re concentration for the x-axis is not meant to suggest that the trends in the plot are solely or even partially due to changes in Re content.   Rather, the concentration of Re can be used as a measure for distance from a dendrite core, with higher concentrations of Re being closer to a core. Note that for 5 μm diameter samples there is a lot of scatter, with inter-dendritic samples being softer than those near a dendrite core.   This is contrasted by the 10 μm diameter samples, which show less dependence of flow stress on sample location.   Figure 11 is a log-log scaling plot of 1% engineering flow stress versus sample diameter for <1 2 3> oriented micro-compression samples both in and out of dendrite cores. Included in the plot is data from the experimental alloy, UM F19, provided in [2]. Note that the large scatter in the UM F19 data, which was measured in random locations, matches reasonably well with the Rene N5 data when both core and non-core data points are included. Also note from the plot that testing from larger sized micro-samples is needed to determine a transition to bulk behavior.
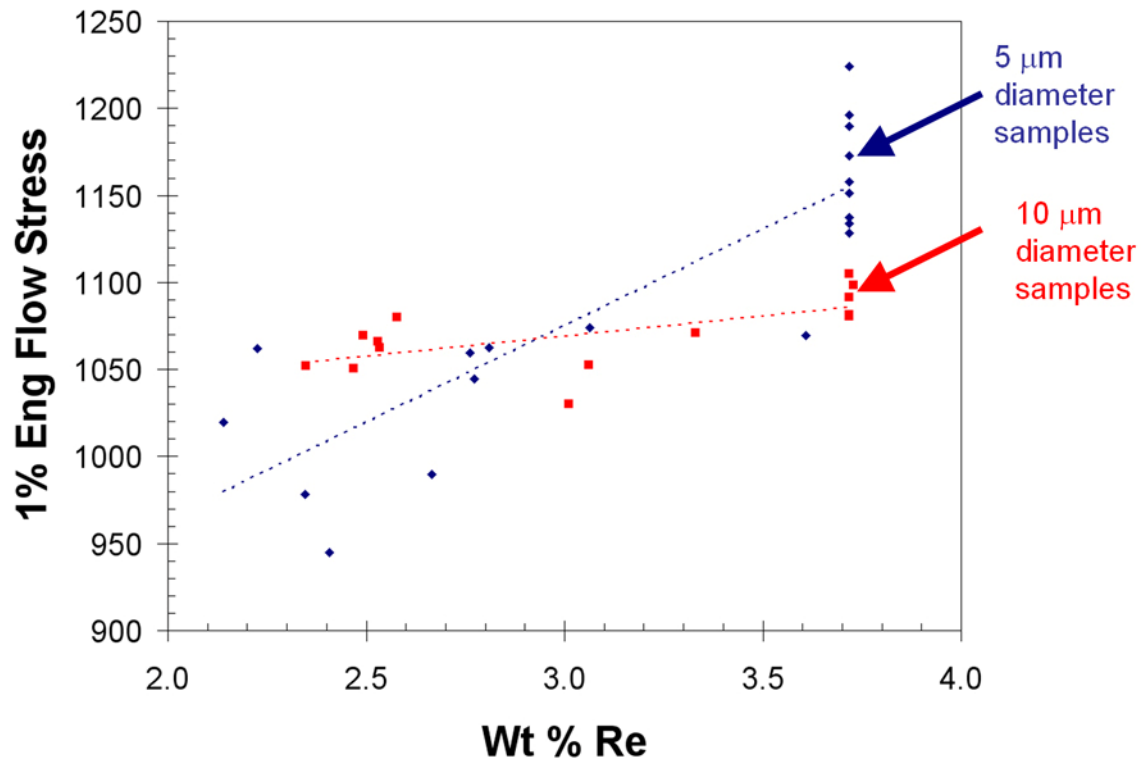
Figure 10. Variation in 1% engineering flow stress for 5 and 10 mm diameter <1 2 3> oriented micro-compression tests. The x-axis should be used as a measure for distance from dendrite core, with higher concentrations of Re being closer to the core.
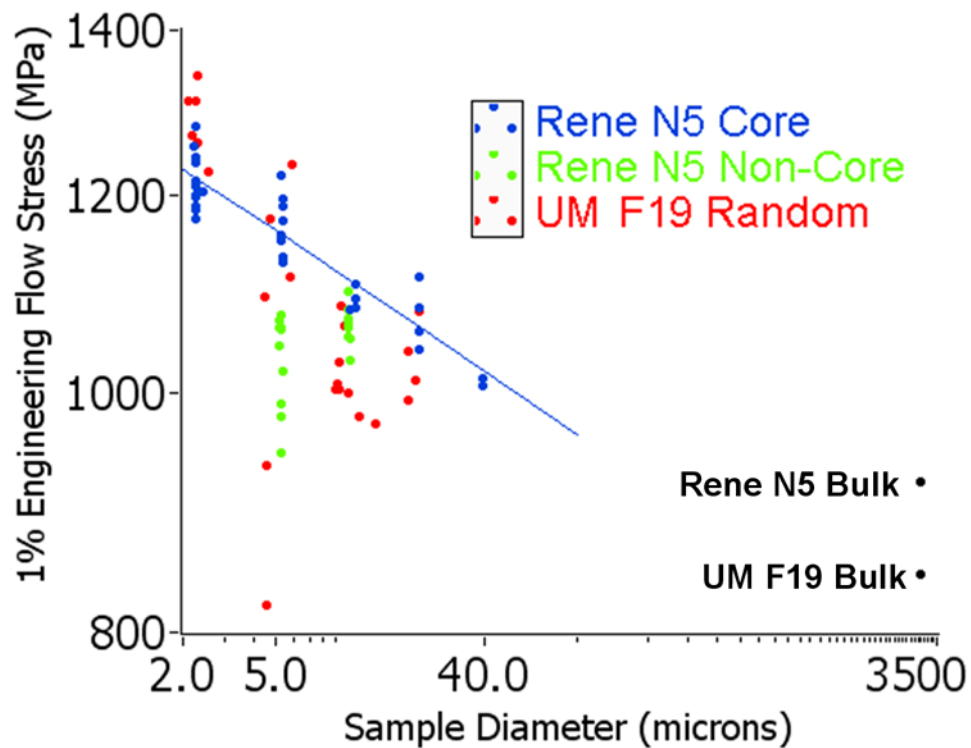
Figure 11. Log-log scaling plot for <1 2 3> oriented superalloy micro-compression testing. The UM F19 data is from [2].

14

The majority of the <1 2 3> oriented tests showed deformation on a single slip system, as expected. For the 2.5 μm and occasionally the 5 μm diameter samples, however, stresses were elevated such that a 'zig-zag' slip mechanism in which multiple slip systems act cooperatively to confine deformation to the γ channels was observed [19,20]. Fig. 12 shows an example of this mechanism on a 2.5 μm diameter sample. Typically, at room temperature the 'zig-zag' slip mechanism is only observed for samples oriented very nearly to <1 1 1> [19,20]. Micro-samples oriented with a <1 1 1> compression axis have also been tested and appear to deform predominantly by the 'zig-zag' mechanism.

In-situ micro-compression tests have been conducted in an SEM using the rig displayed in Figure 5. The tests are conducted by a manner in which the piezoelectric actuator is incremented by a small amount, inducing a small sample displacement, and then held statically while an image is acquired so that a sequence of deform then hold and image, deform then hold and image is utilized. Stresses are calculated based on load cell values while strains are calculated from displacements observed in the images. Labview based control and analysis software has been developed to conduct the above tasks.
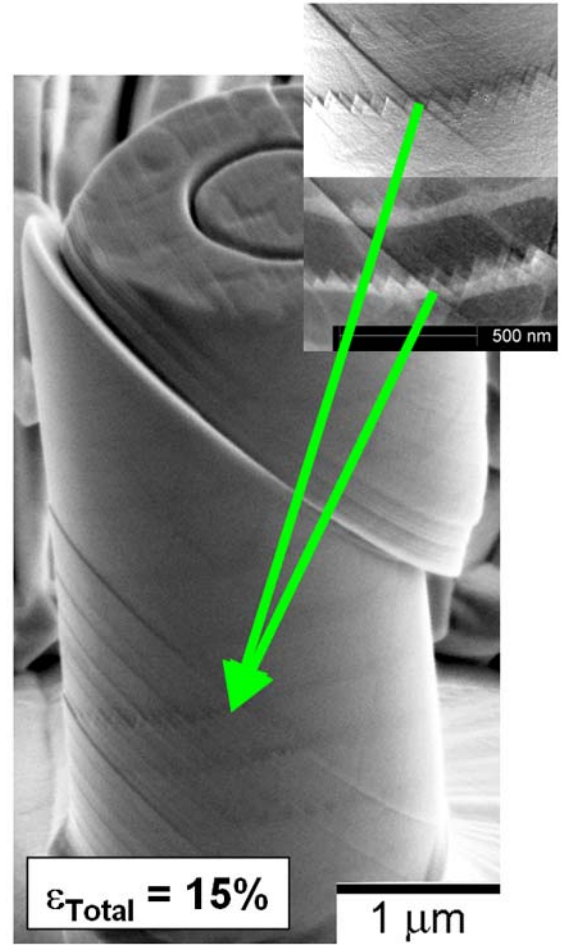
Figure 12. Images of 'zig-zag' slip in <1 2 3> oriented 2.5 mm diameter compression samples. The upper inset image is a secondary electron image while the lower inset is a backscatter electron image.

The in-situ micro-compression tests using the diamond platen have shown higher work hardening rates and a greater degree of barreling than the results obtained from the nanoindenter. The diamond platen used in the in-situ compression tests is laterally stiff. In fact, the lateral stiffness was measured to be ~0.1 N/μm compared to ~0.01 N/μm lateral stiffness in the nanoindenter. It was hypothesized that the laterally stiff in-situ diamond compression platen was forcing behavior similar to a bulk compression test with no lubricant or high friction, that is crystal rotations were imparted, the sample barreled and work hardening rates were artificially high. To test this, a compression platen was constructed from a 10 mm length x 100 μm diameter SiC fiber. The lateral stiffness of the SiC fiber was measured to be less than 0.0001 N/μm. Figure 13 shows images of deformed samples using both the in-situ diamond and in-situ SiC fiber platens. Note that barreling has been eliminated in the test with the SiC fiber. Further, Figure 14 is a plot with representative engineering stress-strain curves from the nanoindenter, in-situ diamond and in-situ SiC fiber platens. Note that the work hardening rate has been significantly reduced by switching to the laterally compliant SiC fiber compression platen.

Despite promising results, the in-situ compression testing still requires work to ensure the data is quantitative. For example, it is unclear why the flow stresses measured with the in-situ rig do not match those measured in the nanoindenter. It is expected alignment issues are at least partially responsible for the inability to obtain matching results.
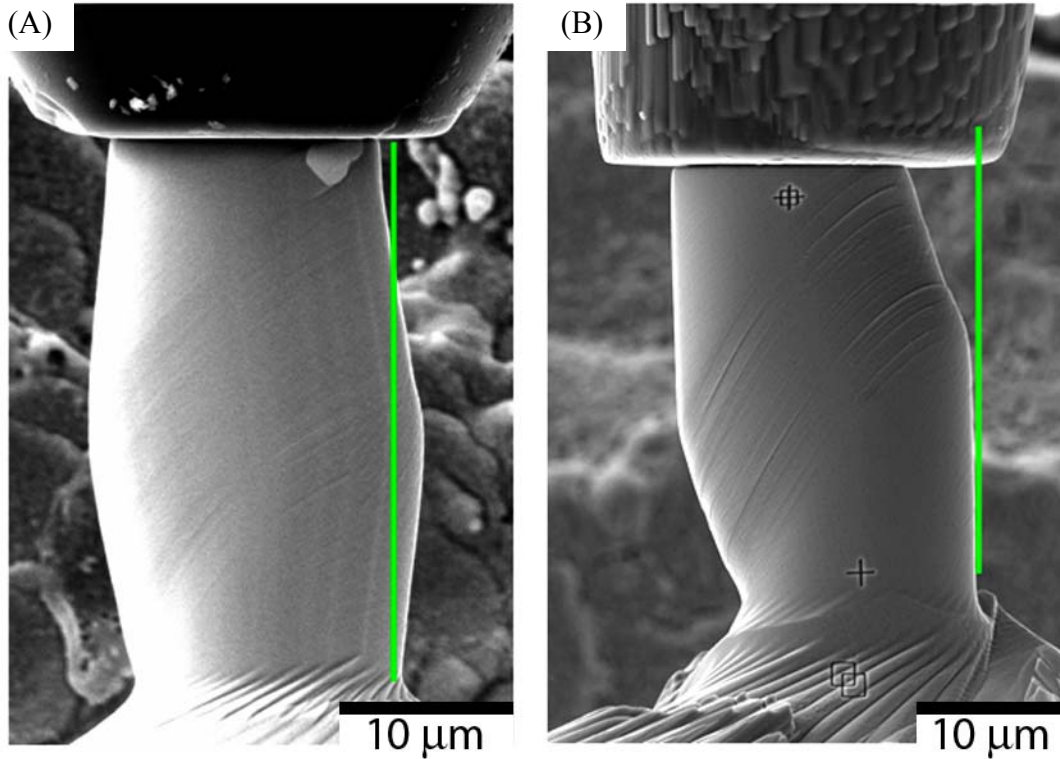
Figure 13. Images of <1 2 3> oriented micro-compression samples deformed to 18% engineering strain using the in-situ testing rig. (A) is using the diamond platen which has a lateral stiffness of ~0.1 N/mm. (B) is using the SiC platen which has a lateral stiffness of <0.0001 N/mm.
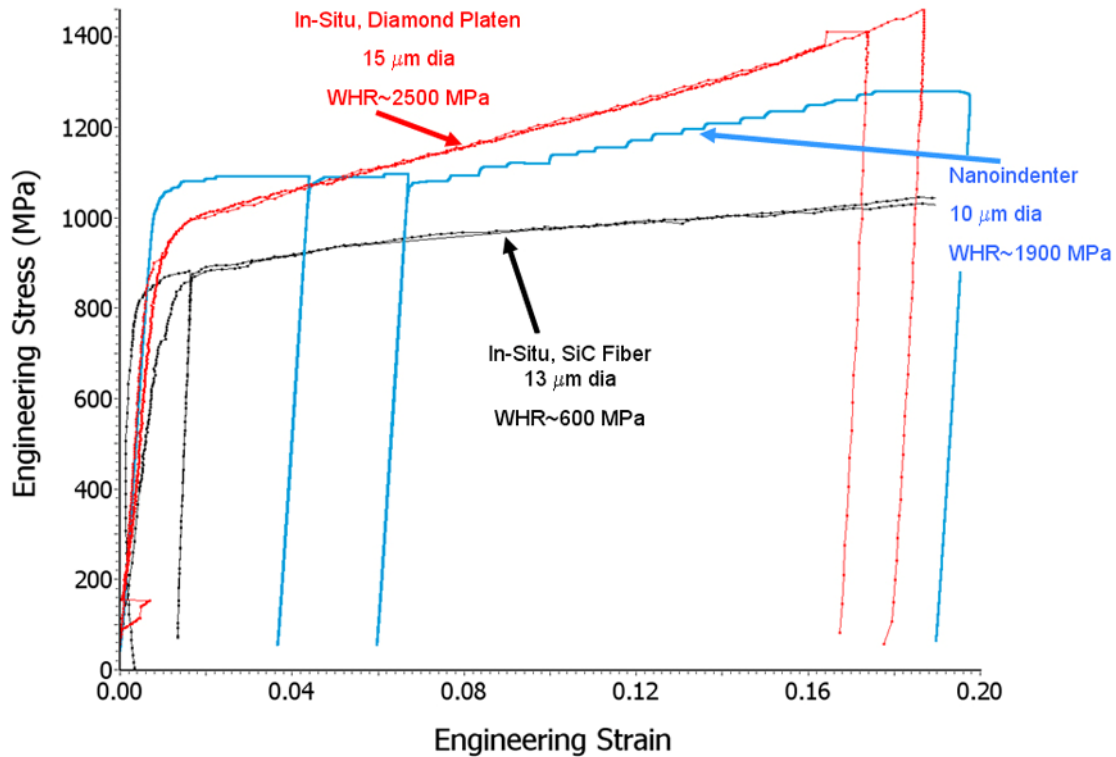
Figure 14. Comparison of representative engineering stress-strain curves using the nanoindenter, in-situ test rig with the laterally stiff diamond platen and the in-situ test rig with the laterally compliant SiC fiber platen.

A grip was machined into the end of a SiC fiber to modify the in-situ testing rig for micro-tension, as can be seen in Figure 6. The tension tests are conducted in a deform then hold and image, deform then hold and image sequence, similar to the in-situ compression testing. Again, stress is measured from load cell readings and strain is calculated from displacements in the images. A piezoelectric positioning stage is used to drive the tension samples into the grips shown in Figure 6. Figure 15 shows an engineering stress-strain curve taken from one of the micro-tension tests as well as selected images from various points in the stress-strain curve. Of interest, an upper yield point is observed. This was unexpected and is presently a topic of investigation. Also note from Figure 15 that deformation propagates by rapid strain bursts. As in the in-situ micro-compression testing, the in-situ micro-tension testing is presently considered qualitative only and work is needed to ensure results are truly quantitative.

Extensive work is needed to characterize the deformation behavior observed in the results described above. Presently, the FIB is being used to prepare foils both perpendicular and parallel to slip bands in the microsamples. These will be evaluated with the transmission electron microscope (TEM) to provide insight into the evolution of dislocation networks. FIB based

17

serial sectioning experiments are also underway to evaluate in a three-dimensional sense the intermittency of deformation and why a slip band forms at a certain location as opposed to directly above or below.
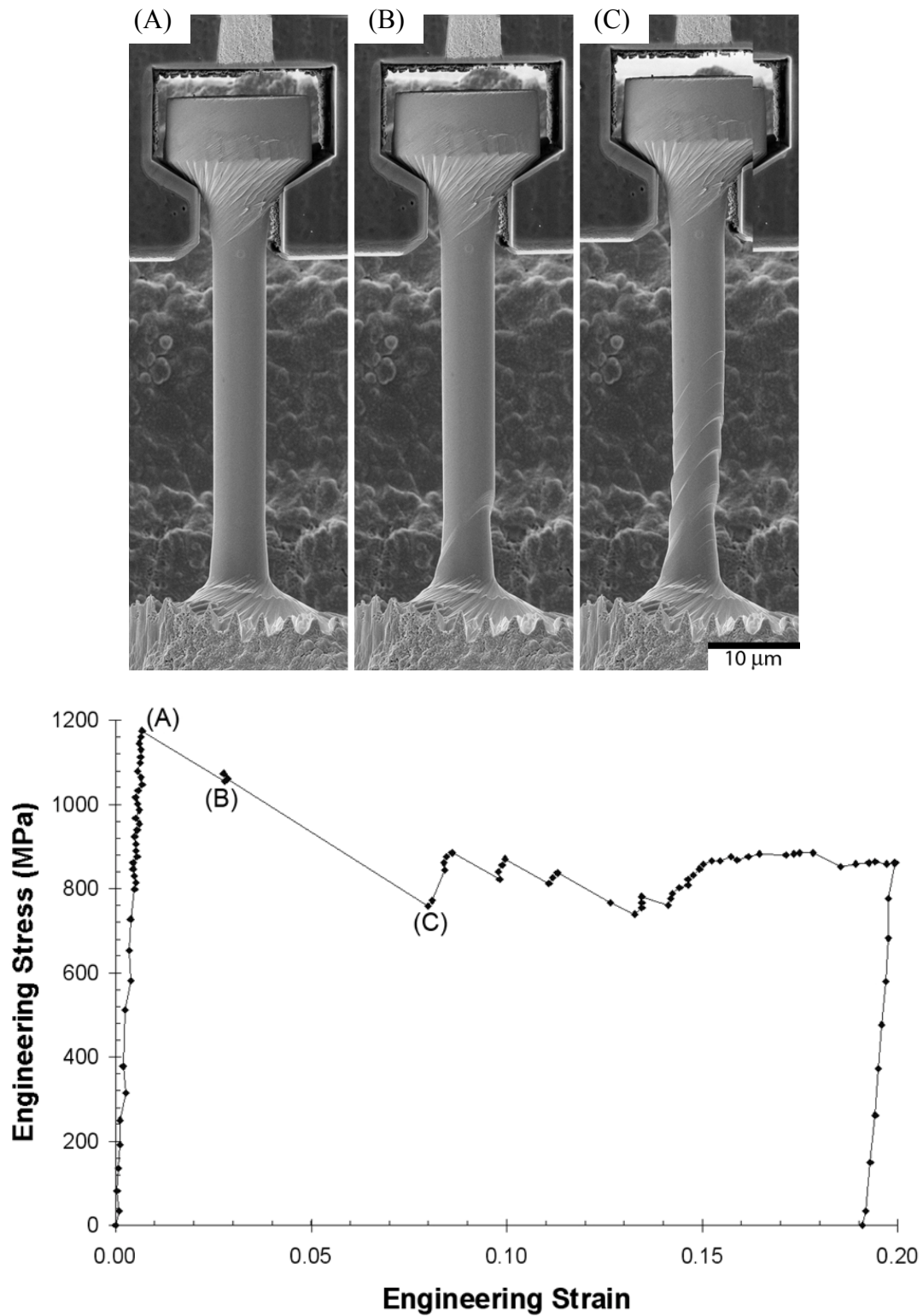
Figure 15. In-situ micro-tension testing. The images A, B and C above correspond to the data points A, B and C in the stress-strain curve.

4. Conclusions

It was demonstrated that the engineering single crystal nickel based superalloy Rene N5 exhibits sample size dependent behavior. Smaller samples were observed to have an elevated and stochastic flow stress, increased small-strain work hardening rate and intermittency of deformation. Compression samples with diameters as large as 40 μm were observed to behave differently than bulk, although this may be related to selective avoidance of defects such as carbides or micro-porosity in the microsamples. The samples were oriented for single-slip and this was predominantly observed with the exception of the observance of 'zig-zag' slip in the smallest samples. An in-situ test rig has been developed for conducting micro-compression and micro-tension experiments in the SEM. While encouraging, the in-situ test results are presently qualitative only. Future characterization work, such as TEM defect analysis and FIB serial sectioning is needed to understand the evolution of deformation.

5. References

[1]   M.D. Uchic, D.M. Dimiduk, J. Florando, W.D. Nix, Science 305 (2004) 986-989.
[2]   M.D. Uchic, D.M. Dimiduk, Mater. Sci. Eng. A 400-401 (2005) 268-278.
[3]   J.R. Greer, W.C. Oliver, W.D. Nix, Acta Mater. 53 (2005) 1821-1830.
[4]   J.R. Greer, W.D. Nix, Phys. Rev. B 73 (2006) 245410-245415.
[5]   C.A. Volkert, E.T. Lilleodden, Philos. Mag. 86 (2006) 5567-5579.
[6]   D.M. Dimiduk, M.D. Uchic, T.A. Parthasarathy, Acta Mater. 53 (2005) 4065-4077.
[7]   D. Kiener, C. Motz, T. Schoberl, M. Jenko, G. Dehm, Adv. Eng. Mater. 8 (2006) 1119-1125.
[8]   E.M. Nadgorny, D.M. Dimiduk, M.D. Uchic, Mater. Res. Soc. Symp. Proc. 976-EE06 (2007) 24-29.
[9]   H. Bei, S. Shim, E.P. George, M.K. Miller, E.G. Herbert, G.M. Pharr, Scripta Mater. 57 (2007) 397-400.
[10]   N.A. Fleck, G.M. Muller, M.F. Ashby, J.W. Hutchinson, Acta Mater. 42 (1994) 475-487.
[11]   E. Arzt, Acta Mater. 46 (1998) 5611-5626.
[12]   J. Gil Sevillano, I. Ocana Arizcorreta, L.P. Kubin, Mater. Sci. Eng. A 309-310 (2001) 393-405.
[13]   P. Caron, T. Khan, Aereosp. Sci. Tech. 3 (1999) 513-523.
[14]   R.C. Reed, *The Superalloys Fundamentals and Applications* (Cambridge, New York, 2006).
[15]   D.P. Pope, S.S. Ezz, Int. Met. Rev. 29 (1984) 136-165.
[16]   D. Caillard, V. Paidar, Acta Mater. 44 (1996) 2759-2771.
[17]   D. Caillard, Acta Mater. 44 (1996) 2773-2785.
[18]   M.D. Uchic, D.M. Dimiduk, R. Wheeler, P.A. Shade, H.L. Fraser, Scripta Mater. 54 (2006) 759-764.
[19]   D. Bettge, W. Osterle, Scripta Mater. 40 (1999) 389-395.
[20]   W. Osterle, D. Bettge, B. Fedelich, H. Klingelhoffer, Acta Mater. 48 (2000) 689-700.

6. Names of Personnel

Hamish Fraser (OSU Faculty Member)
Michael Uchic (AFRL/RX Mentor)
Dennis Dimiduk (AFRL/RX Mentor)
Robert Wheeler (UES Mentor)
Paul Shade (OSU Graduate Student)

<u>**Task 2**</u>
Development of Constitutive Relations from Phase Field Modeling of Microstructural Evolution. *Yunzhi Wang (OSU Faculty Member), Jeff Simmons (AFRL/RX Mentor), Youhai Wen (UES Mentor), Billie Wang (OSU Graduate Student)*

I. RESULTS and DISCUSSION

1. Introduction

Phase field modeling has become an important tool to develop fundamental understanding of microstructural evolution during phase transformations and plastic deformation. It has the ability to account for the full complexity of multi-phase, multi-variant and polycrystalline microstructures in advanced alloy systems. In contrast to the "mean-field" description offered by most of the existing models, a phase field model can provide complete microstructural information including morphology and spatial distribution of phases [1,2] (see Figure 1). Utilization of these features could be very useful in modern alloy and component development processes [3, 4]. However, if the phase field is to be developed into engineering models, significant improvements in computational efficiency are required. Some improvements can be made with state of the art parallel algorithms, but these are not expected to be practical for industrial applications because of computing resource limitations, as well as the needs for confidentiality of proprietary information. One approach we have developed in this project is a hybrid method that combines constitutive nucleation and growth laws derived from the classical nucleation theory and diffusion-controlled precipitate growth theory with Langer-Schwartz type approach and quantitative phase field modeling (Figure 2).

With this general approach, it could be possible for the materials developers to produce results in real time during the development process. Because computer modeling can sample regions in processing space that are difficult or impossible to achieve experimentally, it is expected that this method will produce constitutive laws that are significantly more robust than those generated through conventional experiment/data reduction methodologies. Since other types of constitutive methods are common in industry, it is anticipated that resistance to adoption will be significantly lower than for methods that require extra skills to be developed by the practitioners.

2. Methods, Assumptions, Procedures

The overall approach developed in this project for microstructural design is a hybrid approach that involves a synergetic combination of several different methods, as illustrated in Figure 2. The methods are arranged in the order of the most inexpensive to the most expensive so that an optimal reduction of the risks may be achieved, with each successive technique providing additional information. For example, the nucleation and growth analysis based on the constitutive laws is a very fast-acting (real time) method and serves as a simple front-end to the other methods to explore conditions favorable for the formation of target microstructures in advance of experimentation [3,4]. It provides a quick estimate of the nucleation behavior in the untransformed regions. This would be improved by the Langer-Schwartz type model [5], which

21

would relax a simplifying assumption of uniform particle size to produce dynamically evolving particle size distributions. The phase field model improves on this by adding the effects of non-uniformity in the untransformed matrix concentration. For example, the supersaturation is the greatest in center of the channels between the secondary particles and hence tertiary particles tend to form there (see Figures 1 (a) and (c)).

(a)	(b)
(c)	(d)
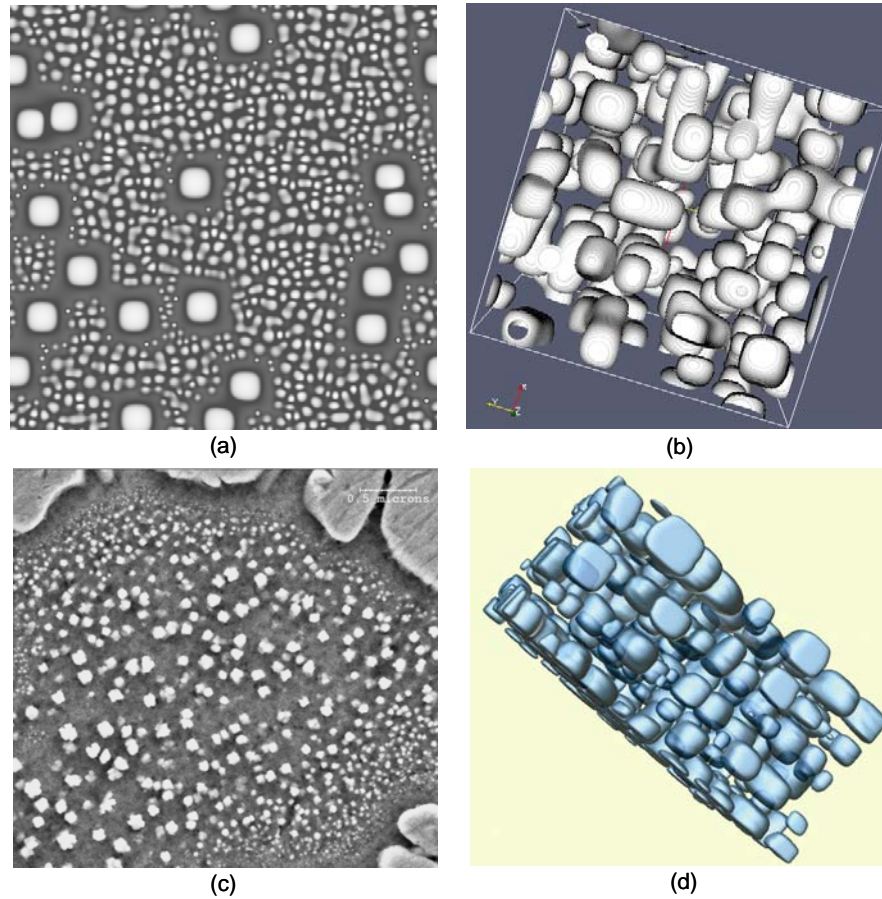
Figure 1. Typical γ/γ′ microstructures in Ni-base superalloys for both disk and blade applications simulated by the phase field method ((a) and (b)) in comparison with experimental observations ((c) and (d)).
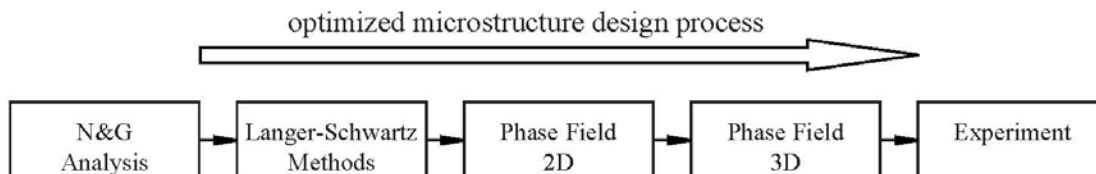
Figure 2. A hybrid model-optimized microstructure design process.

The center piece of this project was the development of a quantitative phase field model [1,2] for the prediction of formation and dynamic evolution of typical bimodal γ/γ′ microstructures in Ni-base superalloys. As any quantitative models, the necessary underpinnings include, among other things, model inputs from quality thermodynamic and kinetic databases and experimental measurements, a robust calibration method and a set of high quality experimental data to calibrate and validate the model against. The quantitative phase field model developed in this project was linked to the critically assessed CALPHAD thermodynamic and diffusivity databases. Calibrations were first carried out against Ni-Al and Ni-Al-Cr systems for mobility, interfacial energy and free energy models that are available from literature [6-10]. Then a five-component model alloy was specially designed and prepared at WPAFB, which has a slow precipitation process so that the nucleation and growth rates of the precipitates can be determined accurately. Quantitative experimental measurements of particle number density, average particle size, and kinetics of nucleation, growth and coarsening of γ′ in the five-component alloy were made and the data were used to calibrate the phase field model for applications to complex industrial alloys such as RN88 or R104.

It is impractical to formulate a complete free energy function of a commercial alloy with 12 to 16 components directly from the thermodynamic database in a rapid and reliable fashion. The time and experimental effort required to calibrate such a model would be formidable as well. Therefore, the possibility was explored for developing a thermodynamic description of a multi-component alloy system in terms of a pseudo-binary formalism for fast phase field simulations and for rapid model calibration. A pseudo-binary free energy model was successfully developed to describe two-phase equilibrium in the five-component alloy by assigning each element to either Ni- or Al-equivalent element. The phase field model using the pseudo-binary free energy formulation was calibrated with carefully designed isothermal experiments and validated against continuous cooling experiments in a quantitative fashion. Different calibration methods to match phase field prediction of the kinetics of precipitate nucleation, growth and coarsening to experimental data were explored.

A heterogeneous nucleation algorithm was developed to show how preferential nucleation sites can lead to bimodal particle size distributions. A simplified mean field nucleation and growth model was formulated to identify processing regions in the temperature-time space for phase field exploration of bimodal particle size distributions. A null-space analysis method is developed for sensitivity study of the accuracy of model input parameters.

3. Results

In order to reduce subjective errors in analyzing TEM micrographs, an automated method for identifying each γ′ particle and computing average particle size and number density was developed. Using a standard automated set of filters, the method was applied to a variety of images and yielded reproducible results (see Figure 3).
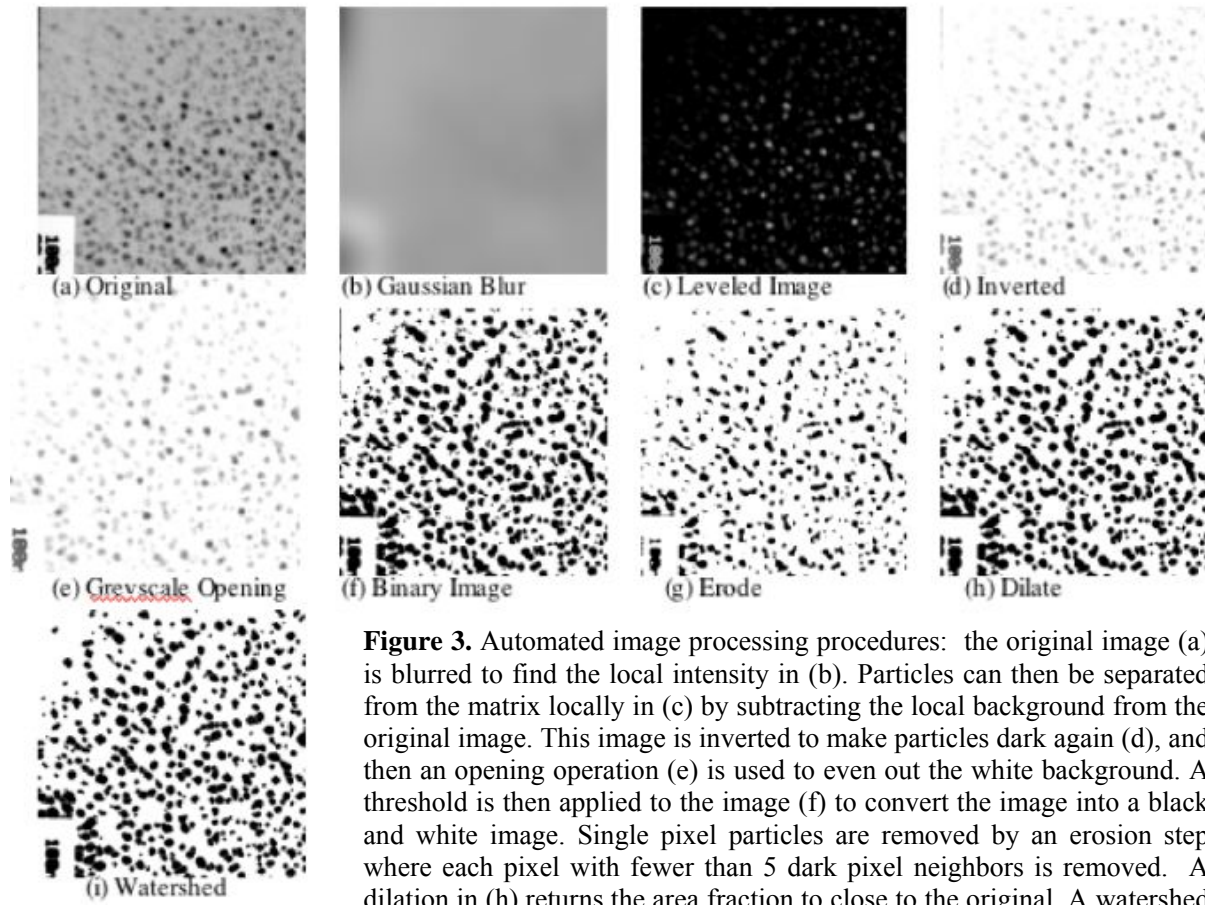
**Figure 3.** Automated image processing procedures: the original image (a) is blurred to find the local intensity in (b). Particles can then be separated from the matrix locally in (c) by subtracting the local background from the original image. This image is inverted to make particles dark again (d), and then an opening operation (e) is used to even out the white background. A threshold is then applied to the image (f) to convert the image into a black and white image. Single pixel particles are removed by an erosion step where each pixel with fewer than 5 dark pixel neighbors is removed. A dilation in (h) returns the area fraction to close to the original. A watershed filter is then used to separate conjoined particles (i).

There exist different levels of uncertainties in phase field model inputs such as free energy, interfacial energy, atomic mobility and kinetic coefficient for atomic ordering for a given alloy system. In order to generate a robust model, optimization over the initial choice of these input parameters is necessary. In this project, a null-space analysis has been developed to vary systematically (in groups rather than individually) model inputs for sensitivity study and for optimization. It was found that if the model inputs were fixed at their initial chosen values (estimated from available data from literature for similar alloy systems), the simulation results agree poorly with the experimental measurements. When certain uncertainties in model inputs such as interfacial energy and mobility were allowed, the best matching between the simulation predictions and experimental measurements through an iterative method has yield an optimal set of model inputs of these parameters. Figure 4 shows the optimal interfacial energy obtained using an amoeba optimization routine. It is obvious that the optimal interfacial energy deviate significantly from the initial choice that is 0.014 J/m^2. Thus accepting the fact that input data have certain degrees of uncertainty allows for establishing a more robust phase field model for the given superalloy.

24

In model validation, the transition point from the nucleation and growth stage to the coarsening stage was identified and used as a reference point to match phase field prediction of the kinetics of precipitate nucleation, growth and coarsening to experimental data (Figure 5). This calibration scheme was found reliable and convenient. The calibrated pseudo-binary model was shown to be able to capture both the kinetics of γ' nucleation and growth and particle number density evolution of the five-component alloy (see, e.g., Fig. 5). The model has been applied successfully to predict the window of cooling rate for the formation of bimodal microstructures in disk alloys, from which improved fundamental understanding of the phenomenon has been developed [10]. The effect of different cooling rates on the number and size of particles in each mode was explored. The maximum and average supersaturation within the untransformed matrix together with the nucleation events were tracked during the phase field simulations. The results were mapped onto the constitutive models based on mean field approximations to explain and predict the phase field results.
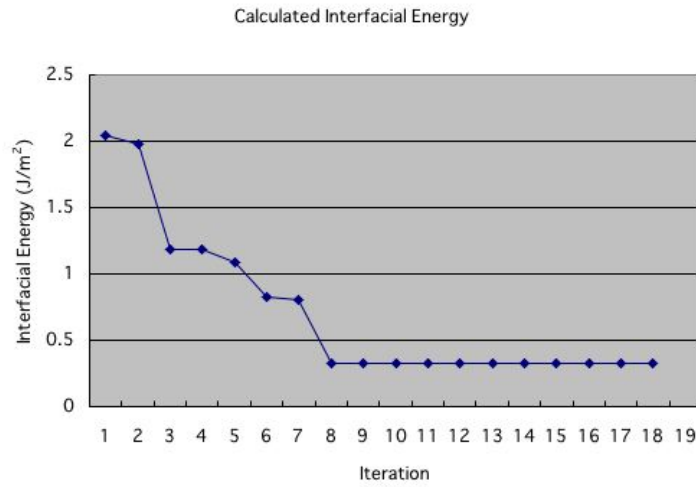
Figure 4. Optimization of model inputs. Each iteration chooses a new set of phase field inputs using an amoeba optimization routine. The plot shows the optimal interfacial energy that gives the best match between phase field prediction and experimental measurement of precipitation kinetics.
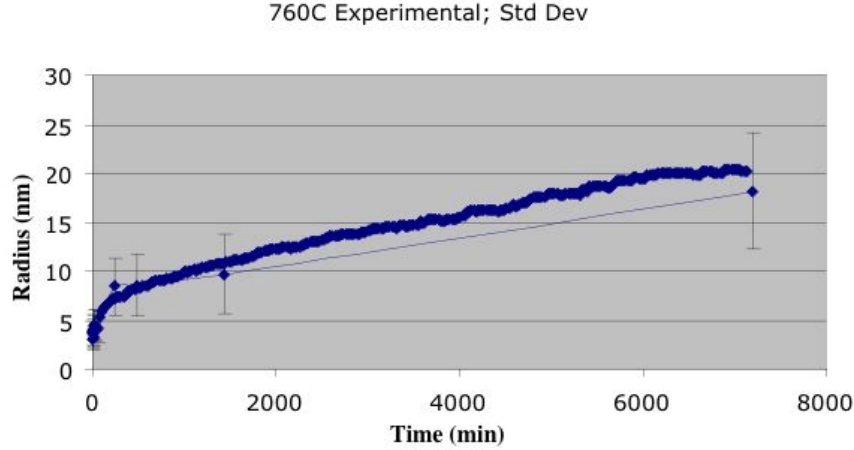
Figure 5. Comparison between phase field model prediction (thick solid line) and experimental measurements (thin solid line with filled diamonds and error bars) of time evolution of mean particle radius.

The phase field model was also applied successfully to explain the formation of mono-modal and bimodal γ/γ' microstructures in a commercial disk alloy during various continuous cooling experiments [11] (Figure 6). Simulation results showed clearly the effect of heat treatment schedule on microstructure evolution. The model is now being used to guide the design of new experiments.

Three-dimensional (3D) phase field simulations using the pseudo-binary model were carried out to study the sensitivity of simulation results to temperature dependent phase field input parameters. In comparison with experimentally observations, it is found that the γ/γ' interfacial energy has to be around 70 mJ/m^2 at 550°C to achieve reasonable agreement in mean particle size evolution although a wide spread of this energy has been reported by fitting to experimentally measured coarsening kinetics.

Phase field simulations in 2D were carried out to study multi-modal particle size distributions (PSDs). The interplays between heterogeneous and homogenous nucleation under various non-isothermal cooling conditions were explored. Tri-modal PSDs were obtained when both heterogeneous and homogeneous nucleation mechanisms were considered during continuous cooling (Figure 7). Each old generation of the γ' particles defines the channels in which the subsequent new generation is most likely to arise. These simulations results may allow for a reasonable explanation for the formation mechanisms of the experimentally observed tri-modal microstructures (Fig. 7(b)). For example, if we assume that the large particles formed through heterogeneously nucleation (the operating mechanism under relatively small undercooling) at high temperatures play a similar role as the primary γ' particles, then the spatial distribution of the secondary and tertiary populations of γ' particles can well be explained. The untransformed matrix between the "primary" particles offers a wide band of solute rich region where the secondary particles form through homogeneous nucleation that becomes operative at lower temperatures. Finally, the narrow bands of untransformed matrix in between the primary and

26

secondary γ' particles are still supersaturated, offering solute-rich channels for the formation of the tertiary particles.

4. Discussion

The full version of the phase field model of γ/γ' microstructural evolution in Ni-based superalloys, its pseudo-binary thermodynamic and kinetic approximations, the fast calibration and validation methodology, coupled with the nucleation and growth analysis developed in this project are useful tools for rapid sampling of materials and processing parameter spaces in digital design of desired γ/γ' microstructures. Such capabilities have been demonstrated through the analyses of the development of multi-modal microstructures that form by dynamic interplays between homogeneous and heterogeneous nucleation and between nucleation and growth during continuous cooling processes.

Bimodal microstructures have been predicted previously using the Langer-Schwartz model [4] and shown to also exist in the phase field model by Wen, et al. [1]. This work gives a systematic methodology for designing microstructures of this type by a simple analysis of the competition that exists between existing and potential particles in the microstructure coupled with the phase field model for treatment of non-uniform effects. By using the simpler analytical model to guide the computationally more expensive phase field simulations, a processing window was determined, within which the bimodal microstructure is expected to form. The phase field simulations account for interacting diffusion fields and can readily account for elastic interactions, both of which are absent in the analytical model.
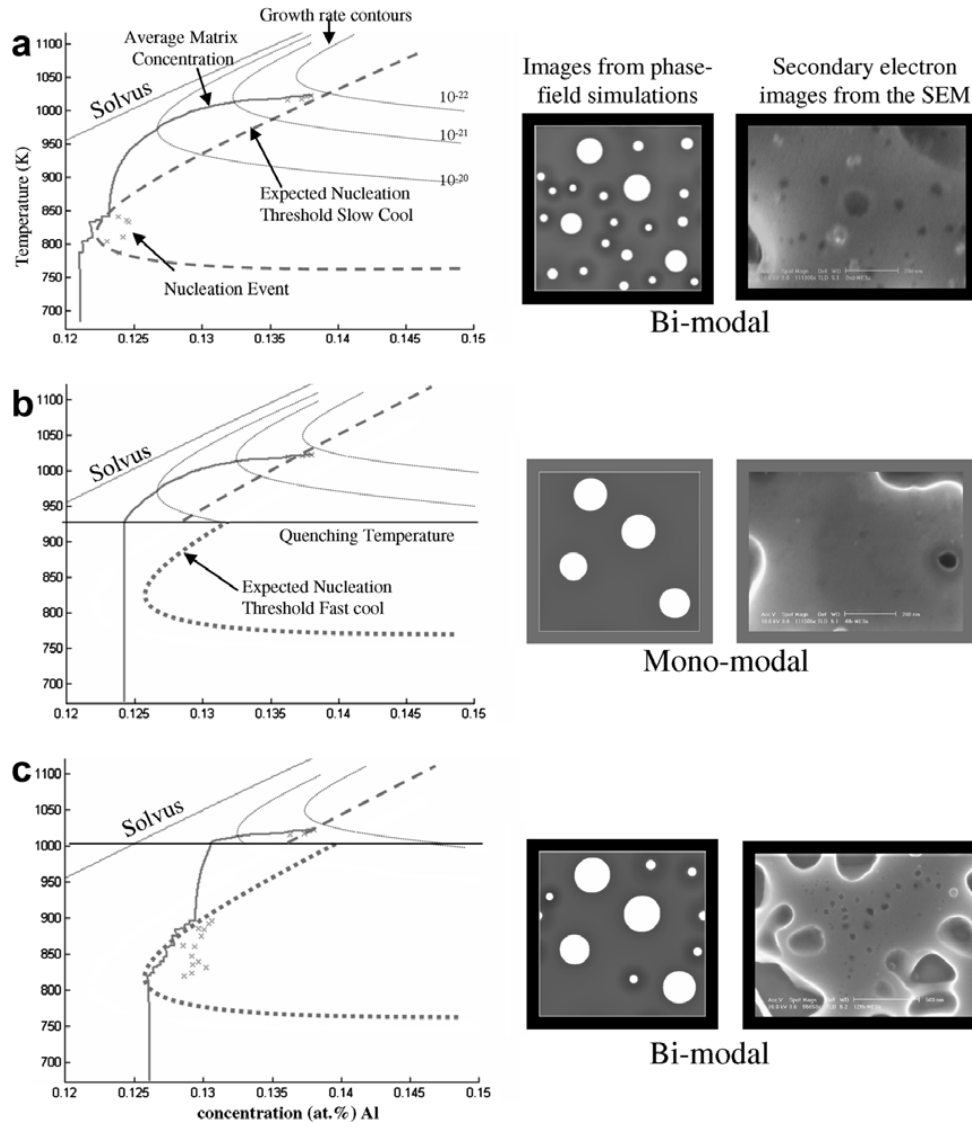
Figure 6. The concentration at the quench initiation influences when tertiary nuclei will form. (a) Shows the slow cooled (unquenched) case; tertiary particles (x's) form when the solute depletion rate slows due to lower diffusivity and allows the average matrix concentration (thick line) to intersect with the nucleation threshold (dashed). Below the quenching temperature (horizontal line), the higher cooling rates shift the expected solute depletion and nucleation threshold. At moderate quench temperatures (b), the concentration at the quench temperature is to the left of the nose of the expected nucleation curve so no tertiary particles are expected. At high quenching temperatures (c), the mean concentration is to the right of the nose, indicating tertiary particles will form on the quench. Growth rates are in m^2/K since they are normalized by the cooling rate [11].
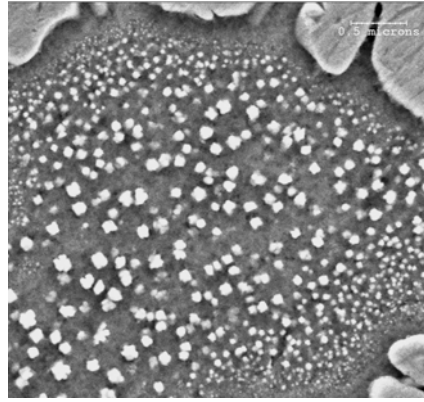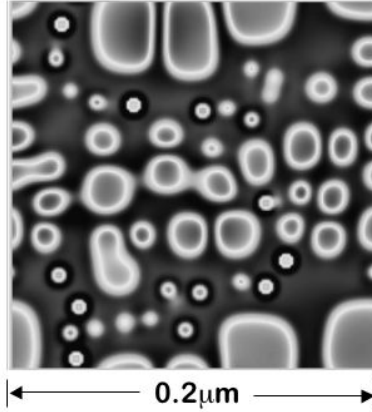
Figure 7. Typical tri-modal γ/γ′ microstructures obtained in (a) experiment and (b) Ni-Al by phase field simulations that account for both heterogeneous and homogeneous nucleation mechanisms under continuous cooling conditions.

This work gives a quantitative explanation for the three limiting cases of transformation behavior, i.e. (1) a soft-impingement regime, where nucleation is stopped by soft impingement, never to start again, (2) a bimodal microstructure regime, where nucleation restarts at a lower temperature due to supersaturation, and (3) a continuous nucleation regime, where the supersaturation is always sufficient to support nucleation. Here, the analysis of the nucleation and growth rates shows that bimodal PSD's can form by the dynamic interplay between these two effects even in the absence of heterogeneous nucleation events. By direct computation of the nucleation and growth rates, these mechanisms for microstructural development were shown to be controllable.

The current work improves on the work by Wen, et al. [1], by finding a processing window for linear dimensional time cooling rates. Wen et al. found dynamic bimodal PSD formation during a linear dimensionless cooling rate, which is generally a curved time-temperature profile in dimensional time. The dimensionless scaling factor between dimensional and dimensionless time varies as temperature changes. With the method used here, the temperature was incremented at a constant rate, which means that the (dimensional) time for evolution at that temperature increased with decreasing temperature. When the real time linear cooling curve is converted into dimensionless time, it resembles an isothermal hold followed by a rapid quench, facilitating the formation of the bimodal microstructure. While linear dimensional cooling rates were chosen for study here, more complex cooling profiles are also possible and are being investigated presently.

The ability to treat microstructural inhomogeneity is often given as an advantage of the phase field method over mean field models. Figures. 1, 6 and 7 show that this inhomogeneity indeed plays an important role in the formation of multi-modal microstructures. Nucleation events can be seen to favor sites near the maximum available supersaturation (Figure 7(b)). Since the nucleation rate is a strong function of the supersaturation, local enhancements in solute in the untransformed matrix are expected to be sites for nucleation of tertiary particles. This would give rise to the realistic microstructures shown in Figure 7 (a).

Since solving the phase field equations requires that the system be discretized, there are generally a minimum of about 100 grid points required to represent a single particle. That is, a minimum of 3 grid points will be required for each feature to be accurately represented. A particle has a boundary on each side and the uniform region in between, and the channel between

29

it and neighboring particles, leading to a minimum diameter of approximately 12 grid points per particle. This gives approximately 100 grid points needed for the whole area. This severely limits the system sizes that can be considered by directly phase field simulations. The hybrid approach developed in this project (see Figure 2) should be much more efficient, through the use of mean-field analytical nucleation and growth models, the insertion of the fast-acting Langer-Schwartz model between the nucleation and growth analysis and the 2D phase field modeling, and finally the insertion of 3D phase field modeling between the 2D phase field modeling and experiment to achieve more quantitative predictions of the kinetics.

5. Conclusions

The close collaboration and interaction among OSU and AFRL/RX mentors and STW-21 student in this project have lead to the development of a framework for designing microstructures by linking analytical models with the phase field methodology in order to narrow the window of heat treatments which needs to be explored experimentally to find microstructures with particular characteristics. Exact representations for complex industrial alloys using the phase field model may be out of the range for engineering applications. However, using the hybrid approach developed in this project, useful predictions can be made to direct experimental research and fast-acting models can be developed for directing real-time engineering applications.

6. Recommendations

The hybrid approach developed in this project has been calibrated and validated against a five-component model alloy in WPAFB materials research laboratory. However, the Langer-Schwartz model as an intermediate step has not yet been inserted. The insertion of the Langer-Schwartz model in the approach and its calibration and validation against commercial alloys and implementation in aerospace industry are strongly recommended for the continuation of the work. This will allow for the development of fast-acting models that are significantly more robust than those generated through conventional experiment/data reduction methodologies and at the same time require little extra effort to be implemented by the practitioners in their daily routine calculations.

7. References

[1] Wen, Y.; Simmons, J.; Shen, C.; Woodward, C.; Wang, Y. *Acta Materialia* **51** (2003), 1123–1132.
[2] Wen, Y.; Wang, B.; Simmons, J.; Wang, Y. *Acta Materialia* **54** (2006), 2087–2099.
[3] Viswanathan, G.; Sarosi, P.; Henry, M.; Whitis, D.; Milligan, W.; M.J.Mills, *Acta Materialia* **53** (2005), 3041–3057.
[4] Gabb, T.; Backman, D. G.; Wei, D. Y.; Mourer, D. P.; Furrer, D.; Garg, A.; Ellis, D. *SuperAlloys* 2000, Warrendale PA, 2000; p 405.
[5] Langer, J.; Shwartz, *A. Phys. Rev.* 1980, A21, 948–958.
[6] Ansara, I.; Dupin, N.; Lukas, H.; Sundman, B. *J. alloy compd*. 1997, 247, 20–30.
[7] Huang, W.; Chang, Y. *Intermetallics* 1998, 6, 487–498.
[8] Ardell, A. *Acta Metall*. **16** (1968), 511–516.
[9] Olson, G. *Science* 2000, 288, 995.

[10] Wang, B., Y.H. Wen, J.P. Simmons and Y. Wang, "Systematic Approach to Microstructure Design of Ni-Base Alloys Using classical Nucleation and Growth Relations Coupled with Phase Field Modeling," *Met. Trans. A.* (2007-in press).

[11] Sarosi, P.M., B. Wang, Y. Wang and M.J. Mills, "Formation of Multimodal Size Distributions of γ' in a Nicle-Base Superalloy during Interrupted Continuous Cooling," *Scripta Mater.* 57 (2007) 767-770.

8. Names of Personnel

Yunzhi Wang (OSU Faculty Member)
Jeff Simmons (AFRL/RX Mentor)
Youhai Wen (UES Mentor)
Billie Wang (OSU Graduate Student)

Modeling and Experiment for Accelerated Insertion of Corrosion Resistant Structural Components. *Rudy Buchheit (OSU Faculty Member), Jaimie Tiley, Donna Ballard (AFRL/ML Mentor), Barbara Padgett (OSU Graduate Student).*

I. RESULTS and DISCUSSION

1. Introduction

Experimentation included three major investigations that were designed to probe the relationship between grain boundary phenomena and the stress corrosion cracking behavior. Understanding this relationship is critical for any future effort to produce a predictive model for corrosion behavior. Testing began with a study of stress corrosion cracking (SCC) behavior of friction stir welded (FSW) AA2099. Then, a thorough survey of grain boundary phenomena of electrochemical behaviors was accomplished. Finally, an investigation into the SCC behavior through standardized testing techniques was completed using a heat treatment array that included time-temperature combinations that enhanced or reduced susceptibility to SCC.

1.1 Friction stir welding of AA2099

Uncontrolled precipitation along the grain boundaries within each weld zone occurred during this solid state welding process. The consequence of this was two-fold. Firstly, the microstructure of the weld zones differed from that of the original plate, as evidenced by mechanical and microscopy data. Secondly, the corrosion behavior across the weld zones varied considerably. Quantification of these variations in behavior was achieved using spectroscopy, mechanical testing, and standard electrochemical techniques.

1.2 Corrosion behavior of grain boundary phenomena

As a precipitation strengthened alloy, AA2099 is microstructurally heterogeneous to develop desirable mechanical properties.[1] However, the far-reaching influence of this heterogeneity when present on grain boundaries is critical to understanding the SCC behavior of AA2099. Consequently, understanding the micro-electrochemistry of each major phase is imperative for the analysis and interpretation of the localized electrochemistry of the bulk alloy. It is with this logic that a characterization of major precipitate phases in AA2099 (T-phases), proposed analogs of the precipitate free zone (PFZ), and other grain boundary anomalies (Zn-modified Al_2CuLi), were investigated using the microcapillary electrochemical cell (designated herein as the microcell).

1.3 Stress corrosion cracking of AA2099

In contrast to the friction stir welding experimentation, precipitation of grain boundary structures was controlled with known time-temperature combinations. The idea was to create grain boundary microstructures that were unique over the large heat treatment array. Then by standardized testing techniques, any differences in stress corrosion cracking behavior could be linked to heat treatment and therefore its accompanying grain boundary structure.

2. Methods, Assumptions, Procedures

2.1 Experimental Procedure for friction stir welding of AA2099

2.1.1 Material and welding parameters.

Two 1.05 cm thick AF/C458 aluminum plates aged to a -T3 temper were friction stir welded by Marshall Space Flight Center, Huntsville, AL. The spindle speed was 200 rpm with a travel speed of 6 ipm. The weld length was about 25 in.

2.1.2 Sample Identification and Orientation.

Figure 1 shows the drastic change in microstructure as well as the nomenclature used to identify each weld zone – parent material (PM), thermo-mechanically affected zones (TMAZ), heat-affected zone on the trailing edge of the weld (HTS) and the heat affected zone on the advancing edge of the weld (HAS). The fine structure of the friction stir weld about the centerline of the weld in shown in Figure 2. Vickers microhardness data (20 sec dwell, 300gf load) on the short transverse (ST) face of the welded plate mirrored these differences by revealing changes in mechanical strength across the weld zones as shown in Figure 3. The hardness testing helped delineate the weld zones so that they might be sectioned from the plate for further testing.

2.1.3 Potentiodynamic Polarization.

Potentiodynamic polarization of the ST face of each weld zone revealed no difference in breakdown potentials (E_{crit}) as shown in Figure 4. Tests were completed in triplicate on a 6 mm polished finish for each weld zone. The open circuit potential was allowed to stabilize over 30 minutes prior to cyclic polarization in deaerated 10mM NaCl. The scan rate was 0.2mV/sec.

2.1.4 Corrosion Immersion Test.

A general survey of the corrosion mode and morphology using ASTM G 110-92 showed no difference in the intergranular corrosion morphologies observed between the weld zones as shown in Figure 5. [2] In this experiment, a sample comprising the whole of the weld (polished to a 1μm finish) was immersed for 30 minutes in a solution of 57g NaCl and 10mL H_2O_2 diluted with 1L of distilled water (at $30^0C \pm 3^0C$).

An intermittent immersion experiment where damage accumulation by weld zone was documented every five minutes by optical microscopy, did reveal some differences in the initiation of inter-subgranular attack (IsGA). The thermomechanically affected zones only showed IsGA after 10 minutes or more of immersion while this corrosion morphology was observed immediately for all remaining zones. Other corrosion morphologies encountered in constant immersion testing were due to borderline intergranular attack (IGA), and pitting; however, they were all observed within the first five minutes of immersion.

2.1.5 Constant Extension Rate Tests (CERT).

Round tensile bar samples sectioned longitudinal and transverse to the welding direction were used for constant extension rate testing as outlined by ASTM G 129-95. [3] Representative stress-strain curves were produced in triplicate using this testing. The gage length of the longitudinal samples encompassed the whole of the weld zone of interest, while the gage length of the weld transverse samples contained all weld zones. All tests were conducted at an extension rate of 2.5×10^{-5} mm/s with an initial load of 31 MPa.

To quantify the amount of embrittlement, the ductility ratio (*D.R.*) was calculated using:

$$D.R. = \frac{\varepsilon_{env}}{\varepsilon_{air}} \qquad (1)$$

Where ε_{env} is the strain to failure (%) for samples tested in 10mM NaCl solution and ε_{air} is the strain to failure (%) in ambient lab air. With this yardstick, HTS was found to be the most susceptible weld zone as shown in Table 1. Fractography data showed intergranular type failure for the nugget in longitudinal specimen and preferential site of failure in the HTS for weld transverse samples.

2.1.6 Transmission Electron Microscopy (TEM).

Samples sectioned from the ST face of each weld zone were electropolished using a 75% methanol and 25% nitric acid solution by volume. The voltage and temperature selected for the polishing was 9.7V and -30°C respectively. A FEI 200kV Tecnai TF-20 electron microscope with a field emission gun was used in the investigation of TEM foils prepared from the weld zone. Scanning transmission electron microscopy (STEM) revealed the size and distribution of the grain boundary particles on low and high angle grain boundaries (Figure 6 and Figure 7, respectively). Electron diffraction patterns confirmed the structure of the precipitates occupying the grain boundary of all weld zones to be primarily Al_2CuLi (T_1). The diffraction evidence for the HTS zone is given in Figure 8.

2.2 Experimental Procedures for Corrosion Behavior of Grain Boundary Phenomena in AA2099

2.2.1 Synthesis of Grain Boundary Phenomena.

Phase analogs for the T-phases and Zn-modified Al_2CuLi samples were synthesized by combining pure metals in the appropriate ratios (Table 2). The result for each case was a multi-phase ingot that included single phase crystals of the desired intermetallic. The crystals were of sufficient size for microcapillary electrochemical testing (>100mm) and occurred in a large volume fraction of the ingot. Precipitate free zone analogs were 99.9999% Al provided by Alfa Aesar and commercially pure Al combined with 2wt% Cu in an induction furnace.

2.2.2 Confirmation of Synthesized Phases.

X-ray diffraction (XRD) was utilized to characterize the structure of all ingots produced.
Electron backscattered detection (EBSD) corroborated the results of the X-ray diffraction data.
Scanning electron microscopy allowed for microstructural characterization of shape, size, and
distribution of the target phase within the ingot as well as compositional characterization using
the EDS (Energy Dispersive Spectroscopy) Genesis® software. Table 3 summarizes these results.

2.2.3 Electrochemical Characterization of Synthesized Phases.

Electrochemical characterization of the synthesized ingots was carried out using the
microcapillary electrochemical cell. It is in essence a miniaturized flat cell with a standard three
electrode setup. The reference electrode was a saturated calomel electrode, while the counter
electrode was platinum wire.

Cyclic polarization scans were completed using the microcell for each intermetallic phase. The
solution for each experiment was an unbuffered 10mM NaCl with an unknown pH. Cyclic
polarization data collection began 100mV below the open circuit potential (OCP) upon capillary
touchdown to the surface. Scans were carried out at a scan rate of 10mV/sec. Averaged values of
the characteristic potentials – corrosion potential (E_{corr}), breakdown potential (E_{crit}), and
repassivation potential (E_{repass}) – are given in Table 4 along with characteristic current densities –
corrosion current density (i_{corr}), current density at the corrosion potential of AA2099 ($i_{@-635mVsce}$),
and passive current density (i_{pass}). Representative cyclic polarization curves for each T phase and
Zn-modified T_1 phase are given in Figure 9 and Figure 10, respectively. The cumulative
distribution plots generated for these phase analogs are given in Figure 11 and Figure 12.

Three cathodic polarization experiments were completed for the each Zn-modified Al_2CuLi (T_1)
phase. All tests were done in unbuffered 10mM NaCl with a scan rate of 10mV/sec used to step
towards $-2.0V_{SCE}$ whereupon the experiment was terminated. Representative curves for the
unmodified T_1 and Zn-modified T_1 are given in Figure 13
Electrochemical impedance spectroscopy was carried out on unmodified and modified T_1
surfaces and chemical analysis of the resulting surface layer was carried out subsequently. A
600s OCP was done in 10mM NaCl solution, and an impedance scan was conducted from
100,000 Hz to 0.005Hz. Immediately after exposure to electrochemical impedance spectroscopy,
imaging of the sample surface was completed using the FEI Quanta® microscope. A porous
copper-enriched layer was found to be present about the circumference of area of interaction for
the microcell as seen in Figure 14. \An enrichment of Zn was also observed in the surface layer.
Table 5 shows the change in composition in the interaction area versus the surrounding crystal
area.

2.3 Stress corrosion cracking of AA2099

Since the experiments are on-going no attempt has been made to interpret the results in the
discussion, however, the procedural logic for this analysis is presented.

2.3.1 Heat treatment schedule of AA2099

Samples were sectioned from the 2.25" thick AA2099 plate supplied by Alcoa then solution heat treated at $600^{o}C$ and subsequently aged for various times at $160^{o}C$ and $190^{o}C$. The schedule of the heat treatment is shown in Table 6.

2.3.2 Mechanical Testing of heat treatment schedule

Changes in mechanical strength due to heat treatment were categorized using Vickers hardness as seen in Figure 3. A dwell time of 20sec and a load of 300gf were used. A single tensile test was completed for each heat treatment as well. Table 6 documents the observed yield stress (σ_{YS}) for each case. The orientation of the tensile specimens was through the thickness of the plate.

2.3.3 Stress corrosion cracking testing of AA2099

The stress corrosion cracking susceptibility of AA2099 was evaluated using ASTM G 44-99. [4] In this standard, samples under constant strain were alternately immersed (AI) in 10mM NaCl solution for a period of 10 minutes and dried in air for 50 minutes. Observation of the corrosion damage accumulation of the samples was tracked for 30 days. Two samples from each for heat treatment (time-temperature combination) were subjected to this study. The goal was to systematically vary the grain boundary microstructure and therefore the SCC behavior of the AI samples.

From time-temperature combinations, four points of interest were selected for further evaluation using CERT. These were the 6 hour and 60 hour times for both the $160^{o}C$ and $190^{o}C$ temperatures. Three of the four points were selected for testing in three environments. The environments of 10mM NaCl and ambient lab air were selected to access SCC susceptibility, again using the ductility ratio as a yardstick. The third environment was a deaerated 10mM NaCl with the sample polarized to $-740mV_{SCE}$ (the lower statistical range of the T_1 breakdown potential), chosen to probe the influence of T_1 particles on the SCC as well as to evaluate any effect of hydrogen embrittlement (HE) in governing the mechanistic SCC failure of AA2099.

3. Results

Table 1. Ductility ratio calculations by weld zone.

Sample	$\varepsilon_{air}/\varepsilon_{env}$
PM	0.88
HAS	0.72
N	0.62
HTS	0.45
Weld transverse	0.98

Table 2. Compositions selected for the production of bulk intermetallics phases to be used in microcapillary electrochemical testing.

Stoichiometry	Phase	Composition of initial charge (at%)				Charge Size (g)
T-phases						
		Al[1]	Cu[2]	Li[3]	Zn[4]	
Al_2CuLi	T_1	53	25	22	n/a	150
$Al_{7.5}Cu_4Li$	T_B	62.5	30	7.5	n/a	250
Al_6CuLi_3	T_2	54	6	40	n/a	300
Al_2Cu	θ	See source [5]				
Zn-modified Al_2CuLi						
$Al_2(Cu, Zn)Li$	T_1-4.0wt% Zn	53	18	22	7	250
$Al_2(Cu, Zn)Li$	T_1-6.0wt% Zn	53	15	22	10	250
$Al_2(Cu, Zn)Li$	T_1-8.4wt% Zn	53	12	22	13	250
PFZ analogs						
99.9999 % Al	n/a	See source [6]				
Al-2wt%Cu	n/a	See source [6]				
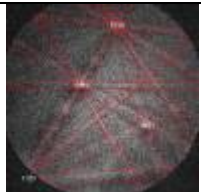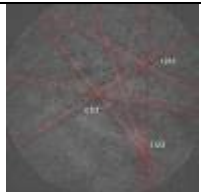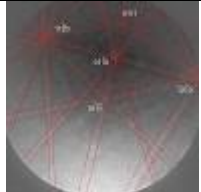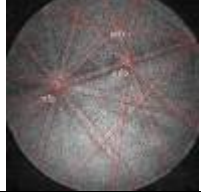
1: Alfa Aesar Puratronic, 99.9999% Al shot

2: Alfa Aesar 99.5% Cu shot

3: Alfa Aesar 99.9% Li rod

4: Alfa Aesar Puratronic, 99.99% Zn shot

Table 3. XRD, EDS, and EBKP results confirming synthesis of phase analogs.

Stoichiometry	Phase	JCPDF card files	EDS (at%)				Indexed EBKP
			Al	Cu	Zn	Al:Cu	
T-phases							
$Al_{7.5}Cu_4Li$	T_B	28-0012 (T_b) 03-1079 (θ) 01-1180 (Al)	68.3 ± 0.2	31.7 ± 0.2	68.3 ± 0.2	2.1	
Al_2Cu	θ	n/a	68.8 ± 0.2	31.2 ± 0.1	68.8 ± 0.2	2.2	n/a[*]
Al_2CuLi	T_1	28-0011 (T_1) 01-1180 (Al)	86.1 ± 0.2	13.9 ± 0.2	86.1 ± 0.2	6.2	
Al_6CuLi_3	T_2	44-1208 (T_2) 03-1079 (θ) 01-1180 (Al)	65.5 ± 0.1	34.5 ± 0.1	65.5 ± 0.1	1.9	n/a[#]
Zn-modified Al_2CuLi							
$Al_2(Cu, Zn)Li$	T_1-4.0wt% Zn	28-0011 (T_1) 01-1180 (Al)	63.8 ± 0.2	33.8 ± 0.1	2.4 ± 0.1	1.9	
$Al_2(Cu, Zn)Li$	T_1-6.0wt% Zn	28-0011 (T_1	64.1 ± 1.0	32.2 ± 0.9	3.7 ± 0.4	2.0	
$Al_2(Cu, Zn)Li$	T_1-8.4wt% Zn	28-0011 (T_2) 03-1079 (θ) 01-1180 (Al)	62.7 ± 0.7	32.1 ± 0.6	5.2 ± 0.5	2.0	

*: confirmed in source [5]
#: "five-fold" symmetry, EBSD not completed

Table 4. Averaged characteristic values of potential and current density for grain boundary phenomena tested using the microcell.

Stoichiometry	Phase	E_{corr}	E_{crit}	E'_{corr}	I_{pass}	I_{corr}	$i_{@-635mVsce}$
T-phases							
$Al_{7.5}Cu_4Li$	T_B	-639 ± 77	-304 ± 114	-737 ± 98	2.8×10^{-4}	3.7×10^{-7}	2.9×10^{-5}
Al_2Cu	θ	-691 ± 99	-408 ± 54	-722 ± 63	2.8×10^{-4}	4.6×10^{-6}	7.2×10^{-5}
Al_2CuLi	T_1	-836 ± 146	-513 ± 150	-816 ± 52	8.8×10^{-4}	5.3×10^{-6}	9.1×10^{-4}
Al_6CuLi_3	T_2	-1061 ± 127	-341 ± 95	-684 ± 44	1.5×10^{-4}	2.9×10^{-6}	1.7×10^{-4}
Zn-modified Al_2CuLi							
$Al_2(Cu, Zn)Li$	T_1-4.0wt% Zn	-820 ± 162	-326 ± 120	-689 ± 99	2.1×10^{-5}	8.4×10^{-7}	1.5×10^{-5}
$Al_2(Cu, Zn)Li$	T_1-6.0wt% Zn	-768 ± 117	-307 ± 83	-757 ± 112	9.6×10^{-5}	3.4×10^{-6}	8.4×10^{-5}
$Al_2(Cu, Zn)Li$	T_1-8.4wt% Zn	-764 ± 252	13 ± 269	-719 ± 249	7.6×10^{-5}	1.0×10^{-6}	1.1×10^{-4}
PFZ Analogs							
99.9999% Al[*]	n/a	-679	-545	n/a	n/a	n/a	n/a
Al-2wt%Cu[*]	n/a	-813	-447	n/a	n/a	n/a	n/a
AA2099 ST face (using standard flat cell)							
AA2099[#]	n/a	-635	n/a	n/a	n/a	n/a	n/a

[*]: see source [6]

[#]:corrosion potential from anodic polarization experiments conducted in aerated 10mM NaCl under same experimental conditions described for the deaerated samples in the FSW

Table 5. EDS analysis of surrounding area (SA) and interaction area (IA) of microcell EIS tests.

Phase	Al$_2$CuLi (T$_1$)		T$_1$-4.0 wt\%Zn		T$_1$-6.0 wt\%Zn		T$_1$-8.4 wt/%Zn	
Element	SA	IA	SA	IA	SA	IA	SA	IA
O	8.4	8.9	2.4	13.7	2.6	4.2	2.4	12.5
Al	32.8	31.3	35.3	27.0	40.1	19.3	38.0	22.0
Cu	58.8	59.8	56.6	54.0	52.9	70.0	54.3	58.8
Zn	N/A	N/A	5.6	5.3	4.4	6.5	5.2	24.2

Table 6. Heat treatment schedule and corresponding mechanical properties for AA2099 specimens aged at 160^{0}C and 190°C.

160°C				190°C			
Time (hr)	Hardness (HV)	σ_{YS}	ε @ 75% σ_Y	Time (hr)	Hardness (HV)	σ_{YS}	ε @ 75% σ_Y
3	92.4	195	0.207	3	86.8	231	0.206
6	95.4	224	0.241	6	97.1	280	0.278
9	123.6	221	0.182	9	113.0	231	0.274
12	97.6	245	0.243	12	129.1	307	0.189
15	120.5	265	0.260	15	101.0	373	0.327
18	99.5	243	0.226	18	86.8	370	0.323
21	153.8	286	0.245	21	130.5	346	0.316
24	162.0	310	0.261	24	129.5	352	0.363
30	136.6	249	0.264	30	125.2	369	0.343
42	151.5	297	0.315	42	141.3	300	0.309
60	155.5	312	0.305	60	152.0	299	0.286
84	163.0	327	0.254	84	155.0	370	0.326
132	166.9	306	0.239	132	177.5	325	0.320
216	177.0	274	0.309	216	145.4	272	0.312
360	174.2	391	0.395	360	136.5	261	0.276
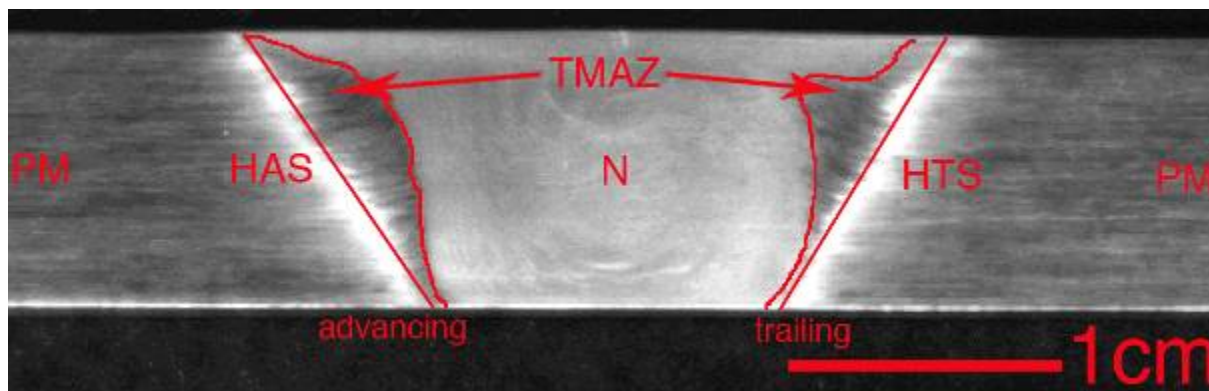
Figure 1. Optical micrograph depicting the effects of friction stir welding on the microstructure of AA2099.
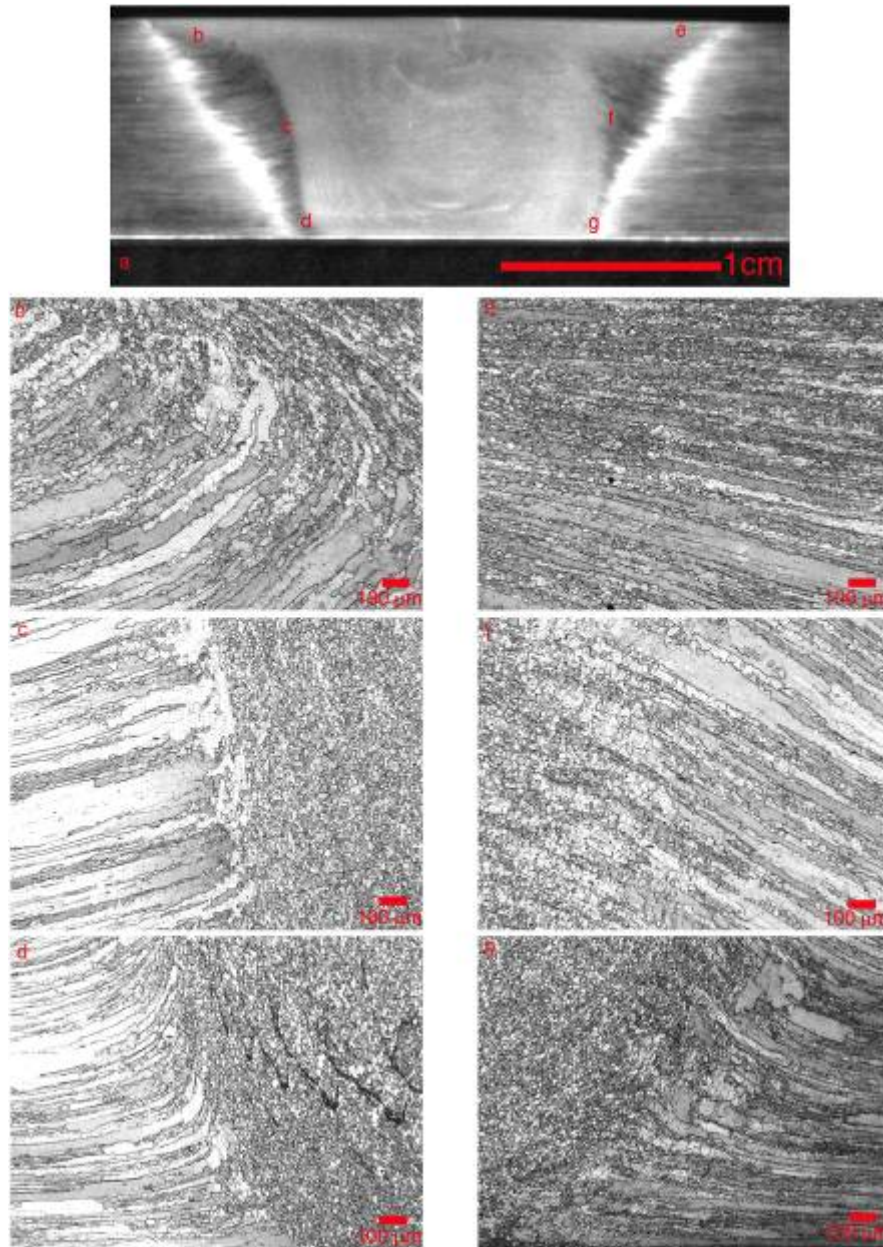
Figure 2. Optical micrographs depicting the change in microstructure around the weld nugget.
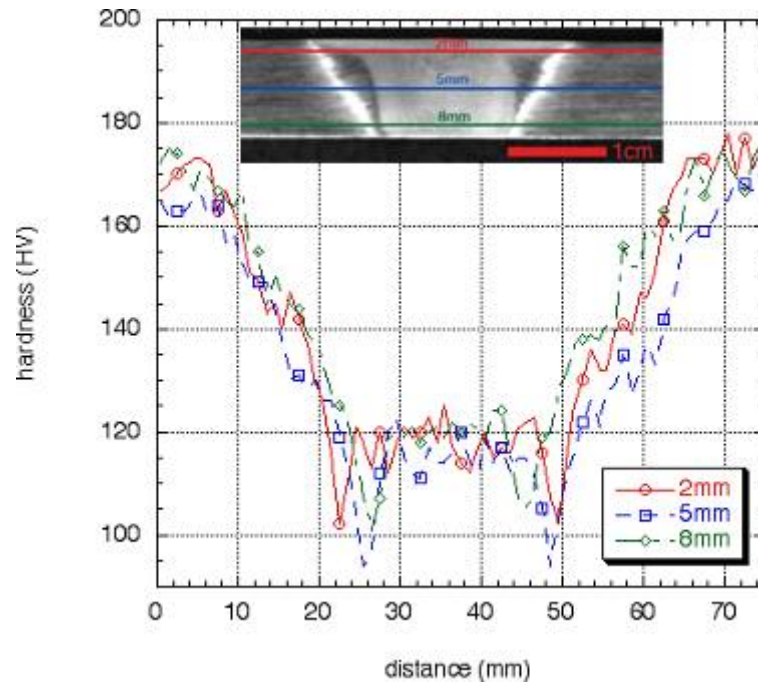
Figure 3. Microhardness profile of the friction stir weld AA2099 plate.
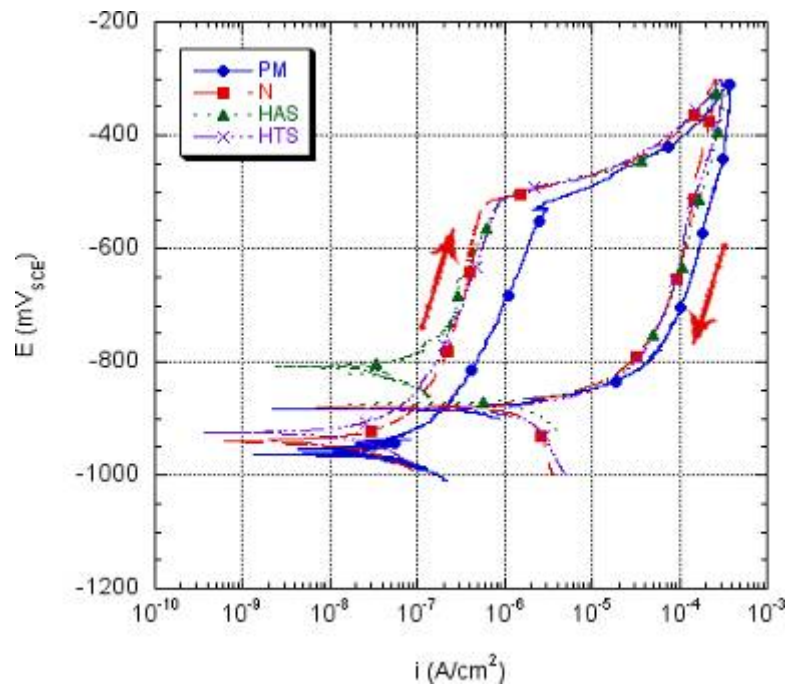
Figure 4. Cyclic polarization scans of the weld zones in deaerated 10mM NaCl.
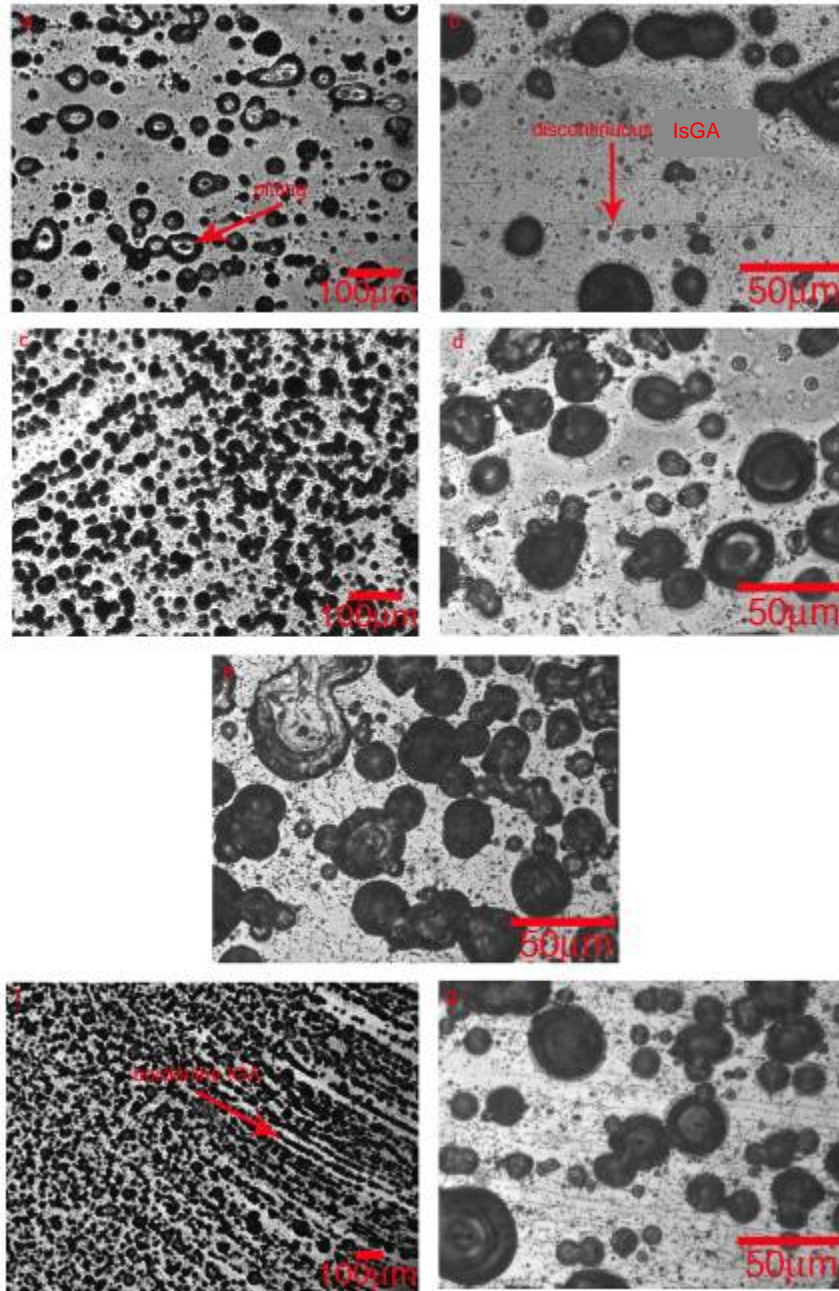
Figure 5. Optical micrographs of the observed corrosion morphologies resulting from ASTMG 110-92 constant immersion testing – (a) low magnification parent material, (b) high magnification parent material, (c) HAS low magnification, (d) HAS high magnification, (e) nugget, (f) HTS low magnification, and (g) HTS high magnification. [2]
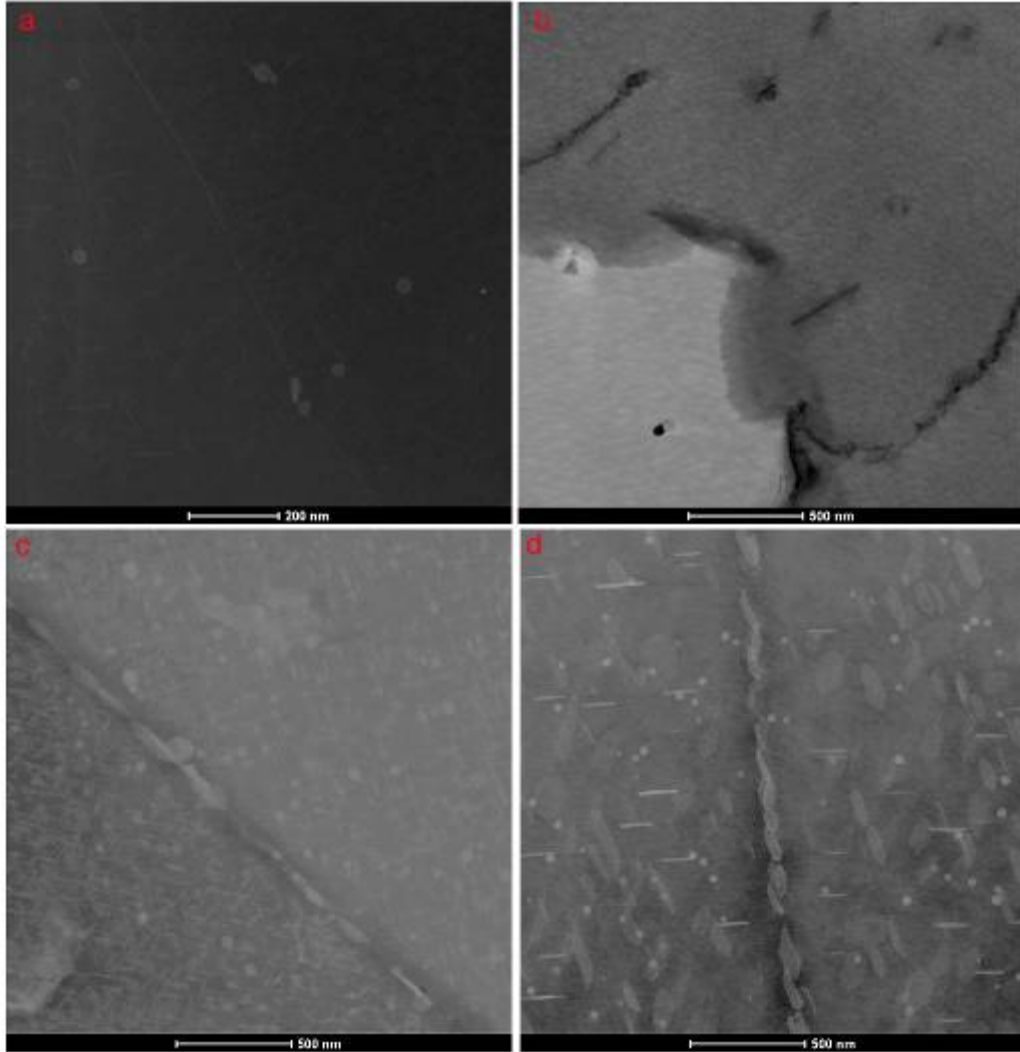
Figure 6. STEM imaging of low angle grain boundaries in (a) PM, (b) N, (c) HAS, and (d) HTS.
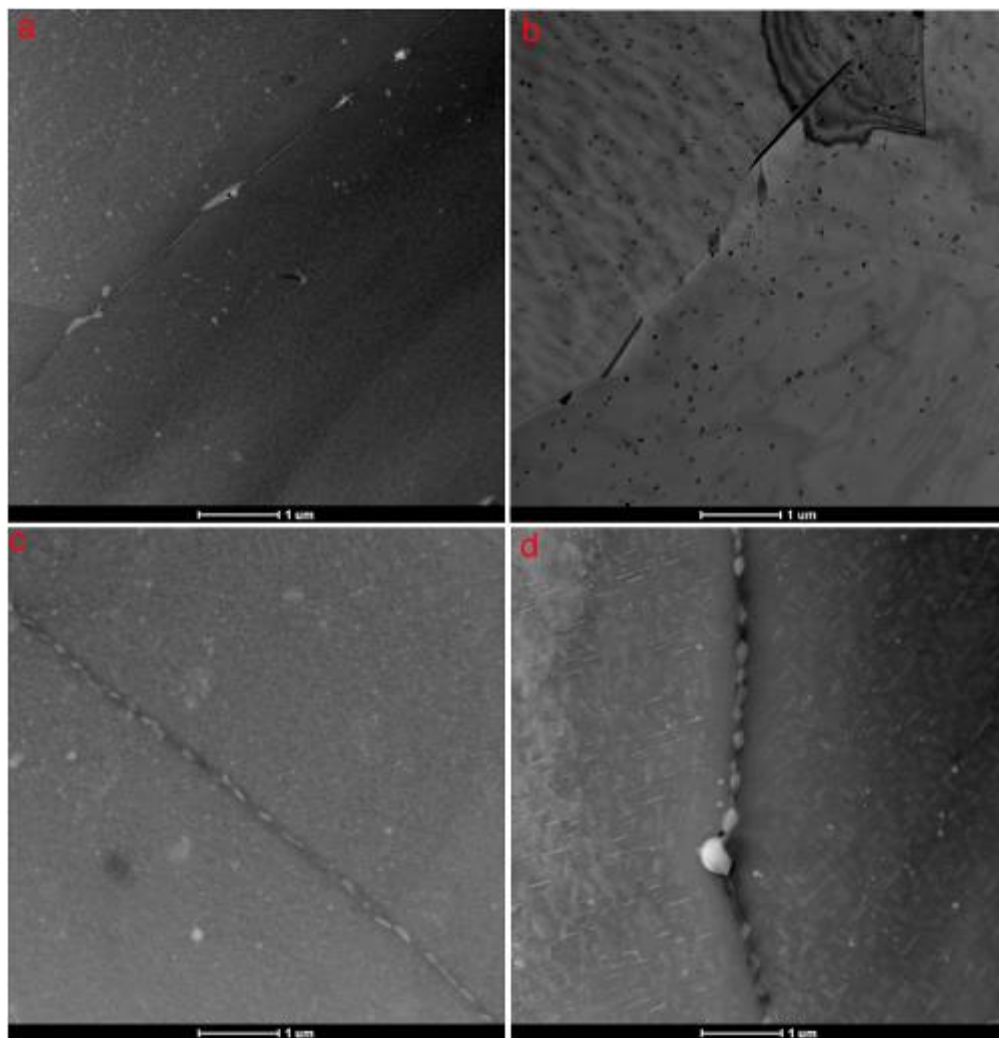
Figure 7. STEM imaging of high angle grain boundaries in (a) PM, (b) N, (c) HAS, and (d) HTS.
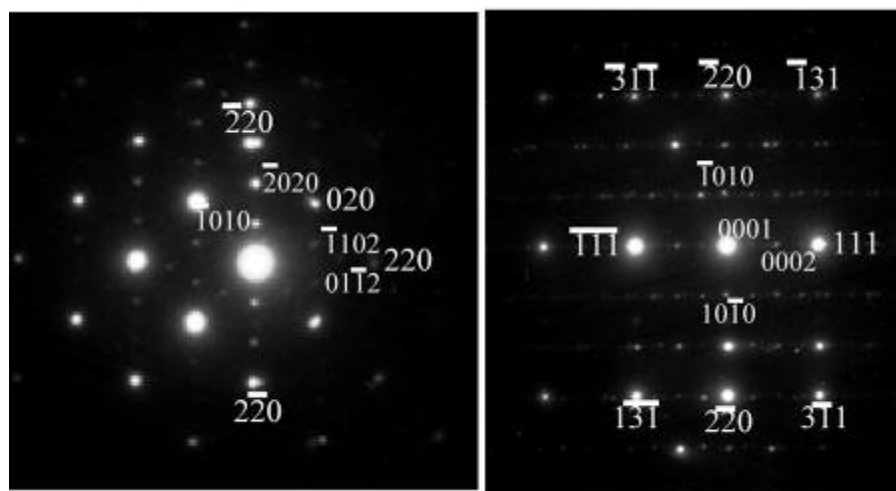
Figure 8. Diffraction evidence along two zones confirming T_1's structure in the HTS weld zone.
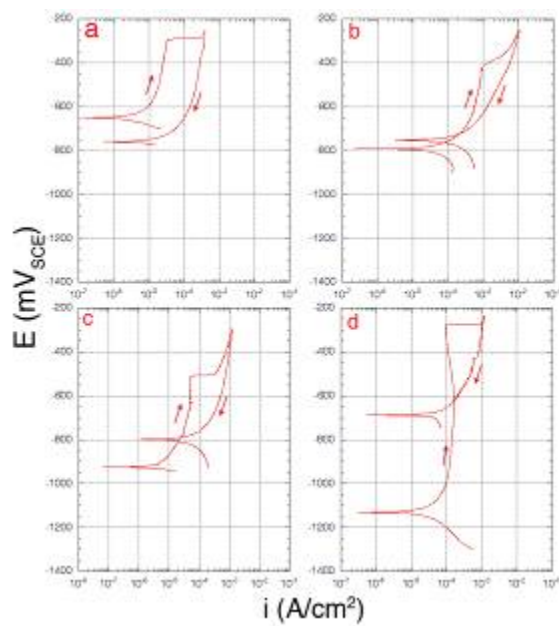
Figure 9. Representative cyclic polarization curves for T-phase analogs
(a) T_B , (b) θ , (c) T_1, and (d)T_2.
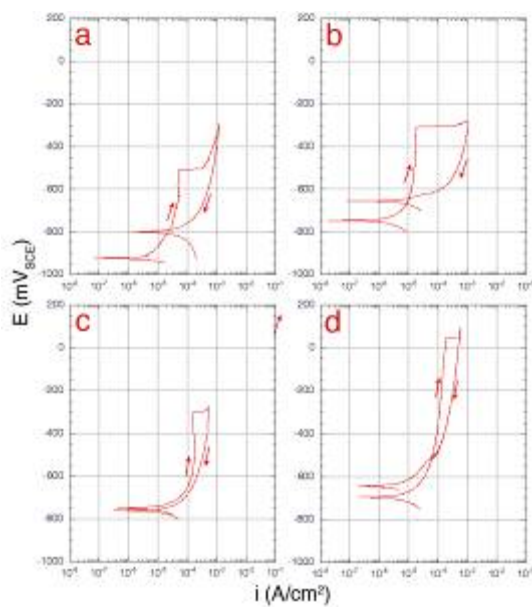
Figure 10. Representative cyclic polarization curves for Zn modified
T_1phase (Al$_2$CuLi) analogs (a) T_1, (b) T_1-4.0wt%Zn, (c) T_1-6.0wt%Zn,
and (d) T_1-8.4wt%Zn.
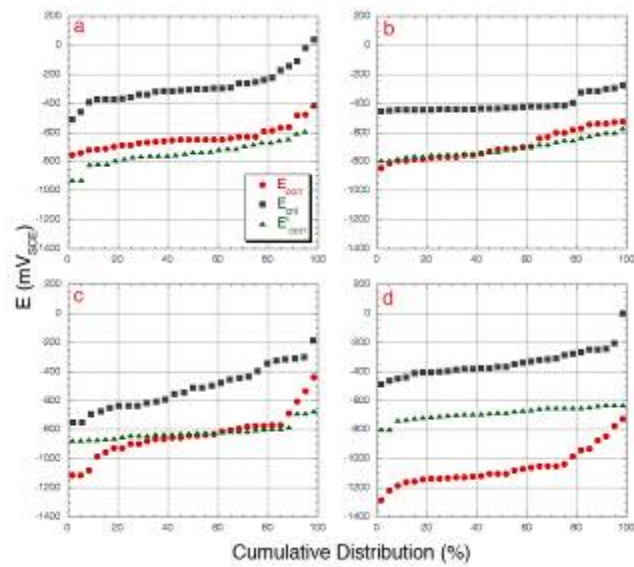
Figure 11. Cumulative distribution plots of T-phase analogs (a) T_B, (b) θ, (c) T_1, and (d) T_2.

.
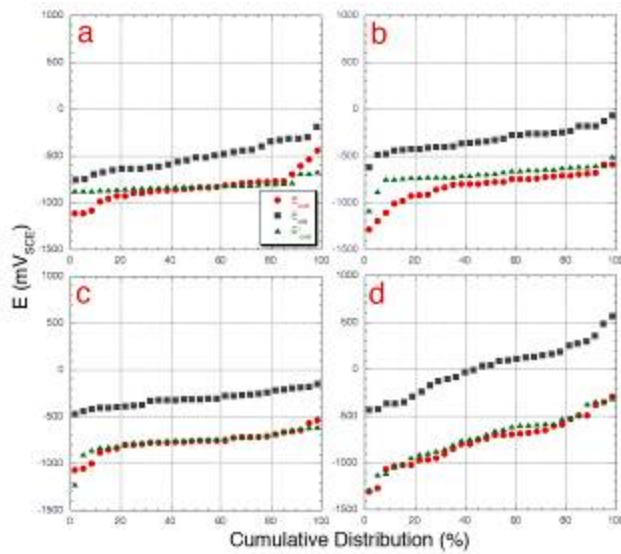
Figure 12. Cumulative distribution plots of Zn-modified T_1-phase (Al$_2$CuLi) analogs (a) unmodified, (b) 4.0wt%Zn, (c) 6.0wt%Zn, and (d) 8.4wt%Zn.
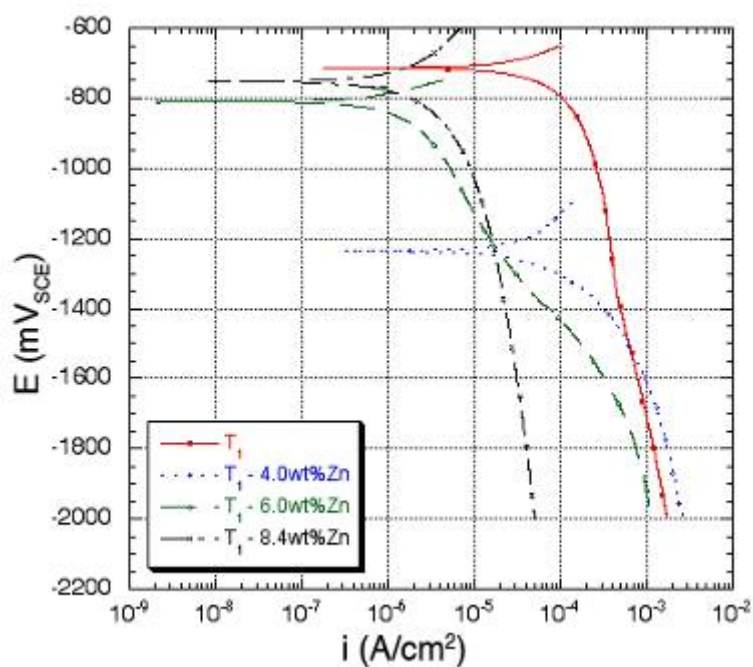
Figure 13. Cathodic polarization experiments done by the microcell on unmodified and Zn-modified T_1 synthesized ingots.
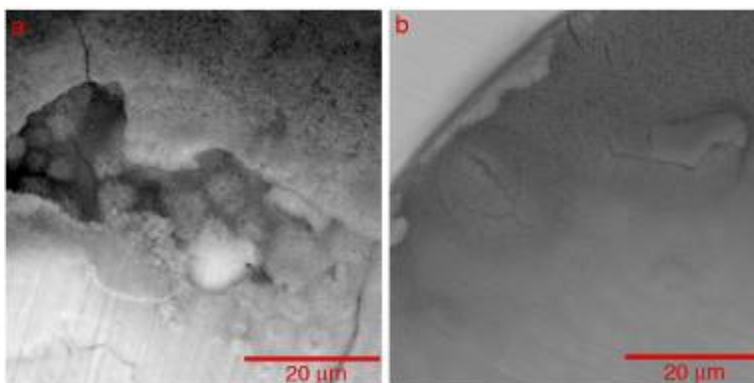
Figure 14. SEM secondary electron micrographs of the interaction area for (a) Al_2CuLi unmodified and (b) T_1-6.0wt%Zn ingots after exposure to EIS testing using the microcell.

4. Discussion

4.1 Friction stir welding of AA2099

Optical microscopy highlighted the significant microstructural changes that occurred in the AA2099 plate as a result of the friction stir welding process. These changes in microstructure vary through the thickness of the sample as well as asymmetrically about the weld line. The resulting variation of microstructure is a result of two separate heat transfer processes. The first is a heating input due to the frictional heating of the material from the rotation of the pin tool used to join the material. The second is cooling from the bulk plate and lower surface of the welding machine that was used to stabilize the plate during welding. Basically this translates to the temperature being greatest at the shoulder of the FSW tool, then decreasing radially in all directions.

It is within the subtler features of the microstructure where the differences between the (heat affected zones (HAZs) and PM weld zones reveal themselves, specifically within the transmission electron microscopy work. When comparing the HAZs and the parent material, the HAZs experienced a sufficiently high temperature and time combination to coarsen both precipitates along the grain boundary and in the matrix. In every case the dominant phase on the boundary was T_1. Now comparing the heataffected zones, the HTS clearly has a larger precipitate size qualitatively than that observed for the HAS. Additionally the widening of the HTS PFZ indicates that the heating was greater for this side of the weld versus the advancing side. Asymmetrical heating about the weld centerline during the welding process has been noted and is strongly dependent on the weld parameters that were selected for joining. [7]

Ultimately these variations in microstructure and mechanical behavior (as seen in the CERT testing in air and the hardness measurements) should have a direct impact on the corrosion behavior of the weld zones. Testing in deaerated 10mM NaCl revealed little difference in E_{crit} and E_{corr}, with the standard deviation encompassing the variation. A plausible explanation for the dissimilarity in E_{corr} is that, prior to polarization; the solution had varied levels of oxygen purged −from? it, resulting in a varied cathodic contribution by oxygen to the current. The variation in the $E_{crit,}$ or the lack thereof, implies that the potentiodynamic polarization scans were not sufficient to draw out any noteworthy differences in corrosion behavior. Another possible and the most likely answer is that, despite the significant variations noted in microstructure and mechanical behavior, there were no appreciable differences in the corrosion behavior between the weld zones.

The initial assessment of constant immersion testing provided similar results; however, intermittent observations showed that time was critical for the initiation of IsGA. For the HAZs, pitting, borderline intergranular attack, and discontinuous IsGA were evident within minutes of immersion, likely due to the heavy precipitation of T_1 on the sub-grain boundaries as observed in the TEM work. The population density of particles on subgrains for these weld zones is quite high as evidenced by the STEM data.

Having observed a difference in the onset of the IsGA corrosion morphology from the immersion testing, CERT testing was conducted to determine if these variations translated into a change in

stress corrosion cracking behavior. Ductility ratios (D.R.) were the first indication of the varied SCC responses across the weld. For all samples tested, a decrease in D.R. was observed; however, the greatest reduction was observed within the HTS. Fractography of the air tested specimen versus the specimen tested in environment was not noticeably different for the PM, HTS, and HAS weld zones, but a transition from transgranular to intergranular type failure was quite apparent within the nugget. This transition is indicative of intergranular stress corrosion cracking taking place. Noting that the dominant grain boundary phase for the nugget and the HTS were the same (T_1), it can be concluded that an enhanced susceptibility to stress corrosion cracking was in fact occurring for the HTS samples. Likely the elongated grain structure of the plate made seeing this transition occurring within the PM, HTS, and HAS very difficult.

This is corroborated with the evidence presented for the weld transverse samples, tested using CERT. For these samples tested in solution, failure occurred in the HTS weld zone for all three samples tested. Though there was no reduction in ductility for testing in solution, the exclusivity of failure indicated preferential failure within the HTS. It is interesting that this was the case considering that the grain boundaries of the TMAZs were oriented parallel to the load axis. If the mechanical aspect of CERT testing was dominating for this set of experiments, the TMAZs should have failed due to the unfavorable loading orientation. But again, the intermittent immersion data indicated that these zones were the last to show the onset of IsGA, indicating a lower population density of T_1 on their sub-grain boundaries.

The relatively insignificant change in D.R. for the weld transverse samples is likely a result of strain localization within the HAZs of the round tensile bar's gauge length. Testing of this type is done with the assumption that when loaded, samples will experience equal stressing throughout the entire gauge length. Because of the softer HAZs, strain was localized to these regions solely, as evidenced by necking in both regions. The reason as to why failure occurred in the HTS versus other weld zones in weld-transverse (WT) tests is a result of the high density of T_1 precipitates populating the grain boundaries as well as strain localization within the weld zone.

4.2 Electrochemical behavior of grain boundary phenomena

Electrochemical characterization of intermetallic phases that could potentially occupy the grain boundaries of AA2099 hinged on the successful synthesis of compositionally and structurally accurate analogs. Consulting of equilibrium phase diagrams for the ternary phases allowed for a general sense of composition for the initial melt charge, even though equilibrium conditions were not observed during melting. It was by the production of multi-phase ingots, which included crystals of the desired phase, that intermetallics were produced. Successful production was confirmed using EDS, EBSD, and XRD. The combined compositional and structural testing allowed for proof-positive evidence of successful synthesis of all intermetallic phases.

In comparing the corrosion potentials of the synthesized intermetallics, a hierarchy of electrochemical reactivity emerges. The same is true of the breakdown potential and repassivation potential as illustrated in Equation 2:

$$E_{corr}: Al_{7.5}Cu_4Li > Al_2Cu > Al_2CuLi > Al_6CuLi_3$$
$$E_{crit}: Al_{7.5}Cu_4Li > Al_6CuLi_3 > Al_2Cu > Al_2CuLi \qquad \textbf{eq (2)}$$
$$E'_{corr}: Al_6CuLi_3 > Al_2Cu > Al_{7.5}Cu_4Li > Al_2CuLi$$

Of the averaged breakdown potentials, the electrochemical weak link is T_1 as predicted in the literature. [8] This value is particularly critical with regard to stress corrosion cracking since failure is often observed to be intergranular. As observed in the friction stir welding work, this intermetallic can precipitate readily on the grain boundary under appropriate conditions. In addition to the highest cathodic breakdown potential, the passive current densities for T_1 is greatest, which is consistent with the notion of the phase being the electrochemical "bad-actor".

In contrast to T_1, T_B is substantially more noble with regard to E_{crit}, having an average value of -304 mV$_{SCE}$. This corroborates suggestions in the literature to this effect. [9] Likely, this is a result of some dealloying process that enriches the surface layer with Cu. As mentioned before, this phase has the least amount of lithium in the structure, which again rationalizes these observations. This argument does not hold however for the case of T_2, which was expected to behave more like T_1 than T_B. [10] Despite the fact that this intermetallic has quite a large Li content, its characteristic values do not show it to be a weighty influence on the characteristic value of E_{crit}.

At the corrosion potential of AA2099 (-635mV$_{SCE}$), most of the equilibrium phases had current densities on the anodic branch of the curve a majority of the time. T_B had the lowest current density at this potential, while T_1 proved to have the largest. A dual nature was observed for both θ phase and T_B with instances of cathodic protection of the phase feasible a fraction of the time.

A portrait of complex electrochemical nature emerges from the potential and current density results for the equilibrium phases. Consideration must be given not only to a galvanic ranking of the characteristic potentials, but to the rate at which the reaction is progressing. There are instances of duality as far as particles acting in both a cathodic and anodic capacity, as well as examples of noble particles showing fast kinetics. With this in mind the investigation moves on to the Zn-modified T_1 phases.

Documented evidence shows that Zn can substitute for Cu in the T_1 phase, but the conditions under which this is considered to occur are not well understood. Only a general observation of increased SCC resistance is noted when these modified particles occupy the grain boundary. [9] An accurate picture of the chemistry after Zn substitution is not present, and therefore it was deemed acceptable to access the affect of Zn by arbitrarily selecting three compositions with progressively greater Zn additions. It is therefore not the contention of this work to make claims that the observed behavior is precisely representative of the particle's electrochemical behavior when present in the alloy.

For these Zn-modified T_1 intermetallic analogs, an increase in corrosion potential is evident with increasing Zn content. A similar result occurs for the breakdown potential and repassivation potential, where again increasing Zn substituted for Cu results in more anodic breakdown potentials. The average values rank as shown in Equation 3:

$$T_1 - 8.4wt\%Zn \; > \; T_1 - 6.0wt\%Zn \; > \; T_1 - 4.0wt\%Zn \; > \; Al_2CuLi \qquad \textbf{eq (3)}$$

Considering the activating nature of Zn, this result could be quite confusing as increasing Zn causes an ennobling effect. This leads to the idea that again the electrochemical behavior for this phase is quite complex and cannot be reconciled by a compositional argument alone.

EIS measurements were conducted in the hope that a variation in surface chemistry might shed some light on this behavior. These tests were completed only with the intention of pre-treating the surface for EDS analysis. No effort was made to interpret the results in the context of surface growth kinetics; however, the current efforts do provide some insight into the complex behavior of this modified intermetallic.

EDS results show a substantial change in Cu content for the case of 6.0 wt% Zn addition, but such a large change in Cu is not readily observed for the 4.0wt% Zn and 8.4wt% addition. However, there is a significant increase in oxygen content for these cases, indicating presence of an oxide film. Most likely, the oxide is from corrosion product and is not actually the surface layer influencing the observed phenomenon. It could be that the oxide layer is preventing an accurate measure of the composition by obscuring the significance of other elements in the EDS spectra. An enrichment of Zn is also observed for the surface layer for the 6.0wt%Zn and 8.4wt%Zn additions. In fact quite a substantial change for the 8.4wt% case was noted.

The morphology of the surface layer after the pre-treatment exercise is indicative of dealloyed surface layer with the porous surface layer outlining the circumference of the microcapillary. It is well known that the Cu containing intermetallics like Al_2CuMg (S phase) dealloy, leaving a remnant layer of Cu which ennobles the surface layer by pushing pitting potentials in the positive direction. [11] This accounts for the observed Cu enrichment of the surface, but the Zn enrichment is indicative of another phenomenon. It is well known that Zn^{+2} acts as a cathodic inhibitor ultimately influencing the kinetics of the oxygen reduction reaction. For the case considered, Zn^{+2} ions present in the porous copper layer are inhibiting oxygen reduction reaction kinetics and in essence improving the corrosion behavior of the T_1 precipitate. This is reinforced by the cathodic polarization curves of the Zn-modified intermetallics where increasing Zn content shows reduced transport limited kinetics, culminating in a decrease of 2 orders of magnitude for the 8.4 wt% Zn-modified Al_2CuLi.

Data reported in reference [6] are used to estimate the electrochemical behavior of solute depleted and precipitate-free zones that form in the alloy. The average corrosion potential and breakdown potential reported for pure Al in 10mM NaCl were -679mV$_{SCE}$ and -545mV$_{SCE}$ respectively. For the case of Al-2wt%Cu, these values were -813mV$_{SCE}$ and -447mV$_{SCE,}$ respectively. As expected there is an ennobling affect in the breakdown potential as a result of Cu in solid solution.

From the information gathered thus far, a model for corrosion damage accumulation on the surface of AA2099 can now be discussed in the context of intermetallic electrochemical behavior. Using local galvanic coupling of grain boundary structures and the surrounding matrix is not uncommon when rationalizing mechanistic explanations of Al alloys.[12] However, it has been suggested, and proven to be a valid concern in this study, that relying only upon a potential-based argument might be insufficient for complete interpretation.[6] It is with this knowledge that the following argument was formulated for speculated damage accumulation on AA2099 along grain boundaries.

For instance, in the case of T_2 the corrosion potential is on average 200mV below that of T_1; however, the corrosion current density for the T_2 phase is less than T_1. At the average corrosion potential of the alloy, this in the case where these phases would exist together, T_1 will preferentially dissolve ahead of T_2 dissolution. With the introduction of Zn substituted with copper, the electrochemical behavior of the T_1 phase completely reverses and becomes comparable to the nobler phases, so that T_2 will dissolve ahead of the Zn-modified phase. As for comparison with other T-phase intermetallics, the traditional interpretation of a galvanic hierarchy coincides with the current density information.

Coupling the information presented for the unmodified T-phases and that present in reference [6] for the PFZs, some conclusions on the galvanic interaction of these particles and the surrounding areas can be made. Strictly from a corrosion potential perspective, the T_1 and T_2 phases would preferentially dissolve in the presence of a PFZ. However, θ and T_B would instead act as a small cathode supporting the dissolution of a much larger anodic area - the PFZ. This is due to the cumulative distribution of the corrosion potential of these intermetallics is anodic to that of the PFZ analogs.

As alluded to in the introduction, the electrochemical behavior of these intermetallics can be critical in producing conditions of stress corrosion cracking susceptibility or resistance. With that knowledge in hand, the anodic dissolution mechanism proposed for AA2099 is somewhat better understood. Noting that the crack path in solution of this alloy is intergranular, the anodic dissolution of the grain boundary structure seems reasonable. Judging from the results presented here, the observation within the literature stating enhanced susceptibility of SCC failure with the presence of T_1 on the boundary is validated. However, instances of SCC resistance with T_B on boundaries only speculated upon were herein confirmed as being in alignment with the electrochemical behavior of the phase. Finally, judgments in the literature with regard to T_2 having a deleterious affect on SCC resistance are not corroborated in this testing survey, but instead found to be resistant to pitting. The findings in this investigation support an image of complex corrosion behavior of intermetallic particles, which extends to a complex interpretation of corrosion behavior of AA2099.

5. Conclusions

5.1 Friction stir welding conclusions

- The friction stir welding process does influence the environmental susceptibility of AA2099 alloy system as observed in CERT. Because of the aging observed on the

trailing side of the weld, precipitation of T_1 was rampant, with the result being a substantial change in susceptibility from the ambient air to environment CERT experiments for this weld zone.

- Potentiodynamic measurements were not explicit in revealing significant differences in electrochemical response with respect to breakdown potentials; however, the time dependent immersion testing showed variation in sub-grain boundary precipitation between the zones.
- STEM imaging of the high angle and sub-grain boundaries showed that the dominant phase on all boundaries in this friction stir welded AA2099 was T_1; however, it was the difference in size and morphology of the precipitate that corroborated the results from the intermittent immersion experiments.
- The HTS was the most susceptible region for environmental attack as indicated by the ductility ratios and the exclusively of failure in the HTS weld zone of weld transverse specimens during CERT.
- AA2099 is susceptible to enhanced stress corrosion cracking when friction stir welded because of electrochemically aggressive T_1 particles populating the sub-grain boundaries.

5.2 Corrosion behavior of grain boundary phenomena

- Compositional and structural validation techniques confirmed the prospect of producing ingots that contain crystals that are representative of precipitate phases.
- Testing of the intermetallic particles revealed specifics about the electrochemical behavior of the phases that had only been previously speculated in literature.
- The microcapillary electrochemical cell can be utilized to reveal electrochemical differences between bulk intermetallics that can be used to better understand corrosion mechanisms.
- Characteristic potentials of corrosion behavior exist within an envelope for the intermetallics investigated.
- When interpreting the behavior of these intermetallic particles, notice must be given to both the characteristic potentials and the kinetics at which the reaction is occurring.
- Zn-modified Al_2CuLi displays complex dissolution behavior, which is indicative of dealloying and cathodic inhibition.

6. Recommendations

6.1 Modeling of SCC

Given the significance placed on the accelerated insertion of newly developed alloys, it seems reasonable to extend the current understanding of AA2099 in this study to modeling. Considering the complex nature of the microstructure, and thus the complex localized corrosion behavior, true accuracy in predicting SCC lies in understanding the corrosion damage accumulation of the surface. With the knowledge gained during this experimentation it is reasonable to conduct stress corrosion crack testing of double cantilever beam specimens using ASTM G 168-00.[13] Heat treatment of these specimens at various time-temperature combinations would result in varied crack growth rates in the samples. These results can be fed into a linear regression model that would relate crack growth rates and heat treatment schedule.

6.2 Complete survey of all phases present in AA2099

A complete electrochemical survey of all phases that may potentially be found within this alloy system is recommended, even for phases such as AlLi (δ) or Mn-bearing dispersoids. Though such studies have been completed at The Ohio State University for 7XXXs intermetallics, there are still data gaps for this particular alloy system that may have bearing on the corrosion damage accumulation observed on the surface. It will also add to the vast volume of knowledge gained by present and past efforts.

6.3 Retrogression and re-aging of FSW AA2099

Efforts should be made to restore the strength and corrosion properties of the friction stir welded AA2099. Within the nugget, there are significant gains to be made in strength by artificial aging in order to restore the strengthening phase (T_1) within the matrix. Additionally, promoting the precipitation of a benign phase over an active one along grain boundaries would significantly help the SCC observed within the HTS of the weld. It is reasonable to suggest that in the future the welding parameters might be adjusted so that uneven heating about the centerline of the weld does not result in asymmetric SCC properties within the weld zones

7. References

[1] A. A. Csontos and E. A. Starke, "The effect of inhomogeneous plastic deformation on the ductility and fracture behavior of age hardenable aluminum alloys," INTERNATIONAL JOURNAL OF PLASTICITY, vol. 21, no. 6, pp. 1097–1118, 2005.

[2] ASTM G 110-92(2003), "Standard practice for evaluating intergranular corrosion resistance of heat treatable aluminum alloys by immersion in sodium chloride + hydrogen peroxide solution," 2003.

[3] ASTM G 129-95, "Standard practice for slow strain rate testing to evaluate the susceptibility of metallic materials to environmentally assisted cracking," 1995.

[4] ASTM G 44-99, "Standard practice for exposure of metals and alloys by alternate immersion in neutral 3.5% NaCl," 1999.

[5] J. R. SCULLY, T. O. KNIGHT, R. G. BUCHHEIT, and D. E. PEEBLES, "Electrochemical characteristics of the Al_2Cu, Al_3Ta and Al_3Zr intermetallic phases and their relevancy to the localized corrosion of al-alloys," CORROSION SCIENCE, vol. 35, no. 1-4, pp. 185–195, 1993.

[6] N. Birbilis and R. G. Buchheit, "Electrochemical characteristics of intermetallic phases in aluminum alloys - an experimental survey and discussion," JOURNAL OF THE ELECTROCHEMICAL SOCIETY, vol. 152, no. 4, pp. B140–B151, 2005.

[7] R. Nandan, G. G. Roy, T. J. Lienert, and T. DebRoy, "Numerical modeling of 3d plastic flow and heat transfer during friction stir welding of stainless steel,"

SCIENCE AND TECHNOLOGY OF WELDING AND JOINING, vol. 11, pp. 526–537, Sep 2006.

[8] R. Buchheit, J. Moran, and G. Stoner, "Localized corrosion behavior of alloy 2090 - the role of microstructural heterogeneity," Corrosion, vol. 46, no. 8, pp. 610–617, 1990.

 [9] J. E. Kertz, P. I. Gouma, and R. G. Buchheit, "Localized corrosion susceptibility of Al-Li-Cu-Mg-Zn alloy AF/C458 due to interrupted quenching from solutionizing temperatures," METALLURGICAL AND MATERIALS TRANSACTIONS A-PHYSICAL METALLURGY AND MATERIALS SCIENCE, vol. 32, pp. 2561–2573, Oct 2001.

[10] Y. L. Liu, Y. Zhang, Z. Q. Hu, and C. X. Shi, "The influence of Mg and Zr on T_2 phase and precipitation-free zone of Al-Li alloy," in Sixth International Aluminum-Lithium Conference (M. Peters and P.-J. Winkler, eds.), vol. 1, (Garmisch-Partenleirchen, Germany), pp. 119–124, DGM Informations-gellschaft, 1991.

[11] R. G. Buchheit, R. P. Grant, P. F. Hlava, B. Mckenzie, and G. L. Zender, "Local dissolution phenomena associated with s phase ($Al_2 CuMg$) particles in aluminum alloy 2024-T3," JOURNAL OF THE ELECTROCHEMICAL SOCIETY, vol. 144, pp. 2621–2628, Aug 1997.

[12] Z. Szklarska-Smialowska, "Pitting corrosion of aluminum," CORROSION SCIENCE, vol. 41, pp. 1743–1767, Sep 1999.

[13] ASTM G 168-00, "Standard practice for making and using pre-cracked double beam stress corrosion specimens," 2000.

8. Names of Personnel

Rudolph G. Buchheit (OSU Faculty Member)
Donna Ballard (AFRL/ML Mentor)
Kumar Jata (AFRL/ML Mentor)
Jay Tiley (AFRL/ML Mentor)
Barbara N. Padgett (OSU Graduate Student)

<u>**Task 4**</u>
Development of Image- Based Crystal Plasticity Computational Models for Fatigue Analysis. *Somnath Ghosh (OSU Faculty member), Dennis Dimiduk (AFRL/RX Mentor), Michael Uchic (AFRL/RX Mentor), Michael Groeber (OSU Graduate Student)*

I. RESULTS and DISCUSSION

1. Introduction

The main intent of this research is to develop computational models of polycrystalline materials that will incorporate accurate morphological and crystallographic components of the microstructure for analyzing mechanical response and fatigue failure in metallic materials. The models will be used to investigate the dependence of cyclic behavior, fatigue crack initiation and fatigue life on material microstructure including crystallographic texture, grain size, grain shape and neighborhood distribution. They will explore variables at different scales to understand damage and failure mechanisms and model the fatigue failure process as a phenomenon of evolving microstructural damage propagating across different length scales. A probabilistic analysis framework will be developed to assess the effect of variabilities in microstructure, material properties and loads, on failure probability and hence on component reliability. To complement the development of these various models, it is intended that they be validated experimentally. In this way, the models will be rendered more acceptable to the design community.

2. Methods, Assumptions, Procedures

The key component of the model generation is a detailed characterization of the polycrystalline structure in 3D. In order to characterize the material in 3D, an experimental procedure for collecting 3D information directly was developed. The size scale of the material investigated, IN100, fit well with the size capabilities of the dual beam Focused Ion Beam-Scanning Electron Microscope (FIB-SEM). The FIB-SEM was automated using custom scripts written during this work. The scripts control the movement of the microscope and the sectioning of the sample to generate a 3D dataset by serial sectioning. The FIB-SEM also provides useful analysis tools, such as electron backscatter diffraction (EBSD). An EBSD map was collected on each serial section and used during the reconstruction and grain identification process. The following figures illustrate the geometry of the samples and the movement of the microscope.
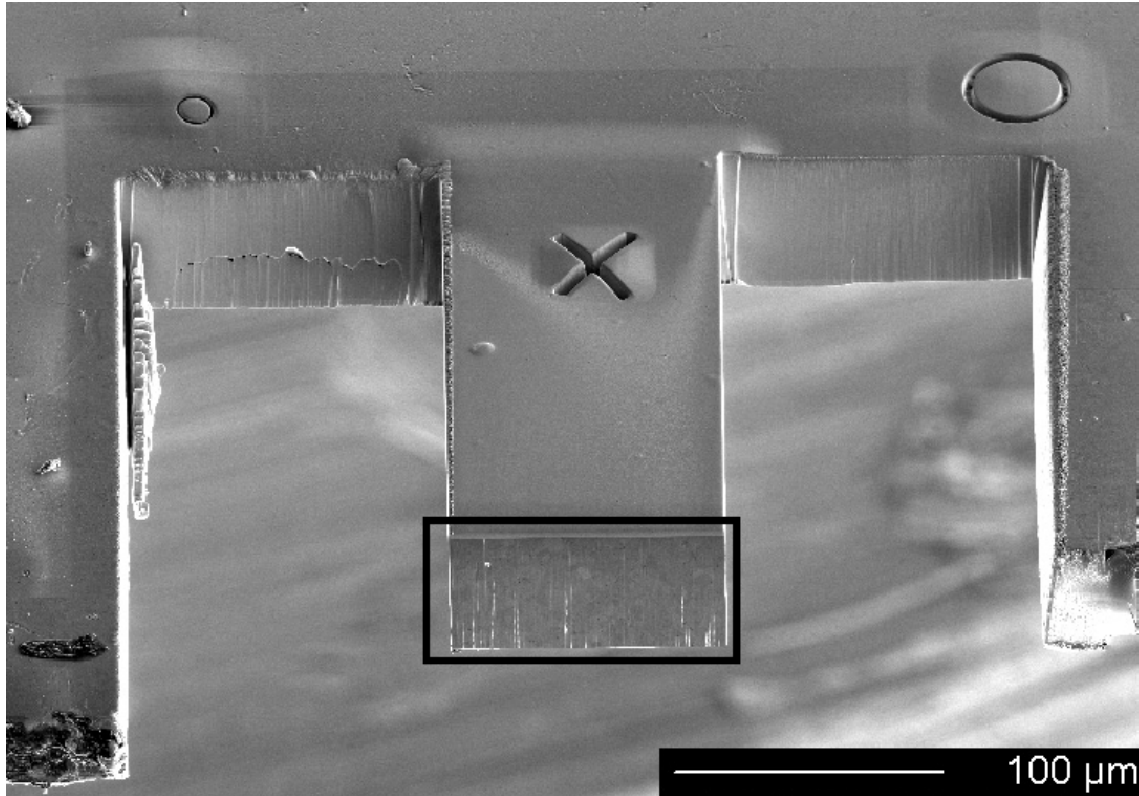
Figure 1. Illustration of the "finger" geometry used during the serial-sectioning process in the DB FIB-SEM. The surface highlighted by the black box is the surface that is repeated removed and mapped by the EBSD software.
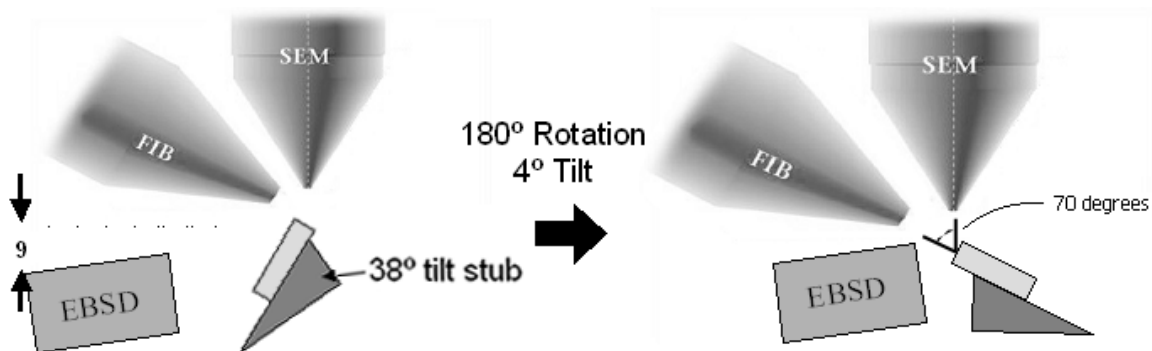
Figure 2. Schematic illustrating the geometries of the two positions during the sectioning experiment as well as the rotation needed to move between them.

Reconstruction, grain identification, and data filtering were all carried out by custom codes developed in this work. The EBSD data obtained during the serial sectioning experiment provides quantitative data that enables the automated segmentation of grains and other features in the volume investigated. The following figure shows the reconstructed volume.
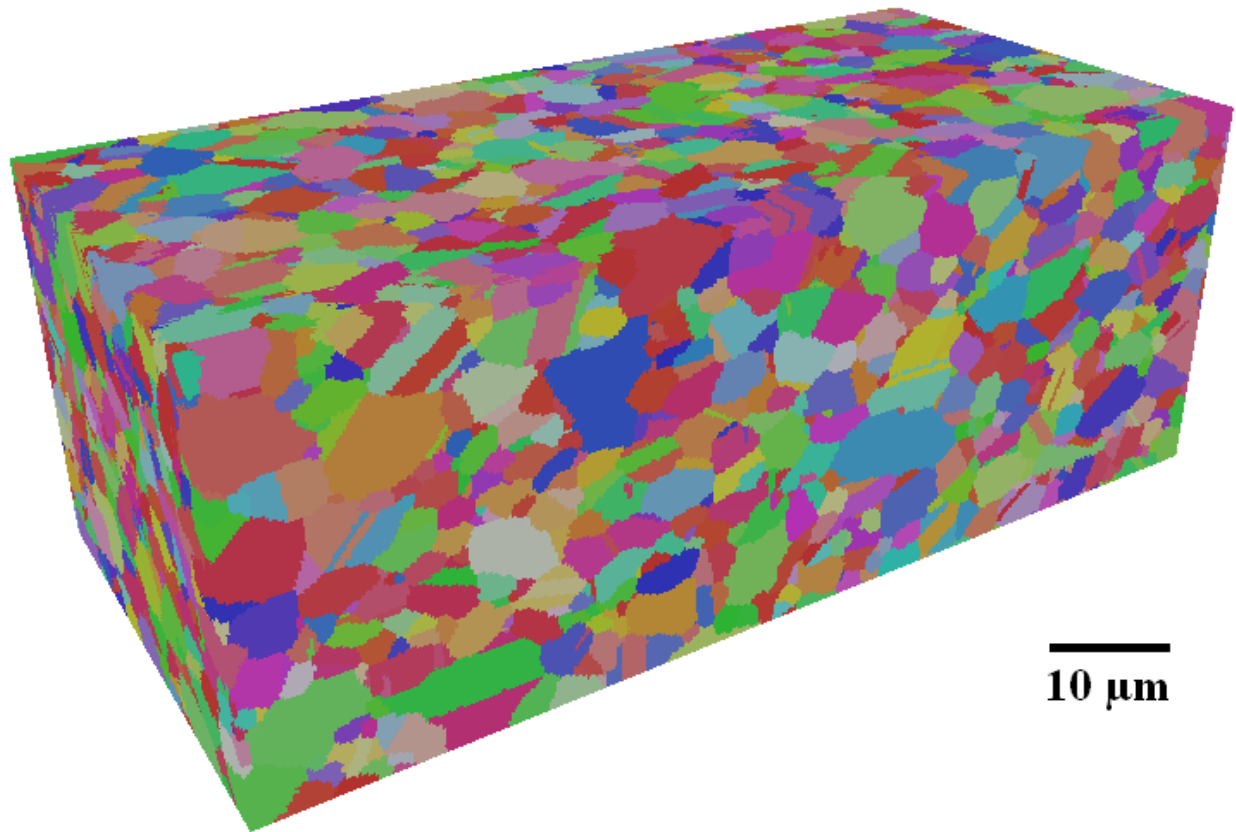
Figure 3. 3D reconstruction of IN100 Ni-Based superalloy. The volume shown is the reconstruction of individual EBSD maps collected during the serial-sectioning experiment and has dimensions 96 μm x 36 μm x 46 μm.

Following identification of grains and features in the volume, a suite of statistical descriptors were measured for the volume. These statistics range from the distribution of grain size and shape to the orientation and misorientation distributions. In addition, the correlation between statistical descriptors was measured, which was made possible through the ability to measure each feature individually. This capability is a direct result of automated segmentation made possible by the EBSD data. The following figures illustrate a subset of the statistical descriptors.
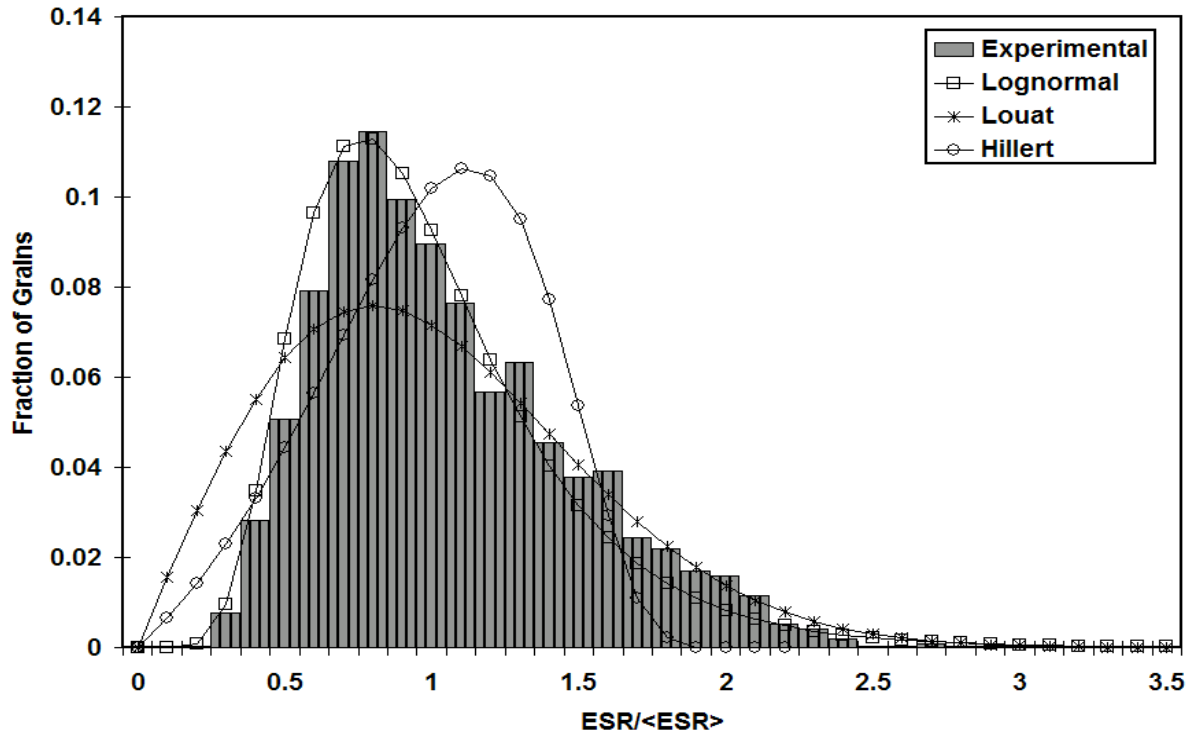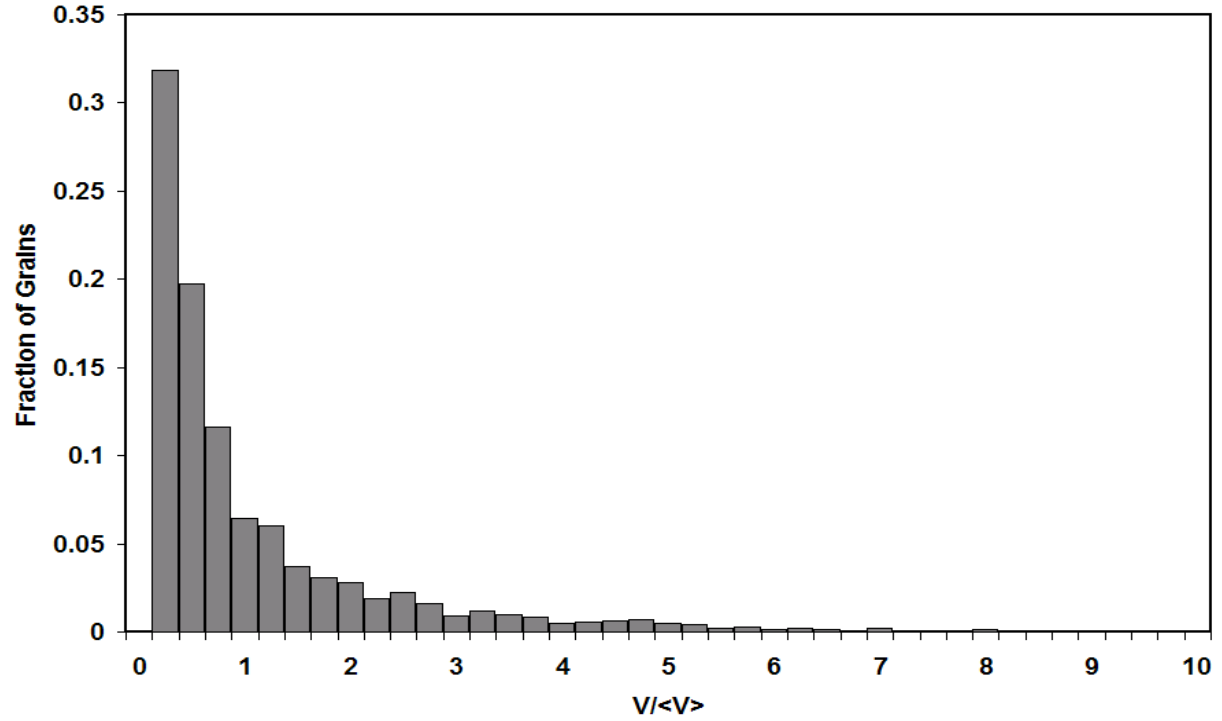
Figure 4. (a) Distribution of grain volume for 2704 grains. $<V_{grain}> = 37.32\ \mu m^3$. (b) Distribution of equivalent sphere radii. $<ESR> = 1.76\ \mu m$. Curves representing the Hillert distribution, the Louat distribution and the log-normal distribution are overlaid on the experimental data.

62
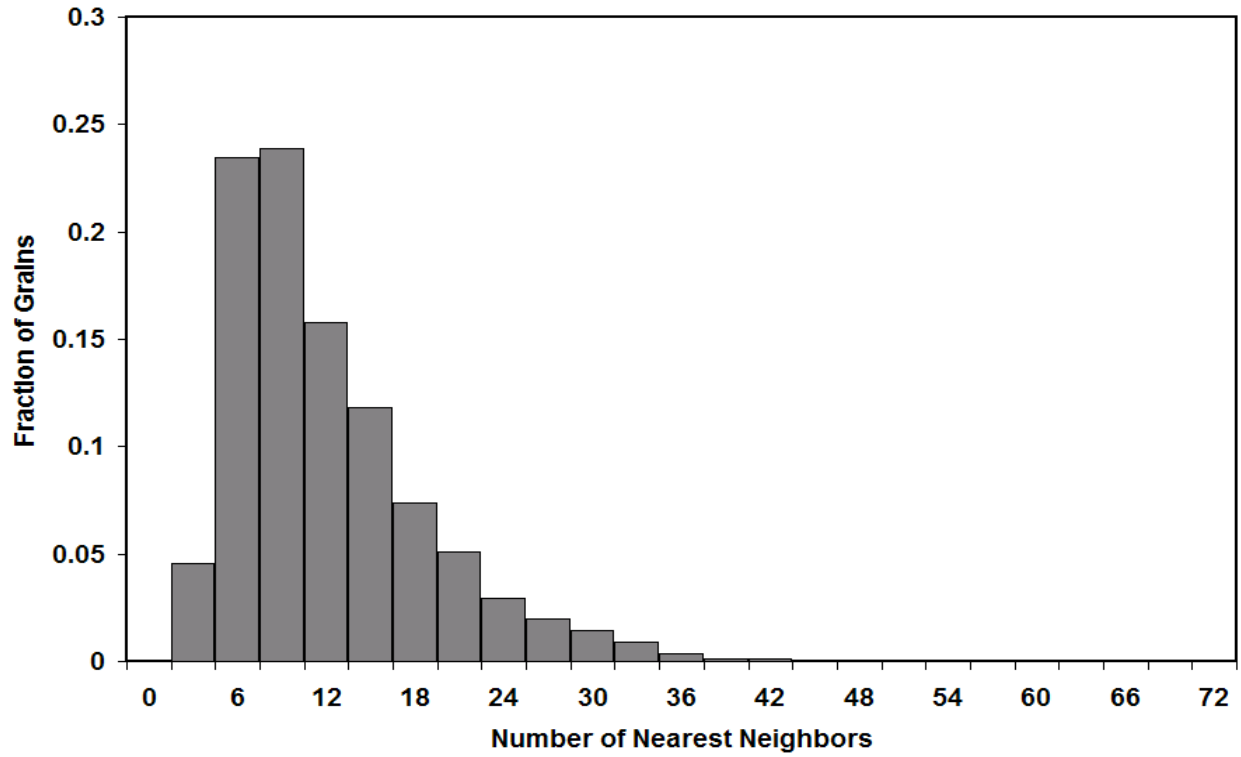
Figure 5. Distribution of number of contiguous neighbors. The mean value of 12.9 neighbors is similar to experimental observations of other metallic alloys.
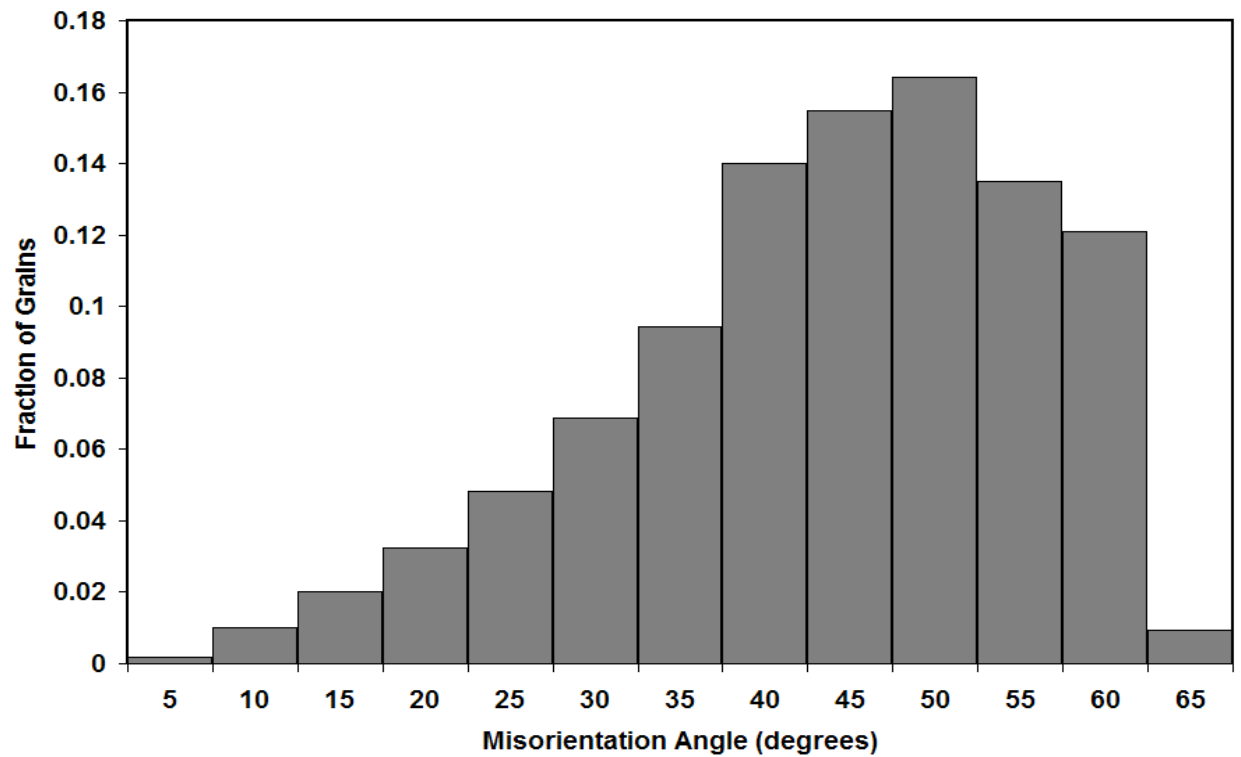
Figure 6. Distribution of misorientation angles.
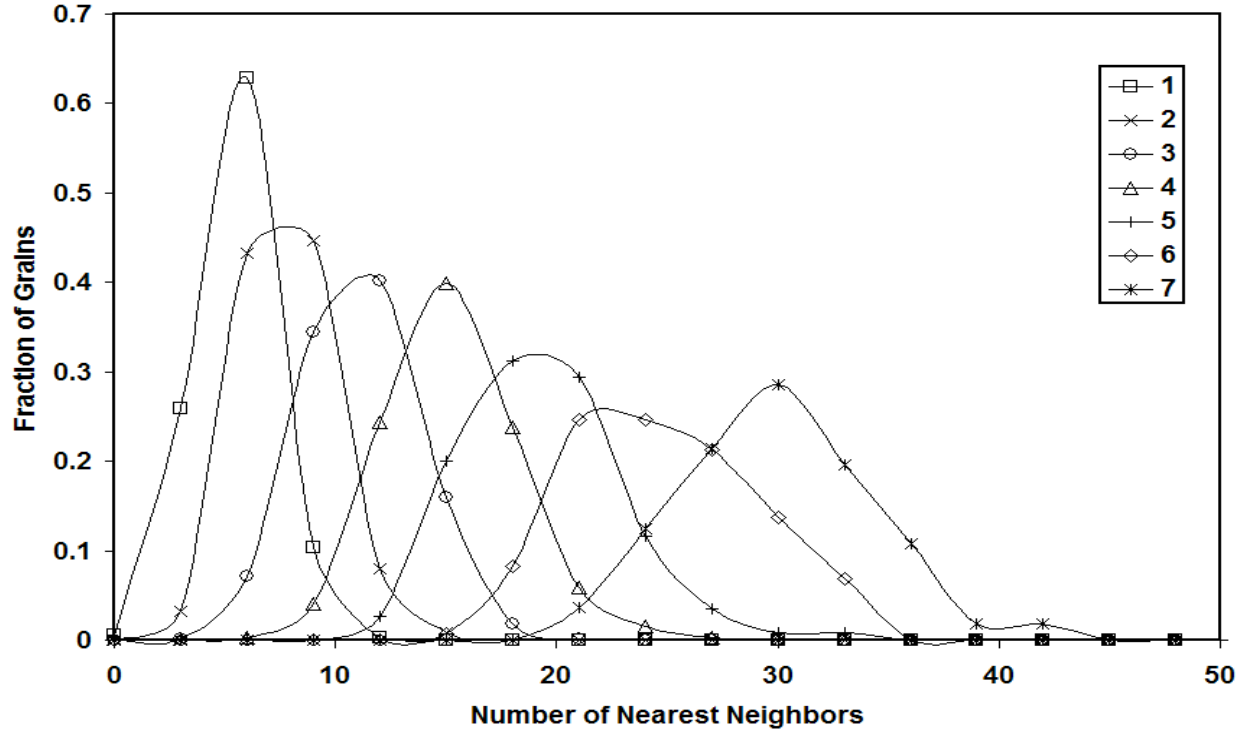
Figure 7. Distribution of number of contiguous neighbors for grains of varying size. Increasing number of neighbors with increasing size matches previous observations. The parameters are clearly correlated by the noticeable shift, and the value of $\eta^2 = 0.84$ determined for the data.

The detailed statistical characterization serves as the input to a synthetic structure generation process. The exact experimental volume after reconstruction and feature segmentation can be used as model volumes. However, in certain cases statistically-equivalent synthetic structures can be quite useful. Codes were developed to create equivalent model volumes using the experimental volume statistics as constraints. The following figures show an example synthetic volume as well as its statistical comparison to the experimental volume.
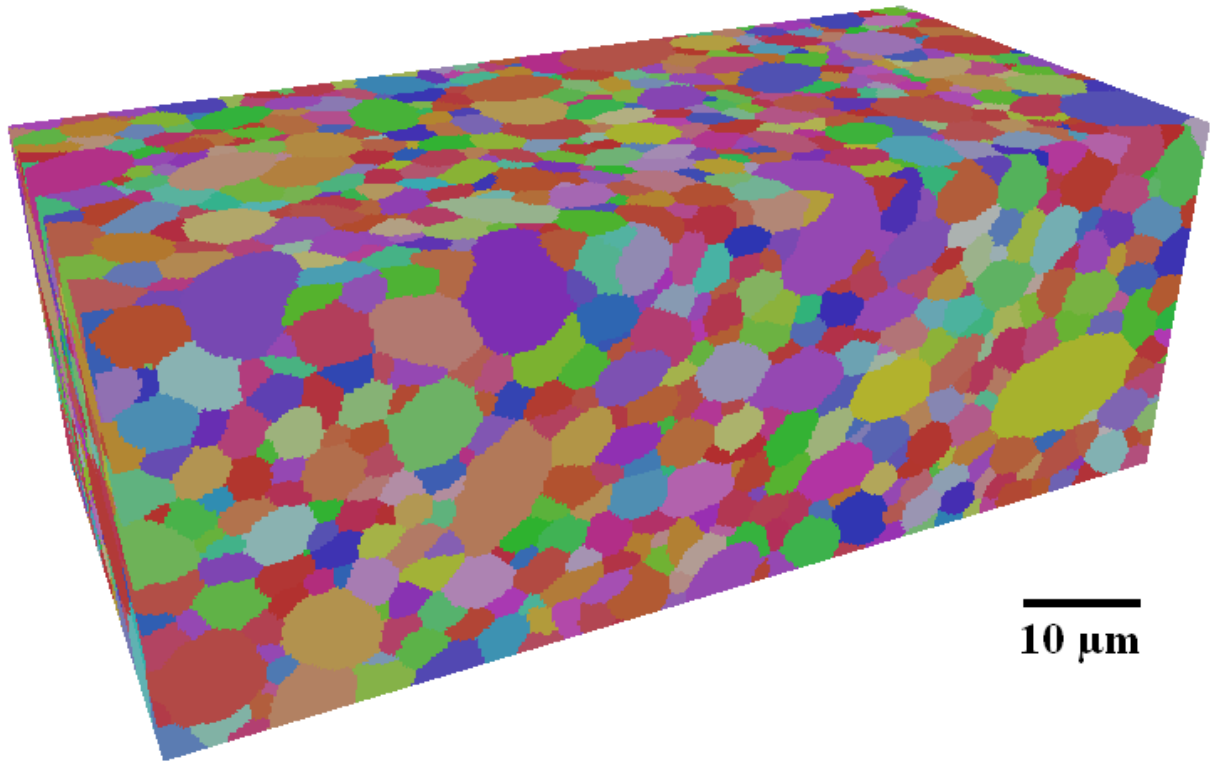
Figure 8. (b) synthetic volume containing 5269 grains.
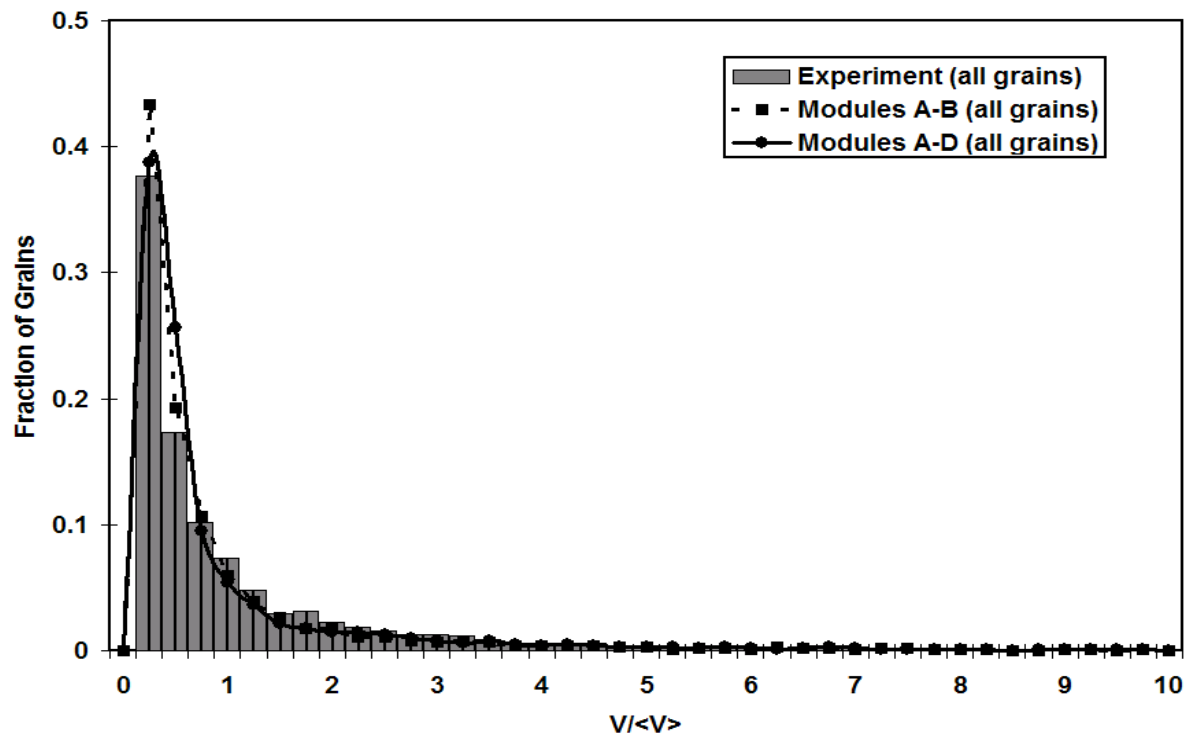
Figure 9(a). Comparison of normalized grain volume.
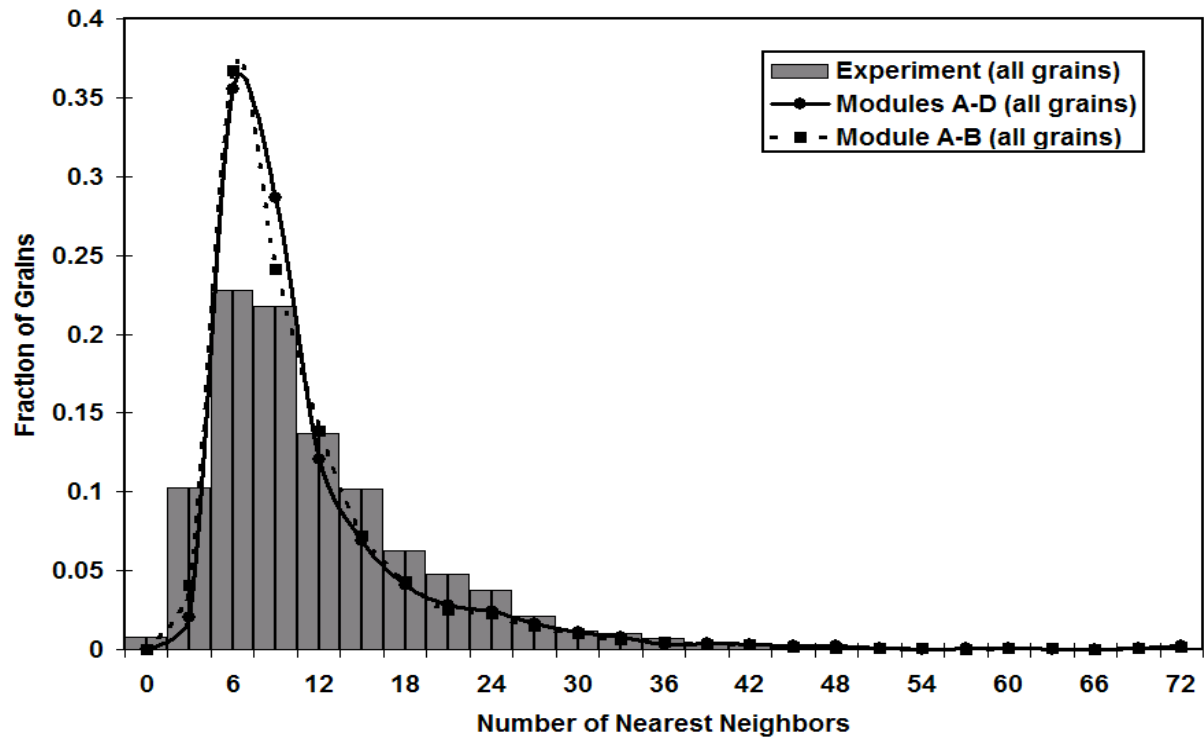
Figure 9(b). Comparison of number of neighbors
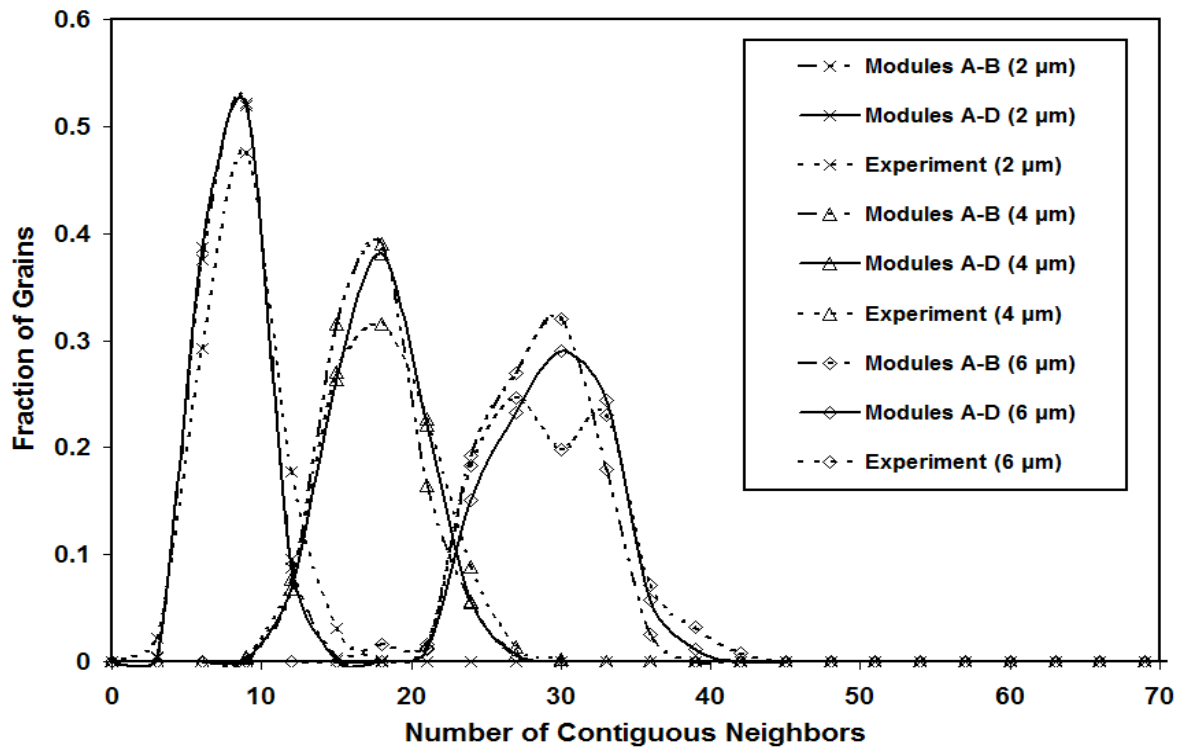
Figure 9(c). Comparison of number of neighbors-grain size correlation.

66
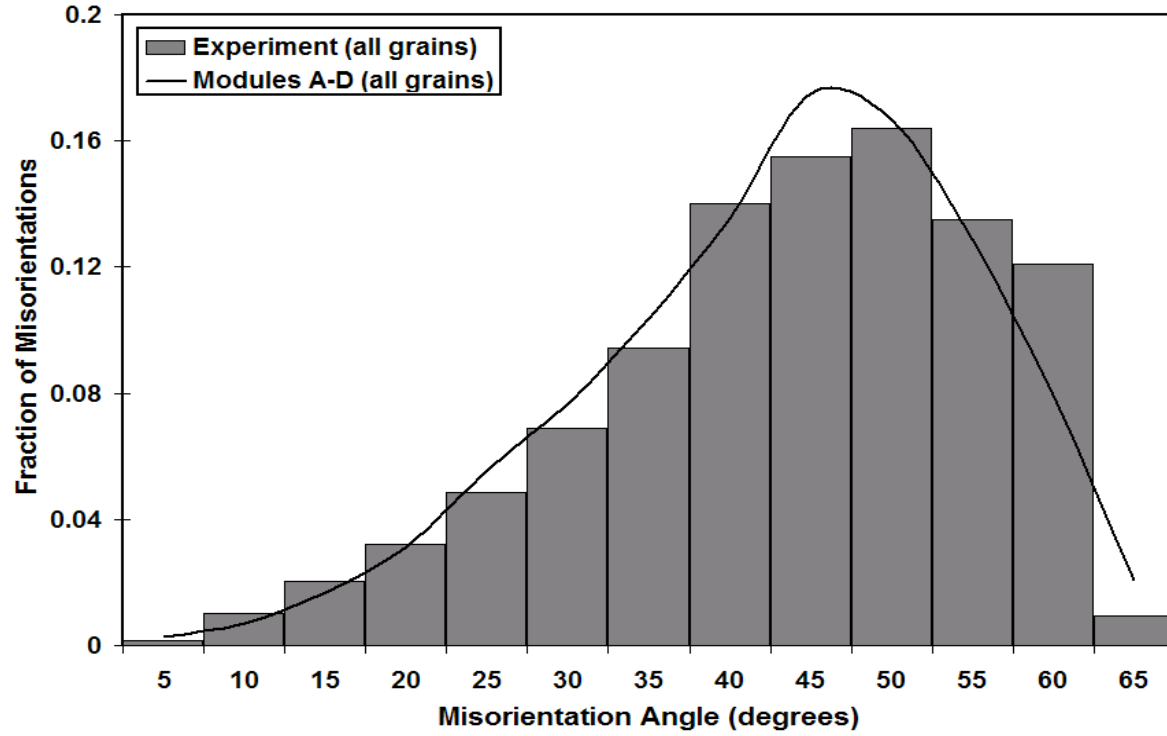
Figure 9(d). Comparison of MoDF for experimental and simulated microstructures at various stages**.**

Figure 9. Comparison of (a) normalized grain volume, (b) number of neighbors, (c) number of neighbors-grain size correlation, (d) MoDF for experimental and simulated microstructures at various stages**.**

Finally, a methodology for predicting 3D structures from 2D measurements was developed. Codes were written to measure statistics on 2D surfaces and probabilistically predict the 3D structure within the 2D surfaces. The synthetic structure generation codes were used to create volumes where the internal structure was known. The surfaces of the volume were then measured and used to predict the internal features with no prior knowledge.

3. Results and Discussions

The results of this work are a "solid" framework for the collection, processing, quantification, and representation of 3D information about material structure. Custom codes were developed to automate this framework and provide an improved clarity to the modeling of polycrystalline materials in 3D. The goal of this work was to provide a pathway for the modeling of materials with special attention to microstructural features. The tools used for data collection, the statistical descriptors used to quantify the microstructure, and the constraints used to produce statistically equivalent structures may all change slightly based on the material of interest. However, the process and ideologies developed in this work should hold true for various materials.

During the development of this larger framework, certain results individually stand on their own as interesting or useful findings. The development of the automated data collection has become

well known throughout the world and implemented at multiple research facilities from Carnegie Mellon in Pittsburgh to Max Plank in Germany. The statistical characterization, specifically the correlation of parameter distributions, offered insights into the local neighborhoods of grains and may yield better understanding of the structure of grains in 3D. Finally, the 2D to 3D prediction tool is proving to be quite intriguing in their current infancy. The power of such a tool is quite obvious and with the abundant information available through tools developed in this work may be realized in the near future.

4. Conclusions

The data collection and characterization tools developed in this work create an unprecedented ability to acquire an abundant amount of microstructural kinematical information for material scientists. Additionally, the representation tools provide a means to design and model true grain structures. The combination of these improved capabilities begins to establish a framework for advancing the way material science treats problems at the microstructural level.

The DB FIB-SEM allows for precise and accurate data collection on a size scale that is useful for many engineering alloys. Automation of the DB FIB-SEM yields not only increased data output, but also creates a level of robustness that reduces the possibility of many data collection errors. Finally, the incorporation of the SEM column opens a pathway to the collection of many different data types, which ultimately may provide more useful data when used in combination. The EBSD data collected in this work is the key link between the data collection and the characterization process. Data-processing and grain segmentation becomes orders of magnitude simpler with the quantitative, unvarying (from section-to-section) data present in the EBSD maps.

The characterization undertaken in this work provides quantitative measures of a number of parameters and their relationships with one another that have until presently been difficult to describe in anything but a qualitative manner. The ability to investigate individual grains or local grain neighborhoods gives material scientists the tools necessary to truly quantify aspects of microstructure, such as correlation lengths, that cannot be clearly determined from macroscopic, mean-field measurements.

The synthetic structure generators created in this work can be useful in a variety of modeling and simulation endeavors. First, the synthetic builder tools can be used to produce many instantiations of the same (statistically) microstructure with some probability of generating features that are not present in the finite-sized experimental data set. Secondly, the synthetic builder tools can be used to generate microstructures from the extrapolated 2D statistics, where 3D experimental data is not present. Finally, the synthetic builder tools can be used in a true microstructure design effort. Idealized microstructures with some set of "optimized" statistics could be developed for testing/simulation without producing a real material with that microstructure.

The 2D extrapolation techniques introduced in this work are the initial steps needed to develop a link between the 3D nature of microstructure and the 2D measurements that are often the only available characterization of a material. The results obtained using this methodology appear promising, at least for some microstructures that can be described by certain geometrical

features. The strength/motivation of this methodology is the limited 2D information necessary to produce a relatively large amount of 3D information.

5. Recommendations

Though a significant step has been taken towards the combination of automated data collection, characterization, and representation, there are still noticeable limitations and areas for further investigation.

The DB FIB-SEM, even with automation, is still limited in the amount of data it is capable of collecting. Especially with the desire to retain a fine resolution of the data, large volumes containing tens of thousands of grains are readily available without significant collection times. The EBSD data is generally the slowest portion of the data collection process and as a result, ongoing efforts are aimed at merging multiple data forms that can provide different beneficial aspects (i.e. increased resolution, quantitative data, fast acquisition).

There are opportunities for further investigation into the data-processing algorithms utilized in this work. First, the combination of information from multiple data types may alleviate the problems of unidentifiable γ' particles and undersampled twin grains. The increased resolution of SEM images (i.e. BSE, IISE, SE images) may likely eliminate the undersampling of twins entirely. Chemical mapping or possibly BSE imaging could provide the information necessary to distinguish γ' particles. Second, a measure of "realism" based on the amount of changes made to the data is a source of ongoing investigation. Selected parameters could be tracked during the various steps of data-processing and the influence of these steps on the resultant data could be better understood. Finally, a more in-depth investigation of "problematic" data is certainly of importance. Improperly identified data could be the result of a data collection error or could be due to a feature/defect in the microstructure and proper handling of these data points becomes an important to retain key features/defects that may be present.

The microstructure characterization also contains points for further analysis. First, more sophisticated measures of shape may yield better descriptions of grain structure. Inevitably there will be microstructures will more topologically complex features than that studied in this work. Thus, the ability to describe more complex shapes accurately and effectively is an important tool to incorporate into this framework. Second, the crystallographic data present in the EBSD provides information that allows for highly in-depth studies of grain boundary character and other macro- and micro- texture issues. The material used in this work did not require such in-depth investigations and as a result, the crystallographic analysis is relatively shallow. Third, the parameter correlations and local spatial descriptions (i.e. the MTF) need to be investigated in a more robust manner to generate quantitative descriptions of correlation lengths with respect to different features. In the case of the MTF, only first nearest neighbors were investigated and certainly higher-order neighbors also contain useful information that may better describe the local clustering of features. Finally, a metric or set of metrics must be developed to quantify the difference between two sets of statistics. If two different microstructures are collected or the same microstructure before and after deformation is measured, there must be some quantitative measure of the difference between the two structures.

The synthetic builder tools developed in this work have some areas which may need added investigation in order to determine their limitations. First, some of the areas of remaining interest center around the improvements in the characterization (i.e. better description of shape and crystallographic parameters), which have already been addressed. Second, the incorporation of additional constraints for including other statistics is not a trivial task and requires deliberate thought. One issue with additional constraints becomes the ability to find acceptable positions for features with reasonable computational efficiency. Third, similar to the characterization section, it is imperative that there is a metric for the comparison of two structures with different statistics. In the synthetic builder there are two points that require that there is convergence between the statistics of two structures. The first point is when the voxelized synthetic structure must be equivalent to the experimental voxelized structure. The second point is when the Voronoi representation of the synthetic structure must be equivalent to the synthetic voxelized structure. This paper has introduced some ability to quantify the second point, but the first point is not as clear. Visual inspection and various parameter comparisons (as done in this work) serve some purpose, but further investigation could likely produce a more precise metric for the comparison of two structures. Finally, the synthetic structure generated must be meshed carefully and efficiently. The meshing of the structure was not a focus of this work and was only addressed briefly, but is certainly one of the most important aspects of the process. Without a proper, efficient mesh, the simulation of the generated structure is not feasible.

The 2D extrapolation techniques presented in this work are a new approach towards estimating 3D parameters from 2D measurements. Further investigation into the validity of the assumptions and limitations of the application to certain microstructures is the focus of ongoing work. Future work will need to focus on the shape of the size distribution, the likelihood of capturing the largest grain, and the link between the 2D and 3D principal axis orientation distribution. Additionally, the output of the extrapolation tools needs to be audited carefully to assess any biases that may be incurred by the method itself.

Ultimately, this work has provided a set of tools that have greatly increased the ability to investigate, collect, quantify, and represent microstructure. There have been significant steps forward, but there are equally significant steps yet to be taken. This work has placed pressure on other fields of study (i.e. meshing and constitutive law development) to improve their methods to incorporate the outputs of this work. Only this combined effort will the full effects of either work become realized.

6. References

Kral MV, Ice G, Uchic MD, Rosenberg RO. Three-Dimensional Microscopy. *ASM Handbook*.

Rhines FN, Craig KR, Rousse DA. Measurement of Average Grain Volume and Certain Topological Parameters by Serial Section Analysis, *Metallurgical Transactions A,* Vol. 7A, 1976, pp. 1729-1734.

DeHoff R T. Quantitative serial sectioning analysis: preview. *J. Microscopy* 1983; 131: 259-263.

Li M, Ghosh S, Richmond O, Weiland H, and Rouns T N. Three dimensional characterization and modeling of particle reinforced MMCs, Part I: Quantitative description of microstructural morphology. *Material Science and Engineering A* 1999; A265: 153-173.

Li M, Ghosh S, Richmond O, Weiland H, and Rouns T N. Three dimensional characterization and modeling of particle reinforced MMCs, Part II: Damage characterization. *Material Science and Engineering A* 1999; A266: 221-240.

J. Spowart: *Scripta Materialia,* 2006, vol. 55, pp 5-10.

Zaafarani N, Raabe D, Singh RN, Roters F, Zaefferer S. Three-Dimensional Investigation of the Texture and Microstructure Below a Nanoindent in a Cu Single Crystal Using 3D EBSD and Crystal Plasticity Finite Element Simulations, *Acta Materialia,* Vol. 54, 2006, pp. 1863-1876.

Dobrich KM, Rau C, Krill CE. Quantitative Characterization of the Three-Dimensional Microstructure of Polycrystalline Al-Sn Using X-Ray Microtomography, *Metallurgical and Materials Transactions A,* Vol. 35A, 2004, pp. 1953-1961.

Ralph B and Kurzylowski KJ. The Philosophy of Microscopic Quantification, *Materials Characterization,* Vol. 38, 1997, pp. 217-227.

Rhines FN. Microstructology, Behavior, and Microstructure of Materials, *Rieder-Verlag, Stuttgart,* 1986.

Kurzydlowski KJ and Bucki JJ. Flow Stress Dependence on the Distribution of Grain Size in Polycrystals, *Acta Metallurgica et Materialia,* Vol. 41, 1993, pp. 3141-3146.

Ciupinksi L, Ralph B, Kurzydlowski KJ. Methods for the Characterization of Grain Size, *Materials Characterization,* Vol. 38, 1997, pp. 177-185.

Vander Voort GF. Grain Size Measurement, *Practical Applications of Quantitative Metallography,* pp. 85-131.

Russ J C and Dehoff R T. Practical Stereology. New York: Kluwer Academic/Plenum; 2000.

Underwood EE. Quantitative Stereology, Addison-Wesley, 1970.

Thompson A W. Calculation of True Volume Grain Diameter. *Metallography 5 1972;* 366-369.

Humphreys FJ. Quantitative Metallography by Electron Backscattered Diffraction, *J. Microscopy,* Vol. 195, 1999, pp. 170-185.

Smith CS. Some Elementry Principles of Polycrystalline Microstructure, *Metallugical Reviews,* Vol. 9, 1964, pp. 1-48.

Smith CS. Metal Interfaces, *Amer. Soc. Metals,* 1952, pp. 65.

Williams WM and Smith CS. *Trans. Amer. Inst. Min. Met. Eng.,* Vol. 194, 1952, pp. 755-765.

Krammer D, Mendoza R, Voorhees PW. Cylindrical Domain Formation in Topologically Complex Structures, *Scripta Materialia,* Vol. 55, 2006, pp 17-22.

Rowenhorst DJ, Gupta A, Feng CR, Spanos G. 3D Crystallographic and Morphological Analysis of Coarse Martensite: Combining EBSD and Serial Sectioning, *Scripta Materialia,* Vol. 55, 2006, pp 11-16.

Xie CL, Ghosh, S, Groeber M. Modeling Cyclic Deformation of HSLA Steels Using Crystal Plasticity, J. Eng. Mater. Tech., 2004.

Deka D, Joseph DS, Ghosh S, Mills MJ. Crystal Plasticity Modeling of Deformation and Creep in Polycrystalline Ti-6242, *Metallurgical and Materials Transactions A,* Vol. 37A, 2006, pp. 1371-1388.

Kurzylowski KJ, Varin RA, Zielinski W. *Acta Metallurgica,* Vol. 32, 1984, pp. 71.

Woodfield AP, Gorman MD, Corderman RR, Sutliff JA, Yamron B. Effect of Microstructure on Dwell Fatigue Behavior of Ti-6242, *Titanium '95: Science and Technology,* 1995, pp. 1116-1123.

Coster M, Arnould X, Chermant JL, El Moataz A, Chartier T. A Microstructural Model by Space Tessellation for a Sintered Ceramic: Cerine, *Image Anal. Stereol.,* Vol. 24, 2005, pp. 105-116.

Lewis AC and Geltmacher AB. Image-Based Modeling of the Response of Experimental 3D Microstructures to Mechanical Loading, *Scripta Materialia,* Vol. 55, 2006, pp 81-85.

Chawla N, Sidhu RS, Ganesh VV. Three-Dimensional Visualization and Microstructure-based Modeling of Deformation in Particle Reinforced Composites, *Acta Materialia,* Vol. 54, 2006, pp. 1541-1548.

Valiveti DM and Ghosh S. Domain Partitioning of Multi-phase Materials Based on Multi-scale Characterization: A Preprocessor for Multi-scale Modeling, *International Journal for Numerical Methods in Engineering,* 2006.

Brahme A, Alvi MH, Saylor D, Fridy J, Rollett AD. 3D Reconstruction of Microstructure in a Commercial Purity Aluminum, *Scripta Materialia,* Vol. 55, 2006, pp 75-80.

Kurzydlowski KJ, Ralph B, Bucki JJ, Garbacz A. The Grain Boundary Character Distribution Effect on the Flow Stress of Polycrystals: The Influence of Crystal Lattice Texture, *Materials Science and Engineering A,* Vol. 205, 1996, pp. 127-132.

Sarma GB and Dawson PR. Effects of Interactions Among Crystals on the Inhomogeneous Deformations of Polycrystals, *Acta Materialia,* Vol. 44, 1996, pp. 1937-1953.

M.D. Uchic: *JOM*, 2006, vol. 58, iss. 12, pp.24.

G. Spanos: *Scripta Mater.*, 2006, vol. 55, pp. 3-5.

D.M. Dimiduk, T.A. Parathasarathy, S.I. Rao, Y.S. Choi and M.D. Uchic: *Numiform 8 Proceedings*, 2004, pp. 1705-1710.

N.R. Barton and P.R. Dawson: *Mod. and Sim. in Mater. Sci. and Eng.*, 2001, vol. 9, pp. 433-463.

D.M. Saylor, J. Fridy, B.S. El-Dasher, K.Y. Jung and A.D. Rollett: *Metall. Trans. A*, 2004, vol. 35A, pp 1969-1979.

C. Zhang, A. Suzuki, T. Ishimaru and M. Enomoto: *Metall. Trans. A*, 2004, vol. 35A, pp. 1927-1932.

A.C. Lewis, J.F. Bingert, D.J. Rowenhorst, A. Gupta, A.B. Geltmacher and G. Spanos: *Mater. Sci. and Eng. A*, 2006, vol. 418, pp. 11-18.

R.T. DeHoff, E.H. Aigeltinger and K.R. Craig: *J. Microscopy*, 1972, vol. 95, pp. 69-91.

C.E. Krill and L.Q. Chen: *Acta Mater.*, 2002, vol. 50, pp. 3057-3073.

J.C. Russ: *The Image Processing Handbook*, CRC Press, 1998, 3rd Ed., pp. 512-515.

F.R. Rhines and B.R. Patterson: *Metall. Trans. A*, 1982, vol. 13A, pp. 985-993.

7. Names of Personnel

Somnath Ghosh (OSU Faculty Member)
Dr. Dennis Dimiduk (AFRL/RX Mentor)
Dr. Michael Uchic (AFRL/RX Mentor)
Michael Groeber (OSU Graduate Student)

Task 5

Accelerated Assessment and Representation of Materials Behavior via Integrated Electron-Optical, Focused Ion beam and MEMS-based Characterization Methods. *Michael Mills (OSU Faculty Member), Dennis Dimiduk (AFRL/RX Mentor), Michael Uchic (AFRL/RX Mentor), David Norfleet (OSU Graduate Student), Stephen Polasik (OSU Graduate Student)*

I. RESULTS and DISCUSSION

1. Introduction

Understanding the mechanical properties of a material has always been of great importance in determining suitable applications. However, recent applications such as microelectronics, functional coatings, and micro-electromechanical systems (MEMS) has confined plasticity to very small volumes of material. The small sizes require knowledge of the mechanical properties on the nano- and micron-size scales. Recent technologies have allowed a means for fabrication and testing volumes of material on the order of a few microns in size on virtually any conductive material. Coupling mechanical results with transmission electron microscopy correlations between the mechanical size effects and sample dimensions can qualitatively and quantitatively be explored across a host of materials and crystal structures. A review paper by Nadgornyi [1] has suggested that a material be classified into either of two categories based on the nature of the dislocation motion: bowing-mode or kink-mode. Bowing mode materials exhibit low lattice frictional stresses, such that the strength of the material is strongly dictated by the obstacles that interact with the dislocation segments. Therefore, these materials are also referred to as "obstacle controlled." The second class of materials, kink-mode, exhibit significant frictional stresses, particularly related to the screw dislocation segments. In most cases, this is a result of the dislocation core structure being dissociated onto multiple slip planes, creating a significant drag on the moving dislocation segments.

This task has addressed the development of methods to measure mechanical properties from ultra-small volumes of materials that cannot be directly measured in traditional nanoindentation tests, such as the yield strength or critical resolved shear stress, ductility, and work hardening rate. Specifically, in this task novel machining methods, including Focused Ion Beam (FIB) machining, have been developed and used to fabricate micro-compression specimens, and a modified Nanoindentor utilized to measure uniaxial response. These procedures and tests have been performed on a variety of materials that were expected to exhibit kink-mode versus bowing-mode behavior, including pure Ni, Ti-6Al and Ti-6242. In addition, a NiTi pseudoelastic alloy was tested to explore the response and possible size effects associated with this martensitic transformation. A variety of distinct sample size effects has indeed been observed for these different materials.

An additional objective of this work has been to develop and apply novel TEM sample preparation techniques from the deformed micro-compression tests in order to develop an understanding of the operative deformation mechanisms. These characterization efforts have therefore shed light on the various sample size effects exhibited by these alloys, and have helped initiate understanding of these size effects.

2. Methods, Assumptions, Procedures

This section provides an overview the experimental procedures that are common to each of the three material systems studied. The procedures specific to an individual system are found in subsequent sections.

2.1 Bulk Sample Preparation

Bulk samples were cut to button size, similar in size to that of a dime, using a South Bay slow speed cut-off wheel, Model 660, to minimize dislocations formed during the cutting process. The button samples were then mounted to a parallel polishing puck with Super-Glue to be used on an Allied High Tech MultiPrep System. This system provides the capability to polish sample surfaces parallel with high fidelity – this becomes very important with regards to sample alignment during compression testing. The two large surfaces of the button samples were polished using silicon carbide polishing paper followed by a lapping of 0.05 μm colloidal silica to reach the desired surface finish. The button samples were then removed from the polishing puck with acetone and attached to a standard SEM stub with silver paint.

Two titanium-aluminum alloys were used in this study. The first, Ti-6Al, is a single-phase (α) hexagonal-close-packed (HCP) crystal structure. The second, Ti-6Al-2Sn-4Zr-2Mo-0.1Si (Ti-6242), is a two-phase material consisting of α and a BCC phase β in a colony microstructure. Large single crystals of Ti-6Al and single α/β colonies of Ti-6242 and were grown using a Crystalox vertical float zone technique at Wright Patterson Air Force Base by J.M. Scott and M.D. Uchic.

Bulk samples were then cut and oriented for maximum shear stress along one of the three basal directions, <11$\underline{2}$0>(0002), to produce single α-type slip in Ti-6Al. The presence of the β phase in Ti-6242 produces an orientation relationship between the α and β phases, resulting in three distinctly different basal slip directions. To minimize strengthening associated with the β phase, the a1 direction, [2$\underline{11}$0](0002), was chosen since it has only a slight misorientation of 0.56° between the two Burgers vectors for the α and β phases. Therefore, the results for the a1-basal orientation for Ti-6242 should be more directly comparable with that for single phase Ti-6Al. Samples were oriented using Electron Backscatter Diffraction (EBSD) on a FEI XL-30 ESEM. These samples were subsequently mechanically parallel polished using an Allied High Tech MultiPrep System to 0.05μm using colloidal silica.

A solutionized and quenched polycrystalline 50.7at% Ni-49.3at%Ti alloy has been provided by Professor Gunther Eggeler of the Ruhr University, Bochum, Germany for these preliminary tests. An extended solution anneal has been used to grow the grains large enough to enable machining of multiple micropillar samples from the same individual grain. An OIM scan of this polycrystal sample is shown in Figure 1(a), and the grain selected for testing is the large green grain which has a surface normal that is very close to a [110] direction. Based on the work of Gall, et al [2-5], this orientation in bulk exhibits a relatively large permanent strain that may be improved at small sample size.

2.2 Microcrystal Fabrication

Microsamples were fabricated with the use of a dual beam Focused Ion Beam (FEI DB-235), whereby large gallium ions are accelerated at the surface of the button samples preferentially removing material. This process involves two steps suggested by Uchic et al. [7]. The first step involves ion-milling perpendicular to the samples surface, such that material is preferentially removed from areas around the center point of the circle. As material is continually removed, a post with tapered sidewalls, a "preform", is created with its base continuous with the substrate, evident in Figure 1b. A second step is required to make the side-walls parallel. This step is very similar to that of a lathering operation, whereby the ion beam is no longer perpendicular to the sample surface, but rather at a glancing angle. An automation script (written by M. Uchic and M. Seekely at Air Force Research Laboratory in Dayton, Ohio) removes material from the tapered sidewall, rotates the sample 5-10 degrees to expose another increment of the tapered sidewall and removes material again. This process is repeated through the 360 degrees needed to make a full rotation. The result is a microcrystal with parallel sidewalls, a constant gauge length and a base continuous with the substrate material. Utilizing these techniques, microsamples were fabricated with sizes ranging from 1 to 60 microns in diameter.

(a) Preform

(b) Compression Specimen
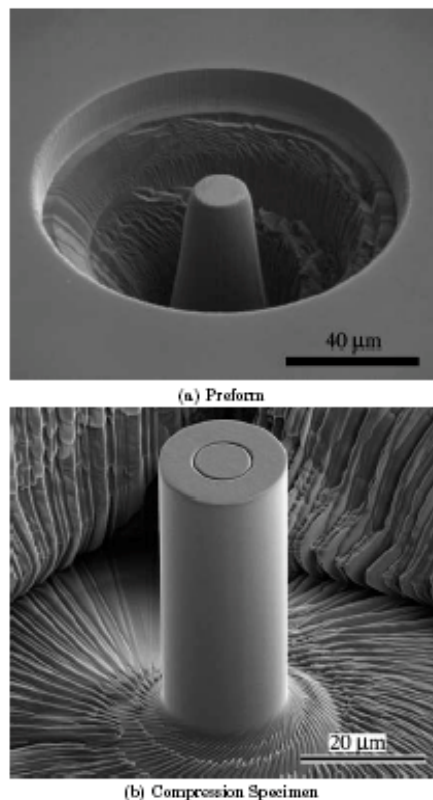
Figure 1. a) A "preform" produced by ion milling perpendicular to the sample surface b) The finished compression specimen produced by lathing away the tapered side-walls.

2.3 Uniaxial Compression Testing

The microcrystals were uniaxially compressed using an MTS Nano Indenter XP outfitted with a flat diamond indenter tip. To ensure proper sample alignment with the indenter tip, a goniometer stage was used to make fine adjustments. Time, load and displacement data were acquired using MTS Testworks software at an acquisition rate of 50Hz.

2.4 Transmission Electron Microscopy

The majority of the foils that have been examined in the study of Ni microcrystals were prepared from once-active slip bands. For these samples, after deformation the primary slip traces are clearly visible. The slip traces were used to align the samples for subsequent transmission electron microscopy (TEM) sample extraction along the primary active slip plane. Due to the small size of these samples, conventional TEM sample preparation techniques were not feasible and, therefore FIB fabrication methods were used to make the TEM foils. This particular study used an FEI Strata DB 235 and an in-situ micromanipulator (OmniProbe™) to extract and subsequently thin the samples to electron transparency.

For most FIB-based TEM foil preparation methods, it is normal practice to deposit a thin film of carbon or platinum on top of the area-of-interest, which keeps this material from milling during the foil-thinning process. However, such a protective film is usually thick enough to obscure surface details when imaging, which makes locating the position of the active slip band difficult after the film is in place. To ensure that the TEM foil contained an active slip trace, a two-step film-deposition procedure was used to define the plane of the active slip band. The first step consisted of depositing fiducial markers of platinum that were placed at multiple locations along a particular slip trace. Here, the fiducial markers were in the shape of a cross, where the intersection of the cross and the surface trace of the slip plane coincided, as shown in Figure 2. The second step consisted of covering the entire slip-plane region with a carbon film to protect the sample during FIB thinning. During the thinning process, the Pt crosses initially appear on the cross-sectional surface as two distinct points along the outer edge of the microsample. As this cross-sectional surface is milled closer to the active slip plane, these two points move closer together and ultimately merge into a single point at the position of the slip trace.
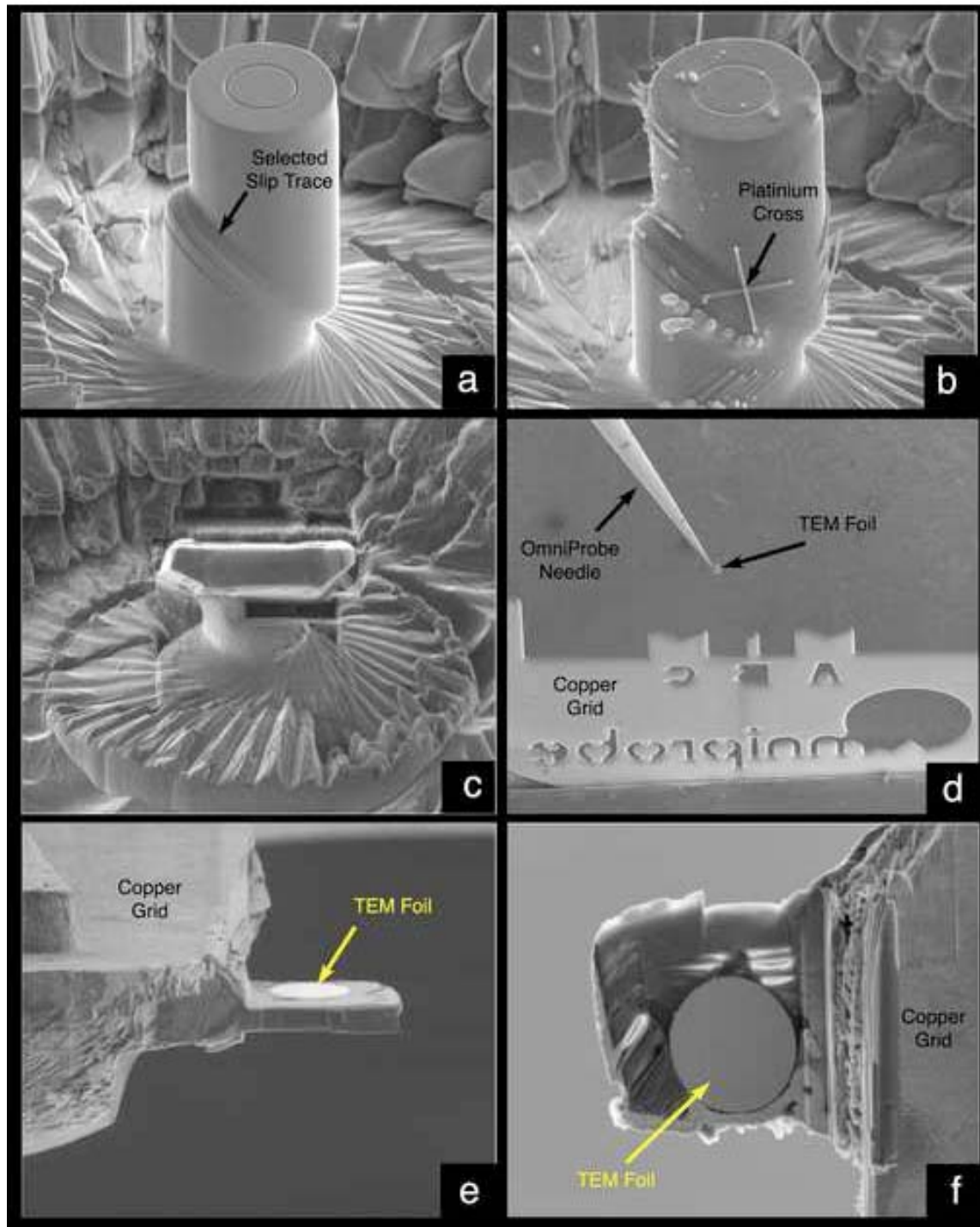
Figure 2. A series of secondary electron images taken from the FIB to illustrate the TEM extraction procedure from a 5μm diameter sample. (a) Typical sample after deformation indicating several slip traces. (b) Platinum crosses are placed along regions of the desired slip trace to act as fiducial marks during the final thinning process. (c) Excess material is FIBd away to leave only the slip trace of interest. (d) The TEM sample is attached to the OmniProbe™ needle and then transferred to a copper grid. (e) The TEM foil is attached to the copper grid using carbon and platinum deposition. (f) The TEM foil is thinned to electron transparency from both sides until the platinum fiducial marks are reached.

After thinning the foil to thicknesses that were marginally electron-transparent with the DB 235, a second milling procedure was employed to both reduce the ion-damage layer produced by the 30 kV Ga$^+$ ions and, to further thin the foil for improved imaging. Although the Ga$^+$ ion damage appears to have a negligible effect on the compression experiment results, these energetic ions produce contrast variations that affect the imaging conditions in the TEM. To minimize this damage, a Gatan Duo Mill was used to perform low-energy milling at voltage settings of 1-2 kV, a beam current of 0.5 mA, and a milling angle of 13 degrees. Milling times varied between 30 minutes to a few hours in order to produce optimal samples. Upon examination of the TEM samples, it was determined that the residual stresses and small sizes associated with these foils accentuate the bend contours imaged by conventional TEM (CTEM) methods. Therefore, scanning TEM (STEM) imaging was used to minimize these effects. Several studies have shown that under certain conditions the time-resolved STEM image is related to the spatially resolved CTEM image by the principle of reciprocity [8-9], whereby the incident angle in CTEM is equal to the exit angle in STEM and vise versa. This principle allows for the imaging of defects, such as dislocations, in bright-field-STEM mode (BF-STEM). Maher and Joy [9] have shown that by increasing the convergence angle in STEM mode the signal-to-noise ratio is increased, thereby minimizing extinction contours such as thickness fringes and bending contours. However, the increase in convergence angle also causes a loss in dynamical information, such as contrast related to dislocations and stacking faults. Therefore, a convergence angle of 9 mRad was used as a compromise between minimizing the contrast of the bending contours while maintaining adequate contrast from the dislocations. Maher and Joy also demonstrated that when using an appropriate convergence angle a two-beam condition can be obtained and "**g·b** analysis" can be performed to determine dislocation Burgers vectors. All TEM microscopy for this study was performed on a 200 kV FEI/Phillips Tecnai TF20 outfitted with a field-emission electron source. Energy filtering and image collection was utilized via the use of a Gatan imaging filter (GIF) and BF/DF STEM detector.

2.5 Dislocation Density Measurement in Ni Microcrystals

Dislocation densities were calculated using two different methods. A line/point-intercept method was used for the TEM foils sectioned parallel to the slip planes, whereby 5 randomly-placed lines of different angular orientation are drawn over the TEM images. This was facilitated by use of the image-processing and measurement software "Fovea Pro 4.0" by Reindeer Graphics. Points are manually placed at the intersection of each dislocation image with the random lines. The dislocation density, r, is simply the number of points, N, divided by the total line length of the random lines, L_r, multiplied by foil thickness, t [10]:

$$\rho = \frac{N}{L_r t} \tag{1}$$

The accuracy of the density measurements determined using this formula relies foremost upon precise measurement of foil thickness which, in the present study, was determined using an energy-filtered convergent beam electron diffraction (EF-CBED) technique [11-12]. In a CBED pattern there are intensity oscillations, otherwise known as Kossel-Möllenstedt fringes, which occur in the {000} and {hkl} discs under a two-beam condition. Knowing the extinction distance and the spacing of these intensity oscillations, the thickness can be deduced [12-13].

These concepts are used in a simulation program developed by P. Stadelmann, "JEMS" [14]. The microscope conditions were input into the simulation package and the intensity oscillations for several thicknesses were compared to the actual CBED image taken on the microscope. From this comparison, the foil thickness was determined. Energy filtering was employed to accentuate the fringe patterns by eliminating inelastically-scattered electrons using an energy window of ±10 eV centered around the 200 keV elastic-energy peak. After collection of the EF-CBED pattern using a CCD camera, pixel averaging in the direction parallel to the fringes was also used to further improve the signal-to-noise ratio. Figure 3 shows a representative pixel averaged EF-CBED pattern compared to a CBED pattern simulated in JEMS. Kelly, et. al., have shown that thickness measurements having an accuracy of ±2% or better are routinely determined using this type of CBED measurement [12].
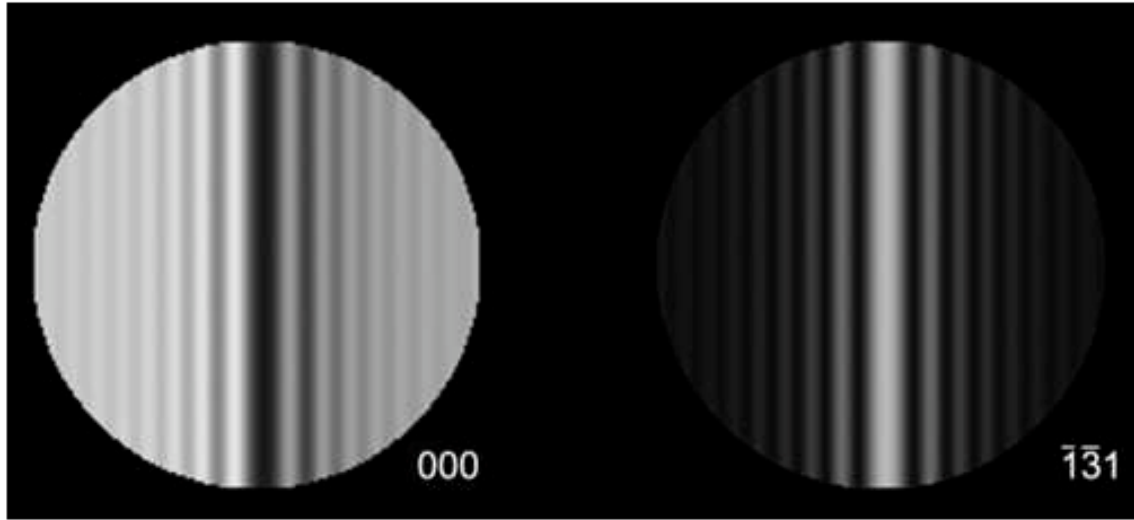
Figure 3. a) Energy filtered convergent beam electron diffraction pattern from a slip-plane foil, acquired on a CCD camera using 200keV electrons.
b) A simulated CBED pattern, using JEMS, for a 117nm thick TEM sample.

A second technique was used to check the reliability of the dislocation-density results obtained from the line/point intercept method. This method calculated the density by measuring the total dislocation line length within the TEM foil, which is a much more difficult task to perform using image-processing software as compared to the line/point intercept method. For selected foils, the dislocation structure was traced manually using "Adobe Photoshop" software, and the total line length, L_t, was calculated using the Fovea Pro software. The total dislocation density, r_t, was calculated using the following relationship [15]:

$$\rho_t = \frac{L_t}{At} \tag{2}$$

where A is the imaged foil area. The difference in the measured densities between the two techniques is minimal compared to other errors that are present during the measurement. For this reason, the line/point method was determined to be sufficient for dislocation-density measurements. For the measurements taken from foils cut parallel to slip planes described in this

study, all imaged dislocation segments were considered which resulted in a measured total dislocation density for the sample (as opposed to the forest-dislocation density).

Note that the "relaxed" diffraction conditions caused by the converged beam under BF-STEM, provides the ideal imaging technique for performing these types of density measurements. The relaxed conditions allow for the imaging of all dislocations present within the TEM foil providing a total dislocation density measurement. It is only when very precise diffraction conditions are applied that invisibility conditions are achieved using BF-STEM.

2.6 Errors Associated with Density Measurements in Ni Microrystals

There are many possible sources of error and uncertainty related to the present TEM-based dislocation-density measurements. One common source of error was mentioned earlier and is associated with measuring the foil thickness, ±2% being typical for CBED measurements. However, this value assumes a constant foil thickness over the viewing area, which is not the case for real samples. During the FIB-thinning of the extracted TEM foils, there is usually a constant taper to the samples from one end to the other, which is evident in thickness measurements taken at different locations within a foil.
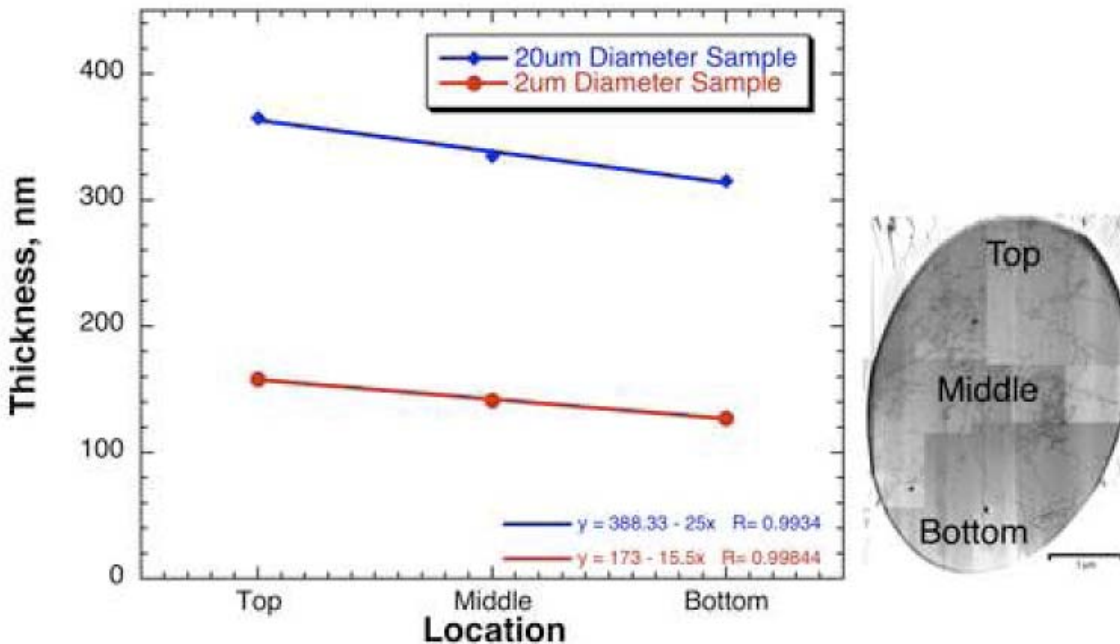
Figure 4. Thickness variation across a 2μm and 20μm slip-plane foil. The variation is caused during the final thinning process of the TEM foil.

Figure 4 shows a plot of three thickness measurements taken along the long axis of the elliptical-shaped view areas of the foils, for both a 2μm- and 20μm-diameter microcrystal. This plot demonstrates that for the preparation methods used in this study the taper is constant and, therefore, one must only measure the thickness in the middle of the foil to make a reasonable determination of thickness. The error associated with a single measurement was determined by fitting a straight line between the "top" and "middle" data points, in Figure 4, and extrapolating

81

this line to the "bottom" data point. Given that the distances between the "top," "middle," and "bottom" are ~10μm for the 20μm samples and comparing the extrapolated value to the measured value, an additional error of 3% was determined. From the analysis of these two foils, it was determined that using only a single measurement increases the error of the thickness value from ±2% to ±5%. Thus, for most of the foils, only a single measurement from the center of the foil was used to determine thickness.

The second source for error is related to the difficulty in imaging dislocations that are grouped closely together, whereby their intensity profiles overlap under bright-field-imaging conditions. The error associated with this overlap was determined by measuring N, the number of line/point intersections, for a given viewing area both under bright-field- and "dirty"-dark-field-imaging conditions and comparing the two measurements. Since conventional two-beam dark-field was not applicable in STEM mode, a "dirty" dark-field was utilized whereby images were acquired by centering the objective aperture around the diffracted beam in a two-beam condition. The difference between the two measurements made by these two imaging methods, having notably different resolutions and susceptibility to image-peak overlap, is an indicator of what is not detected by the readily-performed STEM imaging. From this measurement, it was determined that there is approximately a 30% underestimate in N when using bright-field STEM imaging. These two errors are combined in quadrature and the results are displayed using error bars for the density measurements that are shown in the rest of this study.

There are other errors and uncertainties that are very difficult to quantify. These errors include magnification errors that are related to the imaging of smaller TEM foils at a higher magnification as opposed to a larger TEM foil at lower magnification. Another error is simply related to the geometry of the TEM foil and the dislocations that lie parallel to the foil normal. These dislocation segments are then truncated to roughly the thickness of the TEM foil. As a result, and considering tilting limitations in the microscope, imaging such dislocation segments is difficult and may not be fully counted in the total density measurements. As such, all dislocation values reported here should serve as a lower bound. Naturally, the errors discussed here are associated with the measurements made for each TEM sample. Any uncertainties associated with the representative nature of any given slip trace relative to the overall sample response, or the accuracy with which the samples were consistently extracted from slip traces exist over and above the actual measurement errors. Selected aspects of these uncertainties are discussed later.

3. Results

3.1 Results for Ni Microcrystals

3.1.1 Dislocations in Undeformed Crystal Regions
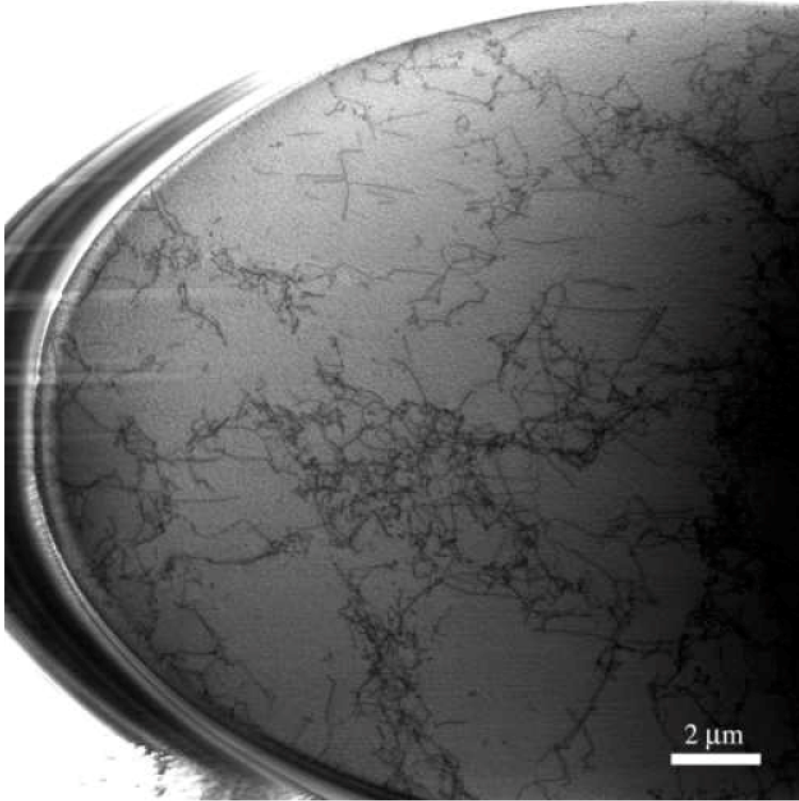
Figure 5. BF-STEM image taken from an undeformed microcrystal along the same (-111) plane that is active in the deformed samples. This image illustrates the large initial dislocation density that is present prior to loading.

In order to establish a reference for interpreting the microcrystal deformation behavior, assessments were made of the pre-existing dislocation structure, r_o, within the macroscopic crystal from which the microcrystals have been machined. For the Ni microcrystals, TEM samples were extracted from fully-machined but untested microcrystals using sectioning planes oriented parallel to the same primary (-111) plane as examined for the deformed samples. A low-magnification view of the undeformed regions can be seen in Figure 5. From this image and others, values of r_o were determined to be ~1.4×10^{13} /m^2. The observed high magnitudes determined for r_o clearly distinguish the initial state of the pure Ni microcrystals studied in [16-17] from that of the near dislocation-free state reported previously for metallic whiskers [18].

In addition to the (-111) foils, TEM samples were also extracted from undeformed material having an orientation off-parallel from the (-111). These foils were extracted at 45 degrees to the loading direction, having no specific foil normal. As a result of selecting such foil orientations, the measured dislocation densities are believed to directly correspond to the forest-dislocation density, r_f, that will be experienced by the glide system(s) of deformation. Such is not the case

83

for foils sectioned parallel to the primary glide plane and for those measurements some correction factor must be used to determine r_f, as discussed later. Density measurements from these off-parallel foils ranged from $r_o = r_t = r_f = 5.5\times10^{12}/m^2$ to $1.6\times10^{13}/m^2$. Note that these values are consistent with a prior study [23].

3.1.2 Dislocation Structure versus Sample Size
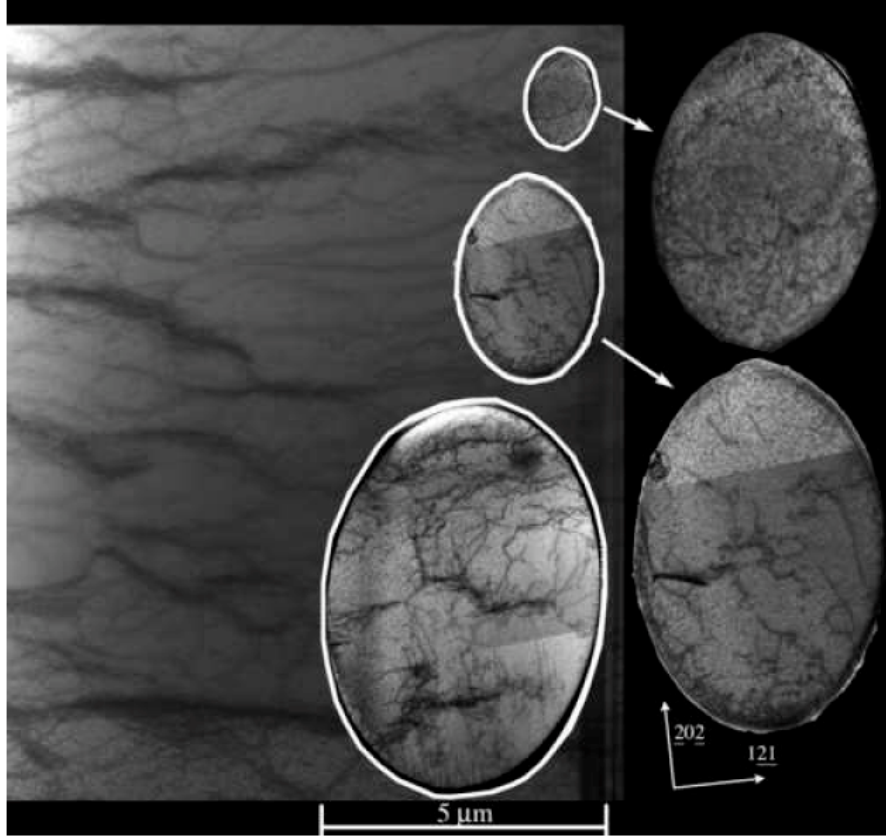
Figure 6. BF-STEM images taken along the (-111) slip-plane from 1μm, 2μm, 5μm, and 20μm diameter nickel microcrystal samples following deformation.

Examination of the slip-plane cut foils from 1, 2, 5, 10 and 20μm microcrystals demonstrates that a deformation structure is evident in all of the foils, as shown in Figure 6. In each case, the dislocation structure resembles that of Stage I glide and contains a dense population of predominately near-edge-character dislocation tangles [19]. These dislocation tangles consist of multipolar dislocation braids that are believed to be formed following annihilation of screw-character segments by cross-slip [20]. Note that the screw-character dipole annihilation distance may be expressed as [21]

$$h_s = \frac{Gb\sin\beta}{2\pi(\tau_o - s\tau_f)}$$

(3)

where b is the Burgers vector magnitude, β the angle between the glide and cross-slip planes (54.7 degrees), τ_o is the frictional stress, s is the ratio of Schmid factors on the cross-slip and

primary planes and τ_f is the current flow stress. Using values appropriate for Ni, h_s takes on values of ~0.5 µm and larger. Thus, for pure Ni screw-character dislocations are expected to have extremely short lifetimes within the crystals because of cross-slip annihilation. The result of such ready annihilation is likely to be an extensive jog-segment forest connected with near-edge-character dislocation debris.

Evidence of these structures implies that despite the fact that the surface slip traces appear to correspond to planar slip, localized cross slip occurs during plastic deformation. Figure 6 also illustrates that the scale of the inter-braid spacing remains nominally constant as the sample dimensions are decreased. The inter-braid spacing was measured to be ~2.2µm for the 20µm diameter microsamples [22]. This spacing agrees well with the estimated strong-obstacle spacing based on a random array of dislocation obstacles [20, 23]. If an average starting dislocation density, r_o, of 5×10^{12} m^{-2} is assumed for the material, only half of these dislocations contribute to the forest [21] and of the forest dislocations ~20% form junctions strong enough to arrest dislocation motion [24-26]. Thus, the strong-obstacle spacing is given by $1/\sqrt{\dfrac{\rho_0}{10}}$,or 1.4µm. Mader, et. al., measured an inter-braid spacing of 10µm in nickel [19], although the initial dislocation density was $r_o = 10^{11}$ m^{-2}, resulting in a larger inter-braid spacing.

Furthermore, Mader, et. al., found that dislocations in bulk deformed nickel lie predominately in directions within the glide plane making angles of 30° or less with the pure-edge line directions. Inspection of Figure 6 illustrates that for the sizes studied a similar dislocation line orientation and character preference is apparent.
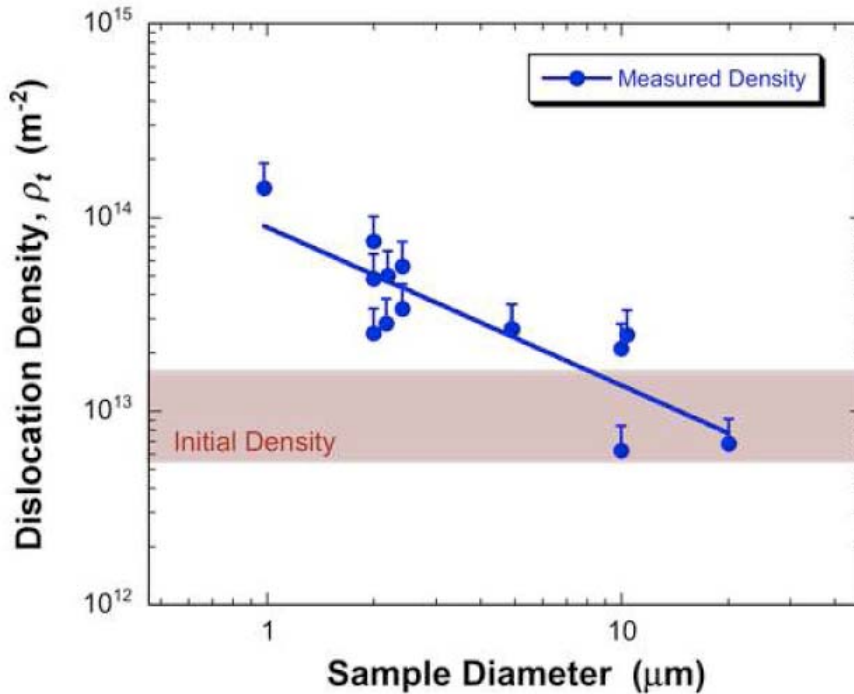
Figure 7. Dislocation density measurements performed using the line/point method indicate an increase in the dislocation density as sample dimensions are reduced.

3.1.3 Measured Dislocation Density versus Sample Diameter

The dislocation densities for several deformed microsamples were measured using the line/point method described previously. These data are plotted on a log-log plot and shown in Figure 7. The most important result from these measurements is the increase in the stored dislocation content as the sample size is decreased. As with any ex-situ or post mortem TEM experiment, the dislocation structure observed is representative of that from the very end of the loading cycle. Careful attention was paid such that the samples were not unloaded until flow had ceased from a strain-burst event; that is, until the natural strain-hardening processes led to a cessation of deformation. Therefore, one is assured that the observed dislocation substructure was able to sustain the final stress prior to unloading, as was the remaining volume of material outside of the selected slip traces. It is this final shear stress and ending dislocation structure that was used in all experimental measurements and calculations, unless otherwise stated.

Note that the increasing dislocation density with decreasing sample size observed after deformation (Figure 7)—in conjunction with the measurements of significant initial dislocation content—contradicts the hypothesis that the increase in strength of microcrystals can be solely attributed to dislocations leaving the microcrystal (one type of starvation mechanism) [27]. Should that be true, one might expect to observe dislocation densities in deformed samples that are equal to or less than the initial dislocation density. A caveat to these measurements is that it is not possible to stop all tests at the same magnitude of strain, especially for the smaller samples, because of the rapid stochastically-occurring strain bursts during testing. As a result, there are variations in the amount of plastic strain imposed from sample-to-sample. Also, nominal-strain values are reported that are obtained by averaging across the entire gage section of the sample, whereas the local strains that a given slip trace experiences are much larger and vary.

The systematic increase in dislocation density may be attributed to several possibilities. The first is related to the density measurement method used in this study. Throughout this study careful attention was paid in all aspects of the measurement process; however, while imaging in BF-STEM conditions there was variability in the magnification used to determine N. The variability in the magnification was not large and as such not likely related to the significant increase in density. A more likely scenario is related to the activation of the secondary slip systems. As indicated by the SEM studies performed by Dimiduk, et. al. [16], secondary-slip systems become more pronounced at smaller sizes. These increase the forest density and increase the effective storage rate of the primary system, creating an increase in total density as sample sizes are reduced. Another possibility may be related to slip localization at smaller sizes. For the larger samples, slip may occur on many possible planes along the gage length of the sample. However, as the sample dimensions are reduced and, because of the expected weakest-link statistical process of slip, the number of possible low-stress slip planes decreases with sample size. This creates a higher probability of localized slip on a given slip trace, resulting in a larger density at smaller sizes.
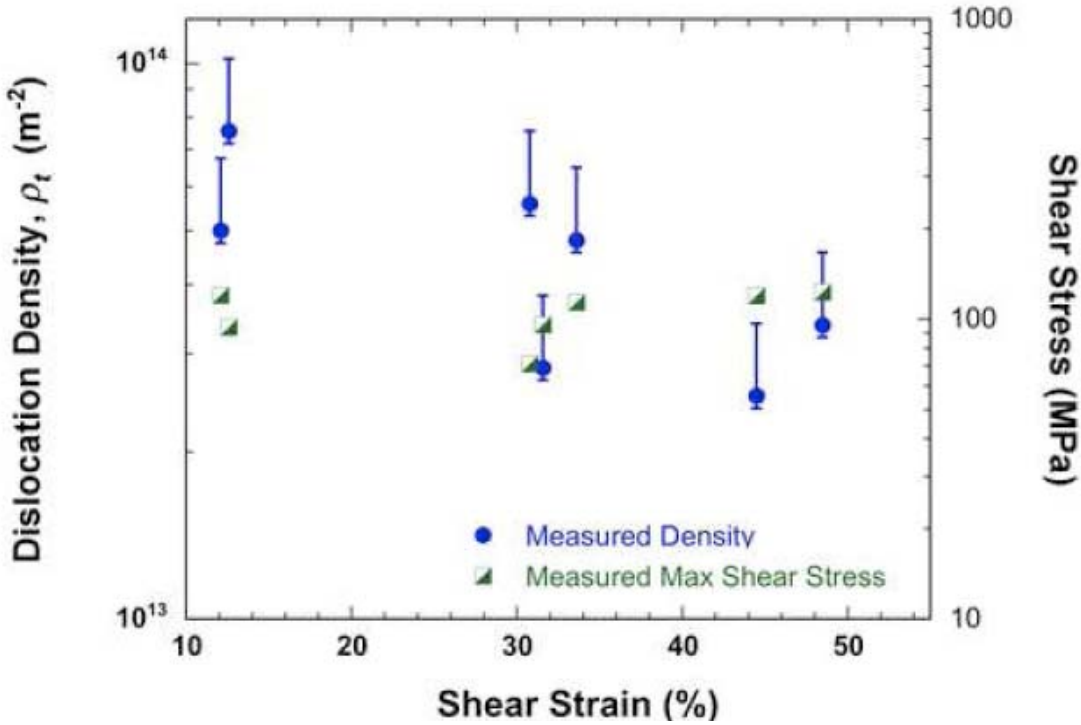
Figure 8. Density measurements from 2µm diameter nickel samples as a function of strain and maximum shear stress.

In spite of the increase in stored density with decreasing sample size, there appears to be no evidence that the observed dislocation density is a significant function of the imposed total strain level, as revealed by the data shown in Figure 8 for 2µm diameter samples. In fact, large measured densities exist on active slip bands after only 11% shear strain. These structures are not substantially changed at higher strains (consistent with the Stage I glide model [20]). The results suggest that dislocation substructure is forming and sustaining the large observed stresses very early in the loading cycle. Perhaps the structures are formed during the early strain hardening, or exhaustion-hardening interval [16], but this point requires further investigation. This result is supported by the shape of the flow curves for 2 micron diameter samples, which exhibit little or no strain hardening after reaching the flow stress, and is also consistent with the patterning of the dislocation substructure that is indicative of Stage I glide. Thus, dramatic increases in density are not to be expected with large changes in strain beyond the initial exhaustion-hardening regime.

In summary, the density measurements performed and described above may contain several systematic uncertainties that may affect the total measured density. Nonetheless. we have made an effort to quantify these densities in microcrystals within our current capabilities for measurement. As such, we suggest that the reader be mindful of such unresolved uncertainties as the measurements are discussed.

3.2   Results for Ti microcrystals

3.2.1 Ti-6Al Compression Results
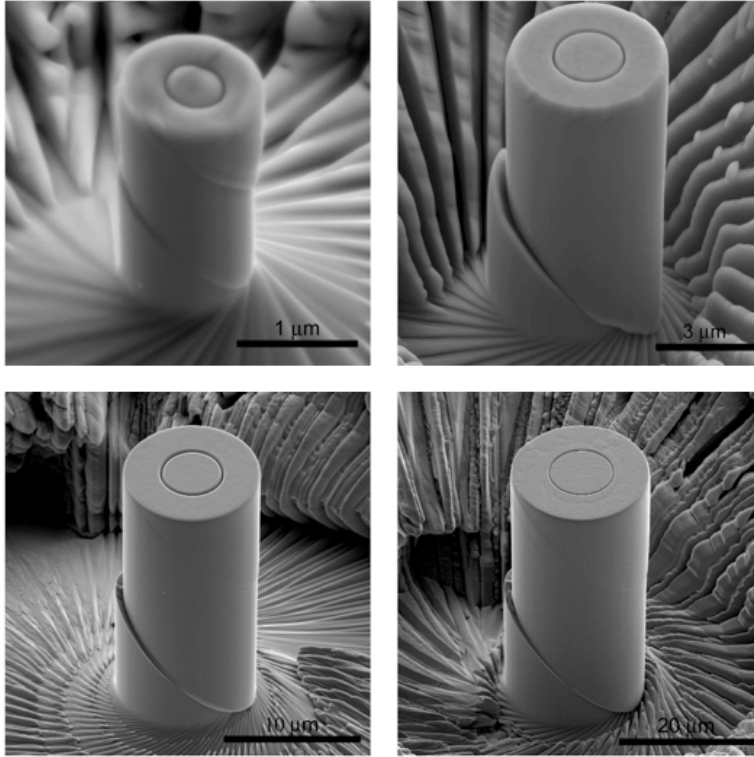
Figure 9. The slip traces observed in Ti-6Al microcrystals originate at the top and/or bottom contact points as these are areas of incompatibilities and stress concentrations. Typically only one or two slip traces are observed for a given sample.
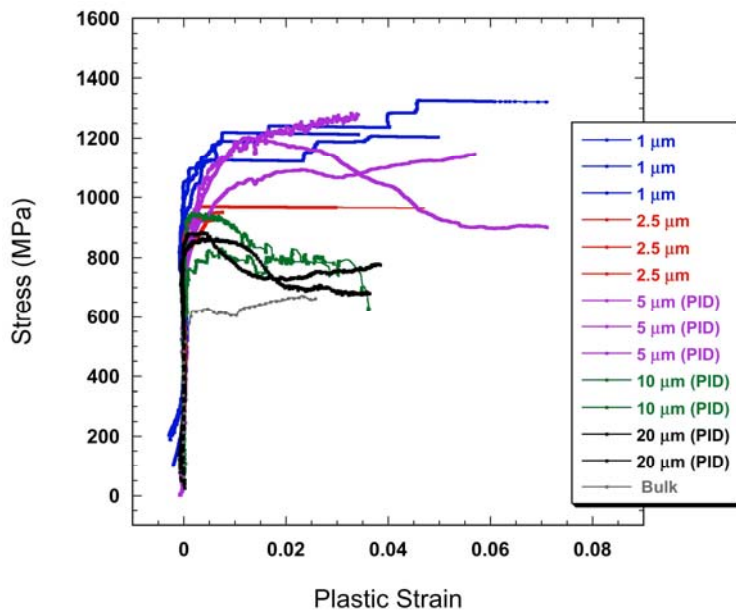
Figure 10. Ti-6Al microcrystal compression results. The yield stresses for all sample sizes, 1-20μm, are larger that that for bulk samples. There is an observable strengthening effect as sample dimensions are reduced, such that the 1 μm samples are stronger than the 20 μm samples.

Scanning electron microscopy (SEM) images, collected using secondary electrons, are presented in Figure 9 for several microcrystals following deformation. For all sizes, the slip traces are consistent with the primary slip system, [2 1 -1 0](0 0 0 1), that was oriented for the maximum resolved shear stress. For the majority of the microcrystals tested, slip traces originate at the top and/or bottom contact points as these are areas of incompatibilities and stress concentrations.

The flow curves for the Ti-6Al microcrystals, ranging from 1 to 20μm, are plotted as stress versus plastic strain in Figure 10. Comparing the yield stresses at 1% plastic strain, it is apparent that all samples achieve strengths larger than that of bulk crystals. In addition, there appears to be a strengthening effect as sample size is decreased. In the larger samples, an upper yield point is observed, followed by a gradual decay in stress that plateaus to values similar to those obtained in bulk compression testing at similar strains. This result suggests that the offset from bulk behavior is related to mechanisms operating at the early stages of plasticity.

Similar to the nickel results published by Dimiduk et al. [16], the 1 mm Ti-6Al microcrystals exhibit stochastic burst events followed by linear elastic loading. However, the burst events in Ti-6Al are much more controlled compared to the nickel bursts. For instance, the 1 micron Ti-6Al flow curves are plotted with a 1 mm nickel flow curve in Figure 11, and it can be seen that the speed at which these events occur is much slower in Ti-6Al. This is evident from the data points plotted on the flow curves for the same displacement and data acquisition rates. There are fewer data points acquired in the nickel sample during a burst event compared to Ti-6Al. This behavior is likely related to the sluggish/viscous dislocation motion present in titanium-aluminum alloys--due to the high Peierls stress along screw orientation as well as other frictional forces due to solute and SRO interactions--along with different hardening mechanisms that are governing plasticity.

These bursts events are not observed in larger titanium samples tested using the PID control method. The 1 mm samples were tested using the OLD loading method, such that the load was never allowed to relax. Therefore, a negative work hardening rate or upper yield point would not be observed in the 1 mm tests. With the PID control method, serrated-flow would be expect with multiple yield points.

In the larger Ti-6Al samples tested using the OLD method (not shown here) only one major burst event occurs such that the sample is not able to recover until the sample is unloaded. This is different from the larger nickel samples that recover from the burst events and are followed by linear elastic loadings. This suggests that the burst events observed in the nickel and titanium may be a related to different mechanisms. The single burst event in titanium suggests that there is one primary barrier to deformation and once this barrier is surmounted, subsequent deformation is easier and supported experimentally by the yield point flow softening observed in several of the flow curves.
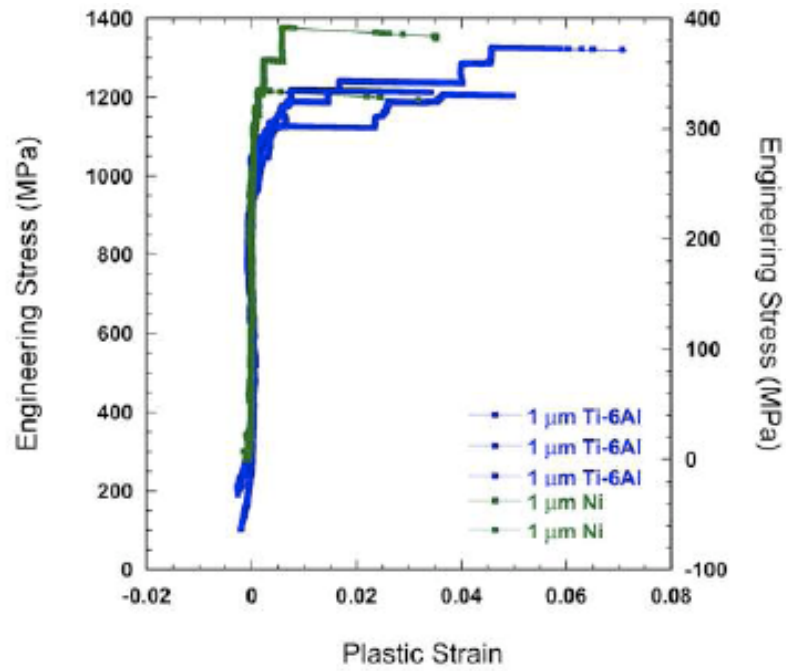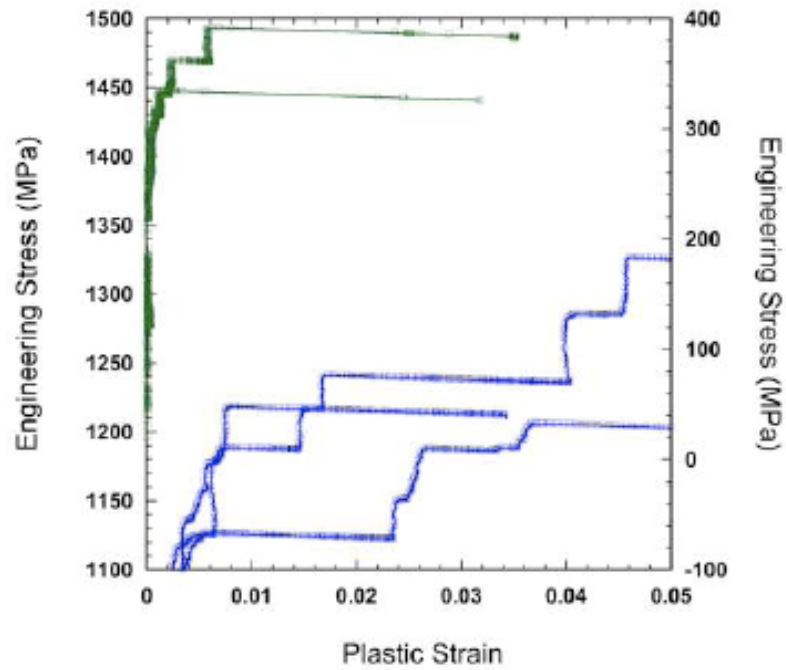
Figure 11. Strain burst events are found in both Ti-6Al and nickel 1mm microcrystals. However, the characteristics are quite different. Using the same acquisition rates, the nickel microcrystal acquired fewer data points during a burst event compared to the Ti-6Al microcrystals. Indicating that the burst behavior is more controlled/slower in the Ti-6Al microcrystals.

3.2.2 Ti-6242 Compression Results

The flow curves from the Ti-6242 microcrystals are presented in Figure 12. Two samples were oriented for a1 Basal slip, such that Sample #2 contains polishing induced dislocation content near the surface to produce a potentially unlimited supply of dislocation sources. Similar to the results from Ti-6Al, for all sizes tested (5-60μm), the measured yield stresses are larger than those observed in bulk crystals. This offset from bulk behavior observed in Sample #2, specifically, suggests that source operation is not a contributing factor to the strengthening effect. However, there is not a clear correlation between the yield point and sample size as observed in Ti-6Al and nickel microcrystals.
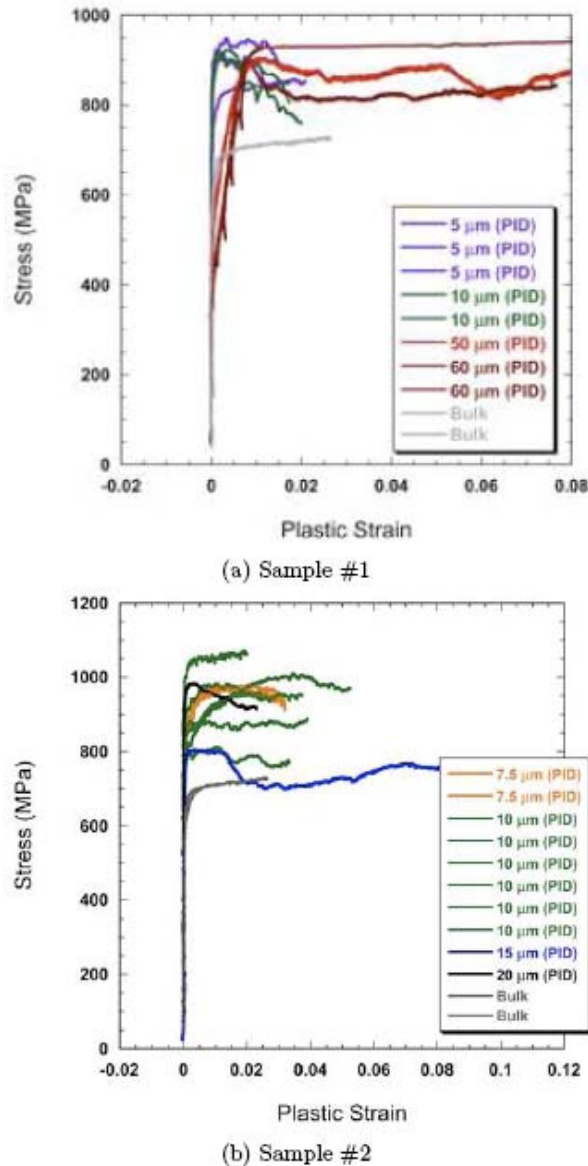
(a) Sample #1

(b) Sample #2

Figure 12. Ti-6242 microcrystal compression results from two samples oriented for slip in the a1 Basal direction. Sample #2 contains a large density of polishing induced dislocation content near the surface of the sample, potentially providing an unlimited number of operable sources. In both Sample #1 and Sample #2 there is an observable strength increase in the microcrystals compared to bulk samples, suggesting that source operation is not causing the offset from bulk behavior.

Furthermore, in nickel, Dimiduk et al. [16] observed bulk properties at sizes greater than ~20 μm in diameter; however, in Ti-6242 bulk properties are still not observed at 60 μm in size. The stress-strain curve from a 60μm sample is found in Figure 13. The sample follows linear-elastic loading up to a stress similar to the proportional limit (PL) for bulk behavior, as indicated by the arrow. Following this regime, there is a change in the loading slope that continues up to the yield point of the sample. This deflection point in the loading slope is not observed during the unloading of the sample, indicating that this is real material behavior and not an artifact from the testing system. Therefore, the proportional limits for the 50 and 60 μm samples are very similar to bulk values, but the subsequent hardening behavior is vastly different, suggesting that source operation is not responsible for the deviation from bulk properties.

(a)

(b)
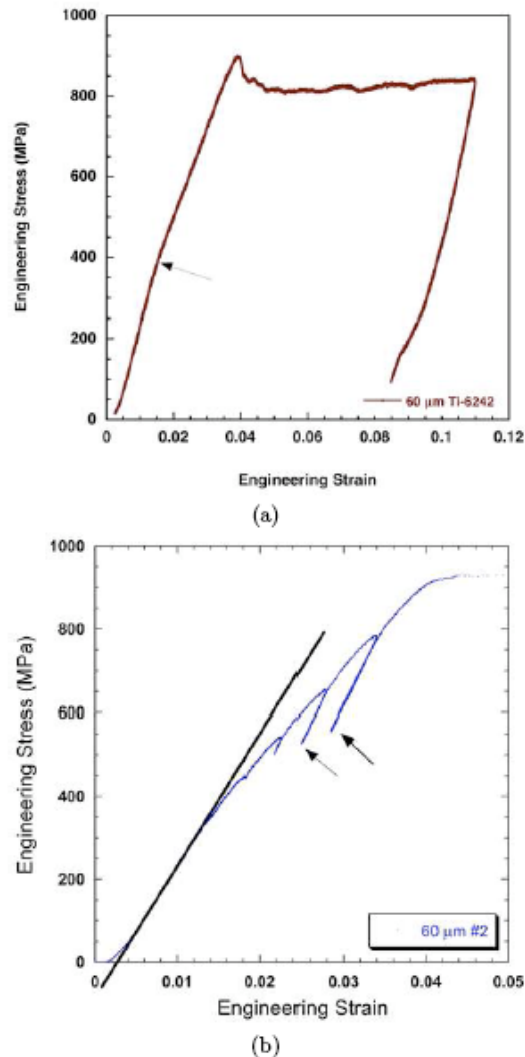
Figure 13. (a) The stress-strain curve from a 60 μm Ti-6242 microcrystal. A significant deflection in the loading curve is observable which occurs at a stress similar to the proportional limit for bulk samples, as indicated by the arrow. (b) Unloading segments, past the proportional limit, follow the elastic modulus of the material. This observation indicates that this region of the curve is real material behavior and not an artifact from the testing system.

92

SEM images indicate the same primary slip system, [2$\underline{11}$0](0001), is operative with the same slip trace characteristics as in the Ti-6Al microcrystals. There appears to be a larger number of observable slip traces compared to the Ti-6Al microcrystals, suggesting that the beta phase may be inhibiting dislocation motion, resulting in the activation of more sources. The beta phase may also provide additional internal source locations, which would also contribute to multiple slip traces.

3.2.3 TEM on Ti-6242

TEM foils were extracted along the primary active slip trace that was observed in the SEM. Imaging was performed using bright-field-scanning-TEM (BF-STEM) to study the dislocation substructure. Figure 14 contains BF-STEM images taken from a 10μm diameter microcrystal that was plastically deformed to 3.4% plastic strain. The dark bands running from top-right to bottom-left are the second phase, β, ribs that constitute this two-phase alloy. At higher magnifications the large arrays of screw segments are apparent. However, due to the large dislocation densities, subsequent analysis was difficult. Therefore, a second TEM foil was extracted from a microcrystal plastically deformed just past the proportional limit to only ~0.1% plastic strain, thus allowing the study of the very early stages of plasticity. SEM imaging indicated that this was the only active slip trace. At only 0.1% plastic strain (0.24% plastic shear strain), the sample sustained a load of 845 MPa, well above bulk values. This flow curve is presented in Figure 15.
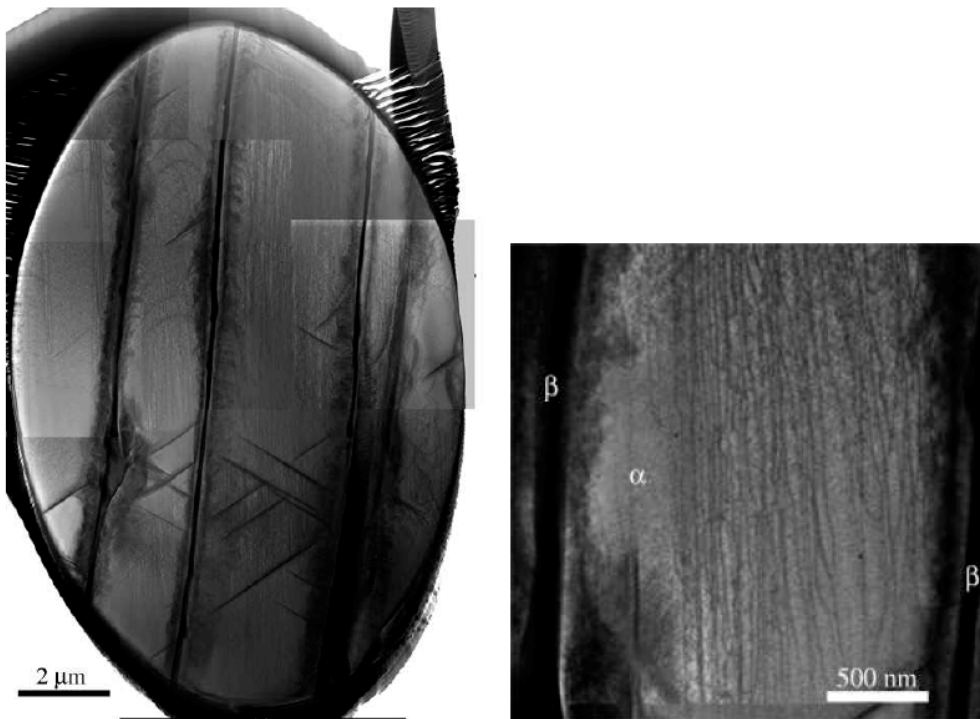
Figure 14. BF-STEM images taken from a 10 μm Ti-6242 slip plane foil. Long screw arrays are visible; however, the large density makes subsequent analysis difficult.

BF-STEM images taken from this TEM foil indicate that two near surface or surface sources were operative on this slip plane, refer to Figure 15. The sources lie within the continuous alpha phase, located between each of the beta laths. As in the previous foil, there are long arrays of screw/mixed character dislocation segments resulting from the low mobility of the screw segments.
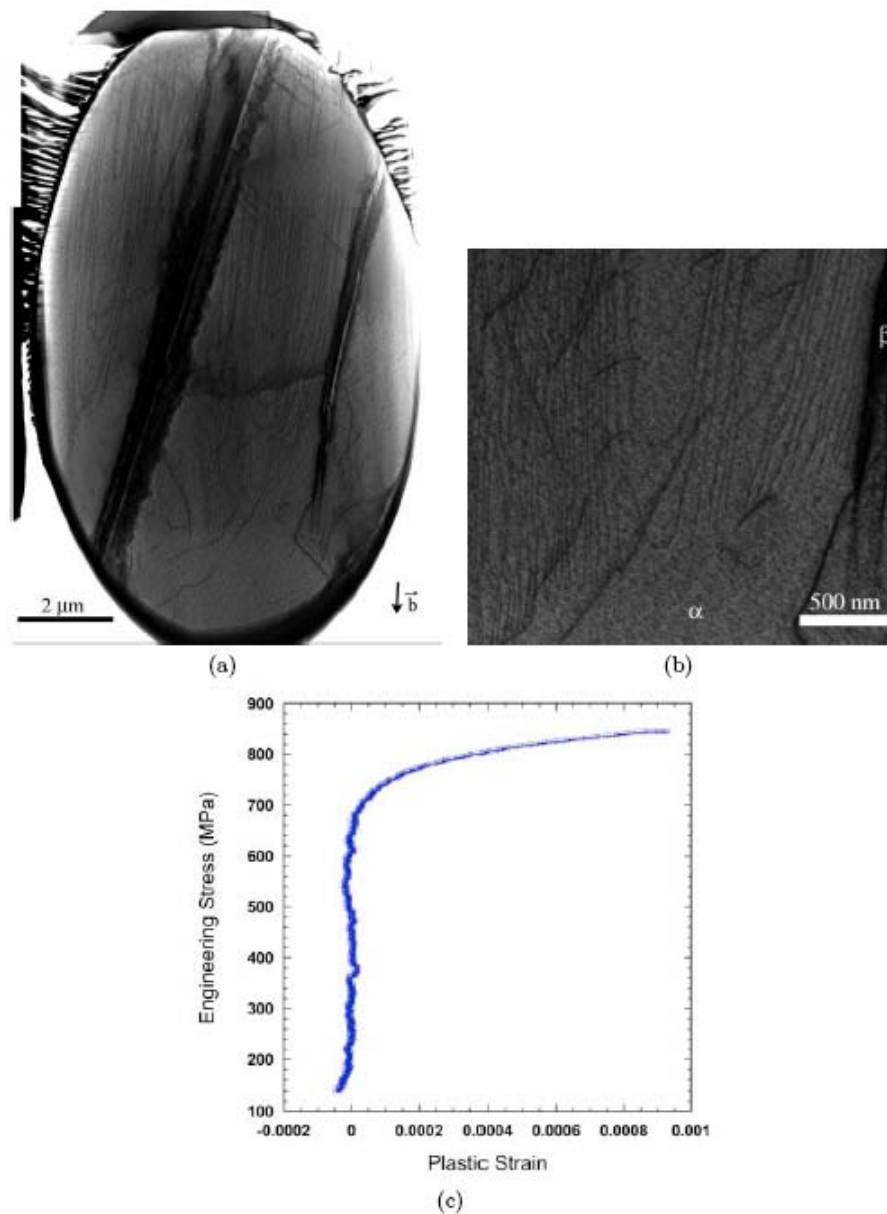
Figure 15. BF-STEM images taken from a 10 mm Ti-6242 slip plane foil. This microcrystal only experienced 0.1% plastic strain, allowing the observation of the very early stages of plasticity.

In order to determine the amount of plastic shear strain, γ_p associated with the propagation of dislocation content from these two sources, the following relationship was used,

$$\gamma_p = \frac{A_{ts}b}{V} \tag{4}$$

where *Ats* is the total area swept out by all dislocations and *V* is the total volume of the compression sample. To determine A_{ts}, the dislocation loops presented in Figure 15 were manually traced using Adobe Photoshop software and the area for each respective loop was determined and summed using Reindeer Graphics Fovea Pro® analytical software. During this process, 12 screw dislocation segments were missing such that the loop area could not be

Figure 16. BF-TEM images taken from a 5 μm Ti-6242 longitudinal foil, such that the Burgers vector is out of the plane of the foil.

determined. For these segments an average area was estimated based on an extrapolation of the observed loops. It was determined that the total area swept, A_{ts}, is ~5.8×10^8 nm^2, resulting in a plastic shear strain of ~0.09%. Therefore, all of the dislocation loops found in this TEM foil, 46, constitute only 1/3 of the total dislocations needed to produce the measured plastic shear strain of 0.24%. This result suggests that many sources must be operating in the micro-plastic regime to produce the measured plastic strain. From this result is seems unlikely that source operation is a contributing factor to the observed offset from bulk strengths.

A TEM foil was extracted from a 5 µm microcrystal parallel to the loading axis such that the Burgers vector is out of the foil plane. BF-STEM images are found in Figures 16 and 17. The short, straight dislocation segments are foreshortened screw segments, truncated due to the geometry of the TEM foil. Several pile-ups are observed at the sample/surface interface, indicating that these screw segments are having difficulty exiting the sample.

(a)　　　　　　　　　　　　　　　　　(b)
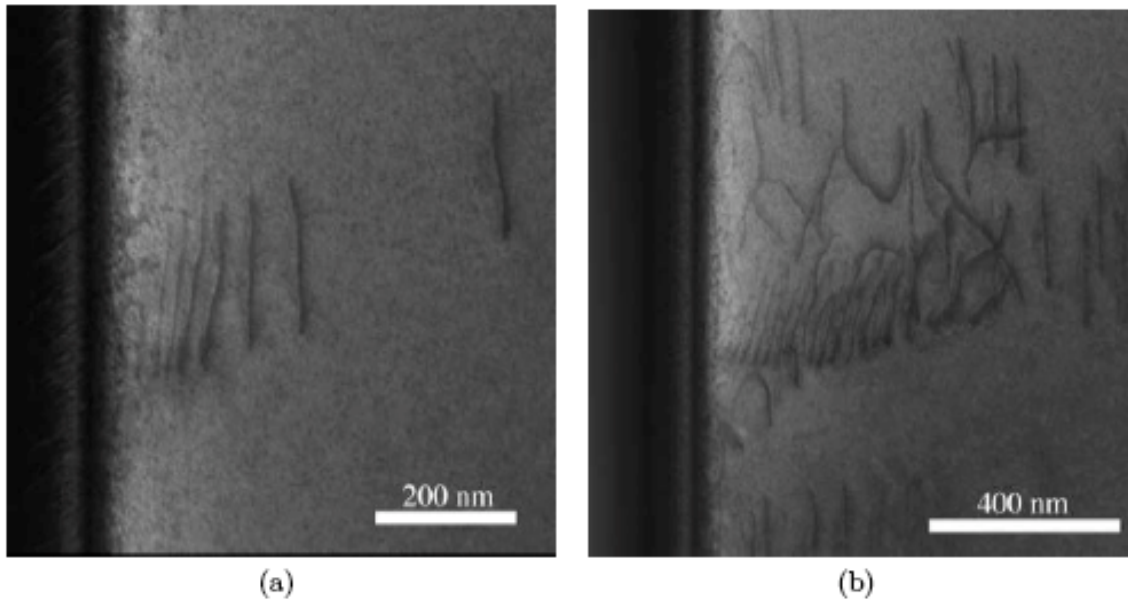
Figure 17. Higher magnification BF-STEM images taken from the 5 µm Ti-6242 longitudinal foil found in Figure 6.5a. Several screw-character pile-ups are visible at the sample/surface interface.

It should also be noted that in a few TEM observations minimal dislocation activity was observed below the base of the sample, refer to Figure 18. This result is not a surprise since the microcrystals are continuous with the bulk below the base. These dislocations are likely being generated from stress concentrations formed at the intersection of the microcrystal and the base. Since the density is small, it is unlikely that these dislocations are contributing to the strength of the microcrystals.

3.3 Results for NiTi Microcrystals

The results of uniaxial compression testing of two 5mm pillars is shown in Figure 19, with the first sample having undergone a single load-unload cycle, and the second sample having undergone two cycles. These pillars were machined into the indicated grain with an orientation close to <110>.
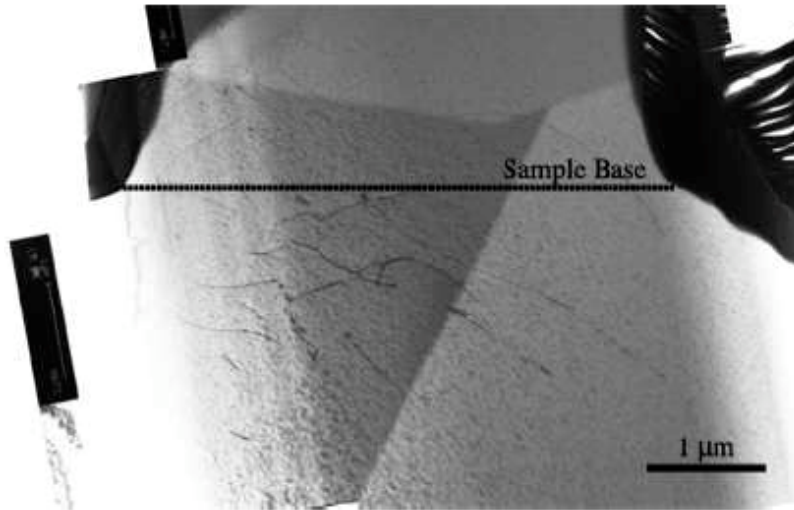
Figure 18. Minimal dislocation content was observed below the base of the sample in a few TEM foils.
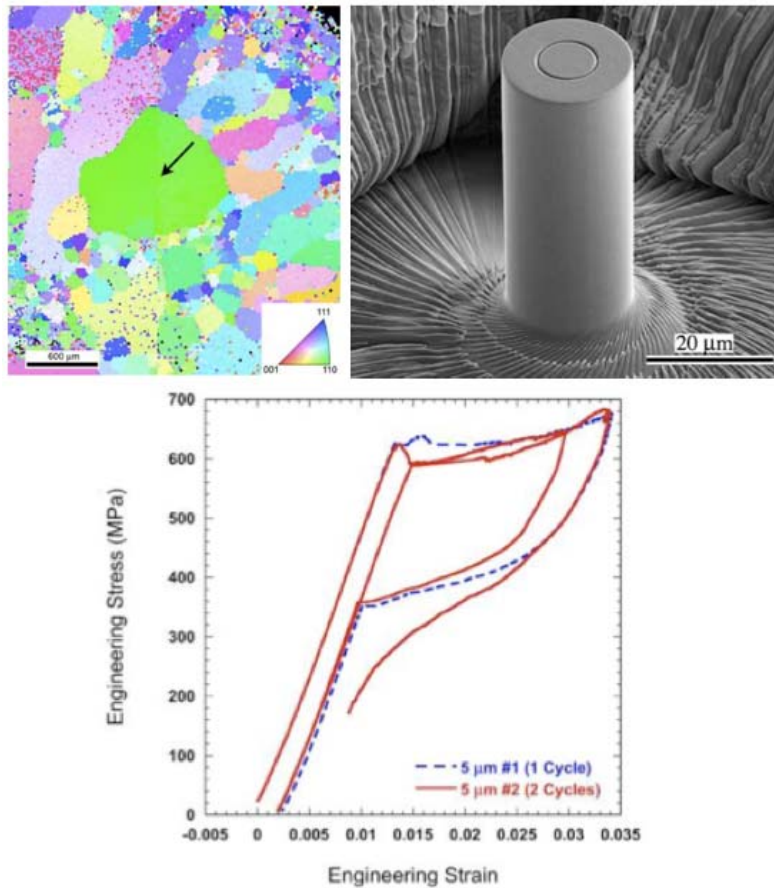
Figure 19. (a) OIM image of annealed polycrystalline Ni-Ti sample, showing the grain selected for pillar testing, with an orientation close to <110>. (b) Machined 20 μm pillar. (c) Stress-strain curves for two 5 μm pillars experiencing one and two cycles.
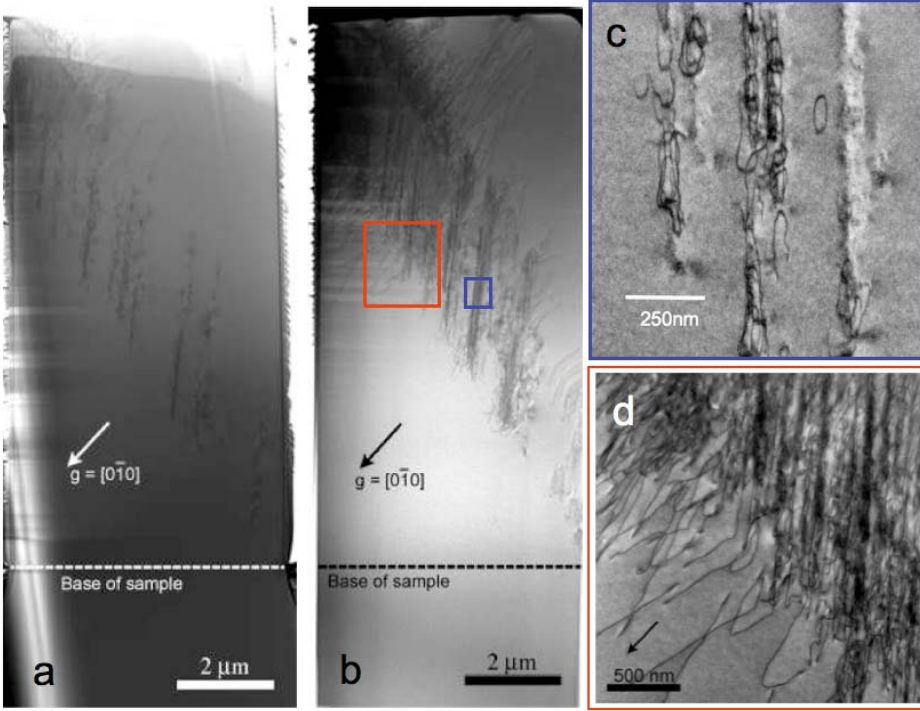
Figure 20. BF-STEM images of longitudinal sections from (a) one and (b) two cycle samples. (c) *a*[010] dislocation loops in previously transformed region. (d) *a*[010] dislocation structure near transition from matrix to previously-transformed region of two-cycle sample.

In order to provide insight into the attractive pseudoelastic response seen in Figure 19, TEM foils were prepared using the FIB by sectioning both the one- and two-cycle samples longitudinally along the axis of the pillar. Figure 20a and 20b show overall views of the pillar substructures for the one- and two-cycle samples, respectively. All TEM data shown here are bright-field scanning transmission electron microscope (STEM) images. In both the one- and two-cycle cases, a substructure feature is seen traversing diagonally across the pillar. As supported by the analytic model presented below, this is a region associated with the formation of a single martensite variant under stress, and containing a significant dislocation density. The model will show that only one of the possible martensite variants would have the observed habit planes relative to matrix and explain the imposed strain level. This result is remarkable considering that this sample is very close to a symmetric orientation for which multiple martensite transformations are expected. The clear evidence for plasticity in this region is at odds with the nearly perfect hysteresis response exhibited after the first cycle. The hypothesis that this dislocation structure is generated by the transformation is consistent with the increased dislocation density in the transverse region following two cycles.

Detailed diffraction contrast analysis indicates that all the dislocation content seen in Figures 20a and 20b, and in the magnified views of Figures 20c and 20d, are *a*[010] dislocations. These dislocations are one of the two most highly stressed Burgers vectors under the applied stress. However, tilting experiments indicate that individual dislocations are on (10-1) planes, which are not the most highly stressed slip system (*a*[010] on (100) is the primary system). In Figure 20c, we see that the vertical features seen in Figures 20a and 20b are actually small, elongated *a*[010]

98

dislocation loops that are arrayed as walls oriented parallel to the deformation axis (the walls are formed parallel to (1-10) planes). It is also noted that the dislocations appear to be injected into the matrix from the transformation zone, indicating that they have been induced by the incompatibility between the martensite and the matrix. Diffraction information from various regions of the sample indicates that the pillar has indeed transformed back to the B2 structure. However, it is possible that some very small pockets of martensite remain, which may be responsible for at least some of the remnant dislocation structure observed. More detailed diffraction studies using convergent beam electron diffraction, which offers better spatial resolution, are presently underway in order to verify the existence of remnant martensite.

To our knowledge, these results are the first detailed analysis of the specific dislocation type and dislocation arrangements associated with the pseudoelastic response in the NiTi alloys. Previous work indicates the presence of a<100> dislocations [28-31], but whether these were associated with the macrostress or intimately tied to the transformation itself has never been clarified. This ambiguity persists since in testing of polycrystals, or even bulk single crystals, activation of multiple variants and multiple transformation zones makes it difficult or impossible to deconvolute the substructure development associated with a single transformation zone. Furthermore, the pillar tests enable a direct measurement of the stress-strain response for singular transformation zones.

4. Discussion

4.1. Discussion of Size Effects in Ni Microcrystals

For discussion purposes, we propose some useful nomenclature that will be employed throughout the rest of this document. Given a single-crystal volume of material, there is an inherent or "reference stress" associated with the combined effects of the initial dislocation-forest density, Frank-Read source operation and the Peierls-Nabarro or lattice-friction stress. In an isotropic FCC material at room temperature the Peierls stress is an essentially negligible constant (for most stress estimates given here, a value of 2 MPa was assumed). Therefore, the reference stress is strongly influenced by the initial forest density and source-operation stresses. All subsequent evolution of the dislocation structure must occur under kinetics governed by attaining an "effective stress" that exceeds the sum of the reference-stress components. Therefore, the discussion proceeds first from an evaluation of the components of the reference stress and then to a discussion of the effective stress. A detailed account of this calculation is provided in [32]. Combining the strengthening terms from the Peirels stress, τ_p, initial forest-hardening stress, τ_f and, the source-truncation hardening stress, $\bar{\tau}_s$, an equation representing the total reference stress of the microcrystals is given in Eqn. 4:

$$\tau_r = \tau_p + k_s G \frac{\ln(\bar{\lambda}/b)}{(\bar{\lambda}/b)} + k_f Gb \ln\left(\frac{1}{b\sqrt{\rho_t/2}}\right)\sqrt{\rho_t/2} \tag{5}$$

This reference stress is plotted as a function of microcrystal diameter in Figure 21. Note that first and last terms are size-independent thus the size dependency arises solely from the source-hardening term. It is apparent, from this plot that at microcrystals larger than ~5μm, the

observed proportional limits can be accounted for as representing the reference stress of Eqn. (4). However, for smaller microcrystals there is a deviation from Eqn (4), suggesting that other hardening mechanisms may be operative in the micro-plastic regime.
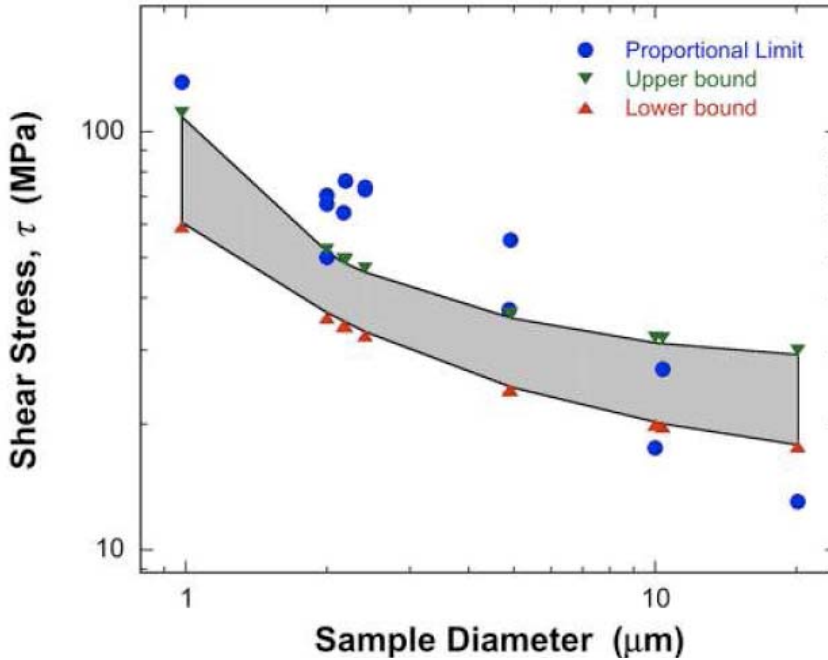
Figure 21. The proportional limit data from experiment is plotted with the total reference stress, τ_r.

Consequently, the combined strengthening effects from all components of the reference stress, with the forest-hardening contribution being corrected for the increase in dislocation density at smaller sample sizes, was computed and compared to the observed flow stresses. A composite plot including the upper and lower bounds of these stresses and the measured stresses was generated and is shown in Figure 21. However, even summation of the evolved components of the reference stress was still insufficient to explain the observed flow stresses. This result, in combination with the result of the initial reference stress being inadequate to account for the observed proportional limits, indicates that whatever the additional strengthening mechanisms that raise the effective stress at small microcrystal sizes, they remain active from the proportional limit throughout the duration of the loading.

The results presented for nickel and gold microcrystals [16, 33-34] indicate a regime that is characterized by burst activity associated with an effective strain hardening rate exceeding that of Stage II hardening. The present work was unable to determine the mechanism associated with this regime due to the stochastic nature of the burst events and the inability to stop an experiment just prior to a event. However, the fact that the nickel microcrystals evolve a dislocation density during the deformation that is larger than the initial density and that this density is stored at the early stages of plasticity, suggests that changes may be occurring within the dislocation forest that are contributing to the strength increases. These changes may be related to a change in the forest density as multiple slip systems become operative at smaller sizes. The changes may also be more complex, related to the creation of stronger junctions/obstacles. However, each of these remains to be proven. Coupling the observations from this study, with the fact that the

combination of the reference stress and a forest-hardening contribution (being corrected for the increase in dislocation density at smaller sample sizes) were insufficient in explaining the observed flow stresses, indicates that further study in this area is needed to explain this behavior. A suitable study would incorporate the observations determined from this work coupled with computational 3-D dislocation dynamic simulations.

4.2 Titanium vs. Nickel and Gold Microcrystals

The purpose of this research was to determine if titanium microcrystals exhibit similar strength characteristics and size effects compared to other metallic microcrystals fabricated with the FIB.

(a)

(b)
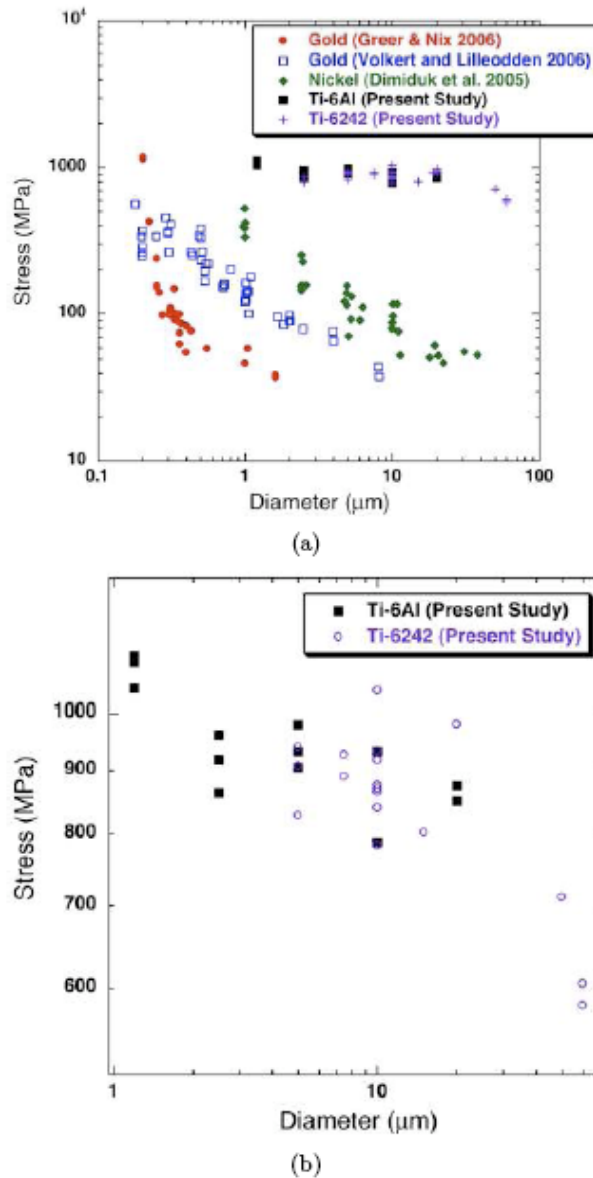
Figure 22. The 0.2% yield stresses for Ti-6Al and Ti-6242 microcrystals are plotted with the yield stresses from previously published FCC microcrystal data. It is apparent from this plot that the increase in strength with decreasing sample size observed in the titanium alloys is not as significant as in the other materials.

101

Figure 22 consists of a composite plot comparing the flow stresses for several of the FIB microcrystal studies. For titanium, the flow stresses were selected at 0.3% plastic strain, as this is the first strain level in the 20μm samples to reach a nearly perfect plastic transition. It is apparent from Figure 22 that there is a clear distinction between the kink-mode controlled titanium materials and the obstacle controlled FCC materials. In the FCC materials, there is over an order of magnitude increase in strength as sample dimensions are reduced. This is clearly not the case for titanium.

It has been reported by Dimiduk et al., that for nickel the scaling relationship follows a $1/D^n$, where n is reported as 0.6 to 0.7. Similar values are also found for the gold data. Using this same scaling relationship, n values of ~ 0.08 were determined for Ti-6Al and Ti-6242 microcrystals, further, indicating that there are dramatic differences in the response of different material structures at small size scales. This also suggests that the strengthening mechanisms associated with nickel and gold, at these sizes, may be very different to the hardening mechanisms that are responsible for the offset from bulk behavior in the titanium microcrystals.

The flow curves presented in Figures 10 and 12 indicate a clear separation in the strength between titanium microcrystals and bulk crystals. The shape of the flow curves, specifically the transition from elastic to plastic, is very similar for Ti-6Al and Ti-6242 microcrystals. Coupling these observations and the fact that both materials experience an upper yield point, it is feasible to consider that the offset from bulk behavior is related to the same micro-mechanisms operating at the early stages of plasticity. Furthermore, the large microcrystals, 50/60 μm, exhibit similar bulk proportional limit values; however, the upper yield points are similar to the smaller microcrystals. This suggests that the micro-mechanism(s) related to the offset from bulk behavior are not related to source operation.

Additionally, the amount of plastic engineering strain that has occurred prior to reaching the upper yield point is ~0.6%, or 1.3% plastic shear strain. This correlates to the activation and propagation of a minimum of 3,700 dislocations based on the following expression:

$$\gamma_p = 0.013 = \frac{\Delta x}{X'} \tag{6}$$

where, Δx is the displacement parallel to the slip plane and X' is the initial slip plane length, given as 60/ cos 45°. The number of dislocations is simply $\Delta x/b$, where b=2.95Å for titanium, yielding 3,700 dislocations. However, due to the low mobility of the screw segments, many more sources may operate making this value much larger and further suggesting that source operation is not the cause for the size effect in these titanium alloys.

Observations of several dislocation pile-ups at the surfaces of the Ti-6242 microcrystals, both of edge and screw characters, indicate that dislocations have difficulty exiting the microcrystals. A high magnification view of one of these pile-ups is presented in Figure 23. Only one-half of the pile-up is visible because during the foil thinning process the other half was ion milled away. However, from this image, the dislocations appear to pile-up along the dark band indicated by the arrow. During the thinning process, ion implantation occurs and is observed as small black dots peppered throughout the foil. These dark spots, resulting from the strain fields produced

from the large implanted gallium ions, appear to have a much higher concentration near the exit surface of the sample, as depicted by the arrow in Figure 23. Therefore, the possibility exists that during the fabrication of these titanium microcrystals a surface layer of gallium damage is encasing the samples and having a large effect on the dislocations exiting the sample, resulting in a strengthening effect and an offset from bulk properties. Interestingly, if the Ti-6Al yield stresses are plotted with Ti-6Al polycrystalline results, similar scaling coefficients are observed. This result suggests that the behavior in the titanium microcrystal experiments may be comparable to that observed in polycrystalline experiments.
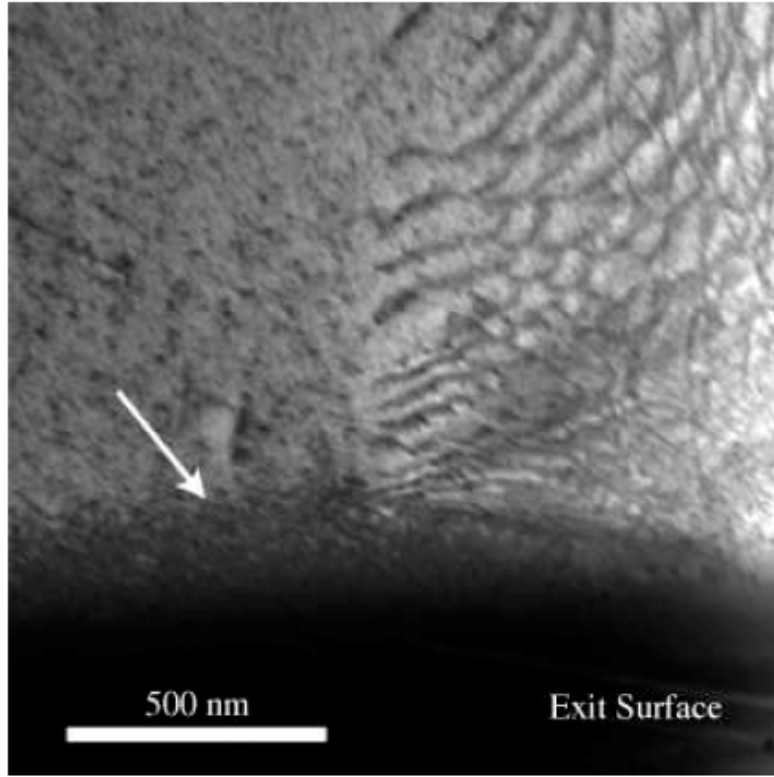
Figure 23. A higher magnification BF-STEM image highlighting an edge character dislocation pile-up at the exit surface of the microcrystal. This pile-up appears to be related to gallium ion damage caused from the microcrystal fabrication process, evident by the increase in ion damage near the exit surface of the sample, indicated by the arrow.

Built on the framework of a pile-up model, a Hall-Petch (H-P) relationship is given by,

$$\sigma = \sigma_0 + kD^{-\frac{1}{2}} \tag{7}$$

where σ_0 is the Peierls stress, k is the H-P slope and D is the average grain size. The ideas of H-P suggest that for larger grain sizes, a larger pile-up of N dislocations can occur, resulting in a larger force on the lead dislocation and a lower yield stress is needed to burst through the boundary. These ideas parallel the possible scenario observed in the titanium microcrystals, from which the microcrystals are of varying diameter with a constant surface barrier. The Ti-6Al results presented in Figure 22 are recast into a H-P plot, by taking a scaling coefficient of -0.5,

103

along with the results from several grain size studies performed on Ti-6Al polycrystals. These results are found in Figure 24. Surprisingly, the Ti-6Al data, specifically k, agrees very well with data published for Ti-6Al polycrystals [35]. In fact, the coefficient of determination, R2, is larger for the linear fit used in the H-P plot, indicating that the H-P relationship is a better fit to the Ti data. Furthermore, using short-range-ordering (SRO) arguments presented by T. Neeraj and M. Mills [36], the pile-up characteristics, specifically the planarity of slip, are greatly influenced by the amount of SRO present in the material. The SRO is influenced by the heat-treatment applied to the material, such that water-quenched (WQ) samples exhibit little to no SRO because the diffusion time is minimal. Consequently, as aging time is increased so does the SRO. The Ti-6Al results presented in Figures 24 contain variations in the SRO state of the material prior to testing: WQ, WQ + Anneal, and Air Cooled (Ti-6Al Microcrystals). These difference are reflected in the H-P slope accordingly, with the WQ samples having the smallest k-coefficient of 0.232, the WQ + Anneal having the largest k-coefficient of 0.453 and the Air Cooled microcrystals somewhere in the middle with a k-coefficient of 0.311.
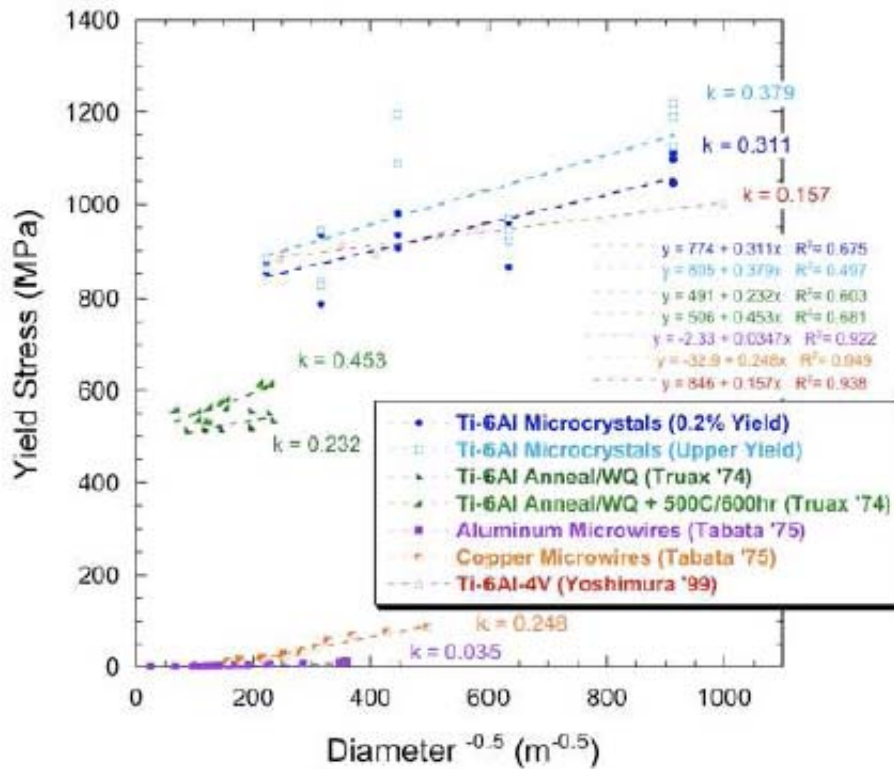
Figure 24. The yield stresses from the Ti-6Al data found in Figure 22 are recast into a Hall-Petch plot. The H-P slope, k, agrees very well with other published data.

Similar hardening effects have been observed in aluminum microwires by Tabata et al. [37], in which the wires contained an oxide surface layer and insitu TEM indicated that dislocations were piling up at the surface, causing an increase in strength.
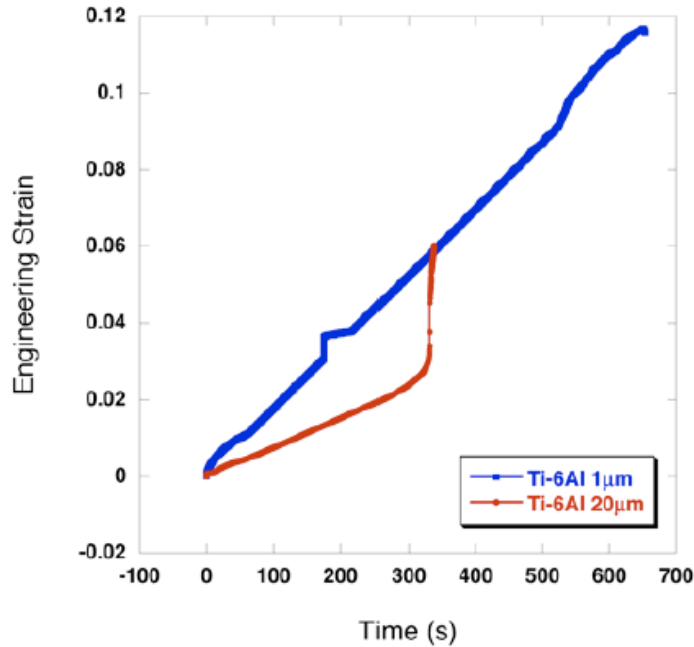
Figure 25. The difference in strain rate behavior between a 1 μm and 20 μm microcrystal loaded using the OLD method. The 1 μm sample was able to recover from a burst event, maintaining a constant nominal displacement rate. This was not the case for the 20 μm sample that experienced a dramatic acceleration in strain rate once plasticity begins. The sample continued to deform at this rate until the sample was unloaded.

Furthermore, observations related to strain rate data support a gallium ion damage layer strengthening effect. Figure 2 is a plot showing the difference in strain rate behavior between a 1μm and 20μm microcrystal. For these tests, the OLD method was used, such that the load was never allowed to drop. In the 1μm sample a constant nominal strain rate is achieved throughout the loading of the sample. Although there are minor increases in the rate, the sample was able to "recover" and plastically deform at a constant rate. This is not the case for the larger samples, as illustrated by the 20μm sample in Figure 25. Once plasticity begins, at ~275 seconds, there is a gradual increase in strain rate until the sample begins to plastically deform in a catastrophic manner. At this point the strain rate reaches a maximum and will continue to deform at this rate until the sample is unloaded.

The difference in this behavior can be attributed to the size of the dislocation pile-up related to each respective sample size. In the 1μm microcrystal, the number of dislocations contributing to the pile-up is likely to be relatively small compared to the 20μm microcrystal based on the proximity of the operating source(s) and the dislocation pile-up (sample surface). As dislocations

pile-up at the sample surface there is an increase in the back-stress on the operating source. The source will shut off once the back-stress reaches a critical value. Therefore, the number of dislocations, n, that can occupy a distance, L, along the active slip plane between the source and the sample surface is given as [38]:

$$n = \frac{k\pi_{rss}L}{Gb} \tag{8}$$

where k is ~1 for screw dislocation segments and $k = 1-v$ for edge segments. This equation (Eqn. 7) assumes that the source is operating at the sample surface. If the source is operating in the center of the sample, then n would decrease by a factor of 4. Therefore, the close proximity of the source to the pile-up in the 1μm sample results in fewer dislocations contributing to the pile-up and yielding a smaller strain rate increase once the ion-damage layer is surmounted.

4.3 Discussion of NiTi Microcrystal Results

Relative to the one cycle sample, there are several remarkable features associated with the stress-strain curves, particularly when compared with the published data of Gall, et al [5] on bulk single crystals and Frick, et al. [39] in sub-micron pillars.

(1) The elastic loading portion of the curves is quite linear, indicating that the top of the machined pillar (see Figure 19) is flat and that there is exceptionally good alignment between the flattened Nanoindenter platen and the top of the sample. Note that in the published stress-strain data from Frick, et al. [39] this elastic loading is not linear, indicating poor sample shape and alignment.

(2) There is an extremely sharp and pronounced transition from the elastic loading portion of the curve. This feature is quite different from the rounded elastic transition seen in the single crystal test of Gall, et al [5] for the [110] orientation. This important difference could indicate the inhibition of matrix plasticity in the micropillar size scale.

(3) The plateau stress, which is normally associated with the stress-induced martensitic transformation, gradually increases with increasing strain. This plateau stress is nearly the same as that obtained by Gall, et al [5], suggesting that the martensite transformation is not strongly affected by the sample size in this orientation.

(4) Upon unloading on the first cycle, there is a very distinct change in unloading slope and a return to the elastic loading line, indicative of the transformation back to the parent B2 austenite. This feature requires a much lower stress for the bulk single crystal test of Gall, et al. [5], suggesting that the back transformation is difficult relative to the micropillar case.

(5) The remnant strain is small (0.2%) compared with that seen in the bulk crystal.

(6) The two-cycle sample exhibits repeatability in the plateau stress and a larger hysteresis loop upon unloading from the second cycle, indicating that there is a development of substructure occurring during cycling.

To our knowledge, these results are the first detailed analysis of the specific dislocation type and dislocation arrangements associated with the pseudoelastic response in the NiTi alloys. Previous work indicates the presence of a<100> dislocations [29-31], but whether these were associated with the macrostress or intimately tied to the transformation itself has never been clarified. This

ambiguity persists since in testing of polycrystals, or even bulk single crystals, activation of multiple variants and multiple transformation zones makes it difficult or impossible to deconvolute the substructure development associated with a single transformation zone. Furthermore, the pillar tests enable a direct measurement of the stress-strain response for singular transformation zones.

5. Conclusions

Microcrystal compression studies on pure nickel, titanium and nickel-titanium were performed to explore sample size effects at the micrometer scale. The results suggest the dislocation micro-mechanisms, inherent to each material, contribute to different sample size effects. In nickel, a obstacle controlled material, an increase in the dislocation density was observed at smaller samples sizes. However, the hardening behavior associated with such densities was insufficient in explaining the observed flow stresses based on a Taylor based model. Furthermore, the contribution from a source hardening mechanism, coupled with the forest hardening behavior, was also unable to account for the large stresses. This result suggests the possibility that a change in the dislocation forest strength may be occurring at small sizes, resulting in an increase in the flow stresses. Further studies using dislocation dynamic simulations are needed to support this hypothesis.

The single phase, Ti-6Al, titanium microcrystals exhibit a size effect that is very different than that observed in nickel. Nickel microcrystals follow the scaling relationship 1/Dn, where n is reported as 0.6 to 0.7. Using this same scaling relationship, n values of ~0.08 were determined for Ti-6Al and Ti-6242 microcrystals, indicating the differences between bowing- and kink-mode materials at small size scales. The possibility that ion damage may be contributing to the size effect in titanium is supported by the following observations.

• Many dislocation pile-ups, both screw and edge character, are observed in TEM foils extracted from the titanium microcrystals.

• The scaling relationship for the Ti-6Al microcrystals follow a Hall-Petch relationship, similar to polycrystalline Ti-6Al.

• Bulk flow stresses are still not observed in the 60μm microcrystals. However, the proportional limits at this size are very similar to that in bulk samples, suggesting that source operation is not a contributing factor to the higher flow stresses.

• Ti-6242 Sample #2 was ”seeded” with polishing induced dislocation content near the top surface, potentially providing an infinite number of dislocation sources. An offset from bulk behavior is still observed in microcrystals tested from this sample, further suggesting that source operation is not the cause.

• The small-strain, 10 μm, sample shows an offset from bulk behavior at only 0.1% plastic strain. The planarity and shape of the dislocation arrays suggest that forest-type hardening behavior is not contributing to the offset from bulk flow stresses.

Unfortunately, the presence of gallium seems to have tainted the fundamental aspects related to dislocation micro-mechanisms as a function of size for kink-mode materials. Therefore, fundamental comparisons between bowing-mode and kink-mode materials at the micron size scale are difficult with the present data set.

The nickel-titanium microcrystals deform differently compared to the bowing and kink-mode materials. Instead of dislocations gliding across a slip plane to induce a shape change, a reversible martenistic phase transformation occurs, contributing to the pseudoelastic behavior. As such, these microcrystal exhibit no size effect related to the transformation stress for the sample sizes tested. However, differences are observed in the shape of the flow curves between the microcrystals and bulk samples. First, the elastic/transformation transition is much sharper for the microcrystals, suggesting that little plasticity is occurring prior to the transformation. Furthermore, the microcrystals exhibit hardening behavior, following the transformation stress, that is much more pronounced than bulk behavior. A similar hardening behavior was observed by Frick et al. in [1 1 1] microcrystals [39]. They suggested that this may be due to gallium ion damage caused during the fabrication of the compression specimens. TEM investigations indicates that dislocations outside of the transformation zone are of type a[0 1 0](1 0 1) and the dislocations inside the transformation zone observe the same invisibility conditions. However, the line directions between the two are very different. The relationship between plasticity and the martensitic phase transformation is not well understood. However, coupling microcrystal experiments with TEM provides a unique method enabling properties to be directly correlated with transformational associated plasticity.

Regarding FIB induced ion damage, the results presented for the titanium microcrystals suggest that a strengthening effect is occurring as a result of this phenomena. However, this does not seem to be occurring in the nickel microcrystals, as indicated by the observed bulk flow stresses in the 20 μm samples. At the present time it is unclear why this would be different between the two materials that deform plastically via dislocation motion. However, one possibility may be related to an asymmetric strain field produced by the crystal structure and SRO in the titanium microcrystals, resulting in a more dramatic strengthening effect for the titanium alloys.

6. Recommendations

• The fabrication of titanium microcrystals using a different process is necessary to determine if ion damage is contributing to an increase in strength. One possibility may be laser fabrication. Another option would be to load a Ti-6Al sample past the proportional limit, but prior to the upper yield point and look for pile-ups in a slip plane TEM foil.

• Since remnants of a recast layer were found on the 50/60 μm Ti-6242 microcrystals, another 60 μm sample should be fabricated and tested. If the characteristics of the flow curve are similar to the samples with the recast, then this is very good evidence that gallium ion damage is a strong barrier to dislocation motion.

• TEM analysis on the ion damage layer to determine the nature of the strain-fields associated with gallium ions in nickel and titanium. This could reveal the difference in hardening behavior between the nickel and titanium microcrystals.

• Dislocation dynamic simulations should be performed on virtual nickel microcrystals, incorporating the TEM results, to determine the nature of forest junction formation and hardening at the micron size scale.

• The fabrication of NiTi microcrystals smaller than 5 μm are needed to study the transformation stress and subsequent hardening behavior at small sizes. Coupling TEM with these results, insights into the relationship between plasticity and the transformation may be achieved.

7. References

1. E. Nadgornyi, *Progress in Materials Science*, Vol. **31**, pp. 1–530, 1988.
2. K. Gall, H. Sehitoglu, Y. I. Chumlyakov and I. V. Kireeva, *Acta mater*. Vol. **47**, No. **4**, pp. 1203-1217, 1999.
3. H. Sehitoglu, J. Jun, X. Zhang, I. Karaman, Y. Chumlyakov, H. J. Maier and K. Gall, *Acta mater*, vol. **49**, pp. 3609– 3620, 2001.
4. H. Sehitolgu, I. Karaman, R. Anderson, R. Sehitoglu, X. Zhang, K. Gall, H. J. Maier and Y. Chumlyakov, *Acta mater*. **48**, pp. 3311-3326, 2000.
5. K. Gall, M.L. Dunn, Y. Liu, P. Labossiere, H. Sehitoglu and Y.I. Chumlyakov, *Trans. AIME*, **124**, pp. 238-245, 2002
6. K. Gall and H. J. Maier, *Acta mater*, vol. **50**, no. 18, pp. 4643–4657, 2002.
7. M.D. Uchic and D.A. Dimiduk, *Mat Sci & Engr A*, vol. **400**, pp. 268–278, 2005.
8. C.J. Humphreys, *Ultramicroscopy*, 7:7, 1981.
9. D.M Maher, D.C. Joy, Ultramicroscopy, 1:239, 1976.
10. U. Matrin, U. Muhle, O. Heinrich, *Prakt. Metallogr*. **32**, 1995.
11. D. Delille, R. Pantel, E. Van Cappellen, *Ultramicroscopy*, 87:5, 2001.
12. P.M. Kelly, A. Jostsons, R.G. Blake, J.G. Napier. *Physica Status Solidi A: Applied Research*, 31:771, 1975.
13. D.B. Williams, C.B Carter, *Transmission Electron Microscopy*, New York: Plenum Press, 1996.
14. P. Stadelmann, JEMS computer code.
15. T. Kruml, V. Paidar, J.L Martin, *Intermetallics*, 8:729. 2000.
16. D.M. Dimiduk, M.D. Uchic, T.A. Parthasarathy, *Acta mater*, **53**:4065, 2005.
17. M.D. Uchic and D.A. Dimiduk, J.N. Florando, W.D. Nix, *Materials Research Society Symposium Proceedings* **753**:27, 2003.
18. S.S. Brenner, *Growth Perfection Crystals, Proc. Intern. Conf*., Cooperstown, N.Y. p.157, 1958.
19. S. Mader, Electron Microscopy and Strength of Crystals, G. Thomas, J. Washburn, editors. New York: Interscience Publishers, p.183, 1963.
20. A.S. Argon*, Phys. Strength Plast*, **217**, 1969.
21. J.G. Sevillano, *Materials Science and Technology*, H. Mughrabi , editor, vol. **6**, p.78, 1993.
22. S. Polasik, Accelerated Assessment and Representation of Materials Behavior Via Integrated Electron-Optical, Focused Ion Beam and MEMS-Based Characterization Methods, The Ohio State University, 2005.

23. J. Weiss, D. Marsan, *Science*, 299, 2003.

24. F. Nabarro, Z.S. Basinski, D. Holt, *Advances in Physics*, 13:193, 1964;
25. S.J. Basinski, Z.S. Basinski, *Dislocations Solids*, 4:261, 1979.
26. W. Pueschl, R. Frydman, G. Schoeck, Physica Status Solidi A: Applied Research, 74:211, 1982.
27. J.R. Greer, W.D. Nix, Physical Review B: Condensed Matter and Materials Physics 73:245410/1, 2006.
28. O. Matsumoto, S. Miyazaki, K. Otsuka and H. Tamura, *Acta mater*, vol. **35**, pp. 2137–2144, 1987.
29. Y.I. Chumlyakov, N.S. Surikova, and A. D. Korotayev, *Fizika Metallov I Metallovedenie*, vol. **82,** pp. 148–158, 1996.
30. J. Hurley, A. M. Ortega, J. Lechniak, K. Gall, and H. J. Maier, *Zeitschrift Fur Metal lkunde*, vol. **94,** no. 5, pp. 547–552, 2003.
31. Y.N. Liu, G. Tan, and S. Miyazaki, *Mat Sci & Engr* vol. **438**, pp. 612–616, 2006.
32. D. M. Norfleet, D.M. Dimiduk, M. Uchic, and M.J. Mills, *Acta mater,* submitted for publication.
33. C.A. Volkert and E.T. Lilleodden, *Philosophical Magazine*, vol. **86**, no. 33-35, pp. 5567–5579, 2006.
34. J.R. Greer and W.D. Nix, *Applied Physics A: Materials Science & Processing,* vol. **A80**, no. 8, pp. 1625–1629, 2005.
35. D.J. Truax and C.J. McMahon, C. J., *Mat Sci and Engr A,* vol. **13**, no. 2, pp. 125–39, 1974.
36. T. Neeraj and M. J. Mills, *Mat Sci and Engr A*, vol. **319**, pp. 415–419, 2001.
37. T. Tabata, H. Fujita, S. Yamamoto, and T. Cyoji, *J of the Phys Soc of Japan*, vol. **40**, no. 3, pp. 792–7, 1976.
38. J. Eshelby, F. Frank, and F. Nabarro, *Phil. Mag*, vol. **42**, p. 351, 1951.
39. C.P. Frick, O.S. Orso and A.E. Artz, *Acta mater*, vol. **55**, pp. 3845-3855, 2007.

8. Names of Personnel

Michael Mills (OSU Faculty Member)
Hamish Fraser (OSU Faculty Member)
Dennis Dimiduk (AFRL/RX Mentor)
Michael Uchic (AFRL/RX Mentor)
Stephen Polasik (OSU Graduate Student)
David Norfleet (OSU Graduate Student)

Physically-based Monte-Carlo Models of Grain Growth and Texture Evolution. *Anthony Rollett (CMU Faculty Member), Lee Semiatin (AFRL/RX Mentor), Christopher Roberts (CMU Graduate Student)*

I. RESULTS and DISCUSSION

1. Introduction

Grain growth is an important phenomenon in metallic systems. It is a result of the force imbalances at the triple junctions which induce boundary curvature to compensate. For many years, models have been proposed to predict how the system will evolve during annealing. For example, a high-purity single phase metal will evolve at a rate linearly proportional to the driving pressure. However, many metals contain solutes and precipitates which introduce additional physics which simple theories cannot account for. These commercial grade metals and alloys typically have constituents which form low volume fraction precipitates. The precipitates can affect microstructure evolution in various ways. In recrystallization, precipitates can act as nucleation sites by reducing the energy barrier whereas, in grain growth, the precipitates exert a drag pressure anti-parallel to the direction of grain boundary migration (aka Zener pinning").
In grain growth, Zener pinning provides a mechanism for controlling the final grain size of a given alloy; grain size control is one of the essential tools for tailoring the mechanical properties of an alloy (and other properties).

Limiting grain size prediction requires one to measure the average particle radius and volume fraction, but this technique may be over-simplified. The Zener equation has been shown to over-estimate the critical grain size, which may be a result of the numerous assumptions associated with its derivation. Therefore, controlled experiments aimed at relaxing or eliminating certain assumptions may help to refine the Zener equation and improve its prediction accuracy. The general form of the Zener equation is

$$D_L = K\frac{r}{f}$$

Where K is a constant, r is the average particle radius and f is the volume fraction.

Thus, the objective of this effort is to establish and validate mesoscale models for grain growth and pinning during the annealing of both single-phase and particle containing alloys. This objective will be met by conducting four interrelated tasks on (i) methods for determination of grain-boundary energy and mobility, (ii) enhancement of code(s) for simulating grain growth, (iii) experimental trials of grain growth in a nickel alloy and (iv) calibration and validation of the code(s).

2. Methods, Assumptions, Procedures

The experimental portion of this work focused on the heat treatment of a nickel-base alloy, Waspaloy. The samples were machined from cylindrical disks into 1cm^3 cubes for annealing at 1100°C where the γ' phase is dissolved. Annealing was performed using a salt bath furnace for

short exposures at high temperatures and an atmospheric furnace for extended annealing times. The soak times ranged from seconds up to 2 weeks. A combination of optical microscopy and electron microscopy were used to evaluate the geometric and texture features of the material as a function of annealing time. The collaboration with Dr. Semiatin's group at the Air Force Research Laboratory was critically important in this part of the work.

On the other hand, the computational investigation utilized a parallel implementation of the Potts-based Monte Carlo algorithm to simulate grain growth and growth stagnation in idealized two-phase digital microstructures. Supercomputing resources including the Aeronautical Systems Center and the Pittsburgh Supercomputing Center were used to conduct the simulation trials. Assistance from Dr. Jim Lill (ASC) and Junwoo Lim (PSC) was of considerable help in accomplishing this aspect of the work.

3. Results

3.1. Morphology

The grain shape was determined by examining two orthogonal planes of the nickel alloy. Figure 1 contains micrographs of the structure and clearly indicates an equiaxed grain morphology on both planes. Mean intercept lengths were measured on both planes and found to be 34μm ± 3.5μm on the axial plane and 38μm ± 2.5μm on the radial plane. More importantly, stereological relationships between two-dimensional and three-dimensional parameters are possible. Specifically, the mean intercept length on a cross-sectional test plane is equivalent to the three-dimensional mean intercept length (i.e. $\lambda_2 = \lambda_3$).
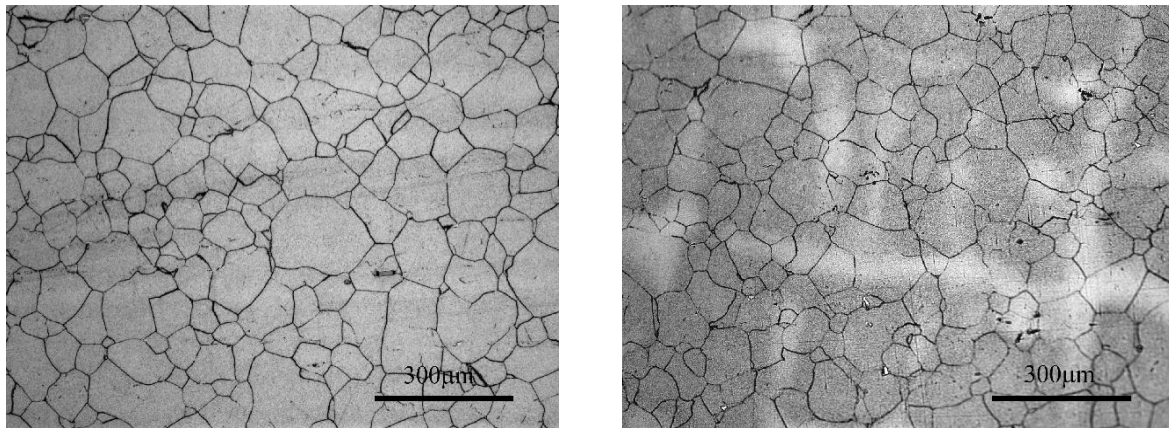
Figure 1. Micrograph of the microstructure on the a) axial plane and b) radial plane.

3.2. Grain Growth

Complex alloy systems with numerous elemental constituents may not behave according to the parabolic grain growth theory because of solute and particle drag. A series of short and long soaks at 1100°C were conducted in order to observe the growth kinetics and the influence, if any, of solute and precipitates. The short soaks required the use of a liquid salt medium in order to obtain accurate measurements of time at temperature. A 1cm^3 sample takes approximately 45

seconds for the center to reach the soak temperature, 1100°C. Both saltpot and atmospheric results were combined into one graph to observe a large spectrum of growth. Figure 2 is a combination of the average grain sizes obtained via the linear intercept method. No change in size is exhibited in the first 30 seconds of the soak. It has been hypothesized that the gamma prime does not fully dissolve until the samples have been at the set temperature, 1100°C, for 30 seconds; however, there may be a contribution from the carbides where the boundaries must "break away" from the particles.
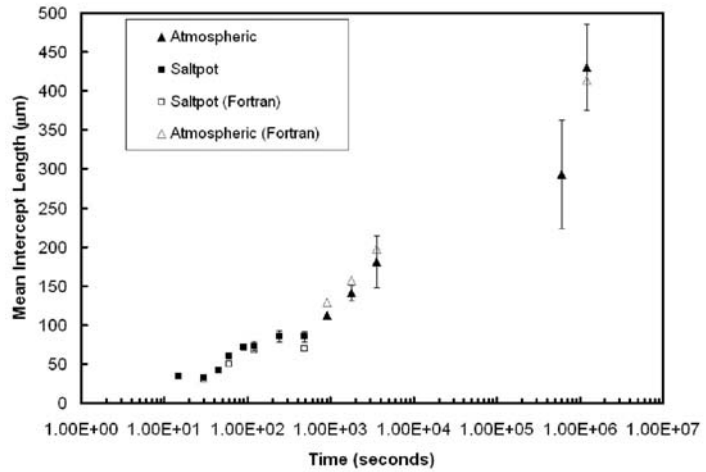
Figure 2. Average linear intercept versus time. Manual and computer generated measurements.

Once this coherent phase has dissolved and boundaries have pulled off the particles, an explosive change in the growth rate occurs. This stage of grain growth is attributed to the initially small grain size, which consequently implies a large driving force due to boundary curvature. Once the grain size has increased by a little over a factor of two, the driving force has been depleted to an extent where the particle drag pressure becomes comparable in magnitude.

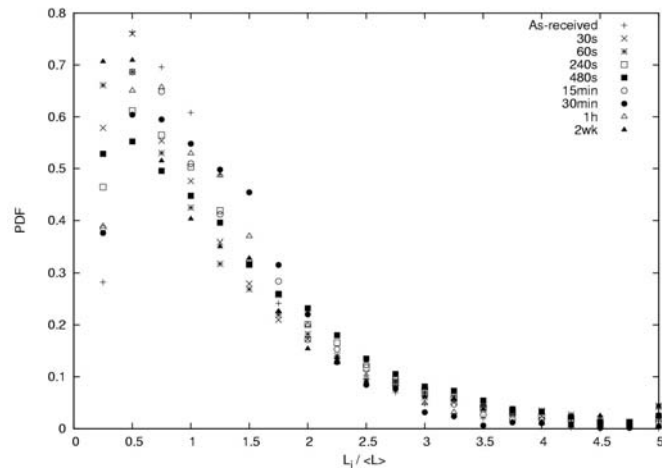Once the average grain size has doubled its original mean grain size, a second "stage" of growth ensues. This region does not exhibit rapid growth, but the mean size continues to increase indefinitely up to 2 weeks. Due to the complexity of the overall grain kinetics, attempts to fit the process to existing grain growth theories and models were unsuccessful. The parabolic growth law ignores the effect of particle drag once the driving force has been depleted following a large increase in grain size. Some models incorporate a Zener term which leads to a reduced driving pressure and eventually causes the growth to stagnate when the drag pressure is equal to the driving pressure [1]. The Anderson and Grong model was applied to the experimental results to determine goodness of fit; however, the predicted limiting grain size, D_L, and exponent, $(1/n - 1)$, are prerequisites for this equation.

The accuracy of this model is significantly influenced by the Zener equation parameters, namely K, r, and V_V. Assuming $D_L = K(r/f)$, $r = 1.2\mu m$, and $V_V = 0.002$, the grain size was estimated for variations in K. An extensive range of values is obtained by varying the

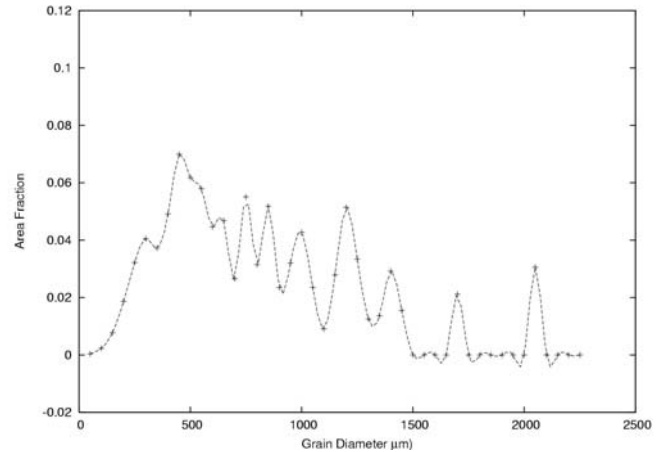**Figure 3.** Grain size distributions. Each distribution is normalized by the mean.

113

constant K. Using an incorrect K will result in large differences between the predicted and observed limiting grain size. Despite this flexibility of the model, it does not account for the second region of growth beyond the first 10 minutes.

Normalized grain size distributions were measured for a number of specimens using the linear intercept method. Each distribution has a right skewed tail indicative of a lognormal distribution and the distributions are invariant with respect to annealing time. Additionally, the micrographs were visually inspected for any evidence of "rogue" (abnormal) grains within the matrix. Figure 4 shows a series of micrographs taken from the etched samples of the saltpot experiment. The grain size appears to increase uniformly without any one grain appearing to be abnormally large relative to the matrix. The invariance of the grain size distributions and the self-similarity of the micrographs are characteristics of normal grain growth (NGG). Each of the specimens was visually inspected to confirm grain size uniformity and most of the microstructures appear to evolve via normal grain growth; however, the sample annealed for 2 weeks exhibited large "rogue" grains and suggests abnormal grain growth (AGG). The normalized grain size distribution in Figure 3 did not reveal this trend because it is a number-weighted distribution. Abnormal grains sparsely populate the microstructure, but the sum of their grain areas (2D) or volumes (3D) is considerably larger implying the abnormal grains can be discerned by constructing an area weighted grain size distribution. Figure 5 distinguishes the large grains from the distribution. The abnormal grains were much larger than the average ($R_{ABNORMAL} > 2R_{AVE}$).
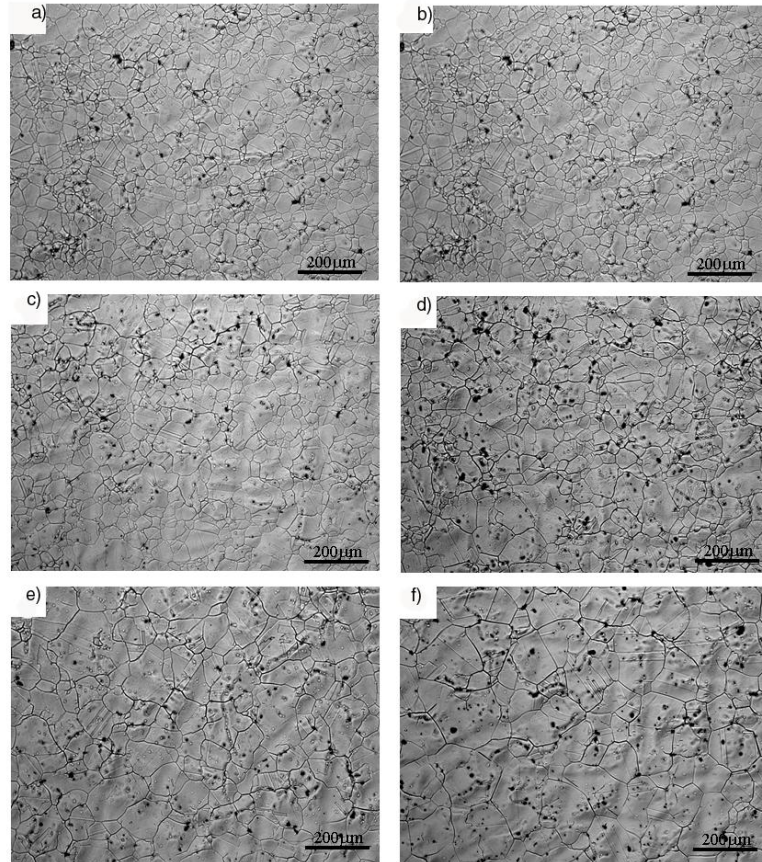
Figure 4. Sequential micrographs for six Waspaloy samples during annealing.


Figure 5. Area-weighted grain size distribution for sample annealed at 1100°C for 2 weeks.

114

The source of AGG may be orientation or texture dependent or a consequence of the particle spatial and grain boundary distributions. To determine the influence of texture, the specimen was analyzed using the OIM. Based on visual interpretation, large grains and their neighbors were scanned to determine the orientation and misorientation relationships. Approximately 13 abnormal grains were located on the sample surface and the average orientations were listed in table I. Each orientation represents the average orientation of the grain. In the presence of a twin boundary, the parent grain orientation is taken to be the average orientation. The orientations of the abnormal grains appear to lack any pattern and indicate any texture component is equally possible. Pole figures were generated for the 13 grain orientations and are illustrated in figure 6. Again, no pattern is observed.

ϕ_1	Φ	ϕ_2
241.017	42.099	84.23
268.925	37.659	117.68
58.692	30.932	306.69
254.736	46.098	108.87
336.368	42.66	42.03
227.517	49.375	140.68
40.182	42.787	318.68
56.747	44.118	320.85
124.01	16.847	212.17
134.719	58.133	223.17
320.719	38.996	18.84
260.474	44.869	124.62
352.147	40.4	329.29
310.466	9.526	41.73

Table I. List of Euler orientations associated with the 13 abnormal
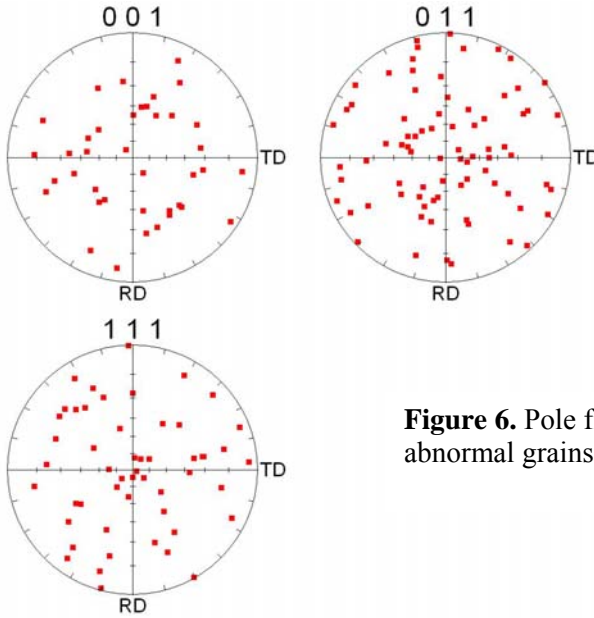
Figure 6. Pole figures associated with the 13 abnormal grains.

A follow-up investigation focused on the misorientation distribution between each abnormal grain and its neighboring grains. The misorientations were found to be random high angle misorientations based on the misorientations obtained for the 13 abnormal grains and their neighboring grains. The misorientations of all grains were plotted in Rodrigues space to visually determine if any clustering patterns were evident. In addition, a random or uniform

misorientation distribution was generated in Rodrigues space. Comparison of figures 7 and 8 indicates a random misorientation distribution between the abnormal grains and their adjacent neighbors. Given that the orientations and misorientations do not exhibit special texture relationships, it appears AGG must be triggered by other means.
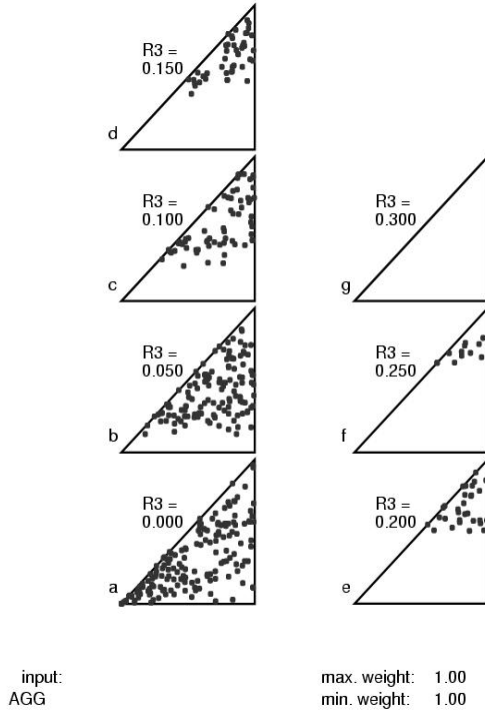
Figure 7. Misorientation distribution for 443 grains surrounding the abnormal grains.
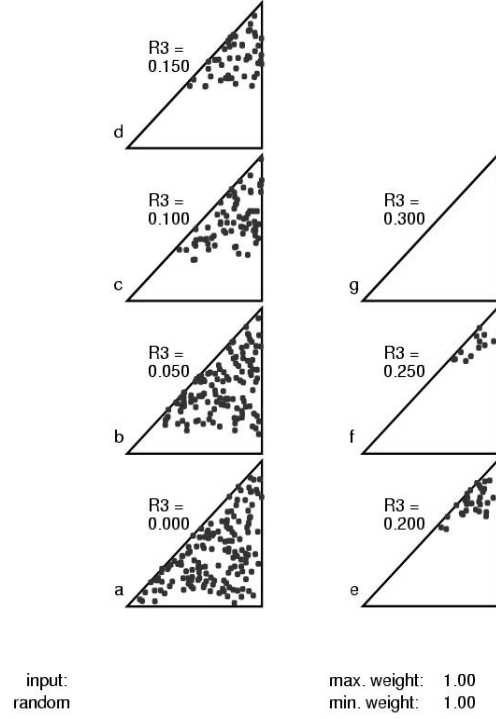
Figure 8. A uniform of random distribution of 443 misorientations in Rodrigues space.

3.3. Grain Growth Cessation

A comparison between the observed limiting grain size and the predicted limiting grain size provides additional evidence for the utility of the Zener equation.

In the original work, it was suggested that the limiting grain size is the spherical equivalent diameter. By measuring the mean intercept length of the abnormal grain microstructure (1100°C/2wk), there is no assumption about grain shape or geometry and a stereological relationship exists to relate to the spherical equivalent diameter [174] where

$$D_{sphere} = \frac{3}{2}\lambda$$

116

The mean intercept length was found to be 430μm ± 55μm which results in a spherical grain diameter of 645μm. Next, the predicted value can be obtained based on the measured particle characteristics of the as-received microstucture. To refresh, Zener's equation is given as

$$D_L = K \frac{r}{f}.$$

A prediction can be obtained using r =1.2, f =0.002, and K = 4/3 . D_L is found to be 800μm. A difference of 150μm is observed between the measured and predicted values. Zener's equation over-estimates the limiting grain size, but this result has been observed in both experiment and simulation [2] where the K value ranges from 0.17 to approximately 1.0. In a recent study of Zener pinning, an alloy of similar composition was examined. This alloy had a 0.02wt%C, which reduces the volume fraction of carbides and increases the maximum attainable grain size. The researchers predicted a size of 1610μm and subsequently measured a 1250μm grain size [private communication]. For both nickel alloys, the original Zener estimate is much larger than the observed grain size and provides additional evidence that Zener's equation is an over-estimation for most cases.

Though the limiting grain size was obtained from a non-uniform microstructure, there is no evidence that suggests the Zener equation is valid only for normal grain growth. This can be further explained by the fact that Zener's equation merely predicts an average limiting grain size and does not in any way address the manner in which the microstructure evolves from a small grain size to a pinned configuration.

3.4. Texture

OIM was used to characterize the texture. In order to obtain a statistical representative sampling of orientation distributions per specimen, numerous scans were obtained and the results were combined into one large dataset. On the other hand, misorientation distributions had to be calculated on a per scan basis and combined with an averaging scheme. The experimental results obtained from samples up to 1 hour exhibited a near random texture. Minor sharpening occurred as a consequence of the decrease in the number of discrete orientations during grain growth. Figure 9 confirms an initially random
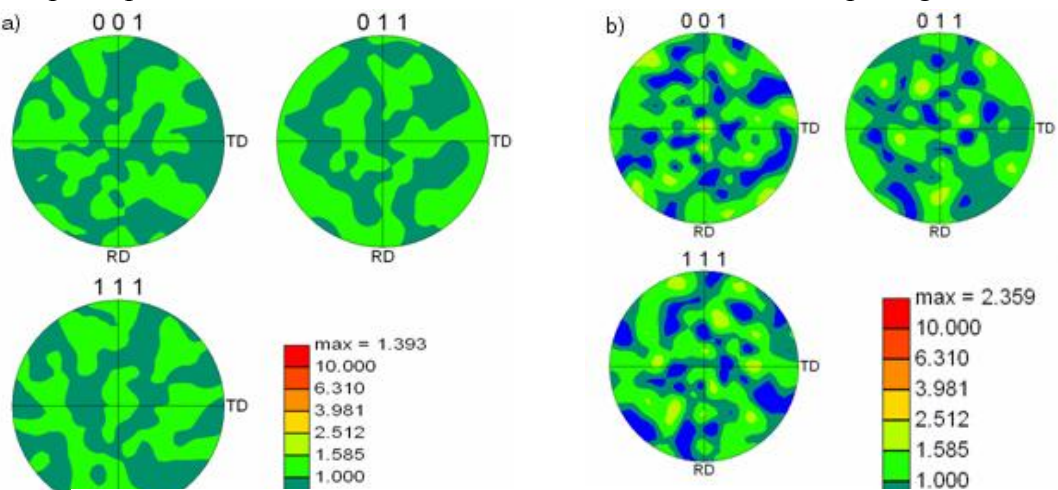
Figure 9. Pole figures a) as-received b) 1100°C/1h.

texture with a slight change in the annealed sample. Pole figures were obtained for other samples, all of which exhibited similar results. Additionally, the OIM provides microstructure maps of the scan area. Figure 10 is a representative sample of the as-received microstructure. When the orientation from point to point varies by more than 5°, it is considered a grain boundary. Both images represent the exact same area, but the major difference is that twin boundaries have been excluded.
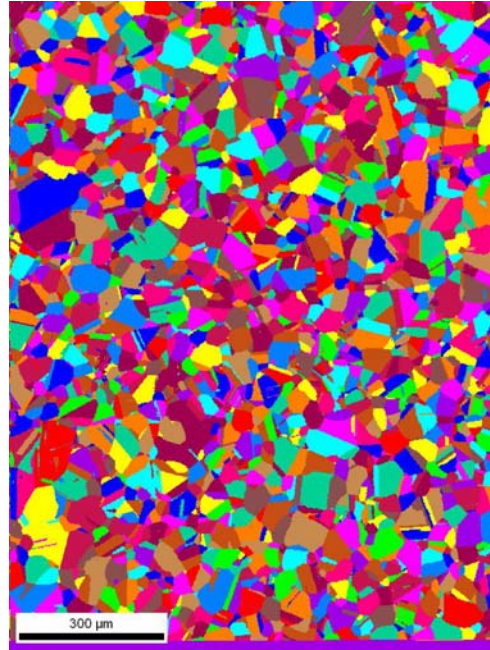
Figure 10. OIM grain map of the nickel alloy. Includes Σ3 boundaries.

The grain boundary texture or misorientation distribution should be analyzed even though the grain texture is random. The nickel alloy has a large fraction of Σ3 boundaries, which are defined as a 60° <111> axis angle pair. The misorientation distribution is given in figure 11 which includes and excludes the special boundaries. If these boundaries are removed from the data set, a near random (Mackenzie) distribution is obtained. The fraction of the Σ3 boundaries is approximately 40% of all boundary types. A subset of the Σ3 fraction is a special arrangement called coherent twins. These boundaries are distinguished by their straight boundaries as shown in the previous figure.
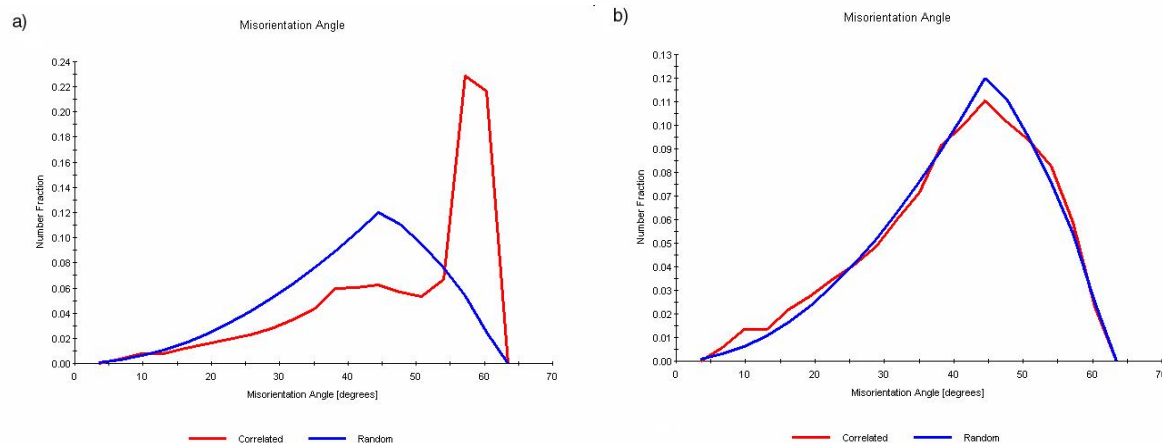
Figure 11. Misorientation distribution of as-received Waspaloy a) including Σ3 boundaries b) excluding Σ3 boundaries

As grain growth proceeds, grain boundaries intersect particles and may become pinned, permanently or temporarily. An overlooked correlation is to quantify the relationship between particles and specific grain boundaries. This distribution of particles with respect to the grain boundaries was obtained through a combined SEM and OIM image registration. The fraction of particles on boundaries versus the bulk was computed while a novel distribution involving particles-grain boundary misorientations was obtained through the image registration procedure [3].

The relationship between carbide locations with respect to the internal grain boundaries was investigated. The expected value was based on a random spatial distribution of mono-sized, spherical carbides. With these assumptions, the observed numb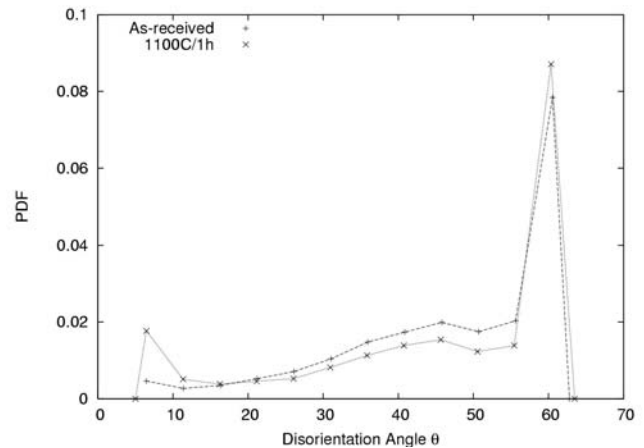er fraction on boundaries (N_{gb}/N_{total}) was significantly higher than the expected fraction for both the as-received and the 1100°C/1h samples. Furthermore, the expected and observed number fractions both decreased with grain growth due to the reduction of grain boundary area per unit volume. In this regard, the carbide size and volume fractions remained constant during heat treatment within the limits of error, thus confirming that the particles were essentially inert during the 1 hour anneal. Pole figures and orientation distributions derived from the EBSD data indicated a near random texture in the as-received material. Inasmuch as the number of grains decreased during grain growth, the minor sharpening in texture evident for the 1100°C/1h sample can be ascribed to poorer sampling statistics.

The as-received grain misorientation distribution function (MDF) exhibited a large, broad peak at 60° and a relatively small peak at relatively low angles (Figure 12). This behavior contrasts with the Mackenzie distribution for a randomly-textured material. By contrast, the strong peak was consistent with the presence of a large number of Σ3 type boundaries. The PMDF would be expected to be exactly the same as the MDF if the Zener assumption of random intersections between boundaries and particles were to apply; however, the observed behavior indicated a different situation. This implies that a large fraction of carbides would be expected to be found on boundaries with the most prevalent misorientation, 60°. However, Figure 13 reveals that the PMDF with its much weaker peak at 60° deviated markedly from the MDF for the as-received material.

Figure 12. Misorientation distribution a) as-received b) 1100°C/1h.

After grain growth during the 1100°C annealing treatment, EBSD and carbide measurements revealed that the PMDF had evolved to become very similar to the MDF. The shapes of both functions were similar, and the intensity at 60° was similar in the two distributions. However, secondary peaks remained in the PMDF at smaller angles. This evolution could be explained in terms of sweeping grain boundaries and the reduction in the number of grains during the heat treatment. These preliminary results suggest

that the PMDF and MDF are highly correlated once the system reaches a lower-energy configuration.

Figure 13. Particle-associated misorientation distribution.
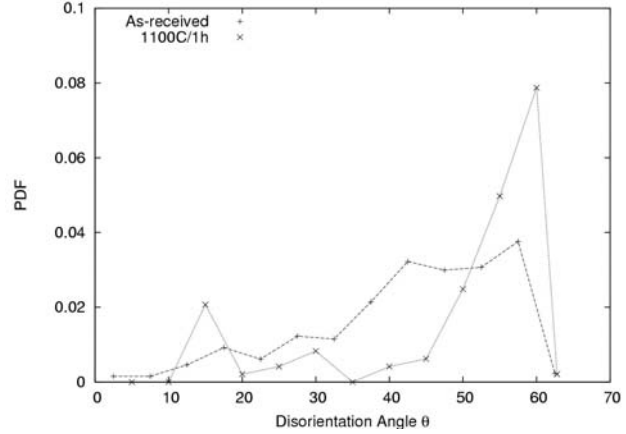
3.5. Computational Results

The study the interaction of particles with grain boundaries and the overall effect on the cessation of grain growth was accomplished by generating microstructures with inert particles and using the parallel Potts-based Monte Carlo model to simulate grain growth. We recall that Zener's equation is given in its general form as:

$$D_L = K \frac{r}{f}$$

where D_L is the limiting grain size, K is a constant, r is the mean particle radius, f is the volume fraction, and m is the volume fraction exponent. This equation is the focal point for the discussion in this section.

The monosized particles were inserted into the microstructure randomly. The particles were not allowed to grow or shrink (i.e. inert) and do not move from their original lattice sites. This is consistent with Zener's original assumptions.

Both isotropic and anisotropic grain boundary energy scenarios were employed.
The pinning of grain boundaries in a Monte Carlo simulation requires a large number of time steps. To reach this point in time, each simulation is run to 1,000,000 Monte Carlo steps to ensure that the boundaries were physically pinned on the particles. Standard personal computers are not suitable for these simulations; therefore, simulations were conducted on massively parallel computers at the Pittsburgh Supercomputing Center and the Aeronautical Systems Center in order to complete a 10^6 step simulation in a reasonable period of time.
Simulations with 0.02, 0.04, 0.06, 0.08, and 0.10 volume fractions of inert precipitates were run using isotropic and anisotropic grain boundary properties.

3.6. Anisotropic Grain Growth Simulations

The average growth kinetics (grain size versus time) from the anisotropic and isotropic simulations were examined and are shown in figure 14. The growth rate of the microstructure

120

appears to be very similar regardless of boundary properties. The lack of anisotropy is a result of the driving and drag pressures being proportionally dependent on the grain boundary energy (γ). That is, the drag pressure exerted by particles is proportional to ($c_1 r\gamma$/area)

Area and the driving pressure is proportional to κ wherein each pressure exhibits a linear dependence on grain boundary energy ($\gamma\kappa$). For a low angle boundary with a small energy, both the drag and driving pressures are proportionally decreased. Therefore, the effect of grain boundary energy anisotropy is cancelled out to the first order and explains the similar behaviors in the isotropic and anisotropic simulations.
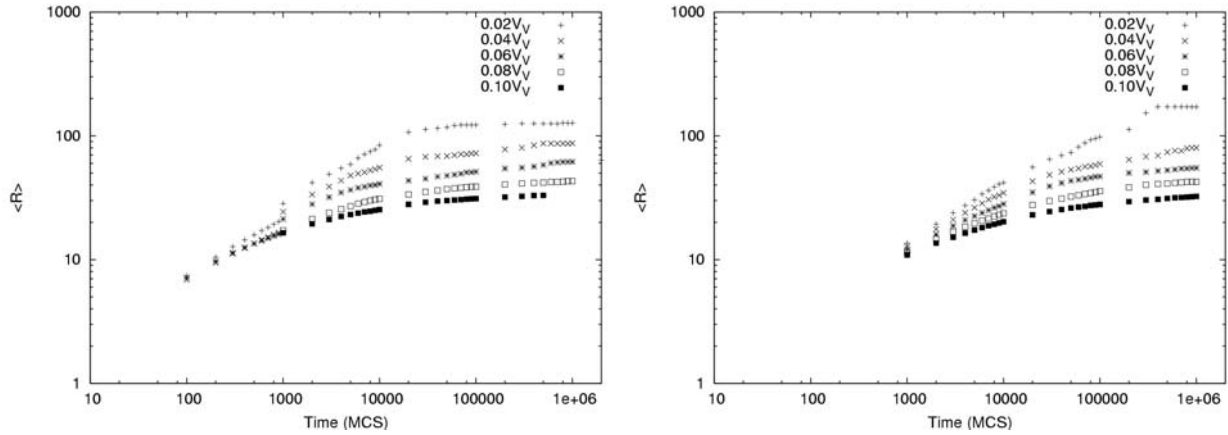
Figure 14. Average grain growth kinetics for a) anisotropic and b) isotropic grain boundary properties.

As the average grain size increases, the driving pressure becomes smaller (i.e. $\kappa=1/D$). At a certain stage, the drag pressure becomes similar in magnitude to the driving pressure. The reduction in mean growth rate followed by growth stagnation (i.e. asymptote) can be attributed to the equilibrium condition $P_Z = P_{GG}$. It is worth mentioning that a pinned configuration (i.e. $dr/dt = 0.0$) is unattainable in the simulation due to the fluctuations induced by the non-zero lattice temperature which accounts for the very slow logarithmic growth at late times [103].

The change in grain size levels off after a certain period of time and the time required to reach the asymptote is dependent on the volume fraction of particles. The kinetics do not adhere to the parabolic grain growth law as is the case for the single phase simulations.

Referring to Zener's original equation, one can examine the power law dependence of the pinned grain size on the volume fraction. Experimental evidence suggests that the volume fraction exponent is on the order of unity, which is identical to Zener's original derivation. Figure 15 shows agreement among Zener, simulation, and experiment where the exponent is assumed to be $m = 1.0$. However, the constant K appears to be less than 4/3, contrary to Zener's equation. The average K value is 1.10 and 1.09 for the anisotropic and isotropic cases, respectively. Upon comparison with the experimental literature, one finds this value to be much higher than K=0.17 for the data shown by Manohar [2].
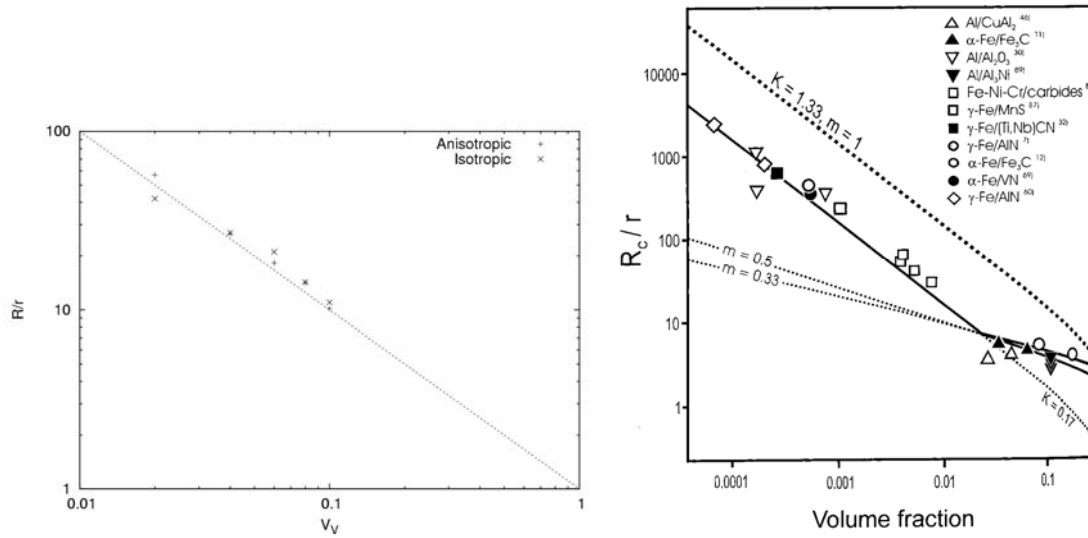
Figure 15. Logarithmic plot of grain to particle size versus volume fraction
a) simulation results b) compiled experimental results.

The "K" deviation could be a result of alloy composition and initial texture. Nevertheless, particle size, shape, and spatial distributions may affect grain growth stagnation. Furthermore, the particles were randomly distributed within the modeling domain. Certain processing techniques inherently lead to distributions which are heterogeneously dispersed and may include some alignment with a sample reference axis. The best examples involve rolled aluminum plates where the precipitates occur in isolated bands along the rolling direction. Likewise, even random spatial distributions may yield non-random correlations with other internal points of reference. In the case of Waspaloy, the frequency of 60° boundaries is significantly higher than the random Mackenzie distribution, and the particle distribution on grain boundaries is undoubtedly non-random. Even so, the particle distribution does not match the grain boundary distribution until the microstructure evolves towards a more stable configuration. Therefore, it is of interest to vary the particle spatial and grain boundary distributions to evaluate its impact on boundary stagnation and how the distributions vary during annealing.

3.7. Non-random Particle Distributions and Zener Pinning

A systematic investigation was conducted to examine the effect of V_V, D, and non-random particle placement on boundaries where table II provides a breakdown of the combinations of the three main parameters that were investigated and is explained by an example. The volume fractions were not smaller than $0.04V_V$ due to the sparse number of grains in the microstructure after coarsening. The fraction on boundaries is given as a number fraction since all particles are cubic with a 27 voxel volume. For example, a 0.04 V_V of particles in a 400^3

| R_0	V_V	Fraction on GB
7.6	0.004	0.3
11.7	0.06	0.5
15.2	0.08	0.7
18.4		
21.5		
24		

Table II. Microstructure configurations for simulated grain growth experiment.

122

domain is equivalent to approximately 94,800 cubic particles. 30%, 50%, or 70% of the 94,800 particles will be placed explicitly on the grain boundaries.

The initial distribution of particles on grain boundaries was pre-selected as given in table II.

Figure 16 is a collection of data points for various simulations wherein the initial fraction of particles on grain boundaries ranged from 30% to 70%. The data points exhibit a range of limiting grain sizes for each volume fraction, but this range is quite limited. An inverse function, f(x)= 3/x, appears to fit the simulation data very well and indicates the volume fraction exponent is 1.0 and the constant, K, is approximately 1.0. Based on the small deviations at each volume fraction, the initial fraction of particles on boundaries does not appear to significantly influence the limiting grain size until the volume fraction decreases to 0.04 V_V.
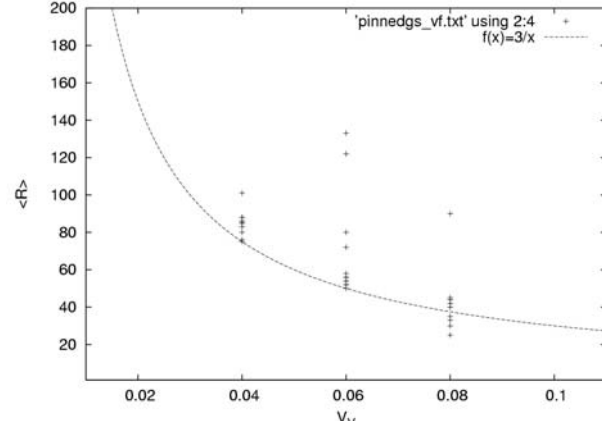
Figure 16. Limiting grain size as a function of volume fraction for initial distributions where 30%, 50%, and 70% of the particles are situated on grain boundaries.

A few of the data points lay well above the f(x) curve. Analysis of the micrographs as various time intervals revealed abnormally large grains. The grain size distributions provide additional confirmation that an initially uniform grain size distribution eventually changes to a bimodal distribution typically indicative of abnormal grain growth AGG. The non-random distribution of particles may be the source of AGG and it occurs over a number of simulations where the initial grain size is in the range $15.2 \leq R_0 \leq 18.4$.

The growth kinetics were compared to examine the significance of the initial grain sizes and particle placement on the form of the growth rate. Figure 17 shows the variation in the growth rate trends for (0.04V_V, 0.70% on boundaries) microstructures as a function of initial grain size (R_0). Interestingly, the microstructures with a larger initial grain size exhibit a delay before the grain growth rate increases to a maximum in contrast to the smaller R_0 microstructures. This behavior must be due to the smaller driving pressure since the driving pressure is inversely related to the grain size and the large density of particles on the boundaries.
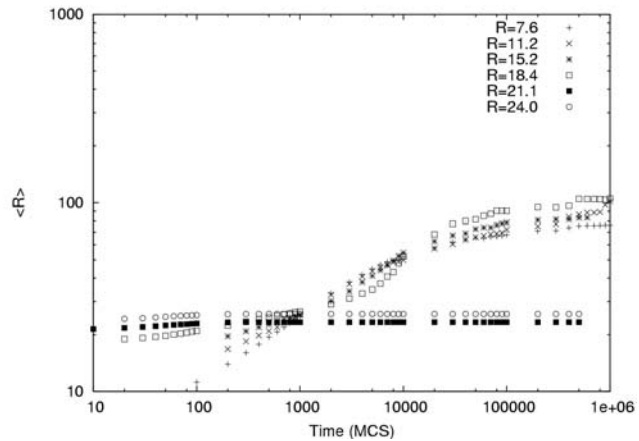
Figure 17. Average growth kinetics as a function of initial grain size using 0.04V_V and 70% of particles on boundaries

123

Additionally, instances of abnormal grain growth were reported. Figure 18 is a compilation of growth rates at a $0.06V_V$ of particles and two different initial boundary fractions, namely 30% and 70%. In each graph, there are three types of behaviors present:
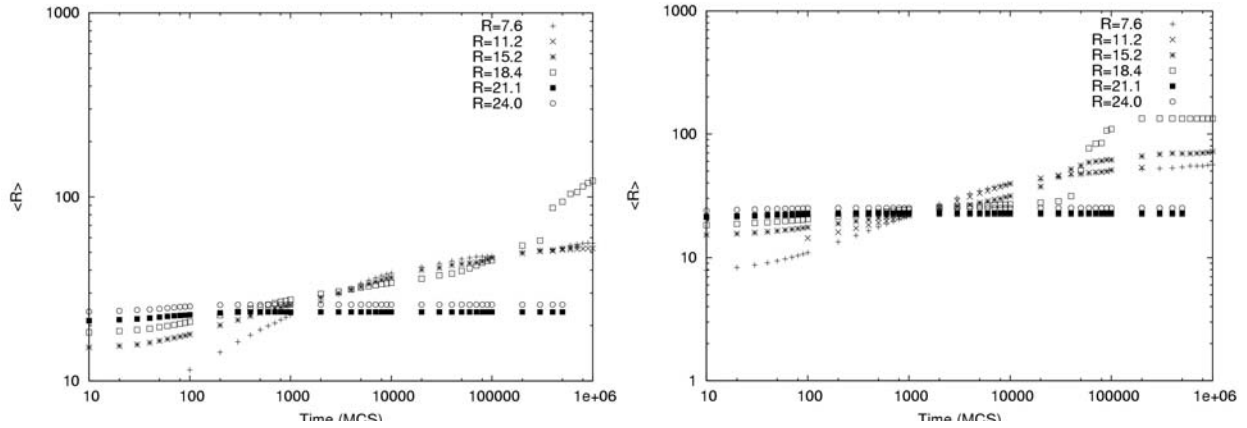
Figure 18. Average growth kinetics as a function of initial grain size using $0.06V_V$ and a) 30% of particles on boundaries. b) 70% of particles on boundaries.

(1) No growth as indicated by curves with no slope (2) normal grain growth and stagnation (3) normal grain growth and abnormal grain growth. The pinned microstructures were a result of the large grain size (small driving pressure) and the large volume fractions of particles. The low fractions on boundaries (30%) were sufficient in exerting a drag pressure that was equal to or greater than the driving pressure. The normal grain growth and subsequent pinning are similar to the results obtained for random particle distributions (see figure 14). The third scenario, which included NGG and AGG, appears to have two regions of growth. The first stage appears to be normal grain growth and what appears to be a cessation in growth, followed by a large increase in mean
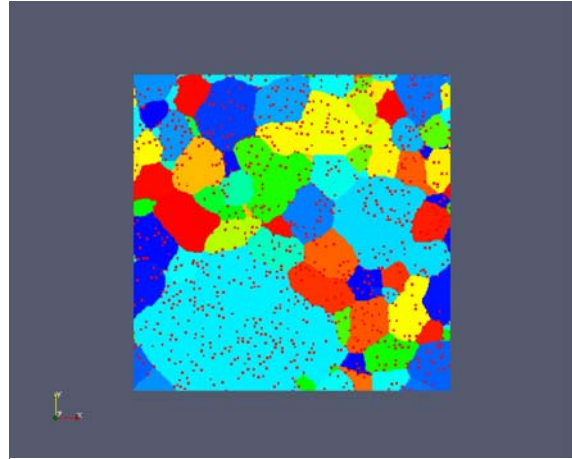
Figure 19. Grain size distribution of a digital microstructure that has undergone abnormal grain growth.

grain size. The grain size distribution indicates that a transition occurs from NGG to AGG at late times (Figure 19) and a cross-sectional micrograph, figure 20, illustrates the presence of a rogue grain.

Figure 20. A micrograph which illustrates the abnormal grain.

124
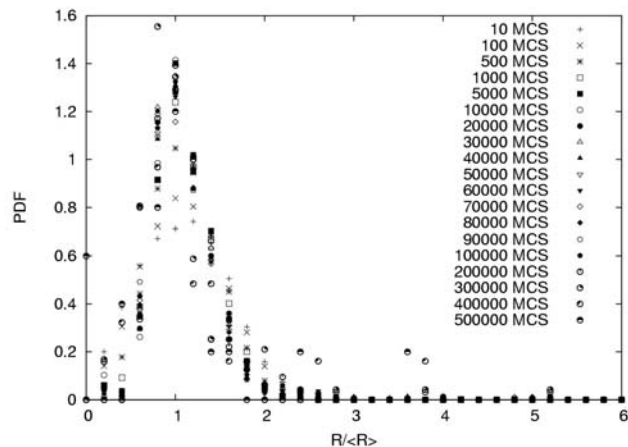
A number density such as N_A or N_S is of interest since the particles on boundaries contribute to the lowering of the system's total energy and is intimately related to the original Zener equation derivation. The number density per unit area boundary is essentially a combination of the number of particles on the grain boundaries and the grain boundary area. Measuring the concurrent changes in these two quantities will provide an indication of the constancy of N_S; however, it is more useful to calculate the number density of particles per unit area boundary. From a energy standpoint, the reduction in the excess free energy is dependent on the grain boundary area replaced by the particles. Measurement of the removed area would provide an estimate of the drag pressure assuming the grain boundary area is known. However, calculating this quantity is not straightforward. The removed boundary area is not equivalent to the surface area or interfacial area between the particle and grain boundary. The quantity is a planar value and difficult to measure in complexly shaped particles.

Consider a spherical particle and a grain boundary. As the boundary sweeps through the particle, the eliminated boundary area is of the form πr^2. On the contrary, consider a particle with concave and convex surfaces and a grain boundary. Attempting to measure the eliminated grain boundary area is much more involved without an analytical description of the area.

In a digital microstructure, one can approximate this quantity by first measuring the "effective" grain boundary area, which is the area between grain boundaries only. Next, permit the microstructure to consume the particle sites and measure the new grain boundary area. The difference of these two areal quantities is approximately the total grain boundary area eliminated by all the particles on grain boundaries. Thus, the number of particles per unit boundary, N_S, would be equal to the number of particles divided by the effective grain boundary area.

On the other hand, a metallurgist would measure the entire grain boundary trace on a two dimensional cross section, including the particle-boundary lengths. This is a consequence of the sample preparation where the particles are chemically attacked in order to delineate the grain boundaries. Another approach using orientation imaging microscopy could provide a better measurement of the grain boundary trace since the specimen must be ground and polished, but this approach is limited by both the resolution of the equipment and the size of the precipitates.

Since this research was a joint experimental and computational study, the measurement of grain boundary area will be taken to be combination of both the effective grain boundary area and particle-removed boundary area (i.e. equivalent to a metallurgical approach).

During the course of grain growth, it was observed that the fraction of particles on grain boundaries varied substantially during grain growth. In this same timeframe, the total grain boundary area decreased continuously. With both quantities decreasing, the rates of decrease will dictate how the particle number per unit area boundary evolves with time.

On certain occasions, when the fraction on grain boundaries and total grain boundary area decrease at the "same" rates, the number density per unit area boundary should be nearly constant as is observed. It asymptotes towards a value similar to the initial value once the grains

have reached the limiting grain size. An example of this case is presented in figure 21. Other simulations showed results where the initial and final N_S quantities were significantly different.

Though N_S, the number of particles per unit area boundary, fluctuates during grain growth, it is interesting to compare against N_A, the number of particles per unit area as was discussed earlier.

Using an initial structure with an average grain size of 7.6 pixels, particles were randomly inserted into the equiaxed microstructure and the ratio, N_S/N_A, were estimated using the two-dimensional quantities, N^{gb}_L and N_L. The results give in figure 22 indicate that N_S is larger than N_A for a random spatial distribution of particles. The extremely large ratios at low volume fractions ($V_V < 0.01$) are presumably a result of low numbers of particles per test plane. The measurement of N_L by dropping random test lines, will result in many instances where no intersections are recorded on a plane. The major point is the number fraction per unit area boundary is not equivalent to the number fraction per unit area, $N_S \neq N_A$.
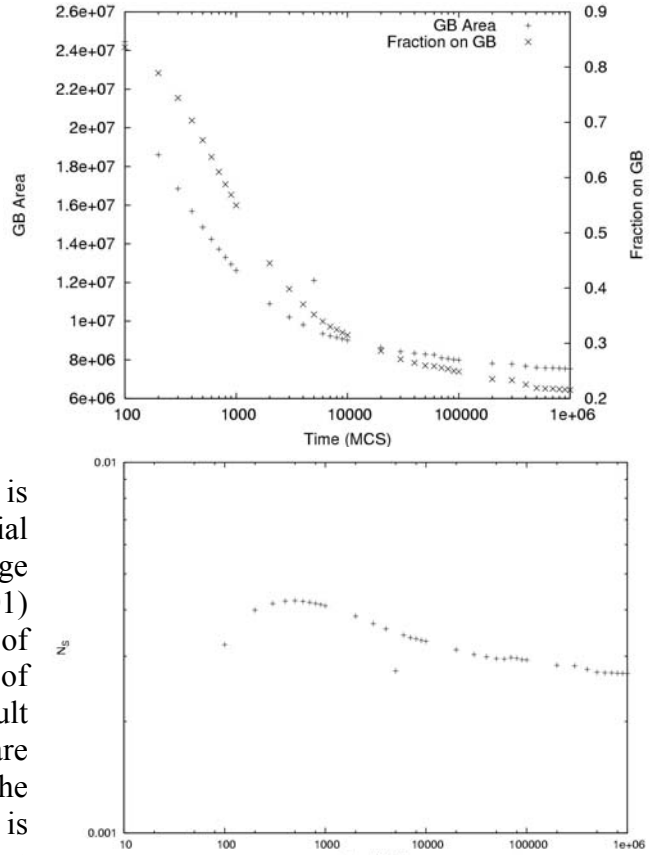
Figure 21. a) Grain boundary area and particle fraction on grain boundaries b) Number of particles per unit area boundary.
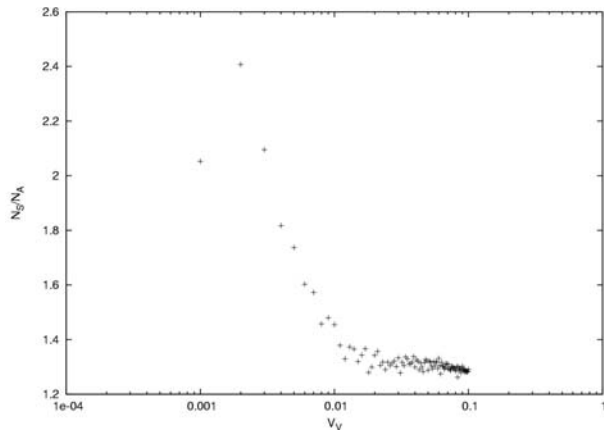
Figure 22. Ratio of N_S/N_A for a random spatial distribution of particles.
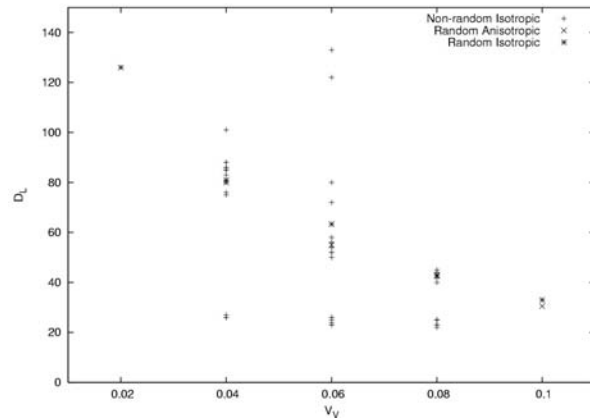
Figure 23. Limiting grain size for the simulations.

Finally, it was interesting to amass the pinned grain size data points onto a single plot. The following graph is based on data with i) isotropic grain boundary properties and random particle injection ii) anisotropic grain boundary properties (i.e. grain boundary energy) and random particle injection, and iii) isotropic grain boundary properties and non-random particle injection with respect to the grain boundaries. Figure 23 illustrates the lack of an effect of the anisotropic grain boundary energy and the locations of particles with respect to the grain boundaries. The data points in the vicinity of 25 pixels were based on a microstructure with a large initial grain size wherein the boundaries were pinned at t=0 and no growth occurred for the duration of the simulation.

Finally, the change in the misorientation distribution was measured for a series of simulations. Actually, this quantity should be referred to as an isotropic MDF because this set of simulations was conducted using isotropic grain boundary properties as a result of the large number of grains and corresponding misorientations. Even though the algorithm is parallel, each processor is required to dynamically allocate an energy array of size Q^2 where Q is the number of grains in the microstructure. At large Q values, the individual processors do not have sufficient random access memory (RAM) to allocate the array. A hash table or an equivalent C++ map is necessary to examine anisotropy in domains with a large number of unique grains (Q>10,000).

The initial microstructures contained a large 60° peak. During grain growth, the magnitude of this peak decreases due to the elimination of boundaries with 60° misorientation angles and is evident in four cases with different initial grain sizes (Figure 24). The MDF migrates towards a random misorientation distribution and was observed in the anisotropic grain growth simulations without particles. As the initial grain size increased, the rate of change in the MDF diminished. This effect can be correlated with the grain growth kinetics wherein the growth rate was reduced as the initial grain size increased.
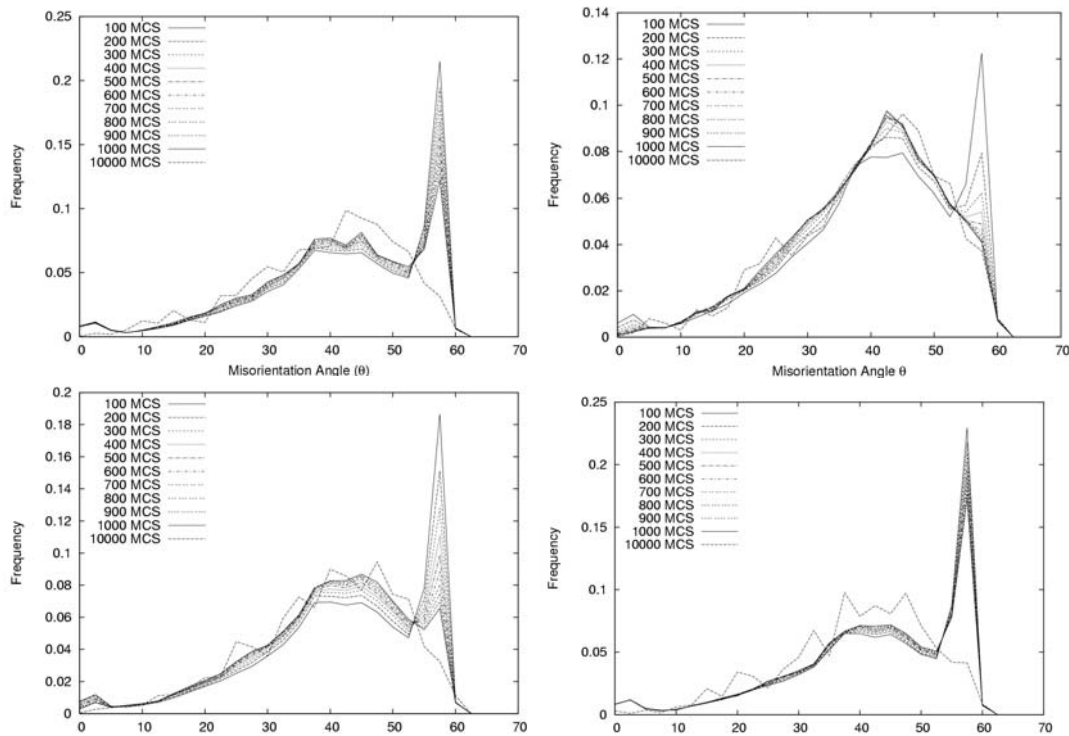
Figure 24. Misorientation distribution (MDF) as a function of time for a 0.04V_V and 30% of particles on grain boundaries   a) R_0= 7.6   b) R_0= 11.2   c) R_0= 15.2   d) R_0= 18.4

4. Discussion

4.1. Grain Growth

In the preceding sections, the microstructure evolution was examined both experimentally and computationally. The computational study focused on variable isolation in order to explain specific behaviors observed in the nickel alloy during annealing to provide partial validation of the model.

Since the annealing experiments were performed at a temperature above the γ' solvus, the nickel alloy could be treated as a 2 component system: matrix and secondary precipitates. With this simplification, the parallel Monte Carlo code was an appropriate choice for modeling grain growth.

First, the grain growth kinetics were compared and it suggests the initial stage of growth can be reproduced in simulation for a specific configuration. After a sufficient amount of grain growth and commensurate decrease in the driving pressure, the growth rate decreases and reaches a limiting grain size. Though the average grain size in the Waspaloy increased by a factor of 2.5-3.0, a similar change was not observed in the simulations and was commonly found to be greater than three times the initial grain size.

The grain size distributions were found to be lognormal and self-similar in both microstructures. In the experimental system, this trend was valid up to one hour of annealing at 1100°C. This observation of grain uniformity was consistent with the visual inspection of the micrographs in both cases.

However, the sharpness of the distribution in the computer simulations resulted in an under-estimate of the larger grains in the microstructure in contrast to the Waspaloy grain size distribution. This point is very important because the texture analysis of the abnormal grains (ODF and MDF) suggests the abnormal grains do not possess an energy or mobility advantage. If the texture does not contribute to the AGG phenomenon, then it could be promoted by large grains in the initial microstructure $(D > 2D_{AVE})$ and/or the precipitates.

In the experimental work, a transition to abnormal grain growth occurred when the sample was annealed at 1100°C for a period exceeding 2 hours. Given the lack of data, it is not possible to definite the exact time. The Waspaloy grain growth curve can be partitioned into two distinct regions: (I) normal grain growth and (II) abnormal grain growth.

Though the simulation does not replicate the experimental trends, a number of important observations have been made. The transition from NGG to AGG was apparent in the <R> versus MCS plots where the curve exhibits the largest slope (i.e. mean growth rate). Second, the abnormal grain growth was limited to the microstructures with larger initial grain sizes, namely R=15.2 and R=18.4. These microstructures have a driving pressure on the order of 1.5-2.0 times smaller than the other microstructures. Additionally, the effective driving pressure $(P_{GG} > P_{Zener})$ is further reduced by the presence of particles on grain boundaries; hence, a longer "incubation" time is observed before a noticeable change in grain size occurs.

An area-weighted grain size distribution GSD was necessary to observe deviations from the unimodal distribution in the experimental alloy, yet in the simulations, a number-weighted GSD exhibited signs of abnormal grains at three times the mean grain size. Regardless, the number and area weighted grain size distributions permit the presence of abnormally large grains in a microstructure to be detected.

It was observed that the initial grain size distributions from the AGG simulations were sharply peaked and log normal. The largest grain size was not more than 2.5<R>. Since the grain boundary properties were isotropic, texture cannot be the source of abnormal grain growth.

In the isotropic Zener simulations with a random distribution of particles in space and on grain boundaries, no instances of AGG were observed. In addition, the grain size distributions were sharply peaked with no grain larger than 2.5<R> as was the case in the other simulations.
Since the only difference between the two simulation studies is the non-random distribution of particles with respect to the grain boundaries, AGG appears to be caused by the non-random particle placement must be a result of either a grain size advantage or non-random particle placement.

4.2. Texture Development

In the experimental work, the orientation and misorientation distributions sharpened slightly, which is expected given the number of possible orientations (grains) decreased during grain growth. The misorientation distribution appears to have a minor increase in the 60° peak in the MDF and is a combination of coherent and incoherent $\Sigma 3$ boundaries. To verify the change in the peak, a program was used to measure the lengths of coherent $\Sigma 3$, incoherent $\Sigma 3$, and random grain boundaries 1. The results are provided in figure 25 and clearly show an increase in the total $\Sigma 3$ population. During grain growth, the length fraction of incoherent boundaries increase while the length fraction of coherent or "twin" boundaries decreases. Since the total length fraction of both coherent and incoherent twin boundaries has increased, the sharpening of the 60° peak in the MDF is not an artifact.
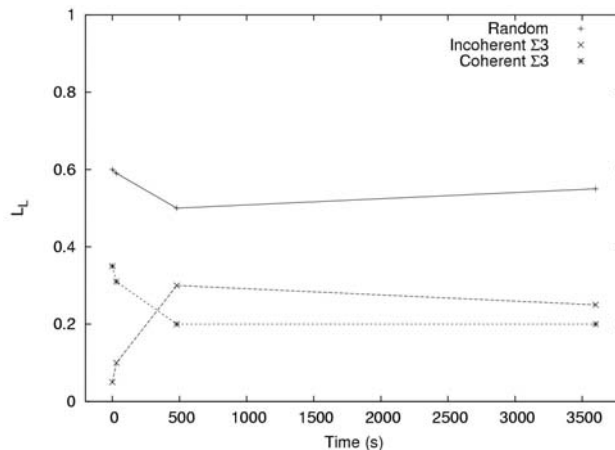
Figure 25. Fluctuations in the length fractions of $\Sigma 3$ type boundaries.

It was of interest to measure the grain boundary misorientations where particles were situated to determine if specific grain boundaries contained higher fractions of particles than random. A stereological analysis [4] of the number fraction of carbides on grain boundaries revealed significant differences between the expected and observed values for the as-received and annealed specimen (1100°C/1h/WQ), indicating a non-random distribution of carbides with

respect to the grain boundaries. However, the system appeared to migrate towards a random distribution with respect to the grain boundaries due to coarsening of the microstructure. The PMDF had two peaks at approximately 15° and 30° with low densities around them, which was different from the MDF. Differences in the two functions could be a result of sparse statistics after grain growth has occurred.

The single phase grain growth simulations revealed that the grain growth kinetics of a random texture do not vary much from the isotropic case. Both the orientation and misorientation distributions do not evolve significantly from their initial values.

On the other hand, the two-phase simulations showed that an initially large fraction of Σ3 boundaries would evolve towards the MacKenzie (random) distribution; however, these simulations used an isotropic energy function where the grain boundary energy is 1.0 for all misorientations. To determine how the anisotropic energy function (i.e. Read-Schockley) would affect the MDF evolution, a microstructure was generated with a smaller number of grains, random orientation texture, and a large fraction of incoherent Σ3 boundaries. Grain growth was simulated for a period of 10,000 MCS and figure 26 is the MDF result.
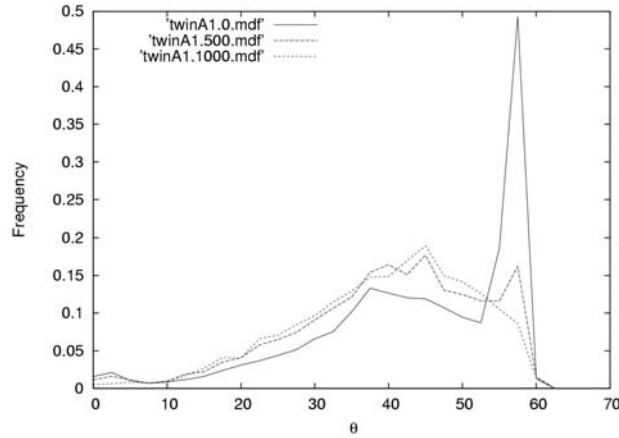
Figure 26. Evolution of misorientation distribution with a Read-Schockley energy function.

It is apparent that the 60° peak decreases, which is similar to the behavior observed in isotropic energy simulations. These results imply the Read- Shockley energy function does not adequately describe the texture evolution observed in the nickel alloy. Therefore, a 3 parameter description of the energy function may be a better treatment, which offers the capability to test both axes and angles that correspond to special configurations (e.g. Σ3, Σ5). All the Σ3 boundaries were incoherent in the digital microstructures even though the Waspaloy had a mixture of both coherent and incoherent boundaries.

The Zener equation has been examined many times and attempts have been made to improve upon the original derivation [2, 5, 6, 7, 8, 9]. The generic form is

$$D_L = K \frac{r}{f}$$

where D_L is the limiting grain size, K is a constant, r is the particle radius, and f is the volume fraction, and m is the volume fraction exponent.

4.3. Volume Fraction Dependence

Researcher have argued that the exponent, m, is a constant value within certain ranges of volume fractions where it can vary from 1.3 to 1 [10 5, 2]. In most cases, the arguments center on specific placement of particles (i.e. triple junctions) or large volume fractions where the assumption of random spacing is not valid and one must consider the mean random spacing or edge-to- edge distances between particles.

In the research, the accumulated simulation results on the limiting grain size suggest that the limiting grain is inversely proportional to the volume fraction. Figure 15 is a logarithmic plot wherein the data points fall very close to line with m equal to 1.0. Based on these simulation results, the volume fraction exponent is 1.0 for the volume fraction range $0.01 < V_V < 0.10$.

4.4. Size and Shape Distribution

Zener assumed a mono-sized dispersion of spheres where r was the spherical radius. In dispersion strengthened alloys, the shapes and sizes vary; therefore, r is the "average" particle radius. Moreover, the estimated values are commonly based on cross-sectional measurements and the average values obtained are less than the three-dimensional quantities. For example, the circular-equivalent radius is a factor of 4 less than the equivalent spherical radius [11]. In addition, there is an inherent assumption on the shape and most often is taken as a sphere.
In spite of this evidence, stereology offers a method for circumventing the problem by relaxing the dependence on shape. Thus, the Zener equation could be rewritten as

$$D_L = K \frac{s}{f}$$

where s is equivalent to an average linear measurement of the particle size.
It has been suggested that the mean intercept length, λ, could be a suitable replacement with the constant of proportionality being absorbed into the K term.

For low volume fractions ($V_V < 0.10$), the constant term is the source of the variability between predictions and observations. Based on the experimental data accumulated by Manohar [98], the K value should be on the order of 0.17, a factor of 7.5 less than Zener's estimate. Provided the limiting grain size has been shown to fall well beneath the Zener estimate, there is reason to re-examine the K value.

The use of this alternative approach using stereological descriptions that relax the assumptions on size and shape is not easily extended to Monte Carlo. The main issue arises from the fact that boundaries and particles vary in morphology and the representation of complex shapes on a discrete grid is not adequate. For example, a sphere is comprised of a number of steps and ledges on a discrete grid. Another grid such as a finite element mesh would be a better format which can, in turn, provide a better approximation of area or linear trace measurements.

4.5. Surface Density

The number of particles per unit area boundary was compared against the number of particles per unit area in order to evaluate the relationship: $N_S = N_A$. The original derivation assumed the relationship held without any justification.

A computational study has found the particle fraction per unit boundary to be greater than the number fraction per unit area by a factor of 1.3 for grain sizes where $V_V > 0.01$. To clarify this point, if one counts the number of particles on grain boundaries and divides by the grain boundary area and compares this quantity to the number of particles on a plane divided by the cross-sectional area, the ratio is greater than unity. Note that the microstructure was equiaxed and particles were uniformly distributed within the domain of the digital microstructure. This might suggest a larger disparity in microstructures where the particles exhibit a non-random correlation with the grain boundaries.

With the number density of particles being larger than random, the pinning pressure is greater than random; therefore, the pinned grain size is a smaller value than that predicted by Zener's original equation. A majority of simulation and experimental results agree with this statement. Furthermore, N_S was found to vary as a function of time during grain growth in the simulations. In some cases when grain growth ceased, the surface density was nearly-equivalent to the initial value; yet, other cases have shown large differences between the initial and final quantities. These observations suggest that N_S should be of the form, $N_S(t)$; however, an experimental study would be appropriate to verify at least one of the observed trends.

A closely related quantity to N_S was investigated in an attempt to more clearly explain the PMDF behavior. The number of particles on boundaries (n_{gb}/n_{total}) was measured during the evaluation of the particle-associated misorientation distributions in the nickel alloy. An as-received and 1100°C/1h samples had shown the number fraction on boundaries to be higher than random, but the significance of this term with respect to Zener pinning was not known.

Using the PMC simulation model, the initial number fractions varied from 30%, 50%, and 70%. During the course of the grain growth simulations, (n_{gb}/n_{total}), varied markedly where this quantity eventually decreased after grain growth. It is intuitive that the total number of particles on grain boundaries will be less than the number of particles on boundaries in the initial microstructure where the grains are much finer. This type of measurement alone does not appear to be a critical component of Zener pinning; therefore, the prediction of the limiting grain size does not require one to measure the number fraction of particles, but the number of particles per unit area boundary is necessary for an accurate estimate of the drag pressure.

5. Conclusions

It was shown that the nickel alloy evolved by normal grain growth, but at long annealing times, transitioned to abnormal grain growth. A slight sharpening in texture was observed due to the reduction in the number of orientations as a result of grain coarsening and shrinking. The

transition from NGG to AGG was not influenced by crystallographic orientation relationships and implies either an initial grain size advantage and/or non-random precipitate spatial distribution to be the cause.

The particle-grain boundary distribution or PMDF exhibited a non-random correlation with grain boundary types. During the annealing heat treatment, grain growth reduced this non-random dependence to a distribution similar to the grain MDF, which would be equivalent to a random particle-boundary distribution.

The observed limiting grain size was found to be less than the predicted value, but consistent with other experimental findings. The over-estimation by Zener' equation may be attributed to the inter-particle spacing. In addition, the number of particles per unit area of grain boundary is not equivalent to the number of particles per unit area and invalidates Zener's original assumption $N_S = N_A$. In addition, N_S is not constant but varies with time.

The simulation modeled grain growth in the presence of inert precipitates to resemble grain growth in the nickel alloy. In the presence of a random spatial distribution of particles, anisotropic grain boundary properties did not significantly alter the grain growth kinetic nor the Zener limited grain size.

Predicted and observed limiting grain sizes did not agree while the volume fraction exponent was found to be unity (i.e. m=1). By systematically varying the initial fraction of particles on grain boundaries, the simulation results showed that the non-random boundary placement did not noticeably affect the limiting grain size.

6. Recommendations

- Experimentally, measure the variation in N_S, the number of particles per unit area boundary, during isothermal anneals where sufficient grain growth occurs. Both low and high volume fractions of precipitates would be useful since it is not known if a critical threshold exists where N_S does not behave similarly for low and high volume fractions

- Examine the applicability and practicality of a stereological parameter such as S_V or L_A as a replacement for the particle spherical radius since the stereological descriptors mentioned are not affected by the shapes of the particles. Given that most experimental analyses are performed on two-dimensional cross-sections, it is necessary to examine the relationship $(4/\pi)L_A = S_V$ and how accurately L_A can estimate the three-dimensional quantity, S_V .

- Since the current study indicated that abnormal grain growth was not caused by special orientation relationships (i.e. texture), a systematic investigation of variable spatial distributions of particles on grain pinning and initiation of abnormal grain growth is recommended to understand the significance of particle locations on the transition to AGG.

133

- Confirm the validity of this analysis be investigating grain size control (via particle pinning) in another alloy system.

7. References

[1] V. Seetharaman and S.L. Semiatin. Analysis of grain growth in a two-phase gamma titanium aluminide alloy. Metallurgical and Materials Transactions A, 28:947, 1997.

[2] P.A. Manohar, M. Ferry, and T. Chandra. Five decades of the Zener equation. ISIJ International, 38(9):913{924, 1998.

[3] C.G. Roberts, S.L. Semiatin, and A.D. Rollett. Particle associated misorientation distribution in a nickel-base alloy. to be published, 2007.

[4] E.E. Underwood. Quantitative Stereology. Addison Wesley Publishing, Reading, Massachusetts, 1971.

[5] E. Nes, N. Ryum, and O. Hunderi. On the Zener drag. Acta Metallurgica et Materialia, 33(1):11{22, 1985.

[6] Y. Liu and B.R. Patterson. Stereological analysis of zener pinning. Acta Materialia, 44(11):4327{4335, 1996.

[7] M. Hillert. Inhibition of grain growth by second-phase particles. Acta Metallurgica, 36(12):3177{3181, 1988.

[8] R.D. Doherty. Role of interfaces in kinetics of internal shape changes. Metal Science, 16:1{13, 1982.

[9] N. Ryum, O. Hunderi, and E. Nes. On grain boundary drag from second phase particles. Scripta Metallurgica, 17:1281{1283, 1983.

[10] C.H. Worner and P.M. Hazzeldine. An analytical model for two-dimensional Zener drag. Scripta Metallurgica, 28:337{342, 1993.

[11] J.C. Russ. Practical Stereology. Plenum Press, New York, 1986.

8. Names of Personnel

Anthony Rollett (CMU Faculty Member)
Lee Semiatin (AFRL/RX Mentor)
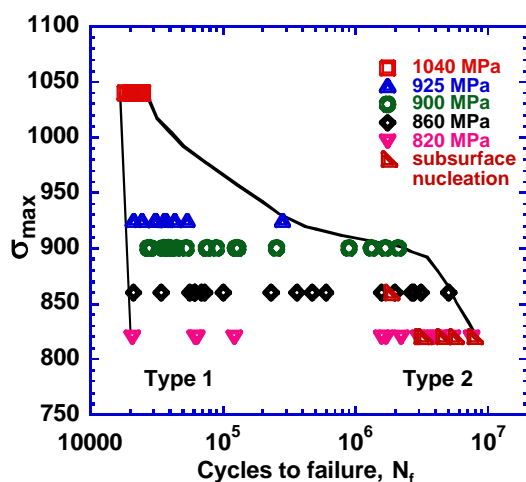Christopher Roberts (CMU Graduate Student)

Task 7

Development of Microstructurally-Based Models for the Prediction of the Fatigue Response in Ti Alloys. *Hamish Fraser (OSU Faculty Member), Michael Mills (OSU Faculty Member), Jim Larsen (AFRL/RX Mentor), Andy Rosenberger (AFRL/RX Mentor), Alison Polasik (OSU Graduate Student)*

I. RESULTS and DISCUSSION

1. Introduction

Titanium alloys have a wide range of applications in the aerospace industry, and fatigue is often the primary failure mechanism for aircraft engine components [1]. The ability to accurately predict the lifetime of components in service would reap significant cost savings for the aerospace industry. On then other hand, the ability to predict the fatigue lifetimes is hampered due to the extraordinary variability in fatigue lifetimes exhibited in this alloy depending on the stress, temperature and environment and most importantly the microstructure. Several studies [2,3,4] have shown a distinct separation of a set of nominally identical samples from a given alloy into two populations on the S-N plot, where for a given stress two distinct ranges of lifetimes are observed. In the past, this increase in variability in lifetimes at low stresses has been attributed to distinctions between surface and sub-surface crack initiation mechanisms [5.6]. Recently, the authors who have observed a similar bimodal distribution of fatigue life cycles in Ti-6Al-2Sn-4Zr-6Mo [6] alloy have offered a different explanation for the variability. In their study, the authors have separated the fatigue test samples into two groups, as shown in Figure 1. Samples that have low fatigue life ($N_f < 10^5$) are said to be controlled by crack growth mechanism (Type I) and those have high fatigue lifetime ($N_f = \sim 10^5$-10^6) are dominated by crack initiation mechanism (Type II). In other words, a major portion of the fatigue life in the latter samples is dependent on crack nucleation. However, the significant increase in the number of cycles spent in the nucleation regime has not yet been linked to any microstructural difference between the two seemingly identical sample populations. On the other hand, when the microstructure was differentiated by choosing between the disk material and pancake, there was no difference in fatigue behavior in Type I regime, but in the Type II regime the pancake forged material performed better [7]. Although the authors in this study strongly suggest that the microstructure playes a crucial role in the differences seen in type II regime, no detailed characterization of the microstructure is provided in this study. These results are particularly interesting because the separation of the samples into two populations at lower stresses suggests the possibility of extending the operational life by suitable modification to the microstructure in the alloy.

Figure 1. Fatigue life variability in Ti-6246 Alloy

With regard to modification of the microstructure, thermo-mechanical processing of α/β titanium alloys can deliver variations in the microstructure, which in turn has a profound impact on their mechanical properties [8-12]. However, a strong inter-relationship exists between the individual microstructural parameters seen in these alloys, so that it is often impossible to use traditional experimental methods to look at the effect of a single microstructural parameter on mechanical properties. Thus, although the potential for improving and tailoring these alloys for specific applications is significant and potentially rewarding, a thorough understanding of the role of microstructural features on the fatigue properties is still lacking. Much of the understanding regarding the effect of each microstructural parameter in α/β titanium alloys on the different fatigue properties have already been summarized in a number of different reviews [1,8-12] To date, the understanding of microstructure-property relationships in titanium alloys is primarily qualitative. A limited number of studies in (α+β) Titanium alloys which have attempted to correlate the fatigue lifetime to the microstructure [2-3,13-15]. These studies have indicated that decreasing feature sizes namely, globular α grain size in the case of α/β processed alloy and, lamellar colony size in β-processed alloy have a positive effect on the mean life times at low stresses [3,14-15]. While it has been known that the crack initiation accounts for a major portion of fatigue life, especially at low stresses, these studies are mostly qualitative or semi-quantitative at best. Apart from this, there have been no systematic studies on the effect of individual microstructural features on fatigue properties. Especially, the mechanisms that dictate the fatigue variability are poorly understood.

The focus of this effort is the identification and development of phenomenological and physics based models for the prediction of microstructure/property relationships in α/β Ti alloys, where the properties of interest are fatigue lifetime, LCF and da/dN. The development of microstructure-based models is not been straightforward. It is necessary to adopt an approach that permits the identification of the microstructural feature that influence fatigue properties, and subsequently the functional dependencies of these properties on the features so that predictive models may be developed. Such an approach requires the creation and analysis of databases that relate properties, processing (e.g., details of heat-treatments), microstructural features, compositional data and orientation factors (e.g., the presence and distributions of micro-textures). While many of the required elements for such a database exist either in the open literature or with our partnering companies, the microstructural details are largely not available. Hence, the production of a suitable database is a primary objective of this task, requiring the exploitation of heat-treatments designed to effect variations in the microstructure, in both α and α/β processed conditions. The microstructure was quantitatively characterized using a rigorous set of stereological procedures that have been developed in CAMM. Sub-scale test samples were machined from the heat-treated materials, and the fatigue lifetimes were established at various stress levels Following this, predictive models and functional dependencies were developed based on rule based fuzzy logic neural network (FNN) approach.

2. Methods and Procedures

2.1. Processing and preparations

Unless otherwise mentioned, all of the material investigated and described in this document is Ti-6Al-4V alloy. The specimens were sectioned from pancake forgings provided by Timet® in

either the β-forged or the α/β-forged condition. Chemical analysis using ICP-OES as well as a Leco Corporation TC600 oxygen/nitrogen analyzer verified consistency of the alloy composition between the two forgings.

Cylinders measuring approximately 1.27 cm by 10.2 cm (0.5 by 4 inches) were sectioned from these forgings by Jett Industries Inc using wire EDM. This was done to facilitate the application of additional thermal processing on the individual cylinders to generate microstructurally distinct sets of samples in order to study the role of microstructure on fatigue in this alloy system. These sample sets are labeled A, B, C and D and the details of forging history and heat treatments for each set are listed in Table 1.

**Table 1.** Alloy processing and HT parameters

Sample	Processing Parameters	Heat Treatment Step 1	Heat Treatment Step 2
A	Forged at 1032°C, 40% strain	none	none
B	Forged at 1032°C, 40% strain	1020°C for 3 min, Cool at 0.33°C/sec to RT	none
C	Forged at 968°C, 40% strain	925°C for 20 min, WQ	880°C for 60 min, WQ
D	Forged at 968°C, 40% strain	925°C for 10 min, AC	none

2.2. Heat Treatment and Sample Sets

Sample set A consists of samples that have not undergone additional processing, and thus is also referred to as the "as-forged" microstructure. Based on the initial fatigue testing results from sample set A or SSA (discussed below in the results section) it was determined that investigating the effects of a larger colony size would be the most advantageous, and thus the specimens in SSB were treated to form large colonies. The heat treatment procedures for SSB were performed using the Gleeble 3800. Specimens in both SSC and SSD conditions come from an α/β-forging and had a mixture of globular α and transformed β grains in the microstructure. Further details on the specifics are presented in the results section of the subtask. All heat treatments for SSC were performed using a drop furnace back-filled with Argon gas to minimize potential oxygen uptake into the material. For SSD, the specimens were heat treated to produce a higher volume fraction of primary α with no secondary α. The heat treatment for SSD samples was also performed in Ar atmosphere followed by cooling was done in laboratory air. Surface oxidation was not an issue in the heated samples since a significant amount (more than half the diameter) was removed in the gage section of the dogbone specimens during the final machining step at Bitec Inc. During the final processing steps, a low stress grinding method was implemented in the gage section.

2.3. Sample Preparation

Following sample machining at Bitec Inc., the fatigue test samples were carefully electropolished on the gage sections at WPAFB in order to minimize the surface roughness and to remove any residual stresses on the surface of the specimens Based on the calibration for the low stress grinding method supplied by Bitec, the residual stresses on the surface of the electropolished samples are expected to be than 10 ksi. A diagram of the specimen geometry used for all conventional fatigue tests can be seen in Figure 2.
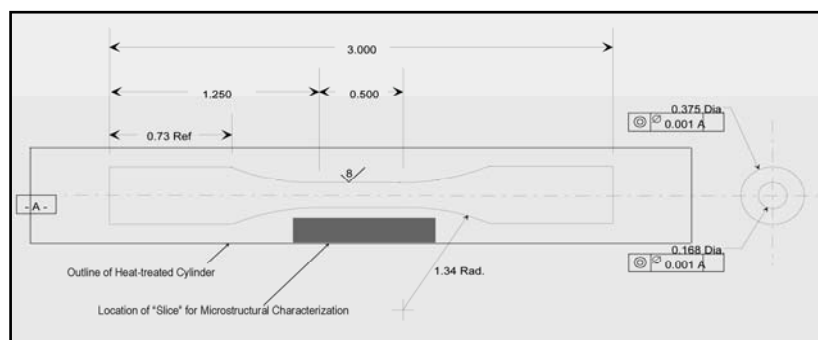
Figure 2. Fatigue specimen geometry

Metallographic specimens were ground and polished to a 0.05µm finish using colloidal silica. Stereological characterization was performed on these slices using optical and SEM methods. Specimens were also etched in Kroll's reagent for 15-25 seconds to reveal the morphology of the prior β grains.

2.4. Fatigue Testing

S-N type fatigue testing was performed on an MTS 810 servo hydraulic test system equipped with a 458 controller. Initial tests were performed at 20Hz in tension-tension fatigue under load-control conditions at room temperature and in a laboratory air environment at WPAFB. A load ratio of R = 0.10 was used for all tests and the number of cycles to failure was recorded primarily at 3 different stresses: 550, 600, and 675 MPa. In order to best duplicate the testing conditions which demonstrated the bimodal distribution in lifetimes in the Ti-6246 alloy [6], the lowest test stress was chosen so as to result in lifetimes on the order of 10^6 cycles. Based on comparisons with fatigue data in literature for lamellar Ti-6Al-4V alloys [16-19], it was determined that this range would likely correspond to stresses of about 550MPa. Additionally, tests were also done at 150Hz using an MTS 831.10 system at OSU in load control and at room temperature. On the other hand, all replicas were taken on samples tested using the 831.10 machine at 150 Hz

In order to more effectively analyze the role that microstructure plays in fatigue lifetime variation, emphasis was placed on the HCF behavior of each specimen set because the variation in the number of cycles to failure is much greater at low stresses. Additionally, because a bimodal distribution of lifetimes has been seen in Ti-6246 for average lifetimes on the order of 10^6 cycles, testing a significant number of specimens at lower stresses allowed us to determine whether a similar phenomenon might exist within the same lifetime range for any of the sample sets in our investigation. Thus, roughly 50% of the specimens in each set were tested at a stress that resulted in lifetimes on the order of $10^6 – 10^7$ cycles at R=0.1. The remaining samples were tested at higher stresses to map out the shape of the S-N curve.

2.5. Fractography, Microstructure Characterization and Stereology

Fractography was done on the failed samples using a FEI/Philips Sirion (at OSU) and a Cambridge S360FE (at WPAFB) scanning electron microscope in secondary and backscattered modes. The objective was here to establish the modes of fracture and to determine whether the cracks had nucleated on the surface of the specimen or below the surface. Quantification of areas

associated with crack nucleation was determined using Adobe Photoshop® and FoveaPro® [20]. Microstructural characterization, imaging and stereology procedures were conducted according to the procedures established by Tiley et al. [12,21]. Depending on the size, shape and distribution of the features under investigation, different instruments were used for imaging to obtain accurate and statically relevant data. For example, Clemex optical microscope was used to obtain 120-160 optical images per sample which were subsequently stitched together using Clemex software and analyzed to obtain the prior β grain size factor and volume fraction basketweave measurements. 10-12 optical images at 200X were used for each sample to measure the colony scale factor. On the other hand, SEM images were used to analyze finer features such as α lath size. Stereological measurements were done on these images obtained with help of Adobe Photoshop® and FoveaPro® and the procedures developed at OSU [12] and outlined elsewhere [21].

2.6. Fuzzy Logic Modeling

The commercial software package CubiCalc RTC® was used to develop the fuzzy logic models for this research. Five input parameters were used to generate the rules for the model: stress (MPa), colony scale factor (μm), thickness of α laths (μm), prior β grain size factor (mm-1) and volume fraction basketweave (%). The fairly large number of inputs coupled with the relatively small number of data sets made it necessary to use fewer adjectives to describe each input. Increasing the number of adjectives increases the number of rules generated, but for small datasets, many of these rules do not lead to a solution. Hence the required number of adjectives was carefully chosen depending on the size of the data set.

3. Results and Discussion

Due to the complexity of the nature of this task, the results will be presented in four distinct sections taking into consideration the nature, importance and the progression of work in this project. Additional information can also be obtained from this tasks published work [22]. In the first section a concise description of the four, microstructurally distinct set of samples tested in this task is given. Next, the results from the fatigue testing done at OSU and WPAFB are presented. The third section provides a detailed description of the stereology results and the results from the modeling efforts via fuzzy logic neural network approach. The fourth section provides a detailed account of additional microstructure characterizations such as site specific OIM, TEM analysis etc., performed to facilitate attempts to elucidate the mechanisms. Finally, a brief outline of proposed future work is given.
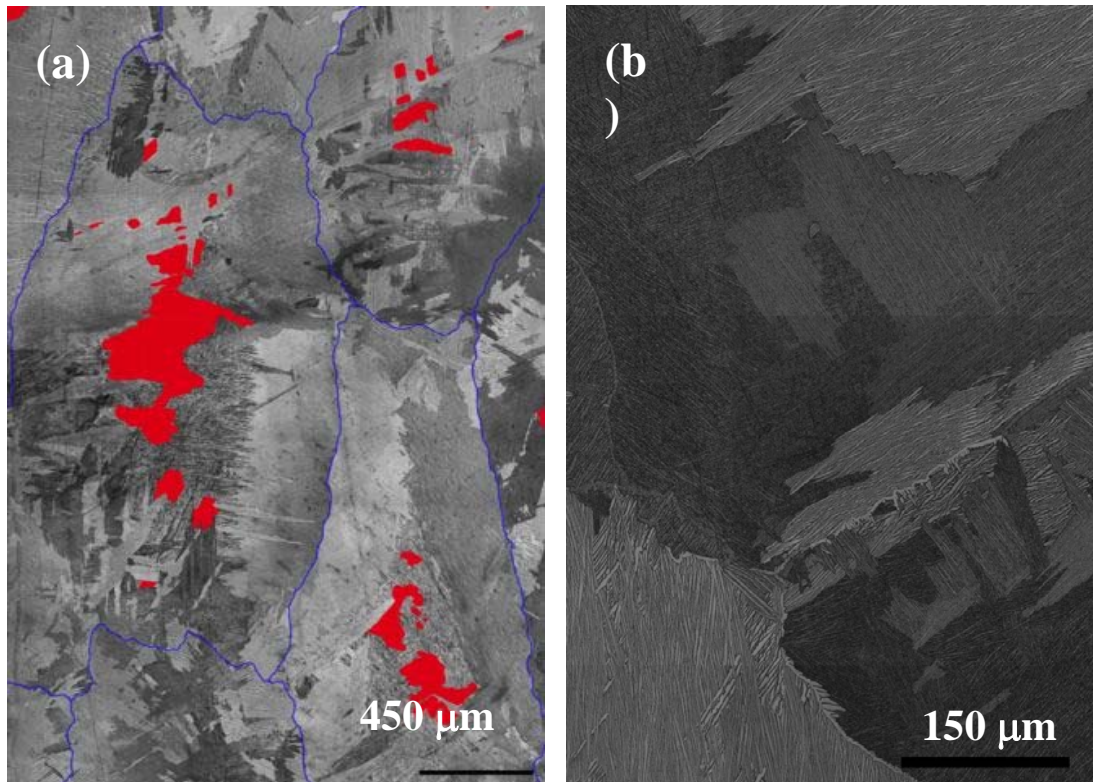
3.1. Microstructures:

SSA consists of samples that have not undergone additional processing, and thus is also referred to as the "as-forged" microstructure. Since these samples were directly extracted from the forged materials, there was an inherent variation in the microstructure, which in fact was beneficial for this effort. The general microstructure consisted of large β grains (200–2000 μm) with predominantly colony microstructure, the size later varying from being larger near the prior β grain boundary and smaller in the interior. Also observed were regions of basketweave microstructure near the center of the grains. A typical example of this microstructure is shown in Figure 3a where the prior β grain boundaries are delineated in blue color and the basket weave

microstructure can be seen painted in red in the middle of the grains. Room temperature tensile tests were performed only on this set of samples. From three separate tests average values of yield strength, ultimate tensile strength, and elongation were obtained as 807 MPa, 949 MPa and 8.5 % were obtained respectively.

Based on the initial fatigue testing results from SSA (discussed latter) it was determined that investigating the effects of a larger colony size would be the most advantageous, and thus the specimens in SSB were given an additional heat treatment above the β-transus and slow cooled to RT using the Gleeble 3800. The microstructure in this case, as shown in Figure 3b, has Specimens in both SSC and SSD come from a α/β-forging. For SSC, the samples were subjected to an initial heat treatment at 925°C for 25 minutes then air cooled, in order to adjust the volume fraction of primary α (to mimic the microstructure of Ti-6246 alloy that has been under investigation by Jha et al. [6,7]. This was followed by a second heat treatment procedure (880°C for 60 minutes followed by water quenching) to induce the formation of secondary α within the transformed β region; an identical procedure was used by Lutjering et al. to form secondary α in Ti-6Al-4V [8]. The microstructure in the end consisted of approximately 40 percent primary equiaxed α grains dispersed in the β matrix with secondary α precipitated in the β matrix.. The grain sizes of the equiaxed grains were in the range 15-30 μm. A typical microstructure is shown in Figure 3c. The tensile properties for this microstructure such as YS , UTS and elongation were determined to be 932 MPa, 1121 MPa and 13.5 % respectively.

 For SSD, the specimens were heat treated to produce a higher volume fraction of primary α but no secondary α. The heat treatment was done at 925°C, 20 minutes in Ar atmosphere followed by air cooling. A typical microstructure is shown in Figure 3d. The room temperature tensile properties for this structure are, YS 842 MPa, UTS as 935 MPa and elongation 18.5%.

Fractography was done on selected samples in the SEM. The analyses revealed that most samples exhibited surface crack initiation and in several of the samples the crack initiation sites were captured. A typical example of this from the fracture surface of an SSA sample is shown in Figure 3e. The nucleation sites are clearly visible by their lack of roughness or smooth topology as compared to the surrounding region. The areas of these regions were calculated using FoveaPro and latter used for fatigue crack growth calculations.

Figure 3. Micrographs showing typical β processed microstructures (a) SSA and (b) SSB samples
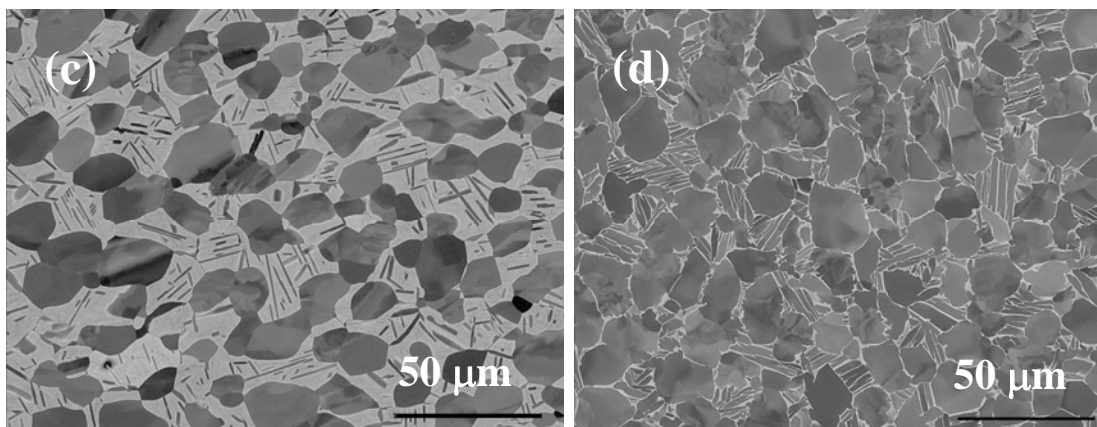
Figure 3 (contd.) Micrographs showing typical microstructures in (α+β) processed samples in (c) SSC and (d) SSD condition.
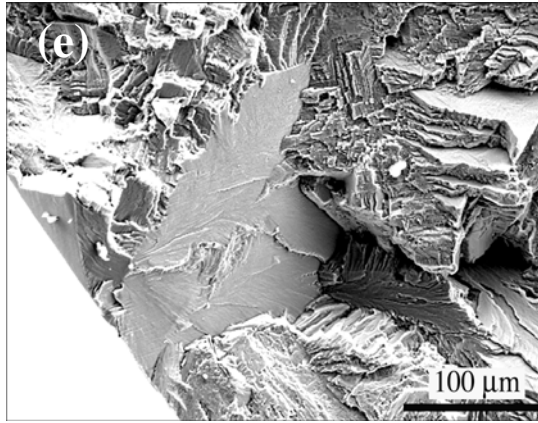
Figure 3e. Fracture surface of a β-processed
specimen shows a surface crack nucleation site.

3.2 Stereology

Stereology was performed on all tested specimens that were included in the neural network models in order to accurately quantify the microstructural features. Because of the significant differences between β-processed and α/β-processed microstructures in Ti alloys, a different set of stereology procedures was used for the β-processed specimens (SSA and SSB) than for the α/β-processed specimens (SSC and SSD).

Features that were measured for the β processed samples are listed below

    (i)   Thickness of α laths (mm)

    (ii)   Prior β grain Size Factor (mm^2/mm^3)

    (iii)   Colony Scale Factor (mm)

    (iv)   Volume Fraction Basketweave (%).

Features measured (in progress) for the α/β processed samples are

    (i)   Primary α grain size

    (ii)   Volume Fraction Primary α (%)

    (iii)   Volume Fraction Total α (%)

    (iv)   Primary α grain spacing

    (v)   Thickness of α laths (mm)

All stereology procedures were performed on high-resolution SEM or Optical images using Photoshop and FoveaPro. Much work has gone into developing the stereological procedures used in this research, and a detailed description of the procedures is outside the scope of this work. However, full description of each of the microstructural parameters measured using stereology illustrating how the parameters relate to the three-dimensional nature of the microstructure can be obtained from standards published by Tiley et al. [12,21]. A summary of individual microstructural features and the stereological results from the β-processed samples included in the neural network modeling are listed in Table 2 (shown in Section 3.4). The stereology on the (α+β) processed samples is in progress.

142

3.3. Fatigue Modeling

3.3.1. Modeling parameters

Fatigue lifetimes obtained from β-processed material have been modeled. The commercial software package CubiCalc RTC® was used to develop the fuzzy logic models. Five input parameters were used to generate the rules for the model: stress (MPa), colony scale factor (μm), thickness of α laths (μm), prior β grain size factor (mm-1) and volume fraction basketweave (%). As described above, the number of inputs was carefully chosen based on the dataset size.

The entire dataset was comprised of 26 samples. Therefore, if 2/3 of the data set was used to train the model and 1/3 was used to test it [3, 8], the accuracy of the model would be compromised because of an insufficient number of data points. Realizing that the resulting model could not be used to accurately predict fatigue life based on input parameters, the entire dataset was therefore used to train the models. In turn, the entire data set was used as inputs for the model to predict lifetimes. The goal of these modeling experiments was simply to determine whether or not any determinations could be made about the individual effect of each microstructural parameter on the lifetimes predicted by the model. It is hoped that the results from these calculations will enable a targeted approach for further research.

A large number of models were created by varying the number of adjectives used to describe each input parameter, thus changing the number and nature of rules created for the model. The same dataset was then used as the input file for the model, and the model predicted values for the lifetime of each sample based on the rules created. The error of each model was then calculated for each specimen in the dataset according to equation (1).

$$\text{error} = (\text{predicted life} - \text{actual life}) / \text{actual life}\ldots\ldots\ldots\ldots\ldots\ldots\ldots\ldots\ldots(1)$$

The errors for each model were then averaged over the calculated errors for all specimens, and the model with the lowest average error was chosen to analyze trends in microstructural parameters vs. lifetimes. Based on the results obtained using the entire dataset for 3 stresses, a second series of models was generated and tested using a reduced dataset that included only the microstructural parameters for the samples tested at 550 MPa. This obviously eliminated stress as an input variable, and improved the accuracy of the model despite the reduction in the number of data sets. The adjectives and corresponding errors for the two models chosen can be obtained elsewhere [22].
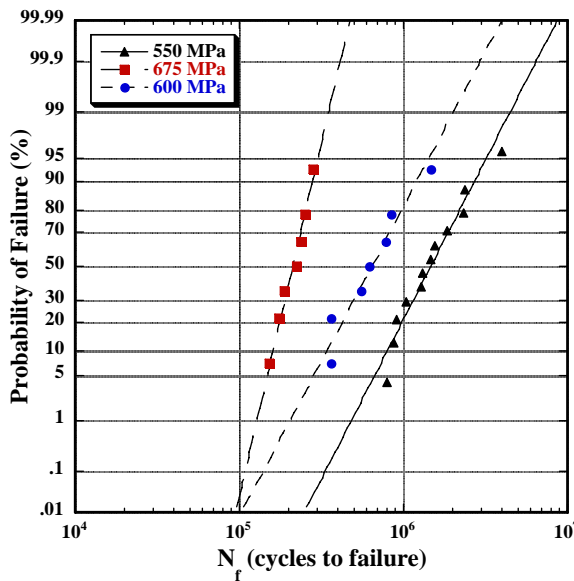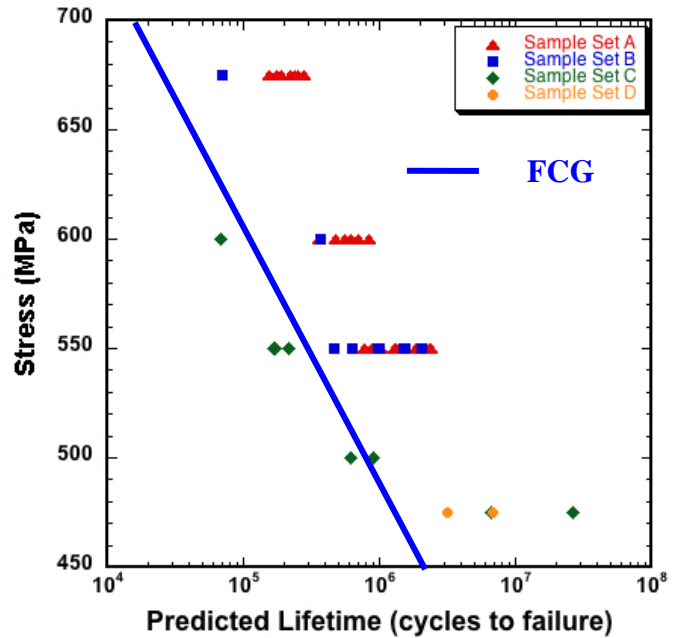
3.4. Fatigue results and Modeling

The plot of stress vs. lifetime (S-N) is shown below in Figure 4 for all the samples, both β and α/β processed, tested and included for the neural network modeling. . It is clear that the observed bimodal distribution in lifetimes at low stresses seen in α/β- processed Ti-6246 [6] was not evident for this alloy system at least in the stress range, i.e. 550-675 MPa, investigated in this study. At lower stresses, a mild separation is observable, and it is possible that if tests were run for this material at stresses below 550 MPa, the lifetime data would separate into short- and long-life samples as is seen in α/β- processed Ti-6246 [6].

Figure 4. Fatigue lifetimes versus applied stress for all samples tested.

The next few paragraphs will focus on the fatigue results and analysis from β processed SSA samples. This is followed by a new set of analyses including samples from both SSA and SSB to address the effect of differences in the microstructural features on fatigue lifetimes.

Probability plots shown in Figure 5 for the β processed SSA samples confirm the absence of a bimodal distribution in the lifetimes for this alloy system. Such a distribution is evidenced in these types of plots by a clear step, which is not seen for the present results.

Figure 5. CDF Plots for the three tested stress levels.

Using standard models for a penny-shaped crack on the surface of a specimen [23], the number of cycles required to propagate a crack of $100\mu m^2$ to failure was calculated at each of the stress levels. Tests performed on a similar β-processed Ti-6Al-4V alloy and published by R.K. Nalla et al. [23] were used for fatigue crack growth data in the calculations. The calculations for the number of cycles spent in crack growth calculated are shown by the blue line in Figure 4. It would appear that, for this material, fatigue crack growth life (FCG) provides an reasonable approximation for the minimum life. Again comparing the work here to that done by Jha et al. [6], it would seem that there are two key differences between this alloy system and the α/β-processed Ti-6246 alloy that may account for the single failure mode and

144

Table 2. Measurements from stereology of β-processed microstructure

| Measurement	Min.	Max.	Avg.	Standard Deviation
α Lath Thickness (μm)	0.272	0.421	0.347	0.04
Colony Scale Factor (μm)	20.48	34.15	25.62	3.55
Prior β Grain Size Factor (mm^2/mm^3)	0.84	3.79	2.32	0.67
Volume Fraction Basketweave (%)	1.8	35.83	12.58	8.06
Colony Scale Factor (μm)	20.48	34.15	25.62	3.55

lack of separation in lifetimes at low stresses for our alloy.

- Microstructure – The availability of equiaxed microstructural features may play role. The size scale of the microstructural features is also a consideration, as the features were much finer for the Ti-6246 alloy.

- Fatigue Lifetime Breakdown – Most of the average fatigue lifetime is spent nucleating a crack in the Ti-6246 alloy, whereas crack growth is the dominating factor in the Ti-6-4 alloy.

Table 2 outlines the results of the microstructural characterization of the samples using stereological procedures. The amount of variation in these measurements is somewhat surprising given that cursory SEM and optical imaging of the microstructure did not reveal any obvious differences in the microstructural feature sizes. This highlights the importance of being able to precisely quantify the microstructural features.
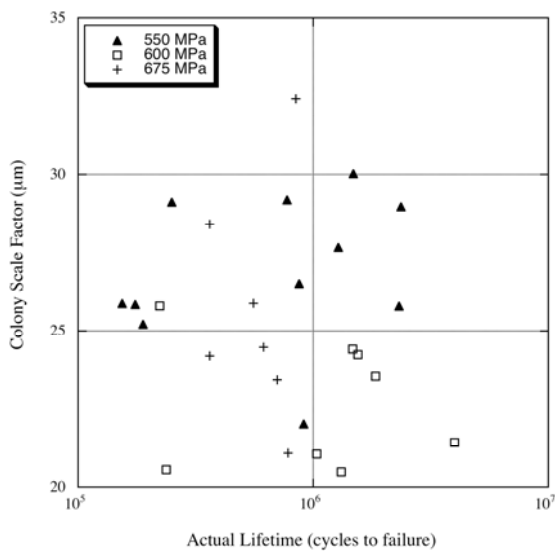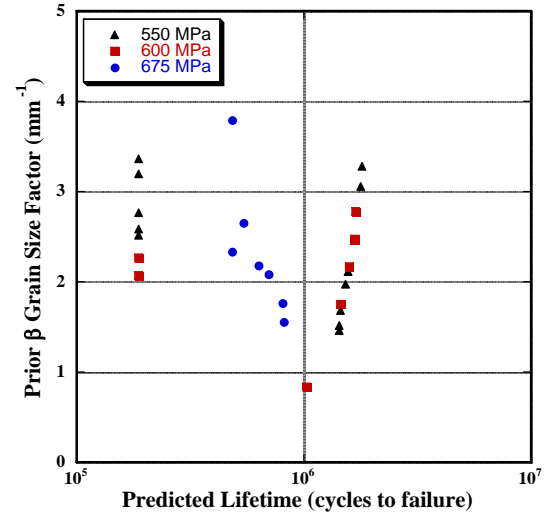

Figure 6. Colony scale factor versus. actual lifetime cycles at all stresses .
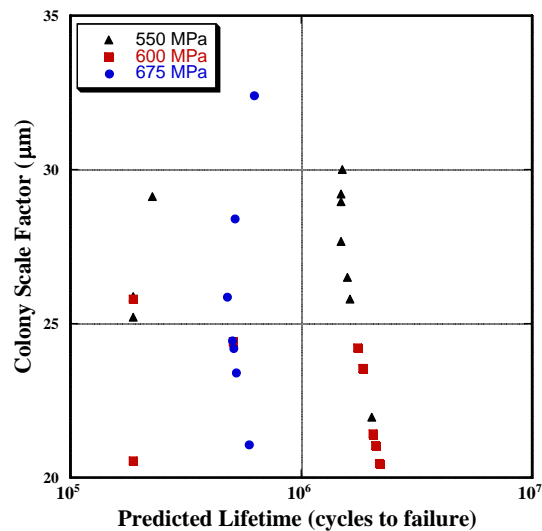
Figure 7. Colony scale factor versus Lifetime predicted by fuzzy logic models
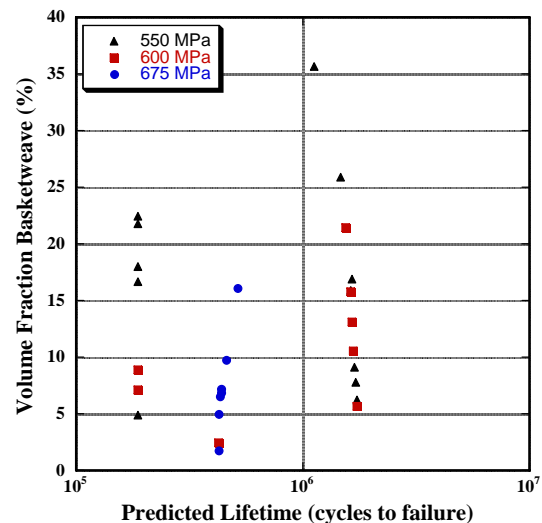
145
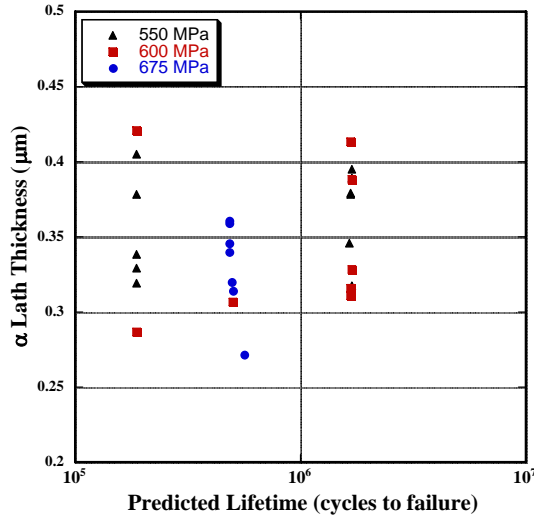
**Figure 8**. α lath thickness versus predicted lifetime; data separated by stress.

Figure 9. Prior β grain size factor versus predicted lifetime; data separated by stress.

Because of the small data set available to work with at this point, the fuzzy logic models are still subject to moderate errors. Additionally, it was possible to use a separate test set to analyze the predictive accuracy of each model. However, it is possible to look at the individual effect of each microstructural parameter. By inputting a separate dataset for each feature, where the feature in question was varied but the measurement for the other features was held constant at the mean value, trend plots of the predicted lifetime vs. the microstructural feature were generated (*see figs. 6-10*). Notice that the data points are designated by testing stress. An interesting observation can be seen when comparing figs. 6 and 7. Figure 6 shows the raw data for the actual or tested lifetime plotted as a function of the measured values for colony scale factor; thus, the actual lifetimes are also influenced by the other microstructural parameters in this plot. In Figure 7, the lifetime values predicted by the fuzzy logic model are shown as a function of colony scale factor, but in this case the other microstructural features are held constant. From these plots, it is clear that the variation in fatigue life predicted by the models was smaller than the experimentally measured lifetimes.

Figure 10. Volume fraction basketweave versus predicted lifetime; data separated by stress.

146
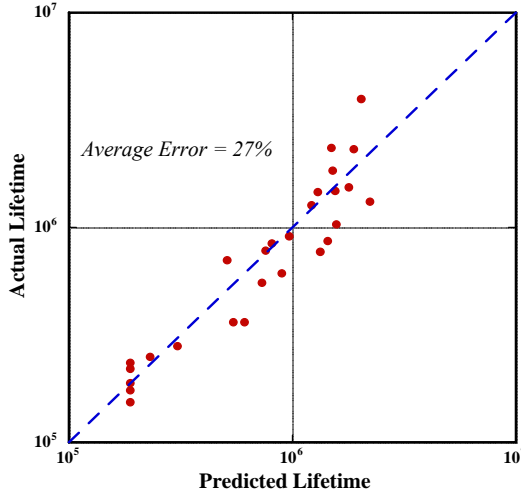
Figure 11a. Actual lifetime vs. Predicted lifetime Samples tested for all stresses.
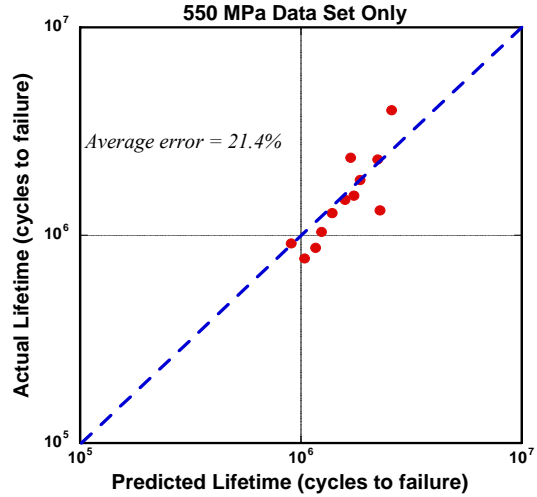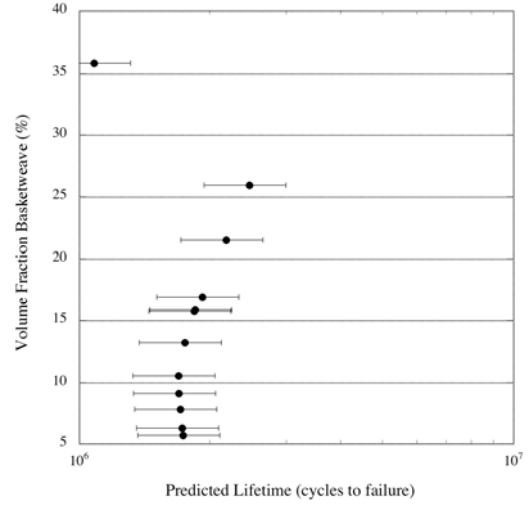
Figure 11b. Actual lifetime vs. Predicted lifetime for samples tested at 550 MPa.

It is also interesting to note that in Figures 7-10, the separation of lifetimes into 3 regions (vertically on these plots) seems to be, at least in part, a function of the different stresses tested. For each modeling experiment (*see* figs. 7-10), the specimens tested at the highest stress (675 MPa) predicted lifetime values in the middle range. From figs. 5 and 6, this effect is not nearly as clear. Additionally, the predicted lifetimes for specimens tested at 550 and 600 MPa separated into two populations with respect to lifetime when plotted as a function of an individual microstructural feature. While it is still early in this investigation to make concrete conclusions from this observation, it is believed that using stress as an input parameter into the fuzzy logic models may introduce a complexity that cannot be easily dealt with when working with a relatively small sample population. This observation led to the removal stress as an input parameter and further modeling experiments using only the 550 MPa data set. Although this resulted in less than half the original number of points to work with, the accuracy of the model was actually shown to improve from 27% error to 21.4% error. The experimental and corresponding predicted fatigue lifetimes obtained from FNN modeling is shown in Figures 11a and 11b. Stress as an input parameter was included for the modeling results shown in Figure 11a but excluded in Figure 11b.

Selected plots for predicted lifetime vs. microstructural parameter for the specimens tested at 550 MPa are shown in Figures 12-14. Trends in microstructural parameter vs. lifetime are more easily seen in these plots. In Figure 14, the trend between colony scale factor and predicted lifetime is clear and indicates that increasing the colony size tends to decrease the lifetime. This supports the observation that colonies tend to serve as the smallest resolvable crack nucleation sites. By comparing Figures 14 and 15, it is again easy to visuzalize the usefulness of the fuzzy logic modeling method. The model has evaluated the independent effect of colony scale factor on lifetime at a given stress, and is able to better rationalize the raw data shown in Figure 15.
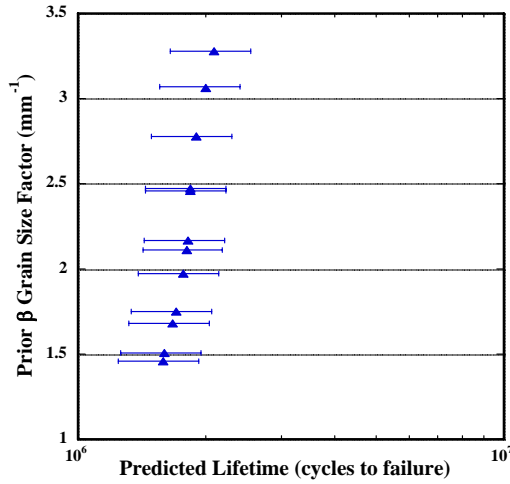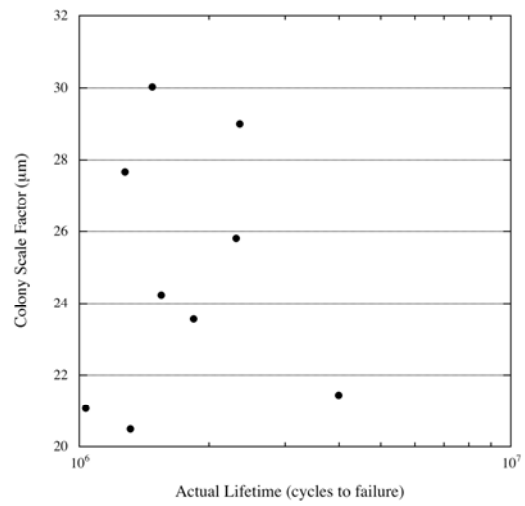
147

Figure 12. Prior β grain size factor versus predicted lifetime for samples tested at 550 MPa

Figure 13. Volume fraction of basketweave versus predicted lifetime for samples tested at 550 MPa.
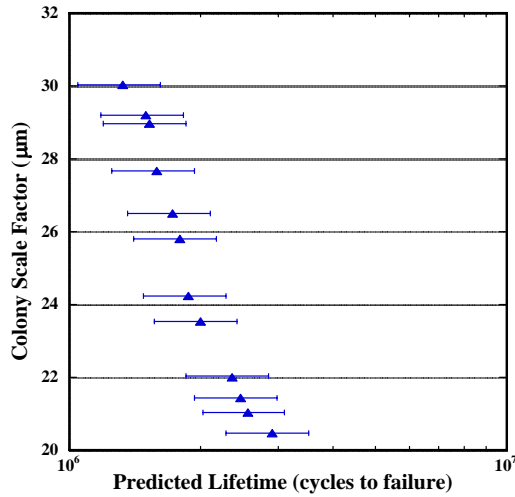
Figure 14. Colony scale factor versus predicted lifetime for samples tested at 550 MPa.

Figure 15. Colony scale factor versus actual lifetime for samples tested at 550 MPa.

3.5. Extension of the FNN modeling to β processed samples from SSB
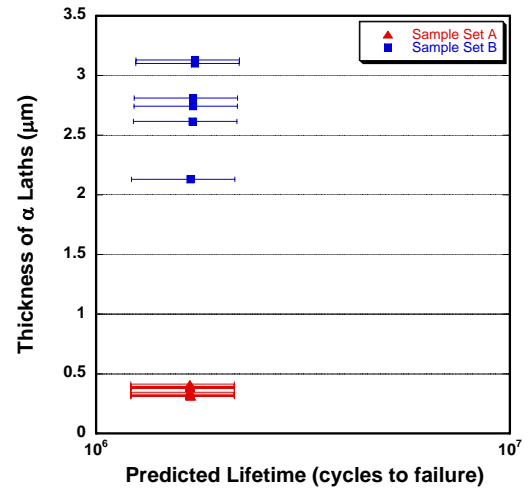
Additional samples from SSB were included for the next set of FNN analysis. Figures 16 through 18 show trend plots of selected individual features on the fatigue life predicted from the entire β processed materials data set. Again in these plots the feature in question was varied but the measurement for the other features was held constant at the mean value. The model predicted the

same lifetime for all input values of α lath thickness as seen in Figure 16, an indication of the relative unimportance of α lath thickness on fatigue lifetime. However, it is important to note that the SSB heat treated condition resulted in larger prior β grains with no basketweave microstructure.
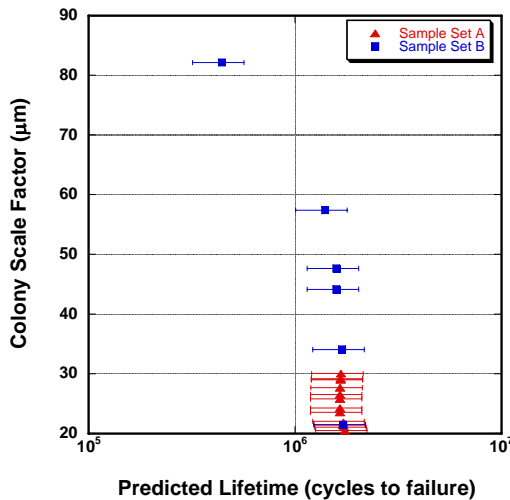
When the measurements of basketweave volume fractions were included in the FNN trend analysis, the results were different. With the same overall mean value for VF basketweave for both sample sets (SSA and SSB), the effect of colony size factor on the fatigue lifetime was not discernable as (*see fig. 17*) . But when the difference in the volume fractions of basketweave constituent of the microstructure between the two sample sets was incorporated into the model input data the remarkable effect of colony size factor is

Figure 16. Lath thickness vs predicated lifetime

observed. In other words, when the mean values of volume fractions of basketweave constituent were calculated separately for each sample set and included in the input data set a distinct inverse relationship between the colony size factor and the predicted life times emerged, as seen in Figure 18.

However, it is not yet clear what effect this separation of the data into the two samples sets might have in the overall predictability of the fatigue lifetimes, but its usefulness in model development will be explored further as the data base is populated with additional tests of varying proportions of colony and basketweave constituents in the microstructure. The researchers also propose to extend the analysis to include α/β-processed microstructures.

Figure 19 provides an illustrative picture of microstructure-fatigue lifetime relationships based on varying proportions of basketweave and changing values of colony scale factors. Based on the results of this virtual experiment, additional heat treatments were done to obtain variations in the

Figure 17. Colony scale factor versus predicated lifetime: basketweave was kept at a mean value.
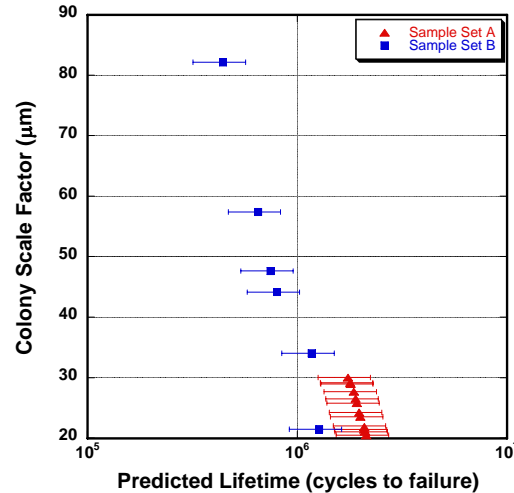
Figure 18. Colony scale factor versus predicated lifetime. Separate mean values for basketweave.

microstructure in test samples for which the fatigue testing is in progress.

Figure 19. Virtual experimentation showing the combined effect of colony size and the basketweave volume at various applied stresses on predicted lifetimes

3.6. Some Aspects of mechanisms for crack nucleation and crack propagation

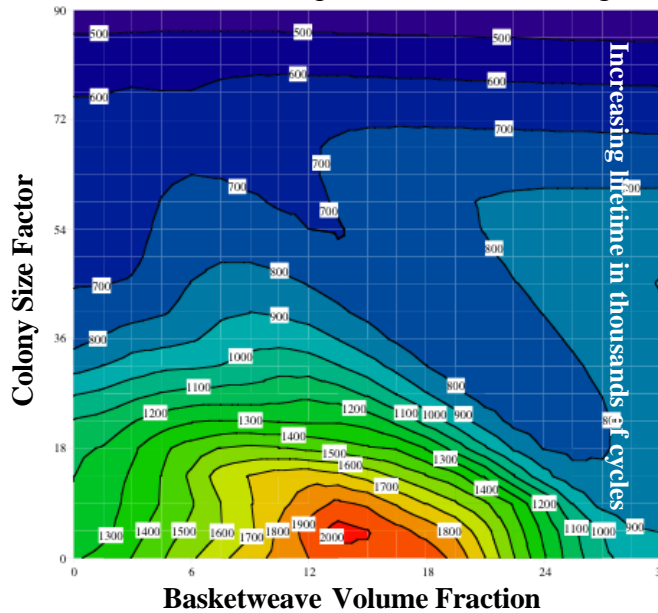Studies were undertaken in interrupted samples to follow and study the crack path in the material. The microstructure was imaged along the crack path and simultaneously the orientation of the microstructure adjacent to the crack was determined through OIM. BSE image in Figure 20a shows a region adjacent to the crack path where the crack can be seen propagating through the microstructure, nearly perpendicular to the loading direction. Along its propagation path, the crack is also observed to be deflected along various α globules indicating the possible influence of micro texture ahead of the crack tip. The texture adjacent to the crack is revealed in the OIM map in Figure 20b – where similarly oriented grains have similar colors. In particular, the specific orientations of the individual globular α grains seem to have a major influence on the crack nucleation and propagation. For example, in Figure 20a, the crack path changes between the globular α grains marked A and B whose orientations according to the OIM results shown in Figure 20b are different (shown as red and blue). Also the unit cell illustrations overlaid on the OIM image clearly show rotations between these two grains and accompanying crack deflection. Although the planes on which the crack has propagated in these two grains can not be determined from these OIM maps, a Schmid factor analysis can show the possible slip systems that have higher resolved shear stresses (RSS) with respect to the applied stress.. Figure 21a and 21b show the OIM maps with the SF values in colors – blue indicating the lowest and the red the highest. The Schmid factor analysis shown in Figures 21a indicate that the resolved shear for basal slip, i.e., (0001)<11-20>, is lowest (blue) for globular α grain A and highest (red) for grain B. On the other hand, the resolved shear stresses are not very different in these two grains for the prism slip, i.e., {1-100}<11-20> as shown in Figures 21b. Based on this analysis, it is speculated that the grain A could have been the nucleation site for deformation via basal slip leading to further crack propagated.
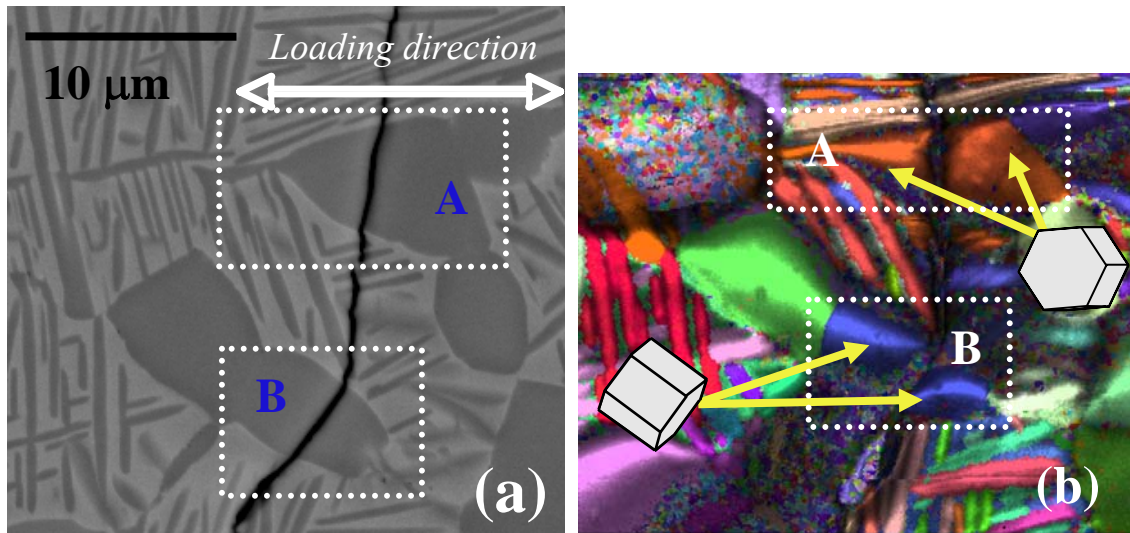
Figure 20. (a) Fatigue crack propagation imaged in back scattered mode in the SEM **(b)** Orientation Map obtained from the adjacent region of the crack path.
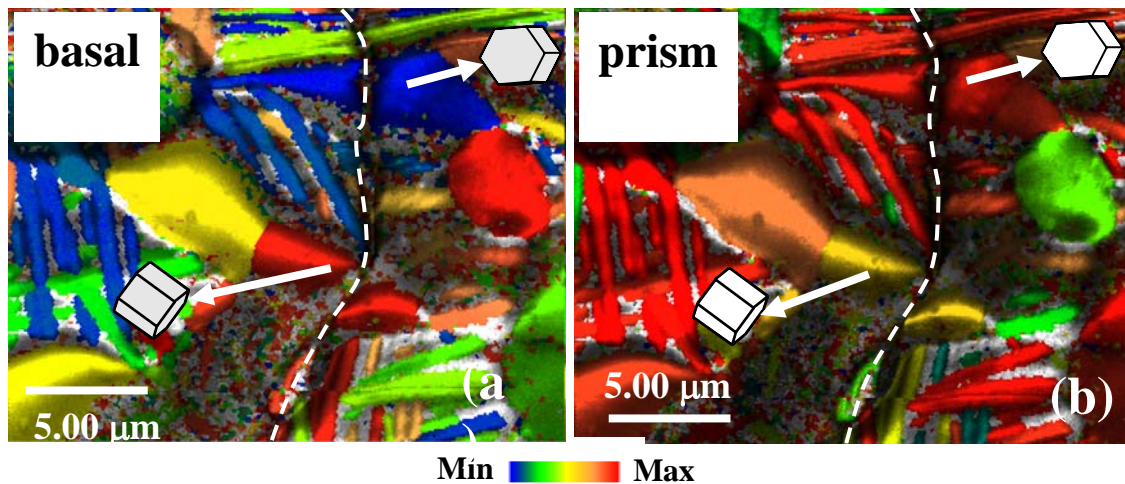
Figure 21. OIM maps show the spread in Schmid Factor values for (a) basal slip and (b) prism slip

3.7 TEM analysis

Limited TEM analysis was performed to elucidate the fatigue damage mechanisms. TEM foils were extracted primarily from three sources. First, foils were prepared from the grip portion of selected fatigue samples to investigate the starting microstructure. Second, a few interrupted tests were performed and foils were extracted from the center of cylindrical dogbones that had been cycled to ~50% of their expected lifetime. Third, site-specific foils were prepared and extracted

using the DualBeam (FIB/SEM) and extracted from regions of localized slip on the electropolished surface of the failed specimens.
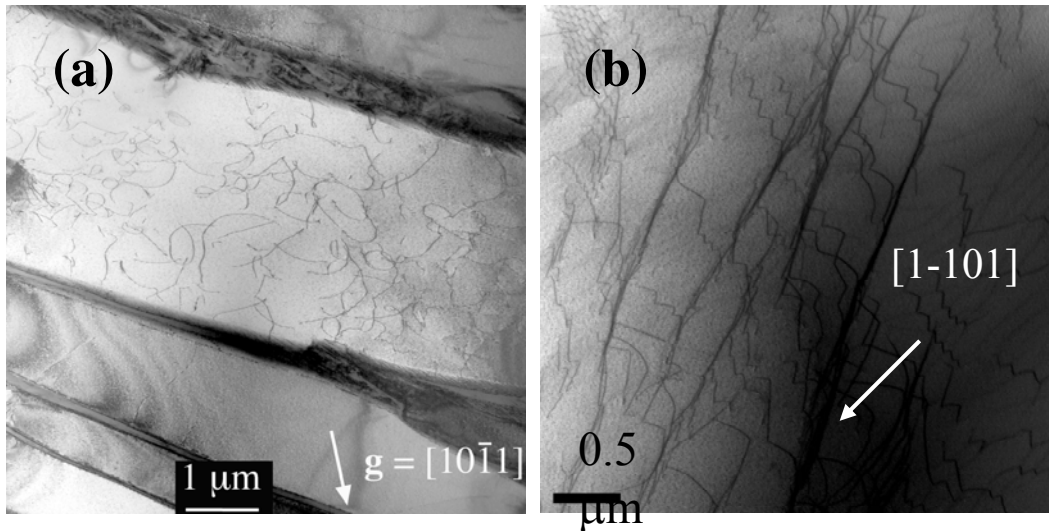
Figure 22. TEM micrographs showing the deformation substructures within the α phase in **(a)** β-processed and in **(b)** (a+β)-processed microstructure.

TEM analysis performed on the undeformed grip portion of the test samples revealed that a moderate dislocation density was already present within the α phase of both the β-processed and α/β-processed microstructure. These dislocations were presumably the result of prior thermo-mechanical processing.

On the other hand, the deformed sections of the interrupted test sample showed varying deformation characteristics. Mainly, the dislocations were of the type **a-**<11-20>, the most commonly reported slip vector in the α phase in Ti alloys. Figure 22a shows that these dislocations are in general homogeneously distributed and possess cuspy and/or loopy configuration, indicative of possibly moderate cross slip during deformation. No further analysis has been done at the present time. On the other hand, the same a<11-20> type dislocations were present in long lengths in bundled or braided fashion *(see fig. 22(b))* within the globular α grains of the α/β processed microstructure. Lastly, the site specific TEM foils prepared from slip traces on the electropolished surface showed the presence of persistent slip bands with a very high dislocation density. Figure 23a shows the region where the slip traces are imaged from the polished surface, but away from the fractured end of the sample. An OIM image obtained from the same region is shown in Figure 23b. Here, the slip trace can be seen shearing the blue colony but not the red. The inverse pole figure from the region *(see fig. 23(c))* shows the orientations of these colonies. Despite the minor differences in the relative orientation, the slip plane is observed to deflect around the colony in red showing the importance of orientation in slip transfer. TEM foils were prepared by FIB technique, normal to the slip trace as shown in Figure 24a. The foil was analyzed in the TEM for deformation substructures. The analysis showed that this particular slip trace or in other words, the persistent slip band was dominated by **a**<11-20> prism slip, as shown in Figure 24b.
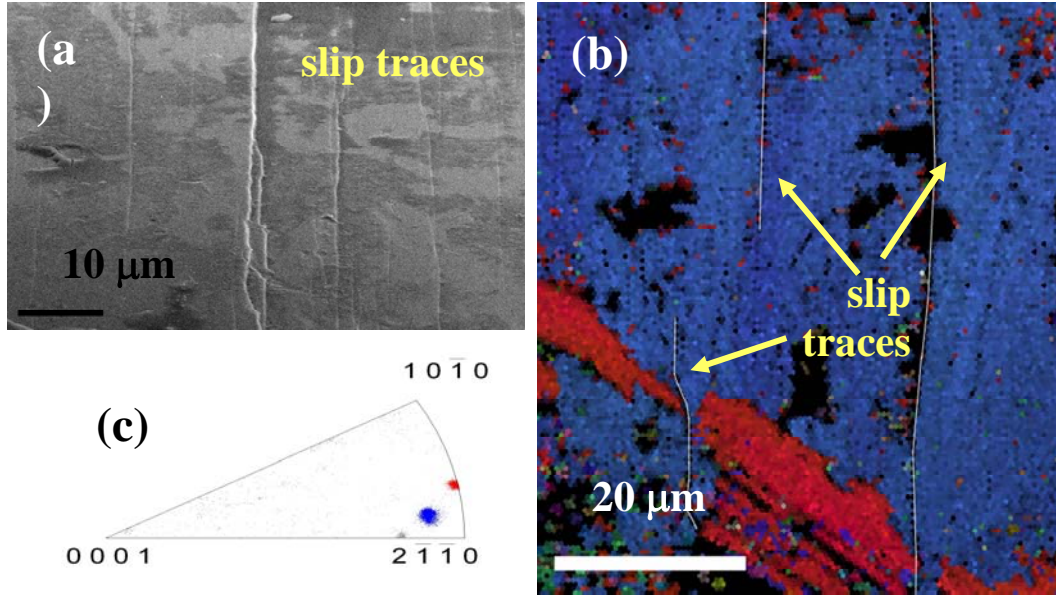
Figure 23. (a) SEM image showing intense slip bands on the surface of the β- processed sample **(b)** OIM map of a similar area showing the adjacent colonies in colors and the slip band propagation within and © inverse pole figure display the colony orientations
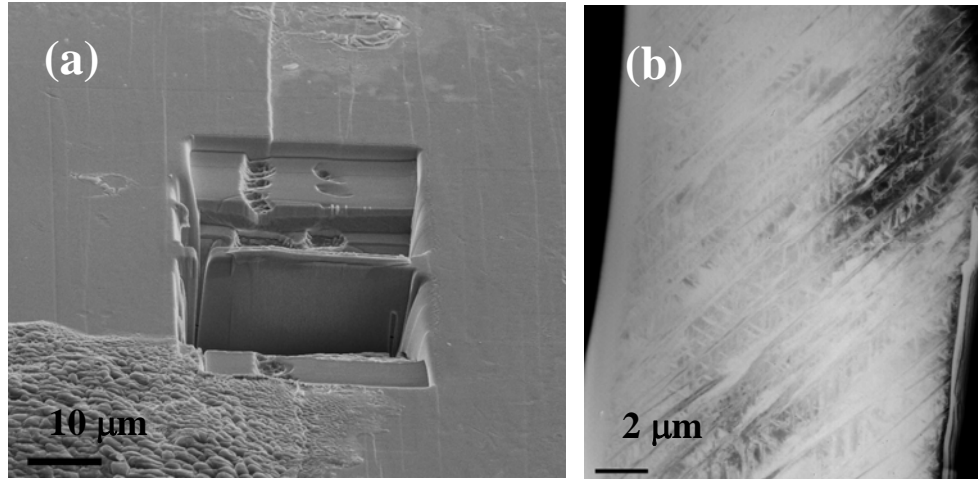
Figure 24. (a) SEM image showing the foil extraction from the slip trace of a β-processed sample **(b)** TEM micrograph showing deformation substructures within colony grain.

Slip traces were also seen on the electropolished surfaces of (α+β) processed fatigue tested samples. They seem to be concentrated near the fracture surface, and gradually diminish in density farther from the fracture surface. A typical example of these slip traces near the fracture surface is shown in Figure 25. In this region slip traces are seen mostly contained within a globular α grain, and rarely extend outside of the grain. Very large steps in slip traces observed in β-processed specimens were not seen in α/β processed specimens.
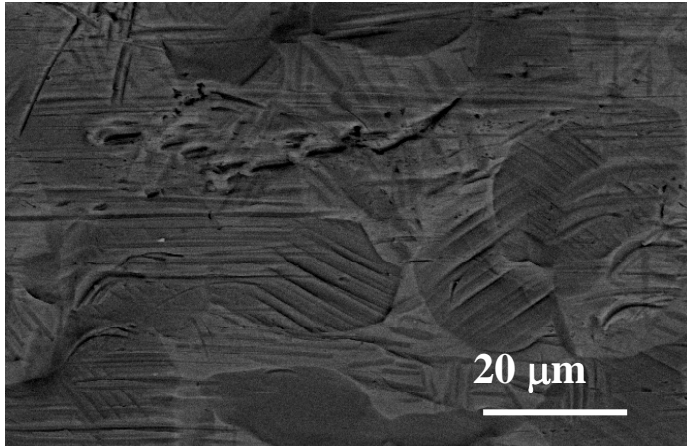
Figure 25. SEM image showing intense slip bands within α grain in (α+β)-processed sample

Site-specific TEM samples were also extracted from the fracture surface of the fatigue sample from the α/β processed alloy as shown in Figure 26a. The heterogeniety of deformation is clearly evident here. This foil contains two grains delineated by a high angle boundary. In one of these grains (marked A in fig. 26(b)), multiple slip bands (persistent slip bands) can be seen while the adjacent grain (marked B in fig. 26(b)), has hardly any deformation substructures at all. The dis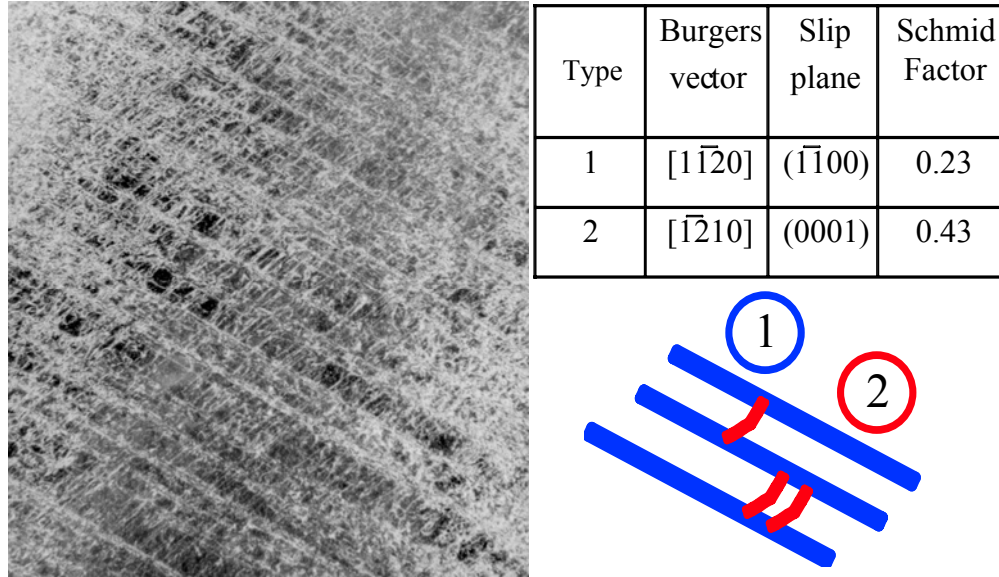location substructures (*see fig. 27(a)*) with the multiple slip bands of the grain A were analyzed to determine their character (*see fig. 27(b)*). The slip systems that were active in this grain were determined to be **a**-<11-20> type on both (0001) (basal) and {11-20} (prism) planes as illustrated in Figure 27.

3.8. Mechanisms Aspects

Examination of the present fatigue literature reveals that considerable differences and discrepancies exist regarding the effect of microstructure on the fatigue lifetimes. Some researchers have mentioned that, in general, α/β-processed titanium alloys have superior LCF and HCF properties as compared to both fully equiaxed and β-processed structures. Their superiority over equiaxed microstructures are attributed to the separation of the α_p phase by lamellar regions, and their superiority over β-processed microstructures are attributed to the finer colony size, in turn smaller slip length [10,25]. In other reviews, the opposite case is made: that α/β-processed titanium alloys have inferior HCF strength as compared to β-processed structures [8,9]. It is suggested that the alloying element partitioning in α/β-processed alloys weakens lamellar colonies acting as crack nucleation sites.

Type	Burgers vector	Slip plane	Schmid Factor
1	$[1\bar{1}20]$	$(\bar{1}100)$	0.23
2	$[\bar{1}210]$	(0001)	0.43

Figure 27. (a) TEM image showing the dislocation substructures within the α grain of (α+β) microstructure whose characters are listed and illustrated.

Improvements in resistance to crack nucleation and propagation of short cracks can often be related to a decrease in the slip length. It has been shown that the slip length in β-processed alloys corresponds to the size of the (α+β) colonies, and thus it is usually *speculated* [8] *but never verified* that the colony size may have positive influence on the HCF and short crack growth properties for fully lamellar microstructures. While it is very difficult to experimentally control one feature of the microstructure without making changes to the other features, this task has conclusively shown through experiments and modeling, the colony size has a powerful influence on the fatigue lifetimes. Additionally, OIM studies conducted on the electro-polished surface of the sample have shown that the α/β colonies, depending on individual orientation, can either transmit or deflect the slip bands which significantly affect the crack growth behavior in this alloy. These slip bands are often indicative of the crack propagation path. Hicks and Brown have [26] shown that in the colony microstructure of IMI685 alloy, the faster growing short cracks tend to follow slip bands across colonies. When they meet up with colony boundaries, additional fatigue cycles are required to reestablish the slip bands into the differently oriented adjacent colony. While the pathways of slip bands are relatively easy to establish, the sites where these intense/persistent slip bands force the cracks to nucleate are very difficult to locate. It has been suggested that fatigue cracks in β-processed microstructures will often nucleate at slip bands within the α laths or in the grain boundary α layer [25]. Nonetheless, in this study evidence for persistent slip activity has been obtained and the slip systems within these bands have been identified and characterized from TEM investigations.

Additionally, modeling has resulted in a new, somewhat surprising finding which was often neglected in earlier studies, i.e., the positive influence of basketweave microstructure on the fatigue lifetimes in β-processed alloy.

In α/β-processed microstructures, the issue of crack nucleation is not clearly understood. Several researchers [3,27] have noted situations under which the cracks nucleate either within the lamellar region or at the boundaries of the α_p phase and the lamellar regions. Others [2,3,25,28] have identified the crack-nucleating microstructural feature to be mainly globular α_p. Thus, it is not currently feasible to make broad conclusions about the role of α_p size on crack nucleation. However, a general rule is that if the crack-nucleating microstructural feature can be identified, then a reduction in this feature size will generally prolong crack nucleation. If the α_p serves as the crack initiation site, then it is likely that the resistance to crack nucleation, and thus the HCF life, would decrease for larger α_p. However, one cannot say decisively that a lack of relationship between the HCF life and the average diameter of the α_p implies crack nucleation in the lamellar region because the relationship between size of α_p and lamellar colonies must first be established. In essence a large data set needs to be developed with significant variations in the microstructure, tested and modeled. This is a huge task, the importance of which cannot be underestimated. In this project several samples with microstructural variations have been produced and tested. Characterization of the microstructure and quantification using stereology has been performed only on limited samples, and work is in progress for rest of the samples. On the other hand, evidence has been obtained to support the hypothesis that globular alpha plays an important role in the fatigue life in α/β microstructure. Both SEM and TEM investigation have shown persistent slip bands developing mostly within the globular α grains. The slip bands on the other hand, can be on either basal or prism planes.

Texture also has an important effect on fatigue properties in alloys with the α/β-processed microstructure because of the anisotropy of the α phase. Investigations have shown that alloys with similar yield strengths can have differing fatigue properties because the presence of a single texture component can allow for easier slip between neighboring grains as well as provide less resistance to crack propagation [15]. Work done by Wagner et al. [27] showed that texture changes affected only the HCF strength in Ti-6Al-4V, although this investigation included only two texture variants. In this study OIM has shown the importance of orientation of individual globular alpha grains with respect to crack propagation,which typically occurs on slip planes with the highest resolved shear stresses.

Summary and Conclusions

Based on the current research on the fatigue life behavior of Ti-6Al-4V the following conclusions can be drawn.

4.1 β-Processed microstructure

Variations in the microstructure were produced in β-processed alloy through processing, selected heat treatment in furnace and targeted heat treatment through Gleeble testing. Detailed microstructural characterization was done by optical and SEM imaging methods. Stereological methods were conducted using FoveaPro and standards developed at OSU to accurately determine the feature size, volume fraction and distribution of various phases.

Fatigue tests were conducted at different applied stresses to obtain stress versus lifetime cycles. Based on the fatigue results obtained, a bimodal distribution in the lifetimes of β-processed Ti-6Al-4V is not evident in the same lifetime ranges seen in α/β processed Ti-6246.

Using microstructure as input variables Fuzzy logic neural network models were able to predict fatigue lifetimes, but the errors in the prediction were significantly high. This was due to the small number of test samples. The errors were somewhat reduced when applied stress was removed from the list of input variables. The errors can be minimized and higher fidelity can be achieved through additional testing of samples with additional variations in the microstructure.

When models were employed to analyze the effect of individual features on fatigue lifetimes, colony size was found to have the maximum influence on the fatigue lifetime. Larger colony sizes led to lower fatigue life. Additionally, the basketweave constituent in the microstructure was shown to have a positive effect on the fatigue life as well.

The persistent slip bands that were seen in the colony structure were orientation dependent and these slip bands presumably cause the cracks to nucleate (potential nucleation sites is unclear at the present time) at colony boundaries that cause failure. The slip systems with the persistent slip bands have been identified.

4.2. α/β-Processed microstructure

Due to the limited number of variations in the microstructure tested no predictive models were attempted for this microstructure. However careful characterization of the tested samples have shown some interesting results. Investigation of the fracture surface combined with SEM and TEM studies, strongly suggest that the intense slip band creation within the globular α grain leads to fatigue failure in this microstructure.

5. Proposed future work and Recommendations

For β-processed microstructure, more testing of samples is necessary with additional microstructural variations to get better predictive capability and improve fidelity in the model. Additional, interrupted tests are needed to observe crack nucleation through replica method. This should be coupled with TEM sample extraction through FIB from potential crack nucleation sites for detailed investigations.

For the α/β processed microstructure, detailed microstructure characterization and stereology procedures need to be completed on the tested samples. More testing with additional microstructural variations in the microstructure is essential for model predication. Testing and fuzzy logic model development will be expanded to α/β-processed microstructure.

Fractography investigations on all the tested samples needed to be completed to locate and obtain as much information as possible from crack nucleation sites such as orientation using OIM and deformation substructure identification of site-specific TEM foils prepared using the DualBeam (FIB/SEM) method.

6. References

1. Lutjering, G. and J.C. Williams, *Titanium*. 2003, Heidelberg, Germany: Springer.
2. Neal, D.F. and Blenkinsop, P.A., *Acta metal.*, 24, 1, pp. 59-63, 1976.
3. Hall, J.A., Fatigue crack initiation in alpha-beta titanium alloys. International Journal of Fatigue, 1997. 19,1, pp. S23-S37.
4. Jha, S.F. and Ravi Chandran, K.S., *Scripta metal.*, 2003, 48, 1, pp. 1207-1212..
5. Chandran, K.S.R. and S.K. Jha, *Acta mater.,* 2005, 52, pp. 1867-1881.
6. Jha, S.K., Larsen, J.M, Rosenberger, A.H. and Hartman, G.A., *Scripta mater.*, 2003. 48: pp. 1637-1642.
7. Jha, S.K., Caton, M.J. and Larsen, J.M., 2007. *Matl. Sci. Eng.* A 468-470, pp. 23-32.
8. Lutjering, G., *Mater. Sci. and Eng.* 1998. A243, p. 32-45.
9. Evans, W.J., Mater. Sci. and Eng., 1998. A243, pp. 89-96.
10. Williams, J.C. and G. Lutjering. *Titanium '80: Science and Technology*. 1980, Warrendale, PA, The Metallurgical Society of AIME.
11. Lutjering, G., Gysler, A. and Albrecht, J., Fatigue '96: Proceedings of the Sixth International Fatigue Congress. 1996, Pergamon.
12. Tiely, J., *Ph.D. Thesis*, The Ohio State University, 2003.
13. Ruppen, J., Eylon. D., McEvily, A.J., Metall. Trans. A, 1980, 11, p.1072.
14. Mahajan, Y., and Margolin, H., Metall. Trans. A, 1982, 13A, pp.257-268.
15. Lutjering, G., *Mater. Sci. and Eng.* 1997. A263, pp. 117-122
16. Eylon, D. and Pierce, C.M., *Metal Trans.*, 1976, 7A, p. 111.
17. Howland, C., Hicks, M.A. and Jeal, R.H., '*Small Fatigue Cracks*', (Eds Ritchie, R.O. and Lankford, J.), 1986, TMS-AIME Warrendate, PA, p. 607.
18. Peters, M., Gysler, A. and Lutjering, G., Metal trans, 1984, 15A, p.1597.
19. Rudinger, K. and Fischer, D., 'Titanium Science and Technology', 1984, Vol.4. p. 2123.
20. J.C. Russ and R.T. Dehoff, Practical Stereology, 2nd Edition (New York, NY; Kluwer Academic/Plenum, 2000, pp.19-27.
21. J. Tiley, T. Searles, E. Lee, S. Kar, R. Banerjee, J.C. Russ, H.L. Fraser, "Quantification of microstructural features in α/β titanium alloys," Mater. Sci. Eng. A372 (2004), pp.191-198.
22. Polasik, A.K., Jha, S.K., Mills, M.J., Larsen, J.M, and Fraser, H.L., G.A., *Scripta mater.*, 2003. 48: pp. 1637-1642.
23. R.G. Forman, V. Shivkumar, Fracture Mechanics vol.17, ASTM STP905, (eds.)Underwood, J.J. , ASTM 1986, pp 59-74.
24. R.K. Nalla et al., "Influence of Microstructure on High Cycle Fatigue of Ti-6Al-4V: Bimodal vs. Lamellar Structures," Metall. and materl. Trans., 2002 33A, pp. 899-918.
25. Wagner, L., Lutjering, G. and R.I. Jaffee. 'Microstructure/Property Relationships in Titanium Aluminides and Alloys' 1991, TMS, Warrendale, PA.
26. Hicks, M.A. and Brown, C.W., 'Intl. J. of Fatigue', 1982, p. 167.
27. Wagner, L., *Fatigue Life Behavior of Titanium Alloys*, 1996, ASM Handbook. Materials Park, OH., pp. 837-845.
28. Szczepanski, C.J., et al. *Materials Damage Prognosis*. 2004, TMS, Warrendale, PA.

7. Names of Personnel

Hamish Fraser (OSU Faculty Member)
Michael Mills (OSU Faculty Member)
Jim Larsen (AFRL/RX Mentor)
Andy Rosenberger (AFRL/RX Mentor)
Alison Polasik (OSU Graduate Student)

Task 8
Microstructural Representation for Development of Materials Prognosis Methodologies.

Hamish Fraser (OSU Faculty member), Michael Uchic (AFRL/RX Mentor), Dennis Dimiduk (AFRL/RX Mentor), Robert Williams (OSU Graduate Student)
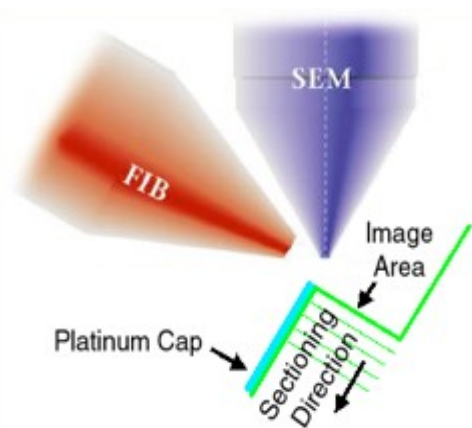
I. RESULTS AND DISCUSSION

1. Introduction

The quantification and representation of microstructures have largely been limited to relying on two-dimensional approaches. Stereology has been used extensively to extract quantitative numbers that sufficiently describe details of the microstructure. While such methods can yield exact solutions (e.g., phase fraction in the absence of strong orientation effects), they often rely on assumptions about the shape of a feature for many calculations, resulting in significant errors when the assumptions are incorrect or there is no a-priori knowledge. Additionally, it is extremely challenging if not impossible to extract details regarding connectivity, distributions, and linkages between microstructural features from two-dimensional images [1]. Therefore, there has been a desire to develop methodologies that provide for the direct three-dimensional characterization of materials. These methodologies would allow for the full three-dimensional representation of microstructural data in the form of *data-sets* that are directly interpretable and measurable without the need for assumptions or prior knowledge of phase shapes and distributions. One such technique incorporating the FEI Dual Beam FIB/SEM (*see Figure 1*) has been used extensively in this task. This technique is based on the serial sectioning and imaging/data collection of microstructures, shown schematically in Figure 2. This task has allowed for the development and refinement of experimental techniques for the extraction of three-dimensional information. These methodologies, including details regarding the data collection, quality, and type (e.g., secondary electrons, backscattered electrons, electron backscattered diffraction datasets) will be described below. Additionally, the methods have been applied to two alloy systems of interest to the Air Force, namely Ni-based super alloys and Ti-based alloys.

Figure 1: Image of FEI DB235 Strata.

Figure 2: Schematic of serial sectioning with a DB-FIB-SEM.

1.1. Establishment of Methodologies

While the history of three dimensional analysis in metallography spans at least from 1918 with Forsman's repeated (serial) sectioning effort to understand the three dimensional structure of

pearlite; current characterizations systems and technological advancements necessitated the development of new techniques and procedures to optimize and accurately collect and analyze serial data sets. In order to obtain the highest fidelity, quantitative three-dimensional reconstructions of microstructural features, rigorous procedures for the ex-situ preparation of samples, the in-situ preparation of samples, and the in-situ collection of data have been developed. Of equal importance is the subsequent post-processing and virtual reconstruction of features, which required development of new procedures. Many of these techniques and procedures have been developed during the past 5 years, and form the basis of a significant amount of work for this task. The majority of this work has been conducted by researchers from The Ohio State University in conjunction with those from the Air Force Research Lab.

2. Methods, Assumptions, Procedures

The techniques described above have been applied to two systems of interests to AFRL and OSU, specifically Ti-based alloys and Ni-based superalloys. Both alloy systems are of interest given their prevalence in aerospace applications, and the variation in microstructures that occur within each alloy system. Additionally, there are modeling efforts currently underway for both Ti-based alloys and Ni-based superalloys which requires full three-dimensional information to validate predictive models or provide detailed information for the identification of specific microstructure-property relationships. In addition to the wealth of microstructural information contained within these datasets, they provide specific examples of microstructural details that are either miscalculated using stereological procedures or not easily interpretable from two dimensional micrographs. These specific examples will be described in detail.
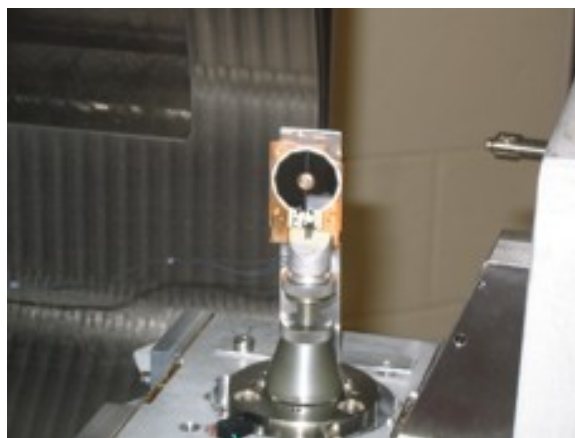
2.1. Ex-Situ Sample Preparation

Large samples of each alloy were sectioned using electrical discharge machining (EDM) to produce a sample with approximate dimensions of 5.0 mm x 5.0 mm x 500 mm. The residual EDM recast layer was removed from the sample surfaces with 600 grit wet/dry SiC paper. Subsequently, the broad faces were polished with an Allied Multiprep parallel polisher using precision metallographic techniques to thin the specimen to a thickness of less than 60 mm. The final polish was a colloidal suspension of 0.05 μm silica. It has been noted empirically that surface roughness on the broad face can affect the milling quality of the viewing surface. Optical microscopy was used to ensure no large scratches covered the eminent milling area.

The samples were then mounted using a conductive medium on a 45° back-tilted holder (Figure 3) for use in the DB-235, or on a standard aluminum SEM stub mounted in a pre-tilted holder for the Nova 600. The back-tilted holder is required in order to automate the collection of serial sections in the DB-FIB given the restrictions imposed by the configuration of both electron and ion columns. This sample prep places the specimen in the correct orientation for milling without tilting which is currently required in order to use the custom installed backscattered electron detector (*see fig. 4*).

**Figure 3:** Sample mounted on 45 degree pre-tilted holder.

161

Figure 4: Custom oriented backscatter electron detector.

2.2. In-situ Sample Preparation

All aerospace materials examined during this task were polyphase and polycrystal. It is known that ion milling rates are dependent on factors such as angle of incidence, crystal orientation and chemistry [2]. The development of these procedures were focused on reducing the overall time required to collect a data set as well as eliminating any artifacts that would hinder collection or prevent analysis and reconstruction of the collected data. The final stages of sample preparation were performed *in-situ* using the ion-milling capabilities of the DBFIB/SEM as well as the tool's ability to locally deposit platinum using the Gas Injection Systems (GIS).

The sample was oriented with the broad face normal to the ion beam and the area to become the viewing surface was nominally parallel to the ion beam. The initial milling step used a 30 kV 20 nA beam to remove any mechanical polishing artifacts and planarize the viewing surface for analysis. After the surface was cleaned sufficiently to enable adequate imaging of the microstructure with the electron beam, an area of interest was located, and protected with a 1-2 µm thick layer of platinum deposited by ion-assisted deposition on the broad face directly above the area of interest (Figure 5) [3]. The Pt layer was deposited with a slightly over-focused ion beam so that large areas could be covered while maintaining a relatively smooth, uniformly deposited layer.
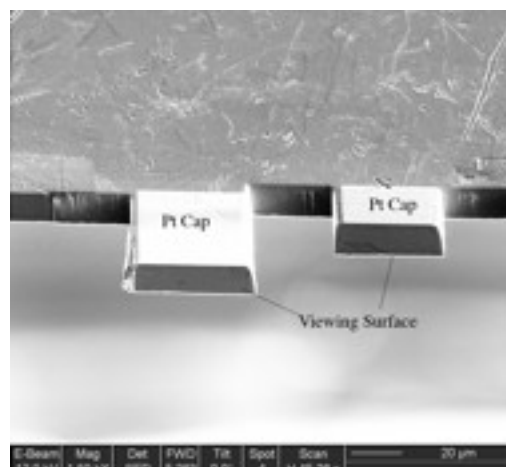
Figure 5: Cantilever volume coated with Pt.

Following the platinum deposition, a 30 kV 20 nA Ga ion beam was used to remove material surrounding the area of interest, such that a small cantilever volume of material remained largely isolated from the remainder of the sample in a cantilever fashion (Figure 5). This was accomplished by cutting two trenches, each ~20 microns

wide. The depth of these trenches need not be significantly greater than the depth of the volume to be sectioned. For instance, if the depth of the volume is 8 microns (e.g., 160 slices @ 50 nm spacing), then the trenches need not be deeper than ~10 microns.   The viewing area was then milled using a cleaning cross section pattern with the same beam current that will be used during serial sectioning. Typical beam currents were 30 kV 1-5 nA in the DB235 Strata and up to 7nA in the DB600 Nova. It should be noted that the beam current was chosen based on producing an optimal imaging surface while reducing overall milling time. The preparation of this isolated volume of material prevented redeposition of milled material from shadowing the viewing area as well as decreased milling time for individual slices. In this fashion, the subsequent collection of serial images was accelerated and the quality of the images improved.

At this point the samples were ready for automated sectioning and image acquisition by Slice and View™ software. It is noted that for custom scripting fiducial markers were placed within the FIB field of view.

2.3. Serial Sectioning Parameters

While the experimental variables described below resulted in high-quality, high-fidelity three dimensional datasets for this body of work, it is noted that parameters must be optimized for each serial collection of data. These parameters are dependent upon not only the details of the microstructural features of interest (e.g., their minimum/maximum size), but also the limits of the microscope (e.g., spatial resolution, ion beam position resolution, available beam time) and the material to be sectioned.

The samples were positioned with the broad face normal to the ion beam and the imaging surface tilted 38° from the vertical axis of the electron column.   For the reconstructions collected during the scope of work for this task, a 30 kV 3-7 nA beam was used to successively remove a slice of approximately 50 nm from the viewing surface (Figure 2). Following each slice, the viewing surface was imaged using the Sirion SEM column and a custom back-scattered electron detector (BSD) at a scan rate of at least 90 seconds in order to provide an acceptable signal-to-noise ratio and intensity distribution (i.e., contrast variation) between phases, resulting in useable digital micrographs.

For example, the majority of serial sections performed for this work have had volumes defined by edges of approximately 30 x 30 x 8 microns with images recorded from slices obtained every 50 nm. Such runs required approximately 18 hours of beam time in addition to 2-6 hours for *in-situ* pre-processing. The maximum volume obtained for this work was defined by edges of 40 x 40 x 34 microns with images recorded from slices obtained every 50 nm resulting in 60 hours of collection time in addition to the 4-10 hours for *in-situ* preparation. Each image in the series was acquired using a custom installed backscattered electron.

2.4. AutoSlice and View™ and Custom Scripting

The initial serial sections were conducted using the commercial software AutoSlice and View™ [4], an automation program supplied by FEI that allows the user to define parameters for milling and image acquisition.   It was designed to produce serial data sets with maximum resolution by using only beam shifts and no stage movements. The DB235 has a stage resolution of 0.5

microns and is subject to post-movement relaxation and drift which can result in significant misalignment of the sample relative to slice thickness after any stage movement. In an attempt to keep the stage static, FEI imposed a maximum limit of 8 microns to the depth of sectioning permissible by the beam shift of the SEM column. Included with the microscope software is a scripting language and built in pattern recognition software that allowed for the development of custom control scripts to overcome this limitation.

Using the custom control scripts, it was possible to direct the built-in pattern recognition software to locate a fiducial mark milled at the end of the cantilever. The distance from the fiducial mark to the end of the finger was defined initially and then subsequently decreased after each slice (Fig. 6). This allowed the user to incorporate stage movements and then accurately and precisely place the next milling box. Essentially, a stage with 0.5 microns of resolution can now be incrementally moved with 50 nm resolution by compensating for error with fiducial recognition and beam shifts.
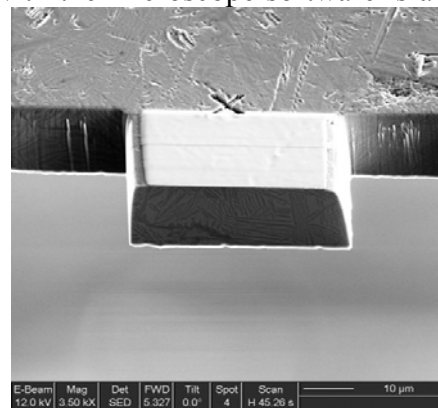
Figure 6: Cantilever volume with fiducial mark.

2.5. BSE Detector

Multiphase metallic systems are best imaged using backscattered electrons, rather than secondary electrons, due to enhanced contrast resulting from compositional differences among the phases [2]. FIB systems do not currently come with a backscatter detector due to space limitations and geometrical restrictions near the pole-pieces and gas injection systems. This lead to the construction of a backscatter detector oriented vertically and away from the pole pieces. In this configuration, the back-scattered electrons resulting from the beam interaction with the inclined surface fell within the solid angle of the detector. This was initially developed by OSU for the DB235 and performed well. Subsequently, with the acceptance of the NOVA 600, FEI delivered an updated version of the previous design to mount in NOVA 600

2.6. EBSD

Electron Backscattered Diffraction (EBSD) is a powerful tool for obtaining crystallographic orientation maps (OM) over large regions of interest. The viewing area created during serial data collection is not only a reasonable size for collecting an OM but should also posses a nominally flat surface after milling. A strength of this additional characterization technique is the automated segmentation of various crystallographic features and same phase variants. This technique was initially proposed by researchers at OSU and AFRL. Groeber et al. applied this technique to a nickel based superalloy to collect a serial data set of OM maps and SED images for grain morphology analysis [5].

This led to a collaboration between OSU, AFRL, and FEI to help develop the next generation of FIB-SEM platforms. FEI has since shown the effectiveness of this technique on aluminum, nickel, and steel specimens [6]. Implementing this technique on Ti-alloys however proved nearly impossible due to an unexpected FIB-induced, surface-damage layer that increased data collection time by at least an order of magnitude as well as distorted the EBSD pattern

sufficiently to prevent indexing relative to mechanically polished samples. This led to investigating the effect of FIB milling on the surface quality of Ti alloys' and the advent of low kV FIB milling to improve pattern quality and reduce OM collection times. For this work, individual OM were used to identify and manually segment alpha/alpha interfaces. The data collection time is prohibitively long for serial collection of OM from Ti-alloys, currently OM is taken subjectively.

2.7. Secondary Electron Imaging with the Focused Ion Beam

The FIB can also be used for imaging in some material systems, such as nickel base superalloys where the increase in channeling contrast is significant enough that collecting FIB images at different orientations produces sufficient variation in contrast to locate microstructural boundaries and different phases [7,8]. This technique does not work with Ti alloys and the phenomenon is not well understood
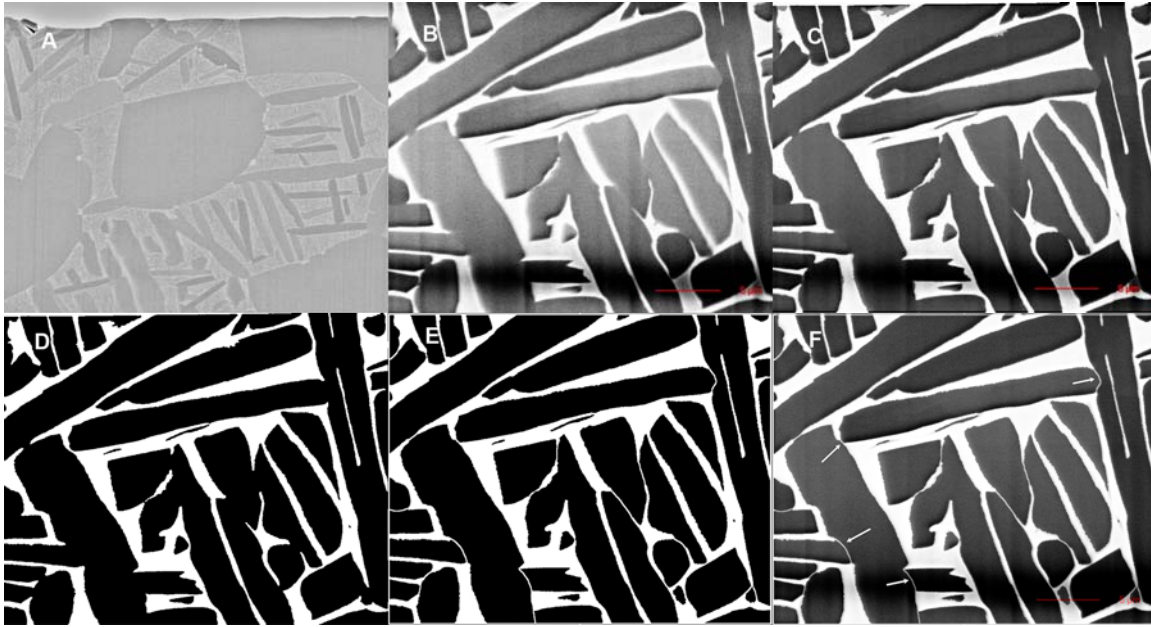
2.8. Image Post-Processing

Foreshortening: The relative orientation of the two columns in the dual-beam FIB (i.e., co-eucentric with an angle between of 52°) creates a foreshortening in the images obtained using the electron column (both SE and BSE images). The two methods of compensating for this foreshortening are to stretch the images in the y-direction by a factor of 1.269 (1/cos(38°)), or to compress the x-direction by a factor of 0.788 (cos(38°)). The latter is the preferred method so as to avoid introducing artifacts into the data.

Image alignment: There are two general methods by which a serial data set of images can be aligned relative to one another. The first method relies on an reference frame external to the microstructure, such as a fiducial mark or series of marks. The second method performs a cross-correlation function to evaluate two successive slices and automatically perform an appropriate image shift. This method requires the microstructure contain various distinctive features which is most easily realized in microstructures containing multiple phases. The microstructure can not be strongly textured; for example, a microstructure that contained only one variant of a precipitate oriented parallel to one another would likely result in a poorly aligned stack for further reconstruction. The reconstructions and visualizations presented in this work have been aligned using xfalign, a cross-correlation function associated with IMOD [9]. The cross-correlations have been effective, given the complex, multi-phase nature of both the β-titanium microstructures (e.g., many different variants) and the Ni-based superalloys with their distribution of carbides. It should be noted that the Pt cap may be used as an additional independent reference frame, if necessary.

Image pre-processing and segmentation: Similar to two-dimensional image analysis techniques incorporating stereology, it is necessary to perform a series of pre-processing steps on the images in the data-set prior to reconstruction and visualization. These steps involve general routines to reduce noise and produce binary ("threshheld") images as well as more complicated routines involving segmentation. The general routines are common in image-processing tool-boxes. For this work, the Fovea Pro plug-ins[10] for Adobe Photoshop 7.0 (and higher)[11] were used for the noise-reduction and threshold routines. It should be noted that the incorporation of the

custom backscattered electron detector resulted in higher-quality, better contrast images (Figure 7 (a-b)) for the titanium alloys, which resulted in more accurate noise-reduction and threshold routines. It can be clearly seen that the secondary electron image (Figure 7(a)) would have insufficient contrast for such pre-processing routines. Indeed, the important variable for a faithful reconstruction of microstructure from a serial dataset are primarily dependent upon the original data. For example, consider the micrographs of Ti-6-2222, shown in Figure 7(b-d). These three images correspond to the original image (Figure 7(b)), the image after a 5 x 5 hybrid median (Figure 7(c)), and a binary image after the threshold routine (Figure 7(d)).

Figure 7: (a) Secondary electron image, (b) Backscatter electron image, (c-e) Post processing of backscatter electron image, (f) Final segmentation.

The threshheld image is visually an accurate representation of the original image. Ideally, it is desirable to define the image processing variables (e.g., gray-scale threshold level) for one image in a dataset and then apply a routine to the entire dataset in order to eliminate user subjectivity. At the time of this work, there was still sufficient variability among the images in the data-sets that some user subjectivity was invariably required to validate and approve images.

The most complex routines involving image segmentation are typically performed after general pre-processing routines, although some are performed in parallel. This segmentation allows for the clear separation of individual features of interest. The general threshold routines failed to identify boundaries of features for cases where boundaries were not clearly associated with strong changes in contrast. Such cases often rely on lengthy, subjective, manual processing steps where consecutive images are compared and still require at least some distinguishing feature for user subjectivity.

2.9. Reconstruction and Volume Rendering

Following image processing the individual two-dimensional data acquired in the DBFIB must be stacked and interconnected to recover the three dimensional nature of desired features. The

166

share-ware program IMOD, from University of Colorado-Boulder, is a set of image processing, modeling and visualization programs used for tomographic reconstruction and for 3D reconstruction of Electron Microscopy serial sections and optical sections [9]. The package contains tools for assembling and aligning data within multiple types and sizes of image stacks, viewing 3-D data from any orientation, modeling and display of the image files. IMOD was then used to apply contours to the interfaces of the binary images and render surfaces to the 3-D reconstruction through linear interpolation. The resulting three dimensional model can be visualized in an interactive manner, with user-control of viewing directions and transparency. Further, 2D slices can be "prepared" on any plane through the volume, and attributes of features, such as distances, surface areas, and volumes, may be calculated. Additional details regarding this program can be found in its documentation (http://bio3d.colorado.edu/imod/).

3. Results and Discussion

3.1. Case-study 1: Titanium Alloys

Recently, there has been considerable effort aimed at developing computational models to predict the properties of Ti-based alloys based on compositional and microstructural inputs. Given the absence of mechanistic models (currently the subject of on-going OSU research programs), researchers have first focused on developing rules-based approaches, such as Bayesian Neural Networks. These approaches require databases relating microstructural features and mechanical properties, and have been historically populated using quantitative values derived from two-dimensional images using stereological approaches; however, such approaches suffer from the following two challenges. Firstly, they often include shape factors derived based upon assumptions of the morphology of features. Secondly, as these methods have intrinsic limitations when handling or identifying connectivity in three-dimensions, they will invariably fail to capture microstructural details only observed in the 3D data-sets,

Feature Measurements: It has been determined that one of the microstructural variables that significantly affects the strength properties of a material is the average thickness of the α-laths. While not directly measurable from two-dimensional micrographs, the thickness can be estimated using the following stereological calculation [12],

$$t_{est} = \left(\frac{1}{1.5(1/\lambda)_{mean}} \right)$$

where t_{est} is an estimation of a-lath thickness and $(1/l)_{mean}$ is the mean of the inverse linear intercepts. The pre-factor 1.5 is based on an assumption of an semi-infinite plate or thin membrane [12].
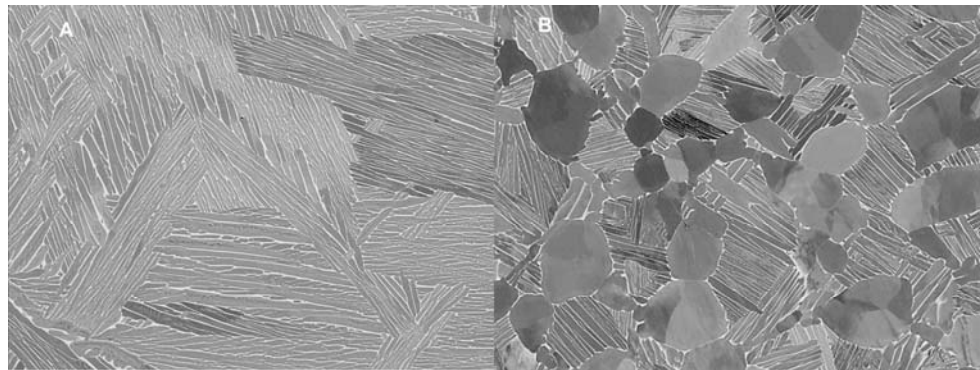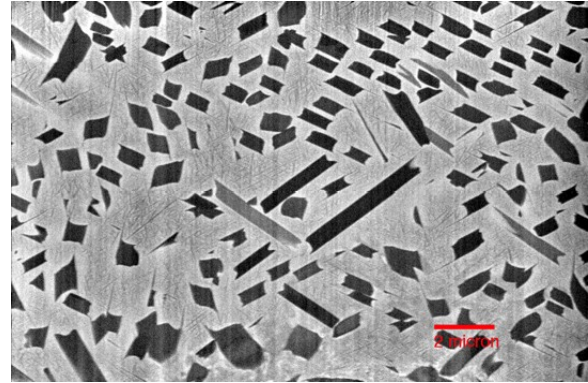

Figure 8 (a) β processed Ti-6Al-4 V, (b) α+β processed Ti-6Al-4 V.

While such assumptions may be appropriate in α/β Ti-alloys where the α-laths exhibit large aspect ratios such as β-processed Ti-6Al-4V (Figure 8(a)), the accuracy of estimations is likely to be significantly reduced as the aspect ratio is reduced. Such reductions in a-lath aspect ratios occur for α+β processed microstructures and for β-stabilized titanium alloys (Figure 8(a))

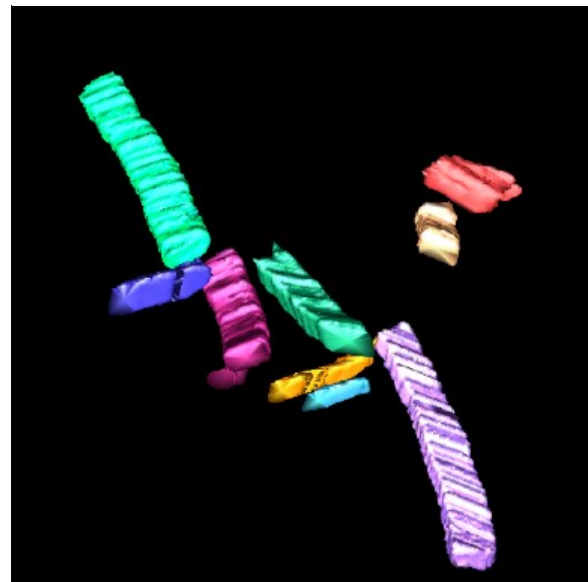Therefore, a study was undertaken to determine which stereological measurements provide a reasonable estimation of α-lath thickness for Ti-6Al-4V in β-stabilized Ti-alloys. For this analysis, one alloy, a binary Ti-13Mo (wt%) alloy was prepared (Figure 9)

A partial three-dimensional reconstruction of the Ti-13Mo alloy is shown in Figure 10. Within this reconstruction, five of the α–laths have been isolated. It is clear that these 5 laths have a relatively small aspect ratio, and do not begin to approximate infinite plates. The distances between their broad faces, edge faces, and incoherent ends have been measured. The classification of these faces is consistent with the published titanium literature. Stereological measurements of the Ti-13 Mo were performed on 15 2D images taken from random planes of orientation throughout the serial section data set. The individual measurements and their mean are shown in Table 1. It is clear to see that the thickness, typically an estimation of the distance between the two broad faces (*i.e., the shortest distance*), is approximately 0.5 mm. However, the estimation of the thickness provided by the proceeding classical stereological approach is ~0.14 mm, (Table 2) an underestimation of approximately one-quarter the true thickness. While the origins of this significant difference are the focus of an on-going study, it is known that the pre-factor can deviate from 1.5, depending on the aspect ratio of the precipitate. It may be possible to recalculate such pre-factors based on what is observed in such reconstructed volumes, based on alloy-type or processing history.

Figure 10: BSD image of Ti - 13 Mo alloy.

Figure 10: 3-D reconstruction of alpha laths in a Ti-13 Mo alloy.

Missing Microstructural Details: The reconstruction shown in Figure 10 shows discrete laths. However, in alloys with less β-stability, this work has demonstrated that the connectivity among the microstructural features may not be as clear. For example, consider the α+β alloy Ti-6246. Two of the

	X	Y	Z
Lath 1	0.38	0.66	1.76
Lath 2	0.459	0.642	2.23
Lath 3	0.42	0.715	2.38
Lath 4	0.422	0.697	2.23
Lath 5	0.385	0.568	1.19

Table 1: Dimensions of 5 discrete laths (μm).

laths in this dataset have been reconstructed, and are shown in Figure 11(a-b). It is clear that these are interlocking α-laths. This connectivity would be missed if only two-dimensional information were collected. While the effect of such features on properties is not known, they should be included in any development of mechanistic microstructure-property relationship.
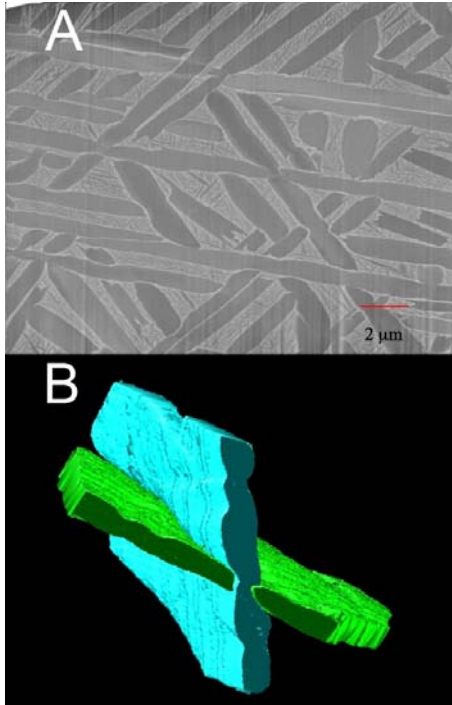
**Figure 11:** (a) SED image of Ti-6-2-4-6, (b) 3-D representation of alpha lath interconnectivity

Table 2: Alpha lath thickness estimations from a classical stereological measurements.

| 1/l	l
4.07	0.16
3.899	0.17
3.82	0.17
8.13	0.08
7.27	0.09
7.32	0.09
6.1	0.11
3.87	0.17
7	0.09
4.35	0.15
7.35	0.09
4.88	0.13
3.76	0.18
3.69	0.18
3.76	0.18
Average l =	0.14

3.2. Case 2: Nickel Superalloys

The distribution of carbides in Ni-based superalloys has been shown to have a significant influence on mechanical properties. Specifically, it is well known that carbides which precipitate along the grain boundary tend to improve the elevated temperature properties by inhibiting grain boundary sliding. Two alloys of interest to the aerospace industry, IN100 and WASPALOY, were analyzed using AutoSlice and View™software. Figure 12(a-b) show traditional backscattered SEM micrographs of IN100 and WASPALOY, respectively. The IN100 has smaller grains with carbides present within the grains. Conversely, the WASPALOY had larger grains with the majority of carbides decorating the grain boundaries. This microstructure also exhibits special, low energy boundaries (e.g., twin boundaries). There are occasional carbides that appear within the grains. Such qualitative statements regarding the microstructure and carbide distributions represent common historical descriptions of these features. The three-dimensional representations of such microstructures contain significantly more information, such as the real distribution of carbides. Figure 13(a-b) show the three-dimensional reconstructions of the same two alloys with the carbides rendered in green. The IN100, shown in Figure 13(a), shows a relatively random spatial distribution of the carbides within the grains. Conversely, the WASPALOY, shown in Figure 13(b), *clearly* shows carbides decorating the grain boundaries. In

this figure, it is possible to see that, for some grain boundaries, the carbides appear as discrete particles, while along other boundaries, the carbides appear as either a sheet of carbides (indicated by an arrow, labeled "A"), or such a high density of carbide precipitates to nearly completely cover the local boundary. Similarly, what appeared as the occasional intragranular carbide precipitate is clearly a plane in three-dimensions that is decorated by several carbide particles (indicated by an arrow, labeled "B"). While such three-dimensional visualizations can provide many answers regarding feature shape and spatial distributions, they also suggest new
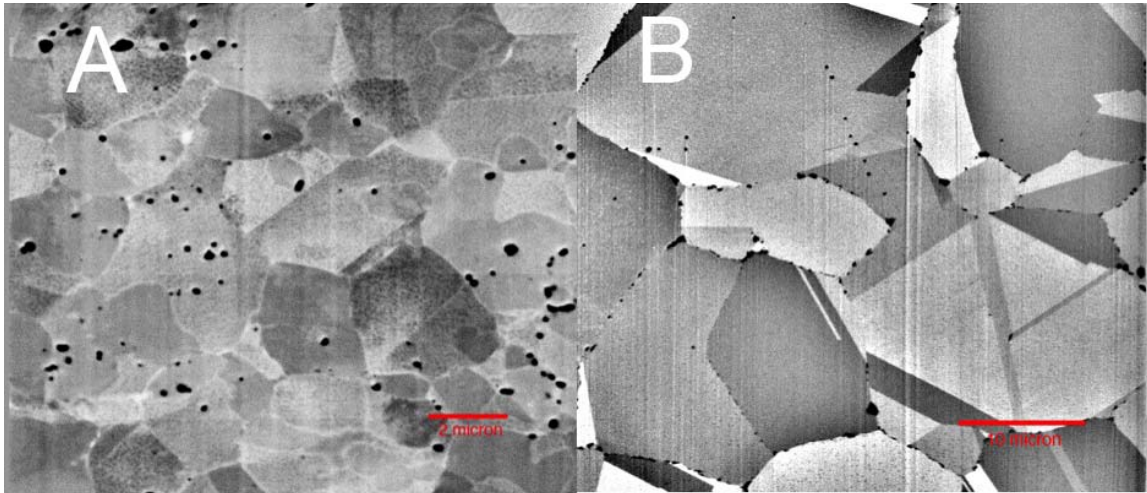
**Figure 12:** (a) BSD image of IN100, (b) BSD image of WASPaloy.
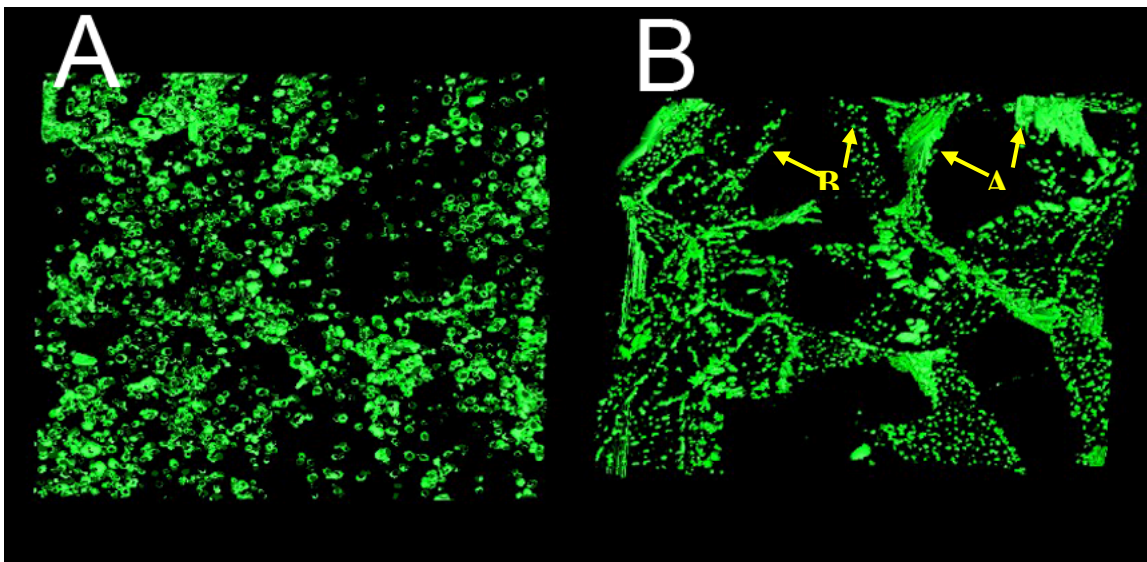
Figure 13: (a) 3-D representation of homogeneous carbide distribution in IN100, (b) 3-D representation of carbides decorating grain boundaries in WASPaloy.

questions. For example, how does the local boundary misorientation effect the density and form of the carbides (e.g., particles vs. coherent sheets). Such questions are also the focus of on-going research.

3.3. EBSD

For this work, EBSD was used to identify alpha/alpha interfaces that exhibited low contrast variation between crystallographic variants. For example, although the original micrograph in Figure 7(a) has several locations where different variants of alpha laths impinge upon one another, the contrast is not sufficiently different to allow for the automated threshold routine to identify the boundary. The contrast variation and physical orientation were sufficient for a user to manually segment the image (Figure 7(e)). Not all collected images have such definitive contrast variation between the alpha/alpha interfaces (Figure 14(a)). As with the previous case, a β-rib was expected to separate the circled laths, however if the β-rib is present, it is at a scale not resolvable using the SEM. Furthermore, the contrast variation between the two laths is not sufficient to allow for contrast-based segmentation routines to identify the boundary. Indeed, it would be equally challenging for users to distinguish the two laths because no physical orientation change is apparent however the inclusion of EBSD techniques, (Figure 14(c)) allows for the identification of this interface and manual segmentation of the laths (Figure 14(b)).

Upon attempting EBSD on a FIB milled surface it was impossible to obtain useable patterns. The underlying mechanisms of this phenomenon are not well understood and are part of on-going research. This phenomenon was initially determined from samples prepared in the
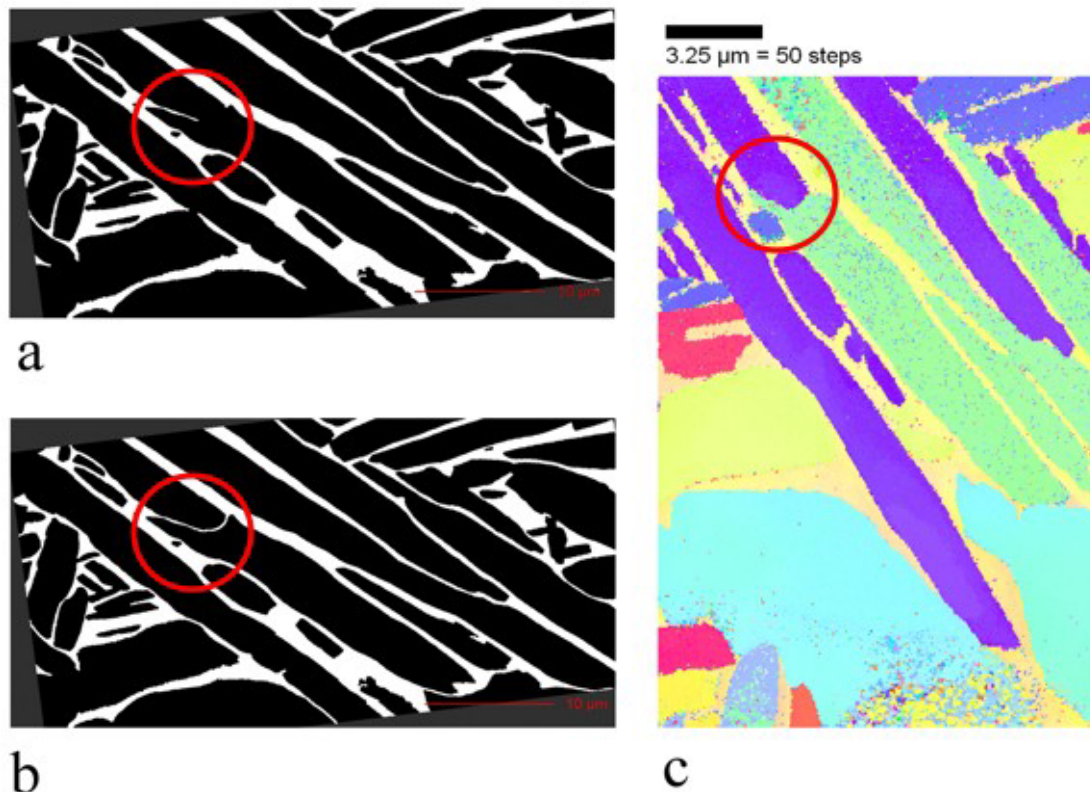
Figure 14: (a) Threshheld image lacking segmentation, (b) Threshheld image with segmentation, (c) EBSD OM identifying crystallographic interface.

DB235. The DB 600 NOVA is equipped with a more advanced ion column that allows for variable ion beam energy from 2 - 30 kV. The damage induced from ion-solid interactions is

well documented in the TEM community and is generally accepted that 1 nm of amorphization will be present for each kV of beam energy; i.e. a 30 kV ion beam should produce ~30 nm amorphous layer. This has been estimated from FIB milled TEM lamellae [13-21]. With the ability to lower the voltage of the ion gun to 2 kV it was desirable to determine if low kV, low angle milling would decrease/remove the amorphous layer from FIB milled surfaces and increase EBSD pattern quality and intensity such that OM collection would possible, even favorable.

The technique of low kV milling is not well established or understood, but was derived from examples used to remove amorphous damage found on FIB milled TEM lamellae [18-25]. Lowering the beam energy decreases the coherency of the beam and thus makes precise milling impossible. Low kV milling is performed at 5 degrees from parallel. EBSD patterns from this experiment are shown in Figure 15.

A Ti-6-2222 alloy was prepared analogous to the aforementioned cantilever procedure to facilitate FIB milling and EBSD collection. The surface was then milled using a 30 kV 9.3 nA ion beam and EBSD patterns were collected from the alpha and beta phases along with a 30 x 30 μm OM. A 5 kV 1.1 nA raster mill was then performed on the as-milled area for three minutes.

Figure 15: EBSD patterns collected from the alpha and beta phases of a Ti-6-2-2-2-2 alloy in the as-milled and low kV milled condition. Quantitative values for points indexed and required time to complete a 30 μm x 30 μm area.

172

EBSD patterns from the alpha and beta phases and OM were collected following the low kV cleaning. Subsequently, 1 micron was milled from the same area at 30 kV 9.3 nA and then raster milled at 5 kV 1.1 nA for 6 minutes. The percentage of correctly indexed points increased 70% and the OM scan times decreased 27%.

Due to the number of factors contributing to EBSD patterns formation, no standard method of quantification exists to rate patterns, other than relative comparison. In an attempt to quantify the improvement in EBSD pattern quality, line intensity profiles (Figure 16) were taken from identical regions of each relative EBSD pattern and plotted (Figure 17(a-f)).
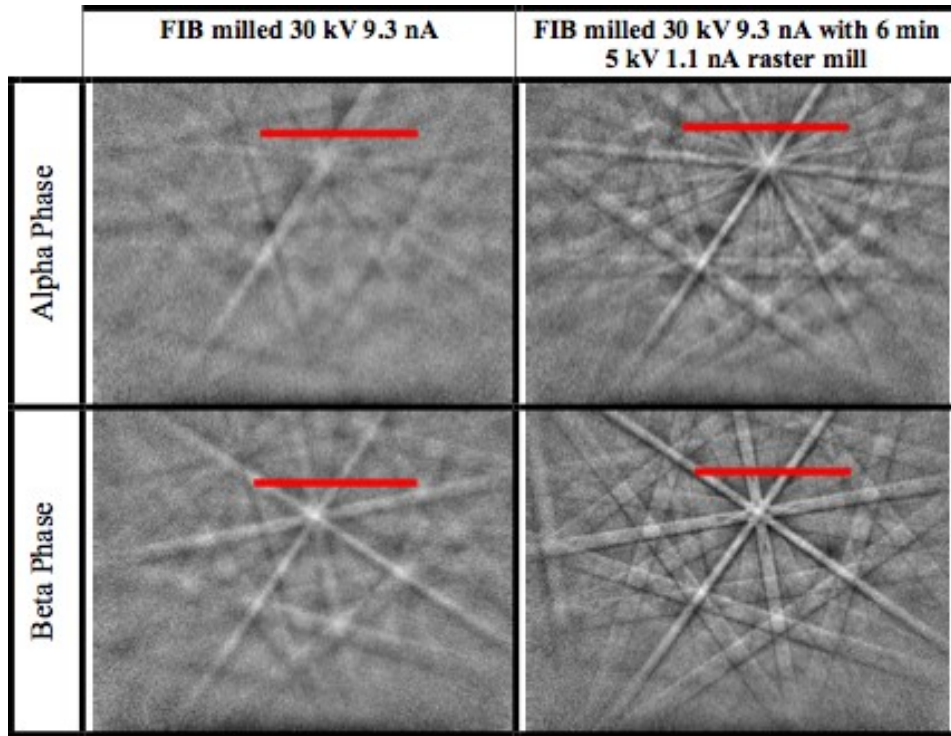
Figure 16: Schematic location of line intensity profiles to show qualitative improvement in EBSD pattern quality from a FIB milled surface following a subsequent low kV milling.

Figure 17(f) of the beta pattern is labeled to show the relative amplitude increase for that EBSD kikuchi pattern. This amplitude increase in intensity was adequate to create the drastic improvement in the percentage of accurate indexed points by the automated indexing programs.
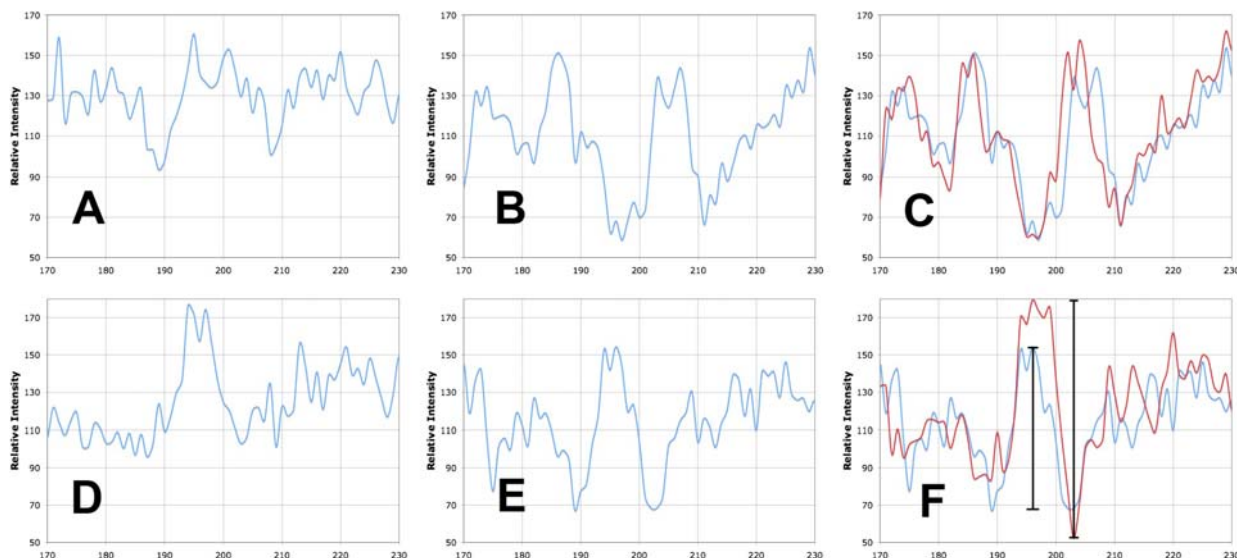
Figure 17: Line profiles from EBSD patterns as shown in Figure 17. (a) Alpha phase following 30 kV 9.3 nA milling, (b) alpha phase following 3 min. raster mill using 5 kV 1.1 nA, (c) alpha phase following 3 min. and 6 min. raster mill using 5 kV 1.1 nA, (d) beta phase following 30 kV 9.3 nA milling, (e) beta phase following 3 min. raster mill using 5 kV 1.1 nA, (f) beta phase following 3 min. and 6 min. raster mill using 5 kV 1.1 nA.

The use of EBSD OM to locate and segment alpha/alpha interfaces demonstrates one example of the wealth of information an individual EBSD OM provides for microstructural characterization. Analogous with the work performed on other material systems, [5,8,26-30] the ability to collect serial data-sets of three-dimensional EBSD OM is highly desirable and provides an abundant amount of information that is not captured by any other characterization technique.

The quality and intensity of EBSD patterns depends on a number of factors and ultimately determines the accuracy and speed with which patterns are collected and indexed. Researchers at OSU prepare samples by low-damage, mechanical polishing techniques that produce EBSD patterns similar to Figure 19. An OM map collected with this EBSD pattern quality on a 30 x 30 micron area at a step size of .1 micron will index properly 90-97 % of points in ~ 3.5 hours. This correlates to indexing ~14 frames/sec, whereas for nickel alloys
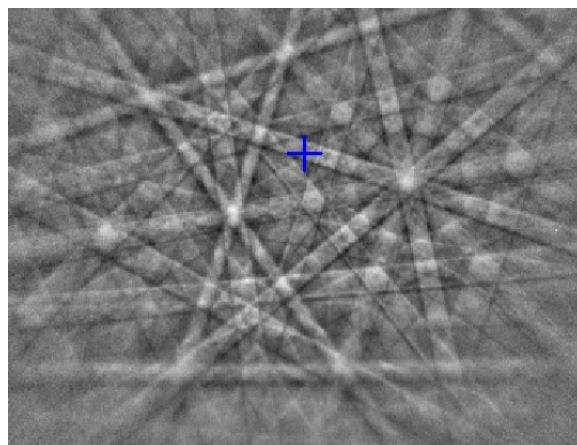
Figure 18: EBSD pattern collected from alpha phase of mechanically polished Ti-alloy

174

indexing has been performed at greater that 50 frames/sec. This discrepancy alone, between the two material systems, makes an identical scan require only 0.5 hours for a nickel alloy sample as opposed to 3.5 hours for a Ti alloy sample. The microstructural features in nickel alloys are such that the step size can be increased as well; further reducing the time needed for collection.

The increase in collection time for Ti alloys renders the serial collection of OM from every section of the interrogated volume impossible. The custom control script language will allow intermittent collection of EBSD OM to be incorporated rather trivially. An alternative approach to EBSD collection from every section is to determine, from microstructural feature size, an intermittent distance that OM can be performed. The crystallographic information can then be extrapolated to rendered volumes created from high-resolution electron images.

In this way, the resolution of the SEM can precisely define the morphology of microstructural features and OM can provide crystallographic information to this three-dimensional representation of microstructure. Nevertheless, removal of the FIB induced damage layer by low kV milling was demonstrated as a successful technique to improve EBSD pattern collection from FIB milled surfaces. Without this technique it is impossible to collect EBSD OM from 30 kV FIB milled surfaces.

The continued effort to characterize the FIB induced damage layer and correlate damage layers between materials systems such as nickel and titanium alloys is worthwhile, not only for EBSD OM collection, but also to the TEM community. The same damage layer that convolutes EBSD collection interferes with HRTEM/STEM and is not well understood currently.

4. References:

[1] R. T. Dehoff (1983). "Quantitative serial sectioning analysis : preview." <u>Journal of Microscopy</u> **131**: 259-263.
[2] J. Orloff, L. Swanson, M. Utlaut (2003). <u>High Resolution Focused Ion Beams: FIB and Its Application</u>. New York, Academic/Plenum.
[3] N.I. Kato, N. Miura, N. Tsutsui (1998). "A plasma-polymerized protective film for transmission electron microscopy specimen preparation by focused ion beam etching." <u>Journal of Vacuum Science and Technology A</u>(16): 1127-1130.
[4] FEI Company, Hillsboro, OR.
[5] M.A. Groeber, B.K. Haley, M.D. Uchic, D.M. Dimiduk, S. Ghosh (2006). "3D reconstruction and characterization of polycrystalline microstructures using a FIB-SEM system." <u>Materials Characterization</u> **57**: 259-273.
[6] JJ.Mulders, FEI Company, Unpublished research.
[7] M. W. Phaneuf (1999). "Applications of focused ion beam microscopy in materials science specimens " <u>Micron</u> **30**: 277-2888.
[8] M.D. Uchic, M.A. Groeber, D.M. Dimiduk, J.P. Simmons (2006). "3D microstructural characterization of nickel superalloys via serial-sectioning using a dual beam FIB-SEM." <u>Scripta Materialia</u> **55**: 23-28.
[9] J.R. Kremer, D.N. Mastronarde, J.R. McIntosh (1996). "Computer visualization of three-dimensional image data using IMOD." <u>Journal of Structural Biology</u>: **116** 71-76.
[10] Fovea Pro, Reindeer Graphics Inc., Ashville, NC.
[11] Photoshop, Version 7.0, Adobe Systems Inc., San Jose, CA.

[12] H. J. G. Gunderson, T. B. Jensen, R. Osterby (1978). "Distribution of membrane thickness determined by lineal analysis." Journal of Microscopy **113**: 27-43.

[13] T. Ishitani (1995). "Monte Carlo simulations of ion bombardment at low glancing angles." Microscopy and Microanalysis **9**: 3303-3306.

[14] T. Ishitani, T. Yaguchi, H. Koike (1995). "Transmission electron microscope sample preparation using a focused ion beam." Journal of Electron Microscopy **44**: 331-336.

[15] S. Lipp, C. Lehrer, B. Frank, E. Demm, H. Ryssel (1996). "Investigation on the topology of structures milled and etched by focused ion beams." Journal of vacuum Science and Technology B **14**(6): 3996-3999.

[16] J.F. Walker, R.F Broom (1997). Surface damage of semiconductor TEM samples prepared by focused ion beams. Institute of Physics Conference Series.

[17] T. Ishitani, H. Koike, T. Yaguchi, T. Kamino (1998). "Implanted gallium-ion concentrations of focused-ion-beam prepared cross section." Journal of Vacuum Science and Technology B **16**(4): 1907-1913.

[18] N.I. Kato, Y. Kohno, H. Saka (1999). "Side-wall damage in a transmission electron microscopy specimen of crystalline Si prepared by focused ion beam etching." Journal of Vacuum Science and Technology A **17**(4): 1201-1204.

[19] W. Boxleitiner (2001). "Simulation of topography evolution and damage formation during TEM sample preparation using focused ion beams." Nuclear Instruments and Methods in Physics Research B **175-77**: 102-107.

[20] J.M. Cairney, P.R. Munroe (2003). "Redeposition effects in transmission electron microscope specimens of FeAl-WC composites prepared using a focused ion beam,." Micron **34**(97).

[21] N. I. Kato (2004). "Reducing focused ion beam damage to transmission electron microscopy samples." Journal of Electron Microscopy **55**(5): 451-458.

[22] L.A. Giannuzzi, R. Guerts, J. Ringnalda (2005). "2 keV Ga FIB milling for reducing amorphous damage in silicon." Microscopy and Microanalysis **11**: 828-829.

[23] J. Mayer, L.A. Giannuzzi, T. Kamino, J. Michael (2007). "TEM sample preparation and FIB-induced damage." MRS Bulletin **32**: 400-407.

[24] J.R. Michael, L.A. Giannuzzi (2007). "Improved EBSD sample preparation via low energy Ga FIB ion milling." Microscopy and Microanalysis **13**(Supplemental 2): 926-927.

[25] S. Bals, W. Tirry, R. Geurts, Z. Yang, d. Schryvers (2007). "High-Quality Sample Preparation by Low kV FIB Thinning for Analytical TEM Measurements." Microscopy and Microanalysis **13**: 80-86.

[26] B.J. Inkson, M. Mulvihill, G. Mobus (2001). "3D determination of grain shape in a FeAl-based nanocomposite by 3D FIB tomography." Scripta Materialia **45**: 753.

[27] J. Konrad, S. Zaefferer, D. Raabe (2006). "Investigation of orientation gradients around a hard Laves particle in a warm rolled Fe3Al-bases alloy using a 3D EBSD-FIB technique." Acta Materialia **54**: 1369-80.

[28] S.I. Lieberman, A.M. Gokhale, S. Tamirisakandala (2006). "Reconstruction of three-dimensional microstructures of TiB phase in a powder metallurgy titanium alloy using montage serial sectioning." Scripta Materialia **55**: 63-68.

[29] Z. Zaafarani, D. Raabe, R.N. Singh, F. Roters, S. Zaefferer (2006). "Three-dimensional investigation of the texture and microstructure below a nanoindent in a Cu single crystal using 3D EBSD and crystal plasticity finite element simulations." Acta Materialia **54**: 1863.

[30] W. Xu, M. Ferry, J.M. Cairney, F.J. Humphreys (2007). "Three-dimensional investigation of particle stimulated nucleation in a nickel alloy." <u>Acta Materialia</u> **55**: 5157-5167.

5. Names of Personnel

Hamish L. Fraser (OSU Faculty Member)
Michael C. Uchic (AFRL/RX Mentor)
Dennis M. Dimiduk (AFRL/RX Mentor)
Peter C. Collins (OSU Research Scientist)
Robert E. A. Williams (OSU Graduate Student)

Task 9
Quantification of High Cycle Fatigue Damage Mode Dependence on Microstructure.
Alten Grandt (Purdue Faculty Member), Jeff Calcaterra (AFRL/RX Mentor), Pat Golden (AFRL/RX Mentor), Ryan Morrissey (AFRL/RX Mentor), Daniel Garcia (Purdue Graduate Student)

I. RESULTS and DISCUSSION

1. Introduction

Overview

Professor A. F. Grandt, Jr. and Purdue University graduate student Daniel B. Garcia spent six and ten weeks respectively working with Metals Branch scientists at the Air Force Research Laboratory Materials and Manufacturing Directorate (AFRL/RXLM) during the summer of 2003. The general goals of this program were to develop close working ties between Purdue University and AFRL/RXLM in the general area of high cycle fatigue (HCF) research and to provide a mechanism for focusing both Purdue and AFRL in-house research efforts toward critical USAF needs. This project was accomplished under a Purdue University subcontract with the Ohio State University Research Foundation (RF Project No. 743924, Purchase Order No. RF00952729, CFDA Number 12.800). The contract period of performance was 1 May 2003 to 30 April 2004. The accomplishments of that effort are briefly summarized below.

2. Methods, Assumptions, Procedures, Results

Accomplishments

Professor Grandt held many individual discussions with AFRL Materials and Manufacturing Directorate engineers and scientists during his six-week stay at WPAFB. He also met with individuals from the AFRL Air Vehicles Directorate and other Air Force organizations at this time. The goal of these discussions was to learn the general nature of USAF research needs in the area of structural integrity and to become familiar with ongoing in-house and contractual research programs in that area. These discussions gave him an excellent "big picture" view of the USAF research needs and he was able to provide some useful suggestions to USAF personnel regarding the progress of ongoing programs and future research opportunities.

In addition to the general indoctrination into the USAF research programs, four specific research topics were pursued at WPAFB with the able assistance of Mr. Garcia: shot-peened Ti-17 fretting contact pads, dovetail experiment contact pads, high frequency piezoelectric test experiment, and high temperature single crystal fatigue experiment. These activities are summarized below.

2.1. Shot Peened Ti-17 Contact Pads

The research on the Ti-17 contact pads was one of the initial goals at the beginning of the AFRL visit. The premise of the research is to perform crack growth threshold

experiments on C-specimens that were created from existing Ti-17 fretting contact pads. The goal is to propagate a fatigue crack from an existing fretting starter crack. This work is an extension of the research by Dr. P. Golden (AFRL/RXLMN), and includes stress intensity factor calculations and fractography. The material was obtained from fretting fatigue experiments sponsored by General Electric Aircraft Engines. The experiments make use of the AFRL/RX high frequency electromagnetic shaker to fatigue test the C-specimens until fracture. Figure 1 is a photograph and schematic of how the high frequency electromagnetic shaker applies the load to the C-specimen. These experiments help create data that can be used to determine the threshold stress intensity factor for the fretted material. The objectives of the experiments are to study the influence of shot peening on fretting, fractography, and threshold stress intensity factor of Ti-17. The goal of the analytic analysis is to provide a numerical that will help predict the crack growth behavior of surface enhanced material loaded in fretting fatigue. The testing is complete due to the assistance of AFRL/RXLM employees Bence Bartha and Andy Lackey, and their help was greatly appreciated.
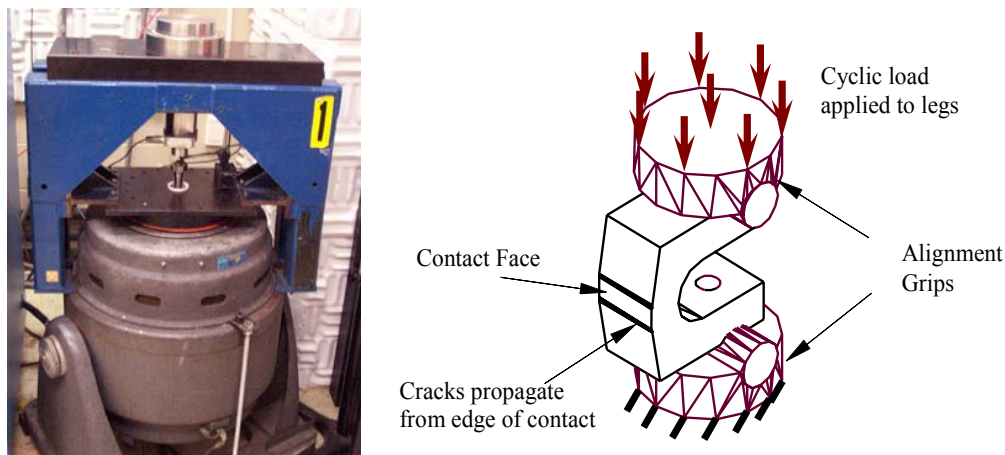

Figure 1. Photograph and schematic of high frequency C-specimen experiment

2.2. Dovetail Specimens

The dovetail fretting fatigue experiment at AFRL/RXLM created by Dr. P. Golden implements fretting contact pad specimens that are similar, but smaller, to the contact pads that are used at Purdue University for similar research. The idea for the dovetail fretting contact pads was to use the knowledge available from the large C-specimens to create a miniature C specimen or "Mini-C" specimen for HCF threshold research. By working with Dr. Golden, we developed a design for the Mini-C specimens and created an adapter fixture so that the HCF shaker test apparatus did not have to be modified from the existing C-specimen test configuration. Upon experimental validation, it was discovered that the Mini-C specimens work well in the HCF load fixture even though the applied loads are smaller than on the large C-specimens. Some modifications to the adapter fixture might still be made, but the Mini-C experiments should work and help provide good experimental data on the dovetail contact pads.

2.3. High Frequency Test Experiment

While working on the large C-specimens and the Mini-C specimens, it was decided to look into the possibility of creating a high frequency test machine for use at Purdue University. That idea came from the high frequency fretting test rig at Purdue that implements piezoelectric actuators. After talking with suppliers and engineers, a feasibility study was performed. In order for a piezoelectric actuator to be used for the C-specimen testing, two main factors were critical – displacement and load. The piezoelectric actuators can provide the load, but the displacement becomes an issue. In order to mitigate the displacement issue, a lever would have to be used which would require large loads. After analyzing the options, it became evident that the Mini-C specimens could be tested in a piezoelectric actuated machine, but the large C-specimens could not be tested as they are currently prescribed. Figure 2 is a plot of the operating envelope of a Mini-C specimen that could be mechanically tested in a high frequency test machine driven by a piezo-electric actuator.
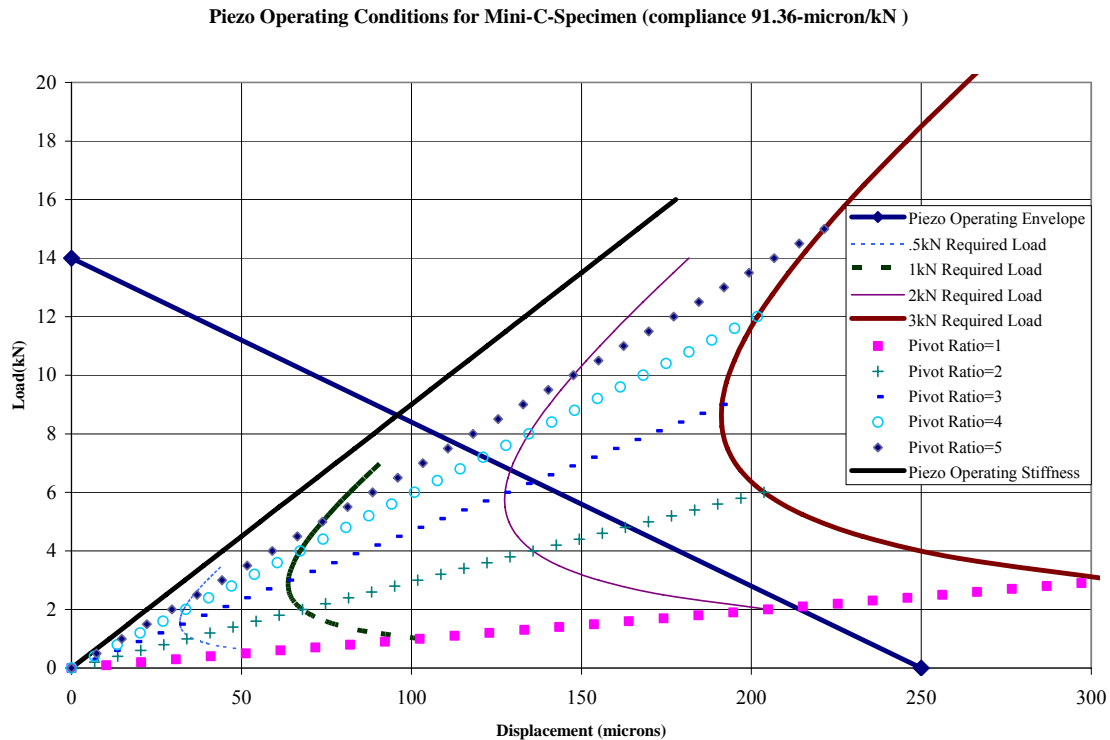
Figure 2. Piezo electric operating envelop for a high frequency mechanical testing apparatus

2.4. High Temperature Single Crystal Experiments

At the beginning of the AFRL/RX visit, it was requested by the Purdue fretting fatigue group that a multiaxial fatigue test be created for PWA 1484, a single crystal nickel superalloy. These experiments would validate or disprove assumptions for using uniaxial fatigue data for a multiaxial stress state created during fretting. The feasibility of

conducting such experiments with AFRL equipment was studied, and although possible, it was decided not to pursue those experiments during the summer of 2003. While researching multiaxial possibilities, it became apparent that secondary crystal orientation influences stresses in concentrator locations. Through analysis, it was found that the influence of the secondary crystal orientation on the stress state is minimal. The recognized stress concentration factor of a plate with a hole loaded in tension of an isotropic material is three, and the maximum values occurs perpendicular to the load axis. For anisotropic materials this is not the case, the maximum stress does not occur perpendicular to the load axis and is not three times the applied stress. Figure 3 shows the effect of anisotropic material on the stress concentration. Creating controlled notch fatigue experiments might provide a better understanding of the failure mechanisms associated with PWA 1484. We are currently working on developing a high temperature experiment that would allow us to observe the influence of crystal orientation on stress concentrators and fatigue life. The goal of this study was to provide some insight and design techniques for handling the influence of the secondary crystal orientation.
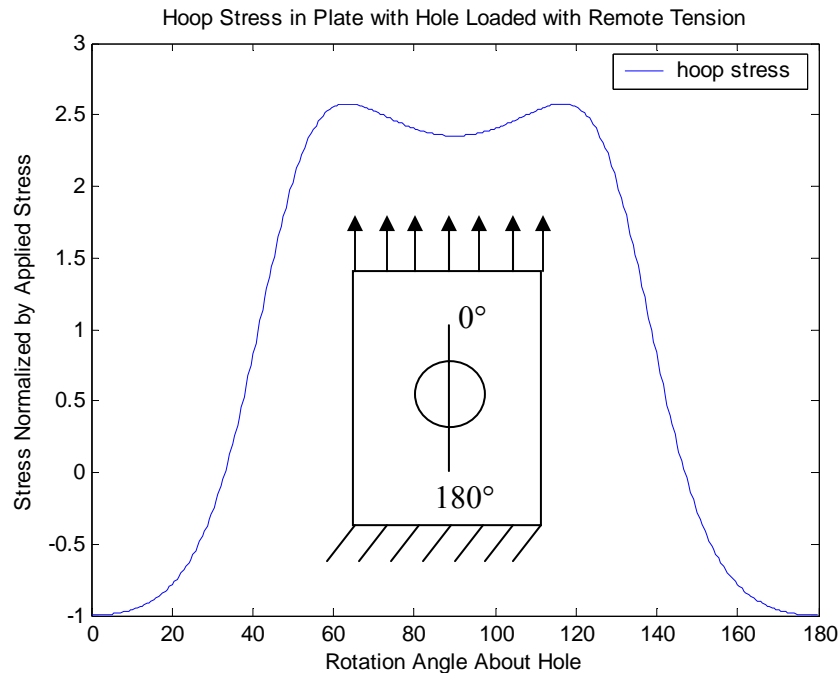
Figure 3. Graph of hoop stress in an anisotropic plate with a center hole loaded in tension

3. Conclusions

Overall, the Summer 2003 Visiting Scientist stay at the Air Force Research Laboratory Materials and Manufacturing Directorate was a success for both Professor Grandt and Mr. Garcia. The opportunities to work and meet with other researchers have proven and will continue to prove to be a great asset. The research started at AFRL on the surface enhanced C-specimens has developed further into a Ph.D. topic for Daniel, and he is

currently progressing in the work and research. He has, for example, successfully completed the Ph.D. preliminary examination in April of 2004.

Development and Characterization of high Temperature Titanium Alloys for High Mach Aerospace Structural Applications. *Hamish Fraser (OSU Faculty Member), Jim Williams (OSU Faculty Member), Daniel Evans (AFRL/RX Mentor, Patrick Martin (AFRL/RX Mentor), Ben Peterson (OSU Graduate Student)*

I. RESULTS and DISCUSSION

1. Introduction

The high temperature creep resistance properties of beta titanium alloys based on Timetal 21S (Ti-15Mo-3Al-2.7Nb-0.2Si, wt%) have been examined for potential use in acreage thermal protection systems (TPS) for aerospace applications. Timetal 21S, a beta titanium alloy with reasonable corrosion and oxidation resistance (see Table 1) and cold rollability also exhibits attractive creep properties, which have similar, if not improved, creep resistance with respect to Ti-6Al-4V, an α/β titanium alloy. This is notable given the fact that beta alloys typically exhibit poorer creep performance than α/β alloys (see Fig. 1). The focus of this project was to explore whether small changes in composition from a starting alloy (Timetal 21S) would result in improved creep resistance without significantly degrading other properties of importance in acreage TPS (e.g., the oxidation resistance and cold rollability).

Table 1. Oxidation properties of titanium and two alloys [1].

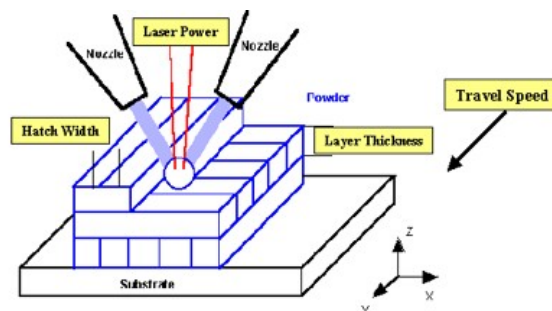| Oxidation Resistance 1200°F (650°C) Exposure				
	Weight Gain (mg/cm²)			
	24 hrs	48 hrs	72 hrs	96 hrs
Timetal 15-3	1.26	1.81	2.29	3.18
CP Ti	0.18	0.27	0.34	0.53
Timetal 21S	0.06	0.07	0.10	0.11
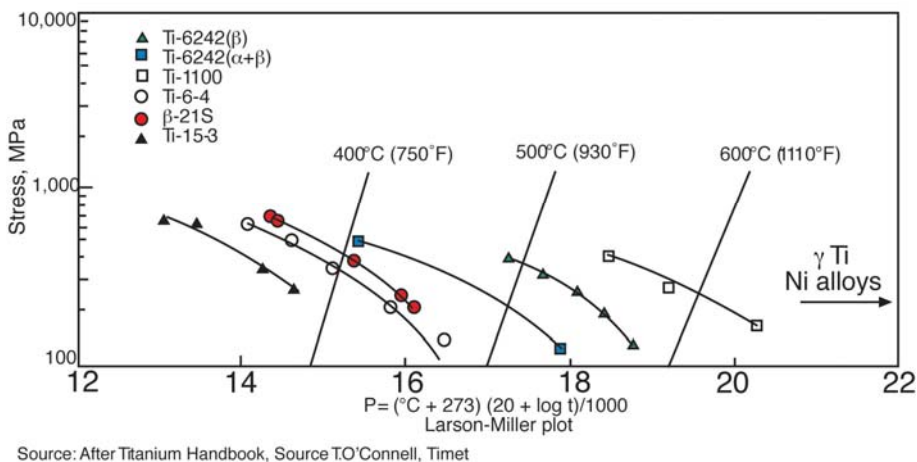
Figure 1. Larson-Miller plot of several titanium alloys [1].

2. Methods, Assumptions, Procedures

This task aims to apply knowledge of creep mechanisms (diffusion or dislocation based creep) to the alloy Timetal 21S in order to explore whether certain *specific* alloy additions affect the creep properties. To achieve this, certain types of elements were identified and added, based on their potential to favorably influence the creep properties of the alloy. The first set of alloy elements were identified to potentially retard diffusion of either the elements or vacancies. These species, large atoms that can be classed as having either a β-

Figure 2. The LENS^{TM} process, creating a three-dimensional solid. The schematic shows the powder feed, laser, and substrate are aligned with each other to melt and deposit the powder.

stabilizing or neutral effect, include variations of two alloying elements already included in the alloy (Mo, Nb) as well as three others - W, Sn, and Zr. A secondary effect of these larger atoms is their potential to impede dislocation motion by solid solution strengthening. To further explore whether α-phase stability or solid solution strengthening could improve creep properties, variations in the α-stabilizer Al were also affected. The second set of alloying elements was identified as ones that potentially influence creep mechanisms that involve dislocation motion and grain boundary sliding. Thus, precipitate forming elements, B and C were added to form coarse precipitates at micrometer length scales while Si and Ge were added to form fine precipitates at nanometer length scales.

2.1. LENS™ deposition and thermal history

Material was produced using the Laser-Engineered Net Shaping (LENS^{TM}) process (see Fig. 2), which is an additive manufacturing process. One benefit of the OSU LENS™ system is the presence of dual-powder feeders. This capability, in addition to the research expertise (OSU was the first to apply this approach), allows for the LENS™ to change the alloy composition quickly in a controlled, programmed fashion, allowing many homogeneous samples of different compositions. Rather than using costly pre-alloyed powder, this work exploited elemental blends of powders, which allow for rapid customization of powder, and therefore, sample compositions. Table 2 contains the elemental powders used for deposition and thermal or physical properties that are often important for laser deposition. For example, high enthalpies of mixing in liquid titanium, ΔH^{mix}, low melting points, low reflectivities, and low densities will tend to favor the LENS^{TM} process by requiring less laser power. For example, the elements of Mo, W, Sn, and Al need special attention to achieve the target composition. The elements Mo and W tend to be lean in the final deposits due to small heats of mixing, high melting points, and higher densities compared with Ti and Al. In contrast, Sn is highly exothermic, has a low melting point, and has a relatively low reflectivity causing many deposits to be Sn rich. The powder quantities were adjusted to achieve the target compositions. Also, aluminum has historically been a difficult element to achieve the target composition because of powder segregation before deposition. A Ti-50Al (at%) master alloy is used to achieve the target composition of Al within ±0.1 wt%. Thus, for the scope of this task, considerable effort was expended to develop the experimental techniques such that each deposit had an experimentally measured composition that was close to the target composition.

Subsequent to the deposition, all samples were solution treated above the beta transus (as determined using both ThermoCalc and Pandat) at 850˚C for an hour, stabilized at 700˚C for eight hours, and furnace cooled at 10˚C per minute. This thermal processing was conducted using a hot isostatic press (HIP), while operating at a pressure of 15 ksi in order to remove residual porosity form the LENS^{TM} process.

Table 2. Important parameters of LENS^{TM} elemental powder additions.

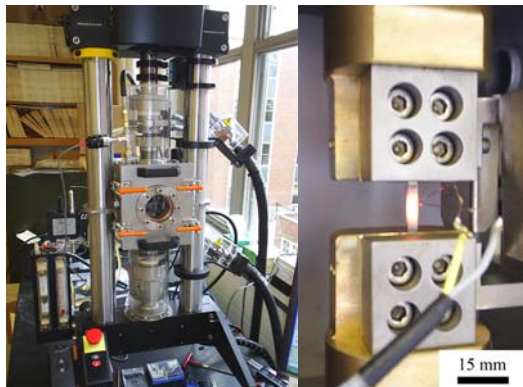| Alloying Element	ΔH mixing w/Ti (kJ/mole)	Melting Point (^{o}C)	Reflectivity at 1.064 μm	Density (g/cm^3)
Ti	0	1668	63%	4.5
Mo	-16	2610	57%	10.2
Nb	10	2468	77%	8.6
W	-26	3410	58%	19.3
Al	-137	660	91%	2.7
Zr	0	1852	16%	6.5
Sn	-139	232	46%	5.8
Si	-211	1410	32%	2.3
Ge	-188	937	40%	5.3
B	-200	2300	15%	2.3
C	-200	3527	17%	2.3

2.2 Simulated Creep Testing

Initial mechanical testing involved strain-rate controlled ($1.0*10^{-5}$ mm/mm/sec) compression tests of right cylinders 15 mm tall with a 5 mm diameter. Fig. 3 is a schematic depicting the original geometry built with the LENS^{TM} process, designed to allow for an investigation of the effect of texture on creep properties. These two orientations, horizontal and vertical, are given with respect to the build direction. It has been established that there is often a growth texture in material deposited using the LENS™ process.
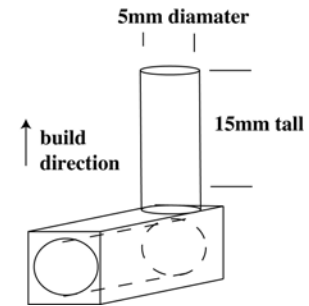
Figure 3. Schematic depicting the geometries initially built with the LENS^{TM} process.

The majority of the testing of samples involved an electrothermal mechanical tester (ETMT) developed by National Physical Laboratories (NPL) and Instron (see Fig. 4). The ETMT is a modified Instron load frame that includes capabilities to resistively heat samples in an accurate and rapid fashion to achieve a desired temperature and mechanically test in either position or load control. The ETMT offers the advantage of testing many samples from a small amount of material. Fig. 5(a and b) depict the configuration of the ETMT and the approximate temperature profile created by the resistive heating. A R-type (PT/Pt13%Rh) thermocouple is attached to the center of the sample via a spot welder for accurate temperature measurement. The temperature gradient has been found to have a constant temperature region

Fig. 4: The ETMT.

of about 5mm in the center of the sample. The ETMT has a small, high-integrity chamber to allow for testing in an inert atmosphere. Ramp rates up to ~200˚C/sec can be achieved eliminating the timely steps of furnace ramp up and cool down. Two identical size and material (Pt13%Rh) wires are spot-welded onto the sample approximately 5mm apart to measure a voltage drop. True strain is determined by measuring the change in potential drop due to a change in length between the wires and the cross sectional area of the sample. Fig. 6 shows a plot of sample strain versus time for data obtained using the ETMT. This plot closely resembles data obtained using traditional creep tests. Constant load tests at 650˚C were performed to determine the minimum creep rate values of the samples of different compositions.
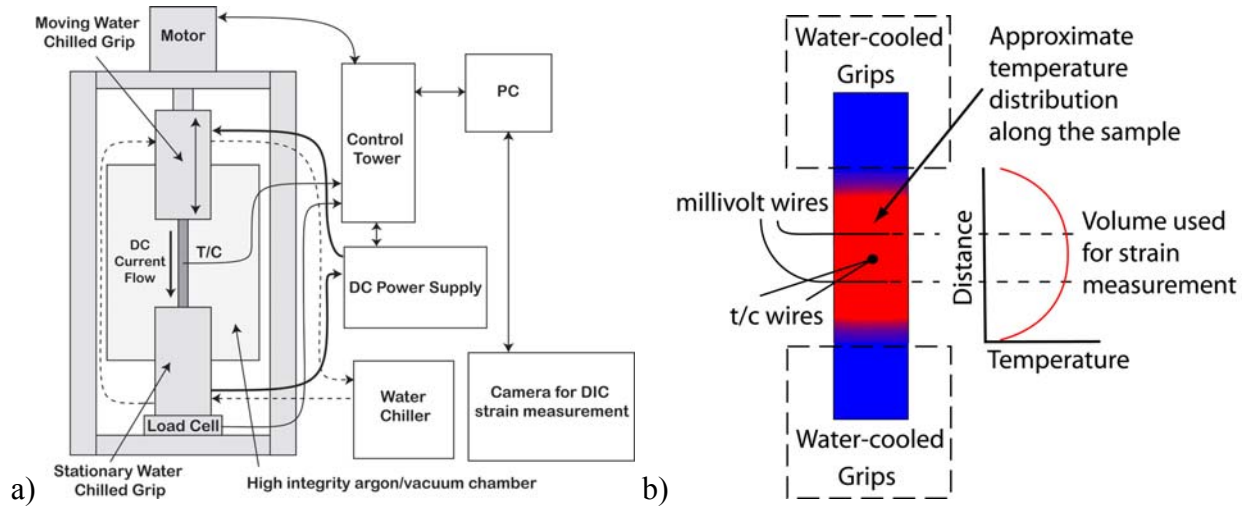
Figure 5. Schematics depicting a) the configuration and b) the thermal profile of the ETMT.

Since the ETMT is a new piece of equipment that is enabling the bulk of the work in this task (i.e., capable of accelerated simulated creep testing in an appropriate strain regime to explore the effect of alloying elements on creep mechanisms/properties), considerable efforts were expended to validate the technique to ensure that it produces data that trends with legacy data. This validation relied on a comparison of legacy data (e.g., Fig. 1) for α/β and β Ti alloys. Table 3 shows the minimum creep rate values for these materials as determined using the ETMT at 650˚C and 50 MPa. The results trend in the same fashion as previous studies: Ti21S, α+β-processed Ti-6242, and β–processed Ti-6242 material have increasing creep resistance, respectively (decreasing minimum creep rates).
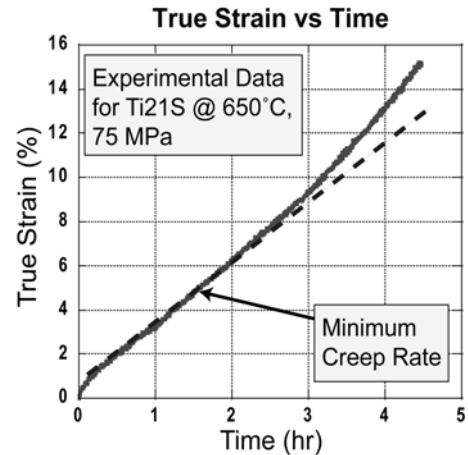

Figure 6. Example data from a constant load creep test of Timetal 21S performed at 650˚C and an initial stress of 75 MPa.

186

Table 3. Minimum creep rates for several titanium alloys tested under load control conditions in the ETMT at 650˚C and 50 MPa.

Material	Minimum Creep Rate (sec^{-1})
Ti21S	$1.1 \pm 0.7 * 10^{-5}$
Ti6242 ($\alpha+\beta$–processed)	$6.9 \pm 0.9 * 10^{-7}$
Ti6242 (β-processed)	$3.3 \pm 1.2 * 10^{-7}$

2.3. Characterization

For each sample, several micrographs (e.g., see *Fig. 7*) were collected using a scanning electron microscope (SEM) operating at 15kV in backscattered electron mode (BSE). In order to quantify the microstructural features, the micrographs were collected in a random and unbiased fashion, and a series of stereological procedures were applied to the micrographs to measure the volume fraction α, average α-lath thickness, and the average β-mean free path were measured. The β-mean free path is a measure of the distance between α-laths. The bulk composition was measured using standardless EDS for each sample.
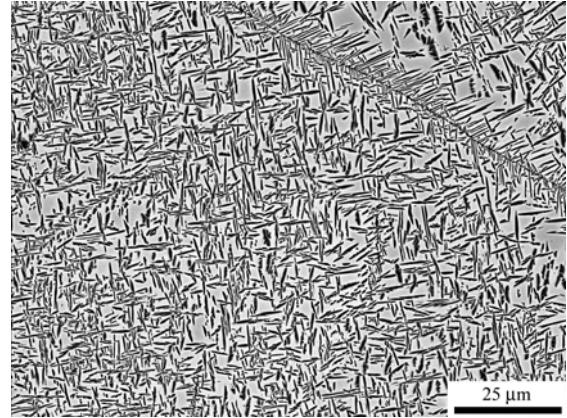
Figure 7. BSE micrograph of a sample microsctructure (LENS™ deposited Timetal 21S). The matrix phase is β-titanium and the dark, precipitates are α-laths.

2.4. Neural Network Development

Several neural networks were developed where the input variables included the experimentally measured microstructural and compositional variables while the output variables were the experimentally measured minimum creep rates. Two types of models have been incorporated in this research – those based on fuzzy logic and those based on Bayesian statistics. While fuzzy logic methods can be used to determine trends from smaller datasets, the outputs are biased based upon choices of the modeler. Conversely, neural networks based upon Bayesian statistics typically require larger amounts of data, are unbiased and can result in better predictions. Models based upon Bayesian statistics have been exploited by the authors for the prediction of tensile properties in both β and $\alpha+\beta$–processed Ti-6Al-4V [2,3]. These approaches have been based on neural network models incorporating Bayesian statistics developed by McKay [4], and include accurate descriptions of the microstructural features based on rigorously developed stereological methods, as described briefly above. The details regarding the development of these models has been described elsewhere. Once developed, the neural network can be used in one of two ways. The first involves the development of a predictive tool, where the properties of a test dataset are predicted. For the previous models, following training and testing, the models for the prediction of tensile properties have resulted in less than 2.5% difference in magnitude from experimentally measured values for both yield strength and ultimate tensile strength [5]. However, while such results have been quite successful in the prediction of tensile properties, the application of neural network models to the prediction of creep properties in beta alloys is expected to be significantly
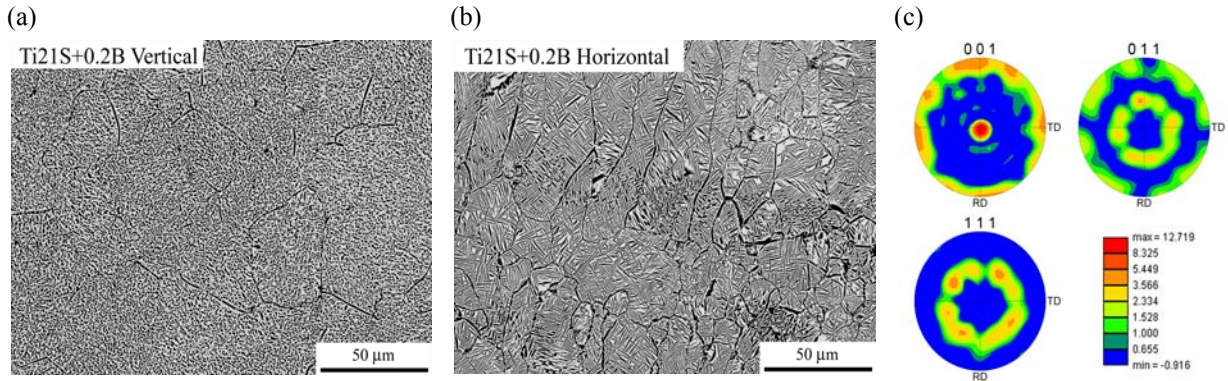
more difficult, and hence, the results are likely less accurate. This is due to the complicated manner in which the material responds to the application of a load at elevated temperatures, and the different creep mechanisms that can operate. The second involved the use of the neural network to perform virtual experiments. These are usually *controlled* experiments where the values of given microstructural features can be set to, or held at, given values (e.g., their average). In this way, it is possible to obtain information from actual experiments where such control of individual microstructural features is not possible. One such experiment is the virtual determination of the functional dependencies. The functional dependencies have been determined by setting all but one variable at a fixed average value, and allowing the variable to vary while observing the change in the predicted minimum creep rate. The predicted minimum creep rate can then be plotted

Table 4. Target and standardless EDS determined compositions of four different categories based on the stabilizing nature of the alloying additions. B & C not determined. O < 1500 ppm determined on selected samples.

		Composition	
	Element	Target Range (wt%)	Actual Range (wt%)
Alpha Stabilizers	Mo	15	held constant
	Nb	2.7	held constant
	Si	0.2	held constant
	Al	1.6 - 4.4	1.4 - 4.1
	Sn	0.1 - 5.2	0.3 - 6.7
	Zr	0 - 7.2	1.2 - 12.4
Beta Stabilizers	Al	3	held constant
	Si	0.2	held constant
	Mo	11.3 - 18.6	11.8 - 21.5
	Nb	0.8 - 4.2	1.3 - 5.7
	W	0.2 - 5.9	2.3 - 9.0
Small Dispersoids	Mo	15	held constant
	Al	3	held constant
	Nb	2.7	held constant
	Si	0.2 - 0.8	0.4 - 1.3
	Ge	0.1 - 1.2	0 - 2.1
Large Dispersoids	Mo	15	held constant
	Al	3	held constant
	Nb	2.7	held constant
	Si	0.2	held constant
	B	0 - 0.4 *	-
	C	0 - 0.6 *	-

directly against this single variable, and can provide insight into the functional dependency of the variable.

For this study, the microstructural variables included the volume fraction α, the average α-lath width, and the average β-mean free path. Similarly, for the compositional variables, variations in α stabilizers (Al, Sn, Zr), β stabilizers (Mo, Nb, W), small (Si, Ge), and large (B, C) dispersoid forming elements are possible. Interdependencies exist among all of the inputs. Therefore, to limit the total number of interdependencies that might occur by limiting the number of input variables, four separate databases were developed based on compositional additions. Table 4 lists these four groups with the target and actual compositional ranges achieved as determined by standardless EDS.

3. Results and Discussion: Progress towards a Creep Resistant β-Ti alloy

(a)   (b)   (c)

Figure 8. (a) and (b) Backscattered electron micrographs showing the effect of texture in a single deposit with an identical composition (note: the horizontal and vertical designations refer the build orientation in LENS™ (see Fig. 3)) and (c) select inverse pole figures of several grains from the face normal to the laser (vertical) in the LENS process with an electron backscattered diffraction (EBSD) pattern from a scanning electron microscope (SEM).
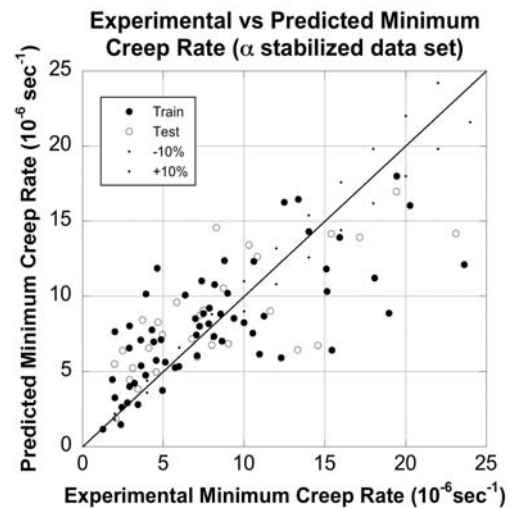
3.1. Compression Tests (strain rate ~ $1.0*10^{-5}$ mm/mm/sec)

The preliminary simulated creep experiments performed using compression tests (strain rate ~$1.0*10^{-5}$ mm/mm/sec) indicated a significant difference in properties resulting from texture differences resulting from the prior LENS™ processing. Figures 8(a-b) show backscattered electron micrographs from horizontal and vertical slices of a single LENS™ deposit. This sample has the same composition, but the texture in the parent, matrix β phase (*see Fig. 8(c)*) results in a strong, preferential distribution of the resulting α-lath precipitates. Fig. 8(c) is a set of inverse pole figures from electron backscattered diffraction (EBSD) patterns from an SEM of the face normal to the laser/build direction from a LENS™ deposit. They show that, on average, the beta grains are oriented with the <001> directions parallel to the build direction and have a nominally random texture perpendicular to the <001> directions. In order to validate both microstructures and properties obtained in LENS™ deposits, a series of arc-melted buttons of various compositions were prepared (thermal history identical to LENS™ deposited materials) and tested using the same slow strain-rate compression tests. The data from all three types of samples (vertical (33 data points) and horizontal (14 data points) LENS™ deposits and arc-melted buttons (21 data points)) were incorporated into a fuzzy logic model, where all the data was used to train the model. The results obtained using virtual experiments are shown in fig. 9. These results show that the horizontal and arc-melted tested material displays mechanical properties that are superior to those of the vertically tested deposits when all inputs are held constant and

Figure 9. The similarity between arc-melted and horizontal samples and display superior yield stress values vs. volume fraction alpha.

the volume fraction α is varied. These preliminary results were important results in developing the experimental procedures that were incorporated for the production of a larger, database of LENS™ deposited horizontal samples and load controlled creep tests.

3.2. Development of database using load-controlled ETMT creep tests

While there are several methods of evaluating the quality of the neural network models, including an analysis of the mean square errors (MSEs), which is often used to guide in selecting the "optimum" model in terms of weighting functions and nodes when developing the original models, the most useful involves a simple, visual analysis of the degree to which the predicted data matches the experimentally determined values. Fig. 10 offers such an analysis by
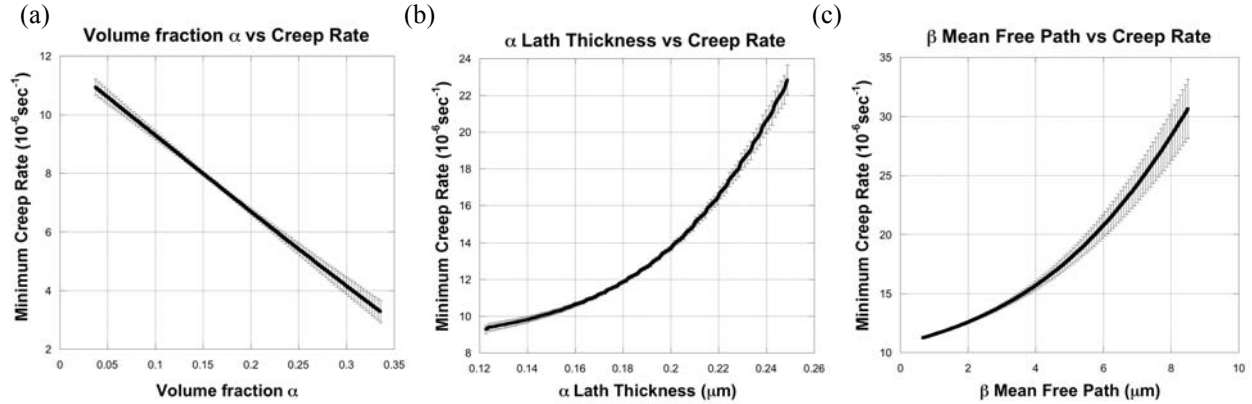

Figure 10. Plot of the experimental versus predicted minimum creep rates for the α stabilizer data set.

(a) Volume fraction α vs Creep Rate
(b) α Lath Thickness vs Creep Rate
(c) β Mean Free Path vs Creep Rate

Figure 11. Virtual experiments of various microstructural features on the minimum creep rate: a) volume fraction α (α stabilizer set), b) α-lath thickness (μm) (β stabilizer set), and c) β-mean free path (μm) (β stabilizer set).

plotting the experimental values against the predicted data for the minimum creep rate. This figure is for the α stabilized data set, where 60 data points were used to train and 28 data points were used to test the model. Similarly, the β stabilized data set used 50 data points to train and 25 data points to test the model. Ideally, a perfect model (i.e., one that captures all of the interdependencies and makes predictions without any deviation from what is experimentally determined) will result in a straight line with a slope of unity. Clearly, the model, which fig. 10 represents, has not captured all of the possible variables, interdependencies, or is a result of an insufficient database. Based largely on this program, work continues to identify the sources of the errors in these models. For example, work continues to explore whether there are any missing input variables.

While the poorer model quality is not surprising, given the complex nature of creep and the number of input variables, it is still possible to explore the effect of each microstructural input on the minimum creep rate. The inputs that most significantly influence the minimum creep rate should still result in reasonable functional dependencies. Fig. 11 (a-c) show the effect that volume fraction α, α-lath thickness, and β-mean free path have on the minimum creep rate in the data sets. It is clear from this figure that an increase in the volume fraction α results in an increase in the creep resistance (decrease in the minimum creep rate), while an increase in the α-lath thickness and β-mean free path both result in a decrease in the creep resistance (increase in the minimum creep rate).

While the underlying mechanisms for these virtual experiments have yet to be determined, some comments will be made regarding each and some early progress at determining the mechanisms. The first functional dependency, shown in fig. 11 (a) shows that as the volume fraction α increases the creep resistance increases. This is not surprising, considering that the α-Ti alloys intrinsically have better creep performance. This has been attributed to both the decreased diffusivity in the close-packed α-phase and the fact that the α-Ti has fewer active slip systems for dislocation glide. Figs. 11 (b-c) are likely related to slip length
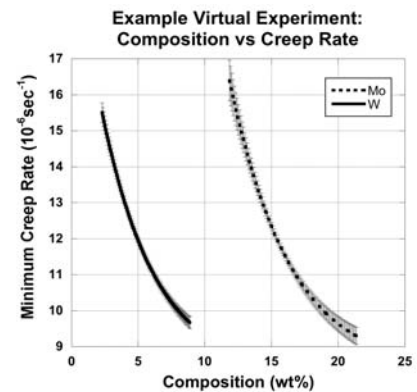
Figure 12. Two virtual experiment depicting the effects of Mo and W, while holding other inputs constant.

190

arguments. A similar trend is observed in the tensile properties of Ti-base alloys as is observed in Fig. 11 (b), specifically, the alloy is weaker as the α-laths coarsen. This has been attributed to slip length at room temperature, but should be extended to dislocation glide arguments at this elevated temperature (a temperature at which it is *expected* that the dominant creep mechanism will be glide controlled). It is anti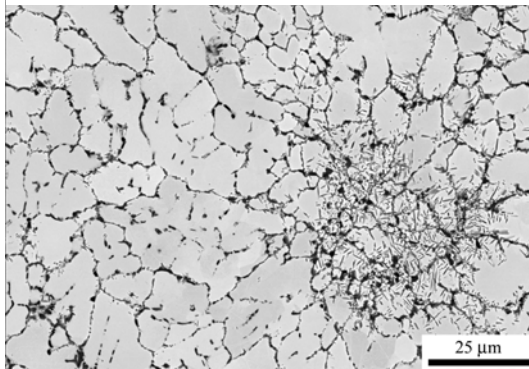cipated that fig. 11 (c) is related to not only the previously mentioned slip-length argument but also to average spacing between pinning events.

In addition to microstructural variables, composition also affects the minimum creep rate. Fig 12 describes the effect of Mo and W and shows that creep resistance is improved. Given that volume fraction α is artificially held constant in the virtual experiment, the improved creep resistance can possibly be attributed to either the decrease in the diffusivity of various elements and vacancies due the large atomic size of Mo and W as compared with Ti, or an increase in retarding effects to dislocation glide due to the solid solution effects. For the diffusion based mechanisms, creep mechanisms including vacancy assisted dislocation climb, will be hindered.
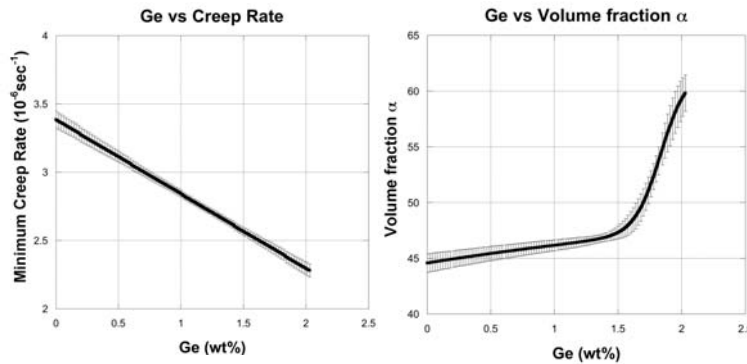
Figure 13. Virtual experiments depicting a) Ge versus minimum creep rate and b) Ge versus volume fraction α.

The small (Ge,Si) and large (B,C) dispersoid compositional datasets did not produce data that was overwhelmingly significant. The most promising of these compositions is the effect of Ge. It was found that it causes a slight improvement on the miniumum creep rate, which may be related to its effect on the nucleation and/or growth of the alpha phase as shown by the virtual experiments in figs. 13(a and b). Implementing elemental B and C (graphite) into the LENS™ deposits proved to be difficult. The microstructures appeared randomly agglomerated with regions of high density of α-Ti, TiC, and TiB phases (see fig. 14)

Figure 14. SEM backscattered micrograph of a sample with carbon and boron additions.

3.3. Effect of composition on microstructure

Another manner in which the neural networks can be used is to explore the effect of composition on microstructural features. Similar virtual experiments can be developed. However, it is important to consider which of the microstructural variables are intrinsic variables (e.g., predominately related to thermodynamics) and which are extrinsic variables (e.g., related to processing – for example, number of nucleation events). For example, fig. 15 (a) shows the intrinsic effect of two stabilizers (Al and Mo) on the volume fraction of α after stabilization at 700°C for 8 hours, while fig. 15 (b) shows the extrinsic effect of Zr and Mo on the β-mean free path after stabilization at 700°C for 8 hours. While the trends in fig. 15 (a) would be expected for

191

any sample of the same composition subjected to the same stabilization treatment, fig. 15 (b) will be affected by any previous processing/working operations. However, while the magnitude of the trends will change in fig. 15 (b), the general form of the curves (i.e., positive or negative) are likely to remain. This is expected unless there is an effect of processing on precipitation sequences or preferential nucleation sites (e.g., formation of ultrafine dispersions of other phases). With respect to fig. 15 (a), in order to maximize the volume fraction α, Al should be maximized and Mo should be minimized. This compositional effect is in keeping with general titanium knowledge (e.g., Mo and Al equivalencies). Nb and W have a smaller decreasing effect, and Sn and Zr were found to be neutral elements. For fig. 15 (b), Mo and Zr appear to have the greatest effect on the β-mean free path, likely due to a retarding in the phase transformation kinetics for the former, and an unknown mechanism for the latter.

The effect of Zr at higher solute contents illustrates a benefit of the combinatorial approach that has been applied in this task. Specifically, it was discovered that Zr, in the presence of Sn and Ti, will form a phase that has a deleterious effect on the properties of the alloy. This phase, observed as a bright white phase in Fig. 16, not only decorates the grain boundaries, but is also present within the grains at a refined scale. TEM standardless EDS has been used to identify not only the enrichment in Zr in this phase (>70 wt%), but also suggests the maximum solubility in the α and β phases prior to the formation of this phase. This solubility is approximately 6wt%. Therefore, any alloys that are further developed must contain less than 6 wt% Zr.
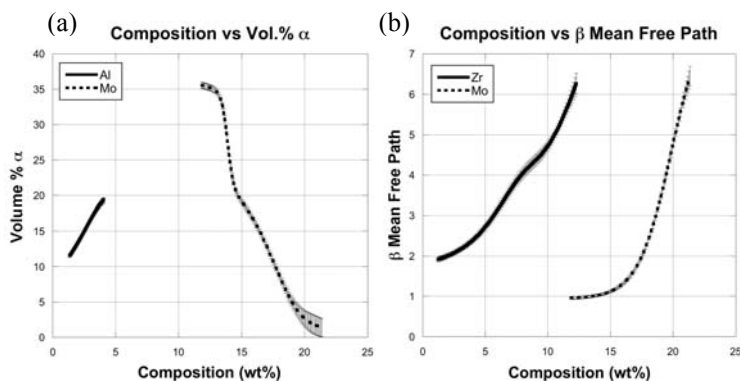
Figure 15. Virtual experiments of the effect of composition on (a) F_V α and (b) β-mean free path.
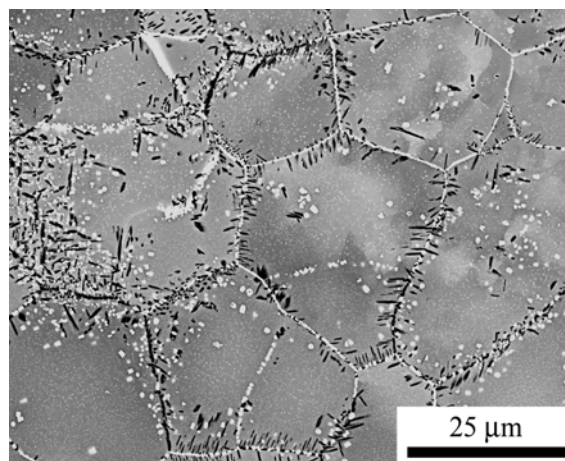
Figure 16. BSE micrograph showing the beta matrix and alpha (dark) and Zr-rich (white) precipitates. (17Mo-4Nb-3.2Al-10Zr-5Sn)
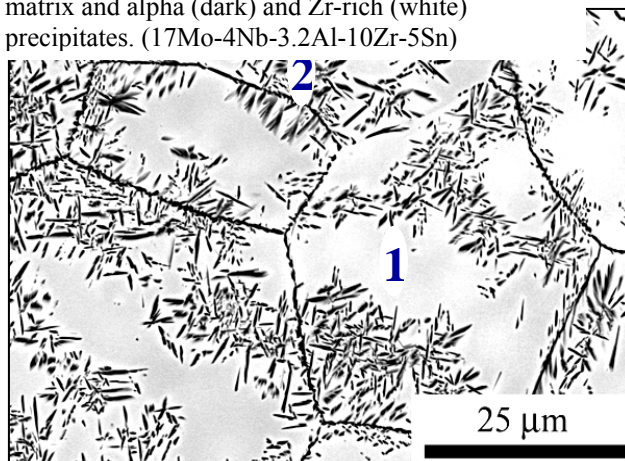
Figure 17. Microstructure of a sample showing the dark alpha phase and light beta phase. Region 1 is the alpha denuded region and region 2 is an alpha rich

3.4. Identification of missing input variables

As described previously, work is continuing on the identification (and confirmation) of missing microstructural variables. One such variable is the large regions of α-denuded β regions (*see Fig. 17*). It is anticipated that if these regions are truly free of α, including sub-scale α-laths that may only be visible in a TEM, the operable dislocations may experience a large region of unobstructed β over which to glide. Similarly, it is expected that there would be a nominal increase in diffusion in these regions, although the absence of boundaries may compensate for this. Therefore, one such model that is currently under development will include the average volume fraction and size of the large regions of beta, the diffusivity of titanium in the presence of the various elements, and composition of the beta phase. Fig. 18 (a and b) shows the difference in dislocation densities and configurations between regions with and without α-laths. The visible dislocations in the region denuded of α-laths appear to be straight and the density is lower than the region with α-laths (see Fig. 18 (a)).

a)   b)
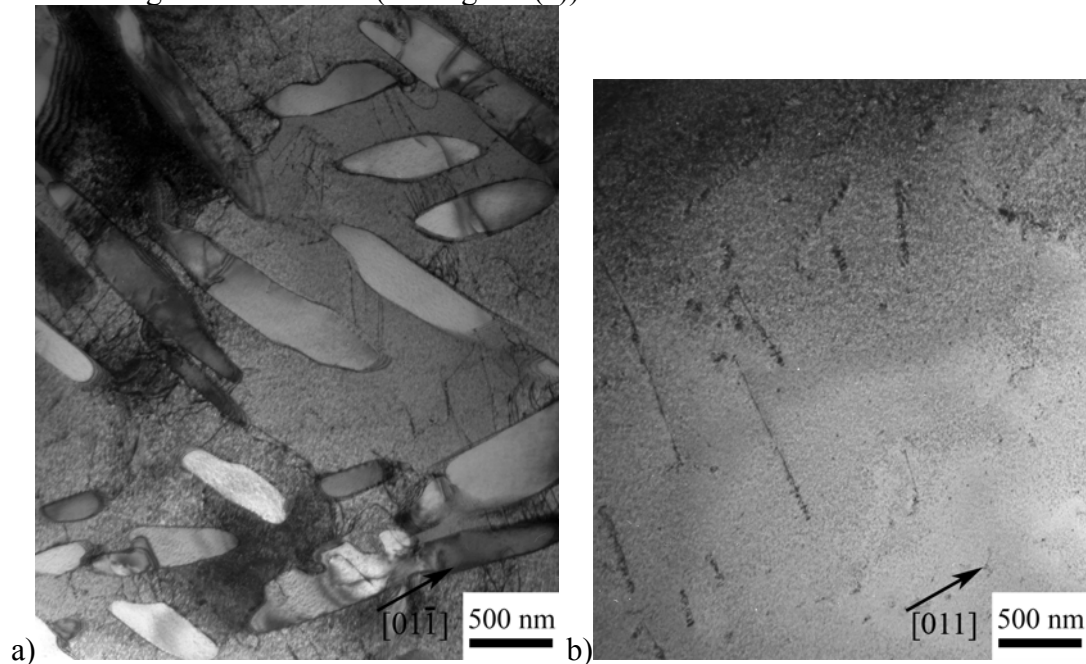
Figure 18. TEM Bright field micrographs depicting the difference in visible dislocation densities and configurations between regions a) with α-laths and b) denuded of α-laths.

4. Conclusions

There has been considerable effort at developing methodologies by which the creep properties of a material may be screened. This work has focused on optimizing creep properties for alloys based on Timetal 21S. Initial work suggests that control of the β-phase will dictate the creep properties in this temperature/stress regime where dislocation glide mechanisms are expected to dominate, while the scale of the α-precipitates will also play a significant role. This includes the β-mean free path. Additional work is currently focused on understanding and controlling the α-denuded regions of the microstructure. Elements that appear to dictate the β-mean free path include Mo and Zr. There may be a solid solution strengthening effect or contribution to vacancy motion upon the addition Mo and W solute additions.

5. References

[1] O'Connell. Titanium Handbook.

[2] Kar, T. Searles, E. Lee, G.B. Viswanathan, J. Tiley, R. Banerjee, and H.L. Fraser: *Metallurgical and Materials Transactions A*, vol. 37A (3), 2006, pp 559-566.

[3] P.C. Collins, S. Kar, T. Searles, S. Koduri, G.B. Viswanathan, J. Tiley, R. Banerjee, and H.L. Fraser, FDM Proceedings.

[4] D.J.C. Mackay: *Neural Computation*, vol. 4(3), 1992, pp 448-472.

[5] Collins, PC, Koduri, S, Welk, B, Tiley, J, and Fraser, HL, "On the Influence of Alloy Content on the Tensile Properties in $\pm\square^2$ Processed $\pm^2$ Ti Alloys" - To be published

6. Names of Personnel

Hamish Fraser (OSU Faculty Member)
Jim Williams (OSU Faculty Member)
Daniel Evans (AFRL/RX Mentor)
Patrick Martin (AFRL/RX Mentor)
Peter Collins (OSU Research Scientist)
Ben Peterson (OSU Graduate Student)

Task 11

Development of a Methodology for Hydrogen Embrittlement Resistance. *Gerald Frankel (OSU Faculty Member), Dallis Hardwick (AFRL/RX Mentor), N. Gingo (OSU Graduate Student), X. Liu (OSU Graduate Student)*

I. RESULTS and DISCUSSION

1. Introduction

Microstructural heterogeneities, such as dislocations, grain boundaries and particle interfaces, play a number of roles in their effect on sensitivity to hydrogen. They can reduce the apparent diffusivity through residence time and trapping effects. Furthermore, they can provide sites for preferential hydrogen segregation and partitioning. The accumulation of hydrogen at second phase particles and precipitates is generally considered to induce fracture or weakening of the particle-matrix interface, thereby promoting microvoid initiation and premature failure. In general, traps characterized by a high saturation concentration and high binding energy are considered to be conducive to hydrogen embrittlement (HE). There are examples, e.g. TD Nickel, in which the presence of strong irreversible traps appears to decrease the susceptibility to hydrogen [1] but the role of trapping in ameliorating HE has not been well studied.

Mechanical alloying (MA) can introduce a fine inert oxide dispersion into matrices that contained desirable alloying elements and imparted good properties. Powder metallurgy (P/M) can provide a means for producing dispersion-strengthened alloys with wide range of compositions. MA754 was the first mechanically alloyed oxide-dispersion-strengthened superalloy to be produced on a large scale. It is an Y_2O_3 dispersion strengthened, nickel-chromium superalloy. The alloy's strength, in conjunction with its high melting point and microstructural stability, made it an attractive material for gas turbine engine components, furnace fixtures and skid rails, fasteners and other applications. But its corrosion properties and hydrogen embrittlement resistance in electrolytes have not been investigated.

In the present investigation, the room-temperature corrosion behavior of MA754 was investigated in 0.1 N H_2SO_4 and 0.1 N NaOH solutions using the potentiodynamic polarization technique. Y_2O_3 particles were expected to have a beneficial effect on the hydrogen embrittlement of MA754 similar to the effects shown for ThO_2 in Ni. To test this hypothesis, the hydrogen embrittlement and the trapping in MA754 and several comparison alloys were investigated.

2. Methods, Assumptions, Procedures

The materials used in this study were nickel-based MA754, Waspalloy, In 600, Ni 200 and Ni-20Cr alloys, and their nominal chemical compositions are given in Table 1. Thin sheet samples sized 20x20 mm were cut using EDM or diamond saw from bulk ingot. Membrane foils for hydrogen permeation experiment were ground up to 1200 grit of silicon carbide abrasive paper, thinned to 40-100 μm thickness and polished to 1 μm. Metallurgical microstructure was examined using optical microscope (OM), scanning electron microscopy (SEM) and transition electron microscopy (TEM).

Table 1. Nominal Chemical compositions of tested alloys

Alloy	Nominal composition, wt.%												
	Ni	Cr	Fe	C	Al	Ti	Cu	Si	Mn	Mo	Co	Y2O3	Other
MA754	78	20	1	0.05	0.3	0.5	-	-	-	-	-	0.6	-
Ni-20Cr	80	20	-	-	-	-	-	-	-	-	-		-
IN 600	72	15.5	8	0.15	-	-	0.5	0.5	1	-	-		0.02
Ni200	99	-	0.4	0.15	-	-	0.25	0.35	0.35	-	-		0.01
Waspaloy	54	19.5	2	0.07	1.4	3	0.5	0.75	1	4.25	13.5		0.13

A thin MA754 foil was mechanically ground and polished to a thickness of 45-50 μm with silicon carbide abrasive papers. Electrochemical jet polishing technique in 10% perchloric acid ($HClO_4$) methanol solution T 20 V DC, 0.1 A, and –40°C in liquid nitrogen coolant was used for further thinning.

Potentiodynamic polarization was performed at RT in three different solutions, 0.1 N H_2SO_4, 0.1 N H_2SO_4 + 1 mg/l As_2O_3, and 0.1 N NaOH, under aerated and deaerated conditions. A platinum auxiliary electrode, a saturated calomel reference electrode (SCE) and tested samples as working electrode were accommodated in flat electrochemical cell and exposed to the solutions. The scanning rate was 0.1 mV/s.

Hydrogen permeation was performed using the electrochemical permeation technique [2]. A bi-electrode cell exposed a membrane foil to different solution on two sides, the cathodic and anodic chambers. At the cathodic side, hydrogen was charged from either 0.1 N NaOH or 0.1 H_2SO_4 + 1mg/l As_2O_3 solutions by galvanostatic polarization at –1 mA/cm^2. Hydrogen atoms that diffused through the membrane were oxidized at the anodic side, which was potentiostatically polarized at 0.0 V SCE. Both sides of the electrolytic cell were de-aerated with argon. Then diffusion coefficients were evaluated using the time-lag and the half-rise time methods.

The technique known as hydrogen ingress analysis by potentiostatic pulsing (HIAPP) was used to study atomic hydrogen trapping [3-6]. In this approach, one surface of a sample was charged with hydrogen at a constant potential, E_c, for a time t_c in the range of 0.5~40 s and then the potential was stepped to a more positive value, E_a, which is 5~10 mV negative to the open-circuit potential. At this potential, the un-trapped hydrogen inside the metal is released, resulting in an anodic transient current. The anodic charge, q_a, associated with the anodic transient current is calculated and the entry and trapping parameters are determined by using an appropriate diffusion trapping model. All measurements were performed at room temperature. A conventional three-electrode cell was used in this experiment. A platinum sheet and saturated calomel electrode (SCE) were used as counter and reference electrode, respectively. A bicarbonate buffer solution, 0.5 M $NaHCO_3$ + 0.01 M NaOH + 15ppm As_2O_3 as a hydrogen-entry promoter, was used in the experiment. The electrolyte was de-aerated continuously with argon gas both before and throughout the data acquisition.

The effect of charged hydrogen on mechanical properties was determined using Constant Elongation Rate Tests (CERT). Threaded tensile specimens of MA754 were machined from a block of the material to dimensions specified in ASTM standard E8. Prior to tensile testing, these specimens were polished on a small lathe using strips of sand paper to 4000 grit with an oil based lubricant. After polishing samples were degreased in ethyl alcohol, blown dry, and checked for

dimensional accuracy. CERT of two of the samples was performed in solution during simultaneously charging. These specimens were cathodically polarized using a current density of 1mA/cm^2 in 0.1 N H$_2$SO$_4$ + 1 mg/l As$_2$O$_3$. Two other uncharged samples were pulled in air for comparison). The strain rate was either 10^{-6} or 3x10^{-7} s^{-1}.

3. Results and Discussion

Polarization curves for MA754 and Ni-20Cr alloys measured in aerated and de-aerated 0.1 N H$_2$SO$_4$ as well as in 0.1N H$_2$SO$_4$ + 1 mg/L As$_2$O$_3$ all showed active, active-passive transition and passive regions. However, MA754 shows larger anodic active current densities and passive current densities than those in Ni-20Cr alloys in both aerated and de-aerated solutions, indicating that MA754 is more active than Ni-20Cr. Similar cathodic polarization behavior was observed in both un-deaerated and deaerated solutions. Both MA754 and Ni-20Cr are spontaneously passive in 0.1 NaOH solution.

Figure 1 shows successive charging and discharging transients for Ni-20Cr in 0.1 M NaOH. During charging, the anodic current initially increases gradually, eventually reaching a steady state value. After turning off the cathodic charging current, the hydrogen flux decreases with time. The diffusion coefficients were evaluated by the time-lag and the half-rise time methods and are shown in Table 2 along with other measured and calculated values.
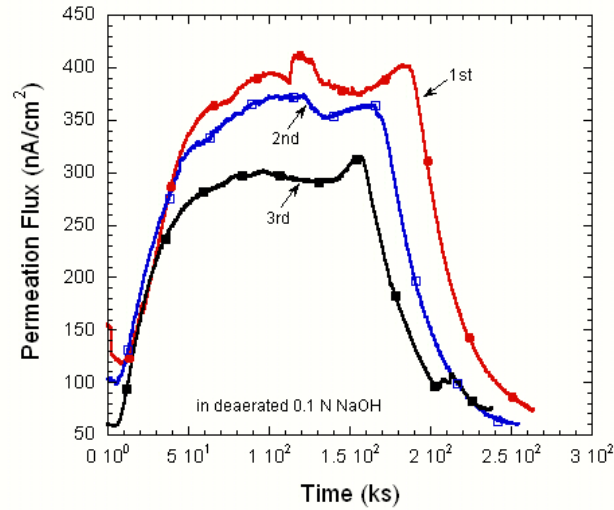
Figure 1. Successive charging and discharging transients for Ni-20Cr in deaerated 0. M NaOH.

Table 2. Data extracted from charging transients in Figure 1, breakthrough time, t$_b$, half rise time, t$_{1/2}$, diffusivities from the two calculations, D$_b$ and D$_{1/2}$, steady state current, i$_{ss}$, and input concentration, C$_0$.

Transient	t$_b$ (ks)	D$_b$ (cm^2/s)	t$_{1/2}$ (ks)	D$_{1/2}$ (cm^2/s)	i$_{ss}$ (nA/cm^2)	C$_0$ (mol/cm^3)
1	12.4	0.83 x10^{-10}	36.9	0.76 x10^{-10}	394.3	2.22x10^{-4}
2	9.3	1.10 x10^{-10}	25.4	1.10 x10^{-10}	362.2	1.54x10^{-4}
3	8.3	1.24 x10^{-10}	23.3	1.20 x10^{-10}	288.6	1.09x10^{-4}

The diffusivity of hydrogen in Ni-20Cr alloy was measured to be around 10^{-10}cm^2/s, which is smaller than the reported data for pure nickel as a result of hydrogen traps associated with Cr solute atoms. In addition, the effective hydrogen diffusivity increased with successive charging transient process, indicating that irreversible traps affected the hydrogen permeation. Consequently, the input concentration of hydrogen, C_0, decreased with transients.

Figure 2 presents a comparison of permeation transients for MA754 and Ni-20Cr. The transient for MA754 is obviously slower, indicating a lower diffusivity. Values of diffusivity taken from the charging and discharging transients are given in Table 3. The diffusivity for MA754 is about half that for Ni-20Cr as a result of the extra traps from the Y$_2$O$_3$ particles.
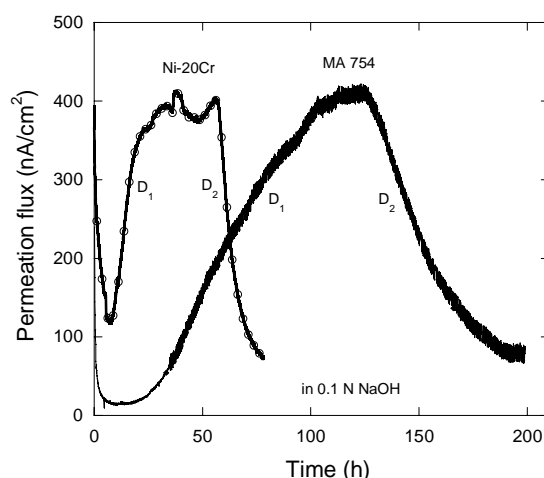
Figure 2. Hydrogen permeation transients for MA 754 and Ni-20Cr alloys in 0.1 N NaOH.

Table 3. Hydrogen diffusivities in Ni-20Cr and MA 754 alloys, D_1 for charging and D_2 for discharging.

Alloy	D_1 (cm^2/s)	D_2 (cm^2/s)
Ni-20Cr	7.6×10^{-11}	1.48×10^{-10}
MA 754	3.4×10^{-11}	8.25×10^{-11}

Figure 3 shows the stress-strain curves for samples of MA754, Waspaloy, and IN600 in air and during charging from CERT experiments at strain rates of 1×10^{-6} and 3×10^{-7} s^{-1}. The Ni-20Cr alloy used in the permeation studies was made in house, and there was insufficient material for CERT testing. Waspaloy is another Ni-based superalloy, but it is higher strength, and thus not a fair comparison with MA754. IN600 is an alloy with strength and ductility measured in typical tensile tests very similar to that of MA754. The curves show that there is less decrease in ductility during charging for MA754 than for either Waspaloy or IN600, suggesting that the Y$_2$O$_3$ particles indeed minimized hydrogen embrittlement susceptibility. The MA754 samples tested during cathodic charging exhibited ductile fracture in the center, but circumferential

secondary cracks on the surface. The embrittlement was clearly limited to the near surface region. A brittle fracture zone about 25μm in depth was observable in the SEM.

a)   b)
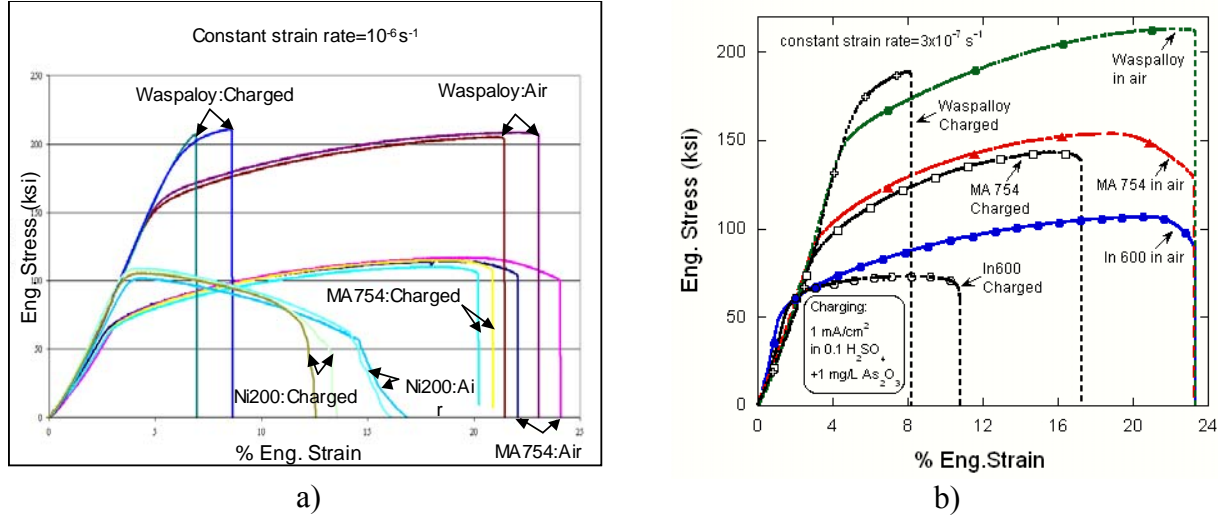
Figure 3. Stress strain curves measured during CERT tests in air and during cathodic charging. Strain rate a) 1×10^{-6} s^{-1} b) 3×10^{-7} s^{-1}.

The current transients resulting from the HIAPP experiments were analyzed using a model in which it was assumed that the hydrogen entry flux across the metal/electrolyte interface was restricted, i.e. an interface control model. According to this model, the total anodic charge is given by Equation 1, where F is the Faraday constant, J is the flux expressed in molcm^{-2} s^{-1}, $q'(\infty)$ is the anodic charge in mCcm^{-2}, k_a is an apparent trapping constant measured for irreversible traps in the presence of reversible traps and t_c is charging time in s.

$$Q'(\infty)=R^{1/2}\{1-e^{-R}/(3.14R)^{1/2}-[1-1/(2R)]erf(R^{1/2})\qquad(1)$$

$$\text{where } Q'(\infty)=q'(\infty)/[FJ(t_c/k_a)^{1/2}], R=k_at_c$$

The rate constant for irreversible trapping, k, is related to k_a by $k=k_a(D_L/D_a)$, where D_a is the apparent trapping diffusivity and D_L is the lattice diffusivity of H in the metal. The irreversible trapping rate constant, k, is the more meaningful parameter as far as hydrogen embrittlement is concerned. The values of k_a and J for the three samples are given in Table 4. If we assumed that D_L and D_a for the three alloys were the same, then k_a would be equal to k. Table 4 shows that MA754 has the lowest value of k_a or k in comparison to the other two alloys. This indicates that MA754 has the lowest intrinsic susceptibility to hydrogen embrittlement. It also has a fairly low value of hydrogen entry flux, J, which means that the build-up of the local concentration of hydrogen necessary to initiate cracking occurs rather slowly. Waspaloy has the highest value of k_a or k and J, indicating that it is more susceptible to HE. These results are in correspondence with the CERT data given above.

Table 4. Values of k_a and J for the three alloys from HIAPP experiments

Alloys	η_c (mv)	E_c (mv/SCE)	k_a (s^{-1})	J (nmolcm^{-2}s^{-1})
MA754	600	-930	$4.6*10^{-9}$	0.75
Ni-20Cr	600	-830	0.0041	0.63
Waspaloy	600	-900	0.079	4.3

4. Conclusions

- The electrochemical corrosion behavior of MA754 and Ni-20Cr is similar in both aerated and dearated acidic and alkaline solutions. In 0.1 N H_2SO_4, anodic curves for both alloys all showed active, passive and transpassive regions. In 0.1 N NaOH, both alloys were spontaneously passive. However, the anodic active current and passive current for MA754 were higher than that for Ni-20Cr alloy; MA754 was more active than Ni-20Cr alloy.

- The diffusion coefficients of MA754 and Ni-20Cr alloy are about 3.4×10^{-11} and 1.10×10^{-10} cm^2/s, respectively. The lower diffusivity for MA754 is the result of trapping associated with the Y_2O_3 particles.

- CERT showed that MA754 was embrittled by hydrogen, but to a lesser extent than either Waspaloy or IN 600.

- The results from HIAPP method showed that MA754 has a lower trap constant than the other alloys, supporting the lower susceptibility to hydrogen embrittlement.

5. Recommendations

Based on the results of this work, it is recommended that MA754 be explored for applications where resistance to hydrogen embrittlement as well as high temperature mechanical properties is required.

6. References

[1] A.W.Thompson and B.A.Wilcox, Scripta Metallurgica, Vol.6, pp689, 1972

[2] M.A.V. Devanathan, Z. Stachurski, Pro, Roy. Soc. London 270A(1962): p90

[3] R. McKibber, B.G. Pound, et al., Acta metall., Vol.35, No.1, 1987,pp253-270.

[4] B.G. Pound, Corrosion, Vol.45. No.1, 1989,pp18-25.

[5] B.G.Pound, Corrosion, Vol.46. No.1, 1990 ,pp50-56.

[6] B.G.Pound, Acta Metal., Vol.38, No.12, 1990, pp2373-2381.

7. Names of Personnel

Gerald Frankel (OSU Faculty Member)
Dallas Hardwick (AFRL/RX Mentor)
N. Gingo (OSU Graduate Student)
X. Liu (OSU Graduate Student)
Z. Sun (OSU Post Doctoral Researcher)

APPENDICES

A. Papers Published

M.D. Uchic, D.M. Dimiduk, R. Wheeler, P.A. Shade, H.L. Fraser, Scripta Mater. 54 (2006) 759-764.

Y.H. Wen, B. Wang, J.P. Simmons and Y. Wang, "A Phase-Field Model for Heat Treatment Applications in Ni-base Alloys, *Acta Mater*. 54, 2087-2099 (2006).

C. Shen, J. P. Simmons and Y. Wang, "Effect of Elastic Interaction on Nucleation – I. Calculation of Strain Energy of Nucleus Formation in Elastically Anisotropic Crystal of Arbitrary Microstructure," *Acta Mater*. 54 (2006) 5617-5630.

C. Shen, J. P. Simmons and Y. Wang, "Effect of Elastic Interaction on Nucleation – II. Simulation Study using Phase Field Method," *Acta Mater*. 55 (2007) 1457-1466.

P.M. Sarosi, B. Wang, Y. Wang and M.J. Mills, "Formation of Multimodal Size Distributions of γ' in a Nicle-Base Superalloy during Interrupted Continuous Cooling," *Scripta Mater.* 57 (2007) 767-770.

C. Shen, J.P. Simmons and Y. Wang, "Simulating Nucleation in Elastically Anisotropic Crystal of Arbitrary Microstructure," Proc. Int. Conf. Solid to Solid Phase Transformations in Inorganic Materials 2005, Vol. 2, ed. JM Howe, DE Laughlin, JK Lee, U. Dahmen and WA Soffa, TMS (The Minerals, Metals & Materials Society), pp375-380 (2005).

NACE poster winner abstract in Materials Performance, Spring 2004, Padgett etal.

Birbilis, N.; Padgett, B. N.; Buchheit, R. G. "Limitations in microelectrochemical capillary cell testing and transformation of electrochemical transients for acquisition of microcell impedance data." Electrochimica Acta (2005), 50(16-17), 3536-3544.

M. Groeber, B. Haley, M. Uchic and S. Ghosh. "Microstructural Characterization Using 3-D Orientation Data Collected by an Automated FIB-EBSD System". *Numiform 8* proceedings, 2004.

M. Groeber, B. Haley, M. Uchic, D. Dimiduk, and S. Ghosh. "Towards 3D Reconstruction and Characterization of Polycrystalline Microstructures Using a FIB-SEM System," Materials Charaterization, 2006.

M. Uchic, M. Groeber, D. Dimiduk, and J. Simmons. "3D Microstructural Characterization of Nickel Superalloys via Serial-Sectioning Using a Dual Beam FIB-SEM," Scripta Materialia, 2006.

M. Groeber, Y. Bhandari, M. Uchic, D. Dimiduk, and S. Ghosh. "An Automated Framework for Microstructure Characterization and Representation" *MMM 2006* proceedings, 2006.

M. Groeber, M. Uchic, D. Dimiduk, and S. Ghosh. "Development of a Robust 3D Characterization-Representation Framework for Modeling Polycrystalline Materials" JOM, 2007.

Y. Bhandari , S. Sarkara, M. Groeber, M.D. Uchic , D.M. Dimiduk, and S. Ghosh. "CAD Based Representation of 3D Polycrystalline Microstructures from FIB Generated Serial Sections for FE Analysis" Computational Materials Science, 2007.

A.D. Rollett, A.P. Brahme and C.G. Roberts, "An overview of accomplishments and challenges in recrystallization and grain growth", Proc. 3rd Intl. Conf. on Recrystallization and Grain Growth, Jeju, Korea, June 2007, S.-J. L. Kang *et al*., eds., Materials Science Forum, Volume 550, pp 33-44 (2007).

C.G. Roberts, S.L. Semiatin and A.D. Rollett, "Particle-Associated Misorientation Distribution in a Nickel-Base Superalloy", *Scripta materialia*, 56, 899-902 (2007).

C.G. Roberts, S.L. Semiatin and A.D. Rollett, "A Parametric Study of Grain Growth during Annealing of Ingot Macrostructures", Materials Solutions 2005, CD-ROM.

B. Papers Submitted

B. Wang, Y.H. Wen, J.P. Simmons and Y. Wang, "Systematic Approach to Microstructure Design of Ni-Base Alloys Using classical Nucleation and Growth Relations Coupled with Phase Field Modeling," *Met. Trans. A.* (2007-in press).

Y. Bhandari , M. Groeber, S. Ghosh. "CAD Based Reconstruction of 3D Polycrystalline Alloy Microstructures from FIB Generated Serial Sections" CAD, Accepted.

S. Manchiraju, M. Groeber, and S. Ghosh. "A Dual-Time Scale Finite Element Model for Simulating cyclic Deformation of Polycrystalline Alloys" Met. Trans. A, In Review.

M. Groeber, Y. Bhandari, M. Uchic, D. Dimiduk, and S. Ghosh. "A Framework for Automated 3D Microstructure Analysis and Representation" JCAMD, Accepted.

M. Groeber, M. Uchic, D. Dimiduk, and S. Ghosh. "A Framework for Automated Analysis and Simulation of 3D Polycrystalline Microstructures, Part 1: Statistical Characterization" Acta Materialia, Accepted.

M. Groeber, M. Uchic, D. Dimiduk, and S. Ghosh. "A Framework for Automated Analysis and Simulation of 3D Polycrystalline Microstructures, Part 2: Synthetic Structure Generation" Acta Materialia, Accepted.

D. M. Norfleet, D. M. Dimiduk, M. Uchic, and M. J. Mills "Examination of Forest-Dislocation Hardening Within Pure Ni Microcrystals," *Acta materialia,* submitted for publication.

C. Papers Prepared

B. Wang, Y.H. Wen, J.P. Simmons and Y. Wang, "Optimization of Phase Field Model Inputs through Experimental Calibrations" (manuscript in preparation).

D. M. Norfleet, D. M. Dimiduk, M. Uchic, and M. J. Mills "Size-Scale Effects in Titanium Alloy Microcrystals," *Acta materialia,* prepared for publication.

D. M. Norfleet, D. M. Dimiduk, M. Uchic, M. Wagner, G. E. Eggeler and M. J. Mills "Pseudoelasticity in Ni-Ti Microcrystals," *Acta materialia,* prepared for publication.

D. Presentations/Posters Given

MS&T 2006, Cincinnati, Shade etal.

MRS 2006 Fall Meeting, Boston, Shade etal.

2007 International Workshop on Small Scale Plasticity, Braunwald, Switzerland, Shade etal.
B. Wang, C. Shen and Y. Wang, "Developing Phase Field Method into Engineering Design Tool by Linking to CALPHAD," ASM International's 14th Annual AeroMat Conference and Exposition, Dayton, Ohio, June 9-12, 2003.

J.P. Simmons, Y.H. Wen, C. Shen and Y. Wang, Invited, "Phase Field as an Engineering Tool for Heat Treatment Applications," 2003 TMS Annual Meeting, San Diego, CA, March 2-6, 2003.

C. Shen, Q. Chen, Y. Wen, J.P. Simmons and Y. Wang, "Phase Field Method and Quantitative Microstructure Modeling," 2003 TMS Annual Meeting, San Diego, CA, March 2-6, 2003.

Q. Chen, B. Wang, C. Shen, Y. Wen, J.P. Simmons and Y. Wang, "Quantitative Phase Field Modeling of Microstructural Evolution," 2003 TMS Fall Meeting, Materials Science and Technology 2003, Chicago, Illinois, November 9-12, 2003.

Y. Wen, S.A. Kajihara, J.P. Simmons, Q. Chen and Y. Wang, Invited, "3-Dimensional Phase Field Model for Heat Treatment Applications," 2003 TMS Fall Meeting, Materials Science and Technology 2003, Chicago, Illinois, November 9-12, 2003.

Y. Wang, Colloquium Speaker, "Modeling Complex Microstructures," Department of MSE, University of Wisconsin Madison, Madison, January 29, 2004.

B. Wang, C. Shen and Y. Wang, "Developing the Phase Field Method into Engineering Design Tool for Microstructural Evolution," ASM International's 15th Annual AeroMAT Conference and Exposition, Seattle, WA, June 7-10, 2004.

Y. Wang, Invited, "Modeling Complex Microstructures in Advanced Engineering Alloys," AFOSR Workshop on Linking Processing, Microstructure and Property Modeling, Freiburg, Germany, May 2-5, 2004.

Y. Wang, Invited, "Development of Phase Field Models of Micromechanics and Microstructural Evolution for the Prediction of Microstructure-Property Relationships in Advanced Structural Materials," International Conference on Advanced Materials Design and Development, ICAMDD, Goa, India, 14-16 December 2005.

Y. Wang, Colloquium Speaker, "Modeling Complex Microstructures Using Phase Field Method," Virginia Tech., Blacksburg, Virginia, Feb. 4, 2005.

Y. Wang, Invited, "Development of Phase Field Models of Micromechanics and Microstructural Evolution for the Prediction of Microstructure-Property Relationships in Advanced Structural Materials," International Conference on Advanced Materials Design and Development, ICAMDD, Goa, India, 14-16 December 2005.

N. Ma, B. Wang and Y. Wang, Invited, "Application of Thermodynamic Database to Phase Field Modeling of Microstructural Evolution in Complex Multicomponent and Multiphase Alloys," TMS2006 135th Annual Meeting, San Antonio, Texas, March 12-16, 2006.

J.P. Simmons, Y. Wen, B. Wang and Y. Wang, Invited, "Phase Field Modeling Qualitative and Quantitative Microstructural Evolution in Ni-Base Alloys," The 135th TMS Annual Meeting, San Antonio, TX, USA, 03/12/2006 - 03/16/2006.

C. Shen, B. Wang, M.J. Mills and Y. Wang*, Invited, "Multiscale Phase Field Modeling of Microstructural Evolution and Deformation Mechanisms during Creep of Ni-Base Superalloys," Symposium A: Superalloys, the International Conference on Aerospace Materials, the 2006 Beijing International Materials Week, China, June 25-28, 2006.

B. Wang, Y. Wen, JP. Simmons and Y. Wang, "Formation of Bimodal Particle Size Distribution in Ni-Al – A Simulation Study using Phase Field Method", Symposium on Solid-State Nucleation and Critical Nuclei during First Order Diffusional Phase Transformations, MS&T'06, Cinergy Center, Cincinnati, Ohio, October 15-19, 2006.

C. Shen, J. Li, MJ. Mills and Y. Wang, Invited, "Multiscale Phase Field Modeling of γ' Precipitation and Deformation in Ni-Base Superalloys," 2006 MRS Fall Meeting, Boston, MA, November 27-December 1, 2006.

C. Shen, J. Li and Y. Wang*, Plenary, "Phase Field Modeling of Structural Phase Transformations and Plastic Deformation in Crystalline Solids: Effect of Extended Defects," International Conference on Materials Behavior: Far From Equilibrium (MBFE2006), Mumbai, India, December 14-16, 2006.

C. Shen, J. Li, M.J. Mills and Y. Wang, Invited, "Multi-Scale Phase Field Modeling of Phase Transformation and Plastic Deformation in Ni-Base Superalloys," Symposium on Properties and Performance of High Temperature Alloys and Coatings, 2007 (136th) TMS Annual Meeting, Walt Disney World Swan and Dolphin Hotel, Orlando, Florida, Feb. 25 – March 1, 2007.

Y. Wang, Keynote, "Development of Physics-Based Models of Microstructure Evolution during Phase Transformation and Plastic Deformation," International Symposium on Plasticity and its Current Applications, Alyeska Prince Hotel, Alaska, June 2-6, 2007.

Y. Wang, Colloquium Speaker, "Integrated Experimental and Computational Study of Microstructural Evolution during Phase Transformation and Plastic Deformation in Ni-Base Superalloys," LEM, CNRS/ONERA, Paris, France, July 10, 2007.

Padgett, Barbara N.; Paglia, Christian; Buchheit, R. G. "Characterization of corrosion behavior in friction stir weld Al-Li-Cu AF/C458 alloy". Friction Stir Welding and Processing II, Proceedings of a Symposia [held during the] TMS Annual Meeting, 2nd, San Diego, CA, United States, Mar. 2-6, 2003 (2003), 55-64.

TMS Spring 2001, New Orleans, LA, Padgett etal.

TMS Fall 2001, Indianapolis, Padgett etal.

TMS Spring 2003, San Diego, CA, Padgett etal.

NACE Spring 2004, New Orleans, Padgett etal.

NACE Spring 2006, San, Diego, CA, Padgett etal.

Gordon Research Conference Summer 2006, New London, NH, Padgett etal.

M. Groeber, B. Haley, M. Uchic, D. Dimiduk and S. Ghosh, "Microstructural Characterization Using 3-D Orientation Data Collected by an Automated FIB-EBSD System", *Numiform*, Columbus, OH, USA, June, 2004.

M. Groeber, B. Haley, M. Uchic, D. Dimiduk and S. Ghosh, "Microstructural Characterization Using 3-D Orientation Data Collected by an Automated FIB-EBSD System", *ASM*, Columbus, OH, USA, October, 2004.

M. Groeber, Y. Bhandari, M. Uchic, D. Dimiduk and S. Ghosh, "Advances in computational modeling through the use of higher-level microstructure characterization", *Materials Characterization*, Portland, ME, USA, November, 2005.

M. Groeber, Y. Bhandari, M. Uchic, D. Dimiduk and S. Ghosh, "Reconstruction and Characterization of 3D Microstructures: An Unbiased Description of Grain Morphology", *TMS*, San Antonio, TX, USA, March, 2006.

M. Groeber, Y. Bhandari, M. Uchic, D. Dimiduk and S. Ghosh, "An Automated Framework for Microstructure Characterization and Representation", *Multiscale Materials Modeling*, Freiburg, Germany, September, 2006.

M. Groeber, M. Uchic, D. Dimiduk and S. Ghosh, "An Automated Framework for Microstructure Characterization and Representation, Part 1: Characterization", *TMS*, Orlando, FL, USA, February, 2007.

M. Groeber, M. Uchic, D. Dimiduk and S. Ghosh, "An Automated Framework for Microstructure Characterization and Representation, Part 2: Modeling", *TMS*, Orlando, FL, USA, February, 2007.

S. Polasik, "Ultra Small-Scale Mechanical Testing," Materials Science & Technology 2003, November 9-12, 2003, Chicago, IL

S. Polasik, "Fabrication and Testing of Ultra Small-Scale Samples," 2004 TMS Annual Meeting & Exhibition, March 14-18, 2004, Charlotte, NC

S. Polasik, "A Practical Method for Extracting TEM Foils from Micropillar Compression Specimen," Materials Science & Technology 2004, September 27-30, 2004, New Orleans, LA

D. M. Norfleet, "Correlating Changes in Dislocation Substructures to Plasticity Size-Effects in Nickel and Titanium Alloys", MS&T Meeting, March 2006, San Antonio

D.M. Dimiduk, "Examination of Lattice Rotations in Deformed Ni Microcrystals," MS&T 2007, March 2007, Orlando, FL

D. M. Dimiduk, "Mesoscopic Size-Effects in Athermal Microcrystal Plasticity", International Workshop on Small Scale Plasticity, September 2007, Braunwald, Switzerland

"Characterization of Grain Growth Behavior in a Nickel-Base Alloy," Materials Science & Technology 2006 conference (MS&T'06), September 2006, Cincinnati, OH., Roberts etal.

"Application of a Parallel Monte Carlo Method to Particle Pinning Stabilization of Grain Size in Waspaloy," Materials Science & Technology 2006 conference (MS&T'06), September 2006, Cincinnati, OH., Roberts etal.

"Grain Growth Behavior in Waspaloy," Carnegie Mellon MRSEC, April 2006, Pittsburgh, PA.
"Adventures with a Parallel Monte Carlo Code," Carnegie Mellon MRSEC, February 2006, Pittsburgh, PA., Roberts etal.

"Parametric Study of Grain Growth during Annealing of an Ingot Macrostructure," Materials Science & Technology 2005 conference (MS&T'05), poster session, September 2005, Pittsburgh, PA., Roberts etal.

Annual TMS 2002 Fall Meeting, Columbus, OH, Roberts etal.

Materials Science and Technology 2003, Chicago, IL, Roberts etal.

Microscopy and Microanalysis Conference 2004, Savannah, GA, 2 Invited Talks Roberts etal.

Materials Science and Technology 2004, New Orleans, LA, Roberts etal.

Microscopy and Microanalysis Conference 2004, Honolulu, HI, 2 Presentations Roberts etal

Materials Science and Technology 2005, Pittsburg, PA, Roberts etal.

Annual TMS Meeting 2006, San Antonio, TX, Roberts etal.

Microscopy and Microanalysis Conference, 2006, Chicago, IL, Roberts etal.

International Congress of Microscopy Conference, September 2006, Japan, Roberts etal.

Annual TMS Meeting 2007, Orlando, FL, Roberts etal.

Microscopy and Microanalysis Conference 2007, Fort Lauderdale, FL, Roberts etal.

Peterson BP, Collins PC, Fraser HL. "*Progress towards the Development of a Creep-Resistant Beta Titanium Alloy based on Timetal-21S*," AeroMat 2007, Baltimore, MD, June 2007.

Peterson BP, Collins PC, Evans D, Martin P, Williams J, and Fraser HL. "*Progress towards the Development of a Creep-Resistant Beta Titanium Alloy based on Timetal-21S*," TMS 2007, Orlando, FL, February 2007.

Peterson BP, Collins PC, Evans D, Martin P, Fox S, Williams J, and Fraser HL. "*A Combinatorial Approach to the Elemental Optimization of a Beta Titanium Alloy for Elevated Temperature Application*," TMS 2006, San Antonio, TX, March 2006**.**

E. Theses

Billie Wang: "Development, Calibration, Optimization and Validation of a Hybrid Approach to Microstructure Design in Ni-Base Superalloys," (Ph.D. Dissertation, in preparation)

 "Stress Corrosion Cracking Behavior of AA2099", Barbara N. Padgett (in-progress)

M. Groeber, "Development of an Automated Characterization-Representation Framework for the Modeling of Polycrystalline Materials in 3D", *The Ohio State University*, 2007.

Stephen Polasik, "Accelerated Assessment and Representation of Materials Behavior Via Integrated Electron-Optical, Focused Ion Beam and MEMS-Based Characterization Methods," The Ohio State University, 2005. (M.S. Thesis)

David M. Norfleet, "Sample Size Effects Related to Nickel, Titanium and Nickel-Titanium at the Micron Size Scale," The Ohio State University, 2007. (PhD. Thesis)

Christopher Roberts, "Grain Growth and Zener Pinning Phenomena: A Computational and Experimental Investigation," Carnegie Mellon University, 2007.